UNIVERSITY OF CALIFORNIA SAN DIEGO

Advances in Ultrasonic Methods for Damage Imaging and Elastic Constant Identification in Structural Components

A Dissertation submitted in partial satisfaction of the requirements
for the degree Doctor of Philosophy

in

Structural Engineering

by

Chengyang Huang

Committee in charge:

Professor Francesco Lanza Di Scalea, Chair
Professor William S Hodgkiss
Professor Hyonny Kim
Professor Michael D Todd

2024

The Dissertation of Chengyang Huang is approved, and it is acceptable in quality and form for publication on microfilm and electronically.

University of California San Diego

2024

DEDICATION

To my wife, Jennie, for your unwavering belief in me. Through challenging times and moments of doubt, you always stood by my side. This thesis is as much yours as it is mine.

To my parents, Mrs. Bo Zhang and Prof. Jianhua Huang, who supported me every step of my way. Thank you for believing in my decision to pursue this tough but rewarding career path.

To my mentor Prof. Francesco Lanza di Scalea, for your guidance, wisdom, and encouragement throughout this journey. I have gained not only the skills to succeed in academia, but also the maturity to live as a responsible man for my family. I will strive to pursue the same curiosity, dedication, and integrity that you embody so well throughout your career.

To Prof. Bill Kuperman, who was not only a pivotal member of my dissertation committee but also an extraordinary mentor who shaped my approach to research, critical thinking, and perseverance. You are deeply missed, but never forgotten.

TABLE OF CONTENTS

LIST OF FIGURES

ACKNOWLEDGEMENTS

This dissertation was funded by the U.S. Federal Railroad Administration under contract no. 693JJ619C000008 (Dr. Robert Wilson, Program Manager), MxV Rail through a University Grand Challenge Contract no. 24-0312-008622 (Dr. Anish Poudel, Program Manager), and the Federal Aviation Administration Joint Center of Excellence for Advanced Materials under FAA Cooperative Agreement 12-C-AM-UCSD (Mr. Lynn Pham, Program Manager). A special thanks to Dr. Anish Poudel and Mr. Brian Linderman at MxV Rail (former Transportation Technology Center) for arranging all the rail sections found in this dissertation along with other technical support. I would also like to acknowledge Mr. Gavin Dao and his team at Advanced OEM Solutions (West Chester, OH, USA) for providing technical advice on SAFT hardware solutions.

I wish to express my deepest gratitude to my advisor, Prof. Francesco Lanza di Scalea, for granting me the invaluable opportunity to embark on this remarkable journey. The example he has set over these difficult years, not only as a mentor but also as a devoted father, has profoundly influenced the way I view and interact with the world. Thank you, sir, for your unwavering commitment to nurturing my intellectual curiosity and helping me develop as an independent researcher. It would be a great honor to continue my academic career and personal life guided by the integrity and wisdom I've gained from him. I wish all the best to him and his lovely children.

I would also like to thank my dissertation committee for all the collaborations and support over the years. A special thank you to Prof. William Kuperman who was originally one of the esteemed members of the committee and passed away months before my defense. Discussing my research with you was one of the most challenging yet rewarding aspects of my PhD journey, as your brilliance in signal processing always pushed me to grow. I especially value the critiques I received from you, knowing they came from a place of honesty and a commitment to excellence.

I have the deepest respect for the unwavering integrity and pursuit of truth that has defined your entire career. I would also like to extend my heartfelt thanks to Prof. Michael Todd for his leadership in the department and his steadfast support during difficult times, to Prof. Hyonny Kim for years of collaboration and invaluable guidance in fostering teamwork, and to Prof. William Hodgkiss for his warm and generous support to serve in my committee following the passing of Prof. Kuperman. Thanks are extended to SE faculty members Prof. Petr Krysl for serving in my preliminary exam, and Prof. Alessandro Palermo and Prof. Qiang Zhu for supporting me through teaching assistantships.

This journey would not have been the same without my amazing colleagues: Albert Yi-Ling Liang, Ranting Cui, Diptojit Datta, Guillermo Azuara, Ali Zare Hosseinzadeh, and Izabela Batista. A special thanks to Prof. Ranting Cui and Dr. Simone Sternini for guiding me at the very first stage of my graduate study, and to Prof. Margherita Capriotti for kindly sharing her old data that led to my first journal publication. I would also like to acknowledge the collaboration with the members of the advanced composites and aerospace structures lab that contributed a lot to my dissertation: Chaiane Wiggers de Souza, Benjamin Katko and Janelle Dela-cueva.

I would like to thank all my friends in San Diego and that represented a fundamental part of my life during these years: Xiaohan Fu, Guofeng Qian, Cindy Xiao, Xinqi Mao, Sijia Li, Di Guan, Mufeng Xie, You Jiang, Chunhao Shen, Xu Shang, Yining Cao, Kexin Feng, Jiaxiang “Jim” Ma, Jin Huangfu, Yuntian Zhao, Xihe Gu, Ziling Yuan, Yang Liu, Bingjiang Wang, Hanyang Feng, Youwei Liang, Boning Yang, Chenyang An, Jiayun Zhang, Shuheng “Alan” Li, and many others! As I write this, it’s hard to believe how many wonderful friendships I’ve formed and the countless cherished memories I’ve gathered over the years. Thank you all for being the best friends that I could have ever asked for!

I am deeply grateful to my mom and dad for their unyielding support. Their love has been the driving force that carried me through even the most difficult moments, helping me move forward when I needed it most. I would also like to express my heartfelt thanks to Prof. Yanfeng Shen, who mentored me during my undergraduate years and introduced me to this incredible field and Prof. Lanza. Your unwavering belief in my academic journey and the exemplary role model you provided before I began my PhD have been a constant source of inspiration.

A special mention goes to my wife Kexin "Jennie" Weng. Before I met her, my career was unraveling, and my life seemed headed for despair. Her unwavering support and encouragement propelled me to reach heights I never thought possible in the second half of my PhD journey. I would like to take this moment to express my gratitude to Prof. Yongxing Shen for offering me the chance to serve as his teaching assistant seven years ago. That opportunity led me to meet the woman who would later become the love of my life, though at the time, she was simply one of my students (note: the dating part came years after the TA job).

This dissertation is a collection of papers that have been published in the past five years.

Chapter 2, in full, is a reprint of the material as it appears in C. Huang and F. Lanza di Scalea, "Application of sparse synthetic aperture focusing techniques to ultrasound imaging in solids using a transducer wedge," *IEEE Transactions on Ultrasonics, Ferroelectrics, and Frequency Control*, vol. 71, no. 2, pp. 280-294, 2024. The dissertation author was the primary investigator and author of this paper.

Chapter 3, in part, is a reprint of the material as it appears in C. Huang and F. Lanza di Scalea, "Rail Flaw Imaging Prototype Based on Improved Ultrasonic Synthetic Aperture Focus Method," *Materials Evaluation*, vol. 82, no. 1, pp. 51-59, 2024. Chapter 3 also contains unpublished material coauthored with F. Lanza di Scalea and A.Z. Hosseinzadeh in "Towards

Efficient 3D Imaging of Internal Rail Flaws in Motion," *Mid-year Report to MxV Rail AAR University Programs* (24 pages), MxV Rail contr. 24-0312-008622, August 2024. The dissertation author was the primary investigator and author of this chapter.

Chapter 4, in full, is a reprint of the material as it appears in C. Huang, A.Z. Hosseinzadeh, and F. Lanza di Scalea, "Ultrasparse Ultrasonic Synthetic Aperture Focus Imaging by Passive Sensing," *IEEE Transactions on Ultrasonics, Ferroelectrics, and Frequency Control*, vol. 71, no. 5, pp. 518-535, 2024. The dissertation author was the primary investigator and author of this paper.

Chapter 5, in full, is a reprint of the material as it appears in C. Huang and F. Lanza di Scalea, "High Resolution Ultrasonic Imaging of Extended Targets via Combined Match Field and Time Delay Beamforming," *Ultrasonics*, vol. 145, p. 107464, 2025. The dissertation author was the primary investigator and author of this paper.

Chapter 6, in part, is a reprint of the material as it appears in C. Huang, A.Z. Hosseinzadeh, and F. Lanza di Scalea, "Damage Imaging in Stiffened Composite Panels by Ultrasonic Sparse Array Matched Field Processing," in *Proceedings of American Society for Composites 39th Annual Technical Conference*, 2024. The dissertation author was the primary investigator and author of this paper.

Chapter 7, in full, is a reprint of the material as it appears in C. Huang and F. Lanza di Scalea, "An Ultrasonic Scanning System for the Inspection of Composite Stiffened Panels from Elastic Constant Identification via Inversion of Guided Waves," *Composite Structures*, vol. 322, p. 117373, 2023. The dissertation author was the primary investigator and author of this paper.

VITA

2019 Bachelor of Science in Mechanical Engineering, University of Michigan-Shanghai Jiao Tong University Joint Institute

2021 Master of Science in Structural Engineering, University of California San Diego

2024 Doctor of Philosophy in Structural Engineering, University of California San Diego

PUBLICATIONS

JOURNAL ARTICLES

1. **C. Huang** and F. Lanza di Scalea, "High Resolution Ultrasonic Imaging of Extended Targets via Combined Match Field and Time Delay Beamforming," *Ultrasonics*, vol. 145, p. 107464, 2025.

2. **C. Huang**, A.Z. Hosseinzadeh, and F. Lanza di Scalea, "Ultrasparse Ultrasonic Synthetic Aperture Focus Imaging by Passive Sensing," *IEEE Transactions on Ultrasonics, Ferroelectrics, and Frequency Control*, vol. 71, no. 5, pp. 518-535, 2024.

3. **C. Huang** and F. Lanza di Scalea, "Rail Flaw Imaging Prototype Based on Improved Ultrasonic Synthetic Aperture Focus Method," *Materials Evaluation*, vol. 82, no. 1, pp. 51-59, 2024.

4. **C. Huang** and F. Lanza di Scalea, "Application of sparse synthetic aperture focusing techniques to ultrasound imaging in solids using a transducer wedge," *IEEE Transactions on Ultrasonics, Ferroelectrics, and Frequency Control*, vol. 71, no. 2, pp. 280-294, 2024.

5. **C. Huang** and F. Lanza di Scalea, "An Ultrasonic Scanning System for the Inspection of Composite Stiffened Panels from Elastic Constant Identification via Inversion of Guided Waves," *Composite Structures*, vol. 322, p. 117373, 2023.

CONFERENCE PROCEEDINGS

1. **C. Huang**, A.Z. Hosseinzadeh, and F. Lanza di Scalea, "Damage Imaging in Stiffened Composite Panels by Ultrasonic Sparse Array Matched Field Processing," *Proceedings of American Society for Composites 39th Annual Technical Conference*, San Diego, CA, 2024.

2. **C. Huang** and F. Lanza di Scalea, "Nondestructive Ultrasonic Testing of Aerospace Composite Parts via Efficient Inversion of Elastic Constants," *Proceedings of American Society for Composites 39th Annual Technical Conference*, San Diego, CA, 2024.

3. F. Lanza di Scalea, **C. Huang**, and A.Z. Hosseinzadeh, "Passive ultrasonic sensing for NDT and SHM," *Proceedings of SPIE Smart Structures + Nondestructive Evaluation*, Long Beach, CA, 2024.

4. F. Lanza di Scalea, **C. Huang**, and A.Z. Hosseinzadeh, "Passive ultrasonic beamforming for fast and efficient imaging," *Proceedings of SPIE Smart Structures + Nondestructive Evaluation*, Long Beach, CA, 2024.

5. **C. Huang** and H. Xu, "Improvements on Focused Tactile Feedback using Time Reversal Mirror," Best student paper award (1st place), *Proceedings of SPIE Smart Structures + Nondestructive Evaluation*, Long Beach, CA, 2024.

6. F. Lanza di Scalea, **C. Huang**, and A.Z. Hosseinzadeh, "Ultrasparse Ultrasonic Synthetic Aperture Beamforming via Passive Sensing," *The Journal of the Acoustical Society of America*, vol. 155, no. 3, p. A101, 2024.

7. **C. Huang** and Lanza di Scalea, "Ultrasound Time Reversal Imaging of Extended Targets using a Broadband White Noise Constraint Processor," *Proceedings of SPIE Medical Imaging*, San Diego, CA, 2023.

8. **C. Huang**, J. Dela-Cueva, B. Katko, H. Kim, and F. Lanza di Scalea, "An Ultrasonic Scanning System for Damage Detection in Composite Built-up Aerospace Panels by Inversion of Guided Wave Dispersion Curves," *Proceedings of SPIE Smart Structures + Nondestructive Evaluation*, Long Beach, CA, 2023.

9. **C. Huang** and F. Lanza di Scalea, "High Resolution Real Time Synthetic Aperture Imaging in Solids Using Virtual Elements," *Proceedings of ASME International Mechanical Engineering Congress and Exhibition*, Columbus, OH, 2022.

10. **C. Huang** and F. Lanza di Scalea, "Improvements to the Ultrasound Synthetic Aperture Technique for Defect Imaging in Solids," *abstract and presentation at the 18th European Mechanics of Materials Conference*, Oxford, UK, 2022.

11. **C. Huang** and F. Lanza di Scalea, "Ultrasonic Imaging in Solids Using Time Reversal Operator and Coherent Matched Field Processing," *Proceedings of SPIE Smart Structures + Nondestructive Evaluation*, virtual, 2021.

ABSTRACT OF THE DISSERTATION

Advances in Ultrasonic Methods for Damage Imaging and Elastic Constant Identification in Structural Components

by

Chengyang Huang

Doctor of Philosophy in Structural Engineering

University of California San Diego, 2024

Professor Francesco Lanza di Scalea, Chair

Ultrasonic testing plays a crucial role in the fields of Non-Destructive Evaluation (NDE) and Structural Health Monitoring (SHM) by enabling the accurate detection and characterization of defects, material properties, and structural integrity without causing damage and, in many instances, without requiring disassembly. This dissertation presents recent advances in the science of ultrasonic testing for NDE and SHM, specifically in applications of (1) ultrasonic imaging of bulk solids and waveguide structures, and (2) identifying the elastic constants in composite panels by wave propagation inversion. Under the ultrasonic imaging topic, active modalities in the Synthetic Aperture Focusing Technique (SAFT) with Delay-And-Sum (DAS) algorithms are

applied to image defects in bulk solids using a linear array mounted on a transducer wedge. Two prototype systems have been constructed to demonstrate quasi real-time 3D imaging of internal flaws in railroad rails using several enhancements in the SAFT methods for improved imaging quality and speed. Additionally, a passive SAFT scheme is proposed utilizing signal deconvolution with a Normalized Cross-Power Spectrum (NCPS) analysis in a dual-output system. This method enables efficient reconstruction of pure transfer functions (or Green's functions) between receivers and demonstrates ultrafast imaging capabilities. Next, the Coherent White Noise Constraint (C-WNC) algorithm is introduced for super-resolution ultrasonic imaging in bulk solids using a linear array. Unlike traditional MUltiple SIgnal Classification (MUSIC) beamformers, C-WNC avoids subspace factorization while offering high dynamic range and precise focus on extended targets through its broadband and adaptive beamforming capabilities. The C-WNC algorithm is also applied to defect imaging in stiffened composites in aerospace structures with embedded sparse transducer array, exploiting the multimodal and dispersive nature of ultrasonic guided waves through data-driven match field modeling. Under the property identification topic, the dissertation presents a non-contact ultrasonic scanning system for the in-situ elastic constant inversion in stiffened composite aerospace panels subjected to impacts. This kind of non-destructive inspection that tracks the elastic constants is shown to be quite effective to detect and quantify impact damage in these structural components. Using the Semi-Analytical Finite Element (SAFE) method as a forward model, the inversion process minimizes the mismatch between experimental and predicted dispersion curves of the propagating guided waves via simulated-annealing optimization. A method is developed for efficient extraction of the dispersion curves by using only two measurement points, i.e. without the need for multiple measurement locations that are instead needed in conventional 2D-FFT techniques.

Chapter 1 Introduction

Structural Health Monitoring (SHM) is essential for ensuring the safety, reliability, and longevity of critical engineering assets in aerospace, ground transportation, and civil infrastructure. Without timely detection and appropriate intervention, material defects or structural damage can compromise the integrity of these systems, potentially leading to catastrophic failures. Hence, the identification and quantitative characterization of such damage, commonly referred to as quantitative non-destructive evaluation (NDE) [1], are of paramount importance yet pose significant challenges. Through quantitative NDE, when a flaw is detected and its size is determined to be beyond acceptable limits, several remediation options are available [2]. These include replacing or repairing the affected component, allowing the component to remain in service if the risk of failure is considered minimal, altering its operational parameters, or conducting more refined measurements of the flaw. Implementing these timely interventions can prevent further material degradation, reduce the likelihood of system failure, and ensure the reliability, structural integrity, and durability of the asset. Moreover, these measures offer substantial economic and societal benefits by enhancing system safety and performance.

Among the various techniques developed for SHM and NDE, ultrasonic testing is particularly well-suited for detecting and sizing flaws embedded within materials or originating from inaccessible surfaces [3]. Several factors contribute to its suitability:

1. **Deep Penetration Capability**: Ultrasonic bulk waves can propagate through thick, solid components, making ultrasonic testing effective for detecting flaws located deep beneath the inspection surface, in contrast to methods like Eddy current testing and potential-drop

techniques, which are limited to surface-adjacent flaws, or visual and penetrant testing, which can only identify surface defects [4].

2. **Wide Area Capacity:** Ultrasonic guided waves can propagate over long distances, making them highly effective for inspecting large areas of waveguide structures, such as pipelines, rails, and aircraft fuselages [5]. This wide-area coverage enables the detection of defects over extended regions from a single sensor location, significantly reducing the number of sensors required and improving the efficiency of inspections in complex or hard-to-access structures.
3. **Sensitivity to Various Defect Types**: Ultrasonic waves are sensitive to a range of flaw types such as porosity, cracks and inclusions, allowing not only the detection but also the characterization of defect location, size and shape [6].
4. **Material Versatility**: Ultrasonic testing is applicable to a wide range of materials, including metals, composites, concrete, and additive-manufactured 3D materials.
5. **Safety**: Ultrasonic testing is inherently safe, unlike methods such as radiography, which involve radiation and require stringent protective measures.
6. **Availability and Portability**: Commercial ultrasonic testing equipment is widely available and often portable, making it suitable for on-site inspections [7].

The interaction between ultrasonic waves and structural defects can significantly affect ultrasonic wave propagation through mechanisms such as reflection, scattering, and mode conversion. A typical damage identification scheme via ultrasonic waves involves the following:

1. **Activation and reception of ultrasonic waves:** The source can be either controlled (e.g. a transducer) or uncontrolled (e.g. ambient vibrations). The arrangement of the transducers (an array) determines the coverage of inspected medium (single beam, limited or full angular

view). Various modalities can be employed depending on the application, e.g. pulse-echo, pitch-catch, passive sensing, etc.

2. **Feature extraction from the received signals:** e.g. time-of-flight (TOF), amplitude, frequency content, etc. Typically, a model of wave propagation should be established at this stage, involving the understanding of the propagating wave modes and their interaction with the structure defects of interest.
3. **Interpretation of the extracted features and correlation to damage severity.** When multiple transducers are employed, a fusion of the features should be performed. The coherence among features captured by different transducers is exploited to enhance the accuracy and reliability of the final decision making.
4. **Analysis of Time Histories of Acquired or Processed Data**: In SHM applications, it is essential to track the evolution of identified defects to effectively monitor the progression of structural damage over time.

An example of basic ultrasonic testing in solid NDE is explained below [2]. A-scan techniques are widely used in metal, welding, and composite inspection. A single transducer emits ultrasonic pulses of bulk wave modes (either longitudinal or transverse) into the material, and the reflected signals (echoes) are captured and displayed as a function of time. Each echo represents a reflection from a boundary, defect, or interface within the material. The size of a defect in solids is usually determined by tracking the amplitude of the defect reflection with different positionings of the transducer. As schematized in Fig. 1.1, when the transducer probe is located right on the top of a horizontal flaw (which is assumed to be perpendicular to the transmitted beam), all transmit beam is reflected from the flaw and the probe receives all transmitted beam energy, which is recorded in the maximum amplitude. When the transducer probe is moved to the edge of the flaw

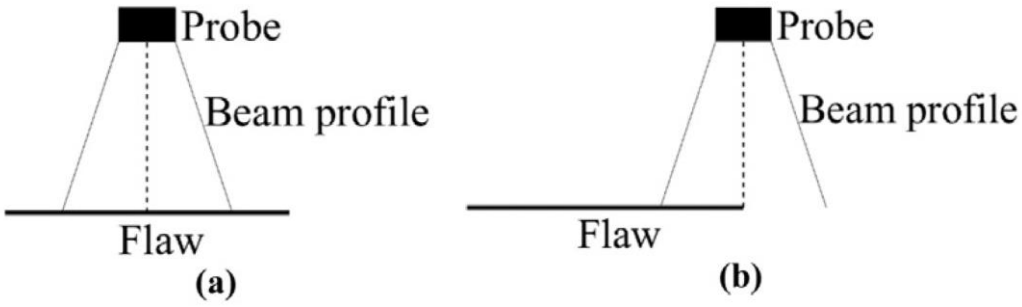

Figure 1.1: The 6 dB drop technique in ultrasonic A-scan [2]. (a) The probe is located above a flaw where the entire transmitted beam interacts with the horizontal reflector. (b) The probe is positioned above the edge of a flaw where half of the transmitted beam interacts with the flaw: the beam scattering amplitude should be half (-6 dB) of the total transmitted beam.

as shown in Fig. 1.1(b), half of the transmitted beam will be intersected by the flaw and received by the probe. Thus, a "6 dB drop" from the maximum amplitude of the defect reflection corresponds to the location of the probe where the broadside (principle axis) overlaps with the edge of the lateral flaw. It is important to note that the -6 dB technique assumes the flaw to be larger than the transmitted ultrasonic beam. Additionally, the method presumes that all regions of the flaw, including sharp edges and extended flat surfaces, exhibit the same scattering behavior.

Despite the aforementioned simplifications, the greatest limitation of A-scan techniques is the inherent subjectivity in interpreting ultrasound signals. The accuracy of flaw detection and characterization relies heavily on the operator's skill and judgment, introducing variability in remediation results. The inconsistencies in assessments of flaw size, location, or severity can reduce the reliability and repeatability of inspections, particularly in complex or ambiguous cases. As a result, the effectiveness of A-scan techniques is constrained by the need for subjective interpretation and experience, limiting its efficiency and utility in applications where consistent, high-precision evaluation is critical.

1.1 Ultrasonic Imaging in NDE and SHM

In the fields of NDE and SHM, advancements have been made towards identifying structural defects using objective and quantitative methods. These approaches are aimed to facilitate more straightforward interpretation and even automation of remediation decisions [7]. Ultrasonic imaging, for instance, can be achieved by virtually back-propagating ultrasonic waves through post-processing or in-situ processing. Analogous to those employed in radar, sonar, and medical imaging systems, the ultrasonic imaging in NDE and SHM applications employs an array of transducers to probe the medium from various spatial locations, facilitating comprehensive scanning and detailed imaging of structural defects [8]. While passive sensing techniques such as imaging with coda waves are available [9], the predominant imaging systems utilize active methods, including pitch-catch or pulse-echo modes. These active modalities offer enhanced control and accuracy in probing the inspected medium, thus relieving the difficulties in the detection and characterization of structural defects.

1.1.1 Measurements of an Active Array

Various modalities are utilized in active imaging systems, and these modalities vary based on the configuration of the transducer array employed, such as linear, curved, volumetric, or sparse arrays. Despite the specific advantages of each array type and modality in different applications, a fundamental aspect of active array measurements is the impulse response function (IRF) between a transmitter element and a receiver element. This function, also referred to as the inter-element response, forms the transfer matrix which characterizes the transfer functions between the transmitter and receiver arrays within the active imaging system. A notable example of this is the synthetic aperture focusing technique (SAFT), a widely used imaging modality in NDE and medical imaging that directly measures the transfer matrix by isolating each inter-element response

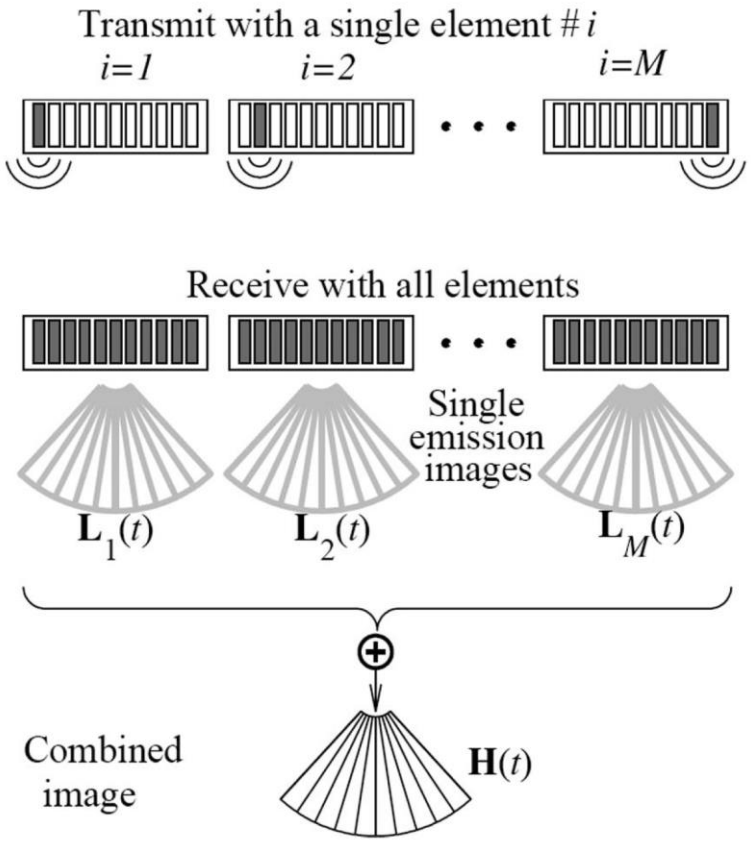

Figure 1.2: Synthetic aperture focusing technique using a linear array [11].

[10]. Such isolation preserves the diversity of ray paths in the captured wave field and consequently builds higher resolution images than traditional focused beam modalities. As shown in Fig. 1.2, in SAFT context an N-element linear transducer array acts both as transmitters and receivers. In each transmission event, only one transmitter element is emitted, and all receiver elements are working in parallel. By repeating this single element transmission over the physical aperture (in this case all transmitter elements), an N-by-N full matrix capture (FMC) of waveforms can be recorded characterizing the responses between each transmitter and receiver. Typically, the signals in FMC scheme can be approximated as the inter-element responses for simplicity. In chapters 4 and 5, it will be shown that to extract the pure transfer matrix using active system, a deconvolution process

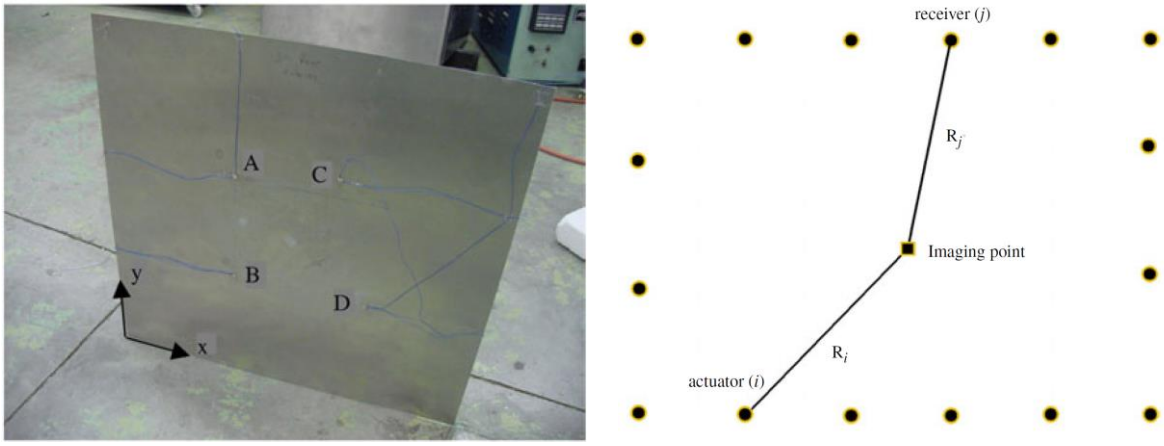

Figure 1.3: Sparse array configuration for in-situ imaging of a waveguide structure (left) and the ray path that connects a pixel in a synthetic image with an actuator and a receiver (right) [12].

needs to be carried out to eliminate the addition of phase and spectral power from the active transmission. The idea of synthetic aperture has been also applied to in-situ monitoring of plate-like structures using a sparse array setup [12]. Fig. 1.3 shows the first synthetic aperture imaging experiment using virtual time reversal of flexural waves. At the signal processing stage, additional care should be taken to account for the dispersive and multi modal nature of guided waves.

1.1.2 Time Delay Type Beamformers

Regardless of the differences in array configurations and wave modes highlighted in previous examples, the standard SAFT scheme offers dynamic focusing capabilities in both transmission and reception by post-processing Full Matrix Capture (FMC) datasets using time-delay beamformers, such as the delay-and-sum (DAS) algorithm [13]. This approach allows acoustic energy to be synthetically focused on any pixel within the region of interest (ROI), enabling virtual beam steering, in contrast to the physical beam steering utilized in traditional phased array modalities. As a result, SAFT significantly enhances resolution and dynamic range

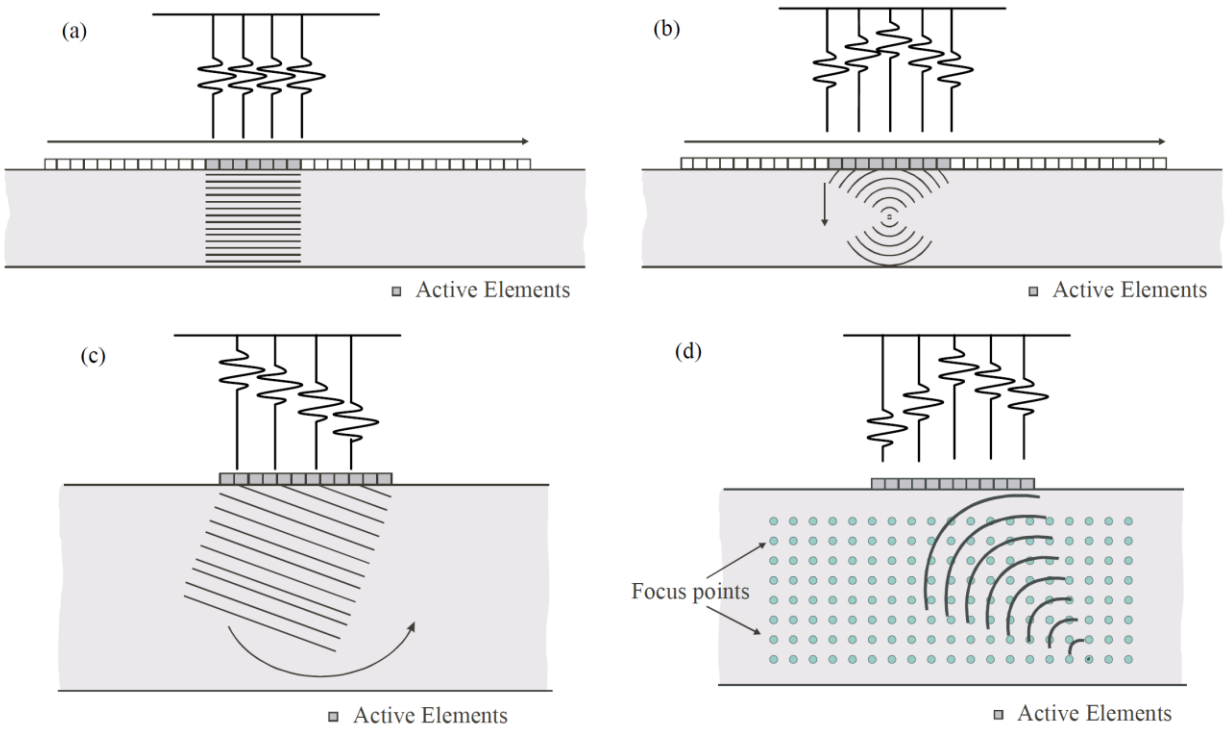

Figure 1.4: Schematic of common active modalities in a linear array: (a) swept B-scan using plane waves, (b) swept B-scan using focused waves, (c) sector B-scan using steering plane waves, and (d) synthetic focus in SAFT using signal channel transmission and reception [13].

over a large inspection area as illustrated in Fig. 1.4(d), while also improving the framerate in imaging without the need to sweep the transmission over the physical aperture as seen in other active modalities in Fig. 1.4 [14]. Wilcox et al. have shown the versatility of the DAS type algorithms to obtain the location, size, and orientation of defects in NDE applications [15]-[17]. Furthermore, one of the key advantages of SAFT imaging is its ability to effectively image individual or combined wave modes, making it particularly well-suited for NDE of bulk solids [18]-[20] and waveguide structures [21].

1.2 Strategies to Improve Imaging Performance

1.2.1 Extensions of DAS Framework

With the boost of computational power, recent DAS algorithms have been extended to different frameworks. Camacho et al. introduced a method that applies phase coherence (PC) factors to weigh the coherent sum output of DAS beamformers, effectively suppressing sidelobes while enhancing synthetic resolution in SAFT images [22]-[24]. This approach has been widely applied in both bulk wave and Lamb wave imaging [25]-[29]. Another weighting technique for DAS, adapted from adaptive beamforming methods such as Capon or minimum variance (MV) beamformers [30], was initially developed for medical ultrasound imaging [11], [31]-[35] and has recently gained broader interest for imaging composite structures [21], [36]-[40]. Unlike passive adaptive beamformers implemented in the frequency domain, these MV beamformers in active modalities focus on determining adaptive apodization weights from the temporal covariance matrix of appropriately delayed signals at different locations in the ROI. In parallel with these advancements in weighting techniques, the delay-multiply-and-sum (DMAS) algorithm has been developed by coupling more transmitter-receiver pairs compared to the standard DAS algorithm, leading to improved resolution and contrast [41]-[46]. Researchers have also explored combining PC and MV weights with the DMAS algorithm to achieve optimal imaging performance [35], [47]-[48]. In the field of NDE, a key area of focus is the implementation of the SAFT technique in multi-layered media [49]. This approach necessitates the accurate identification of refracted ray paths through interposed layers. Common applications include the use of wedges to transmit angled beams for the optimal detection of internal flaws in bulk solids [7], [20], [48], or systems involving non-planar interfaces such as pipelines and composite panels [50]-[52], where the complexity of wave propagation must be accounted for to enhance imaging accuracy.

1.2.2 Active Modalities: Tradeoff Between Contrast and Framerate

Despite recent advancements in algorithmic complexity, active sensing modalities remain the foundational research focus for achieving high-quality SAFT imaging. Two conflicting factors, signal-to-noise ratio (SNR) in active signal acquisition and the refresh rate of the imaging system, pose challenges in real-world applications, necessitating trade-offs between image resolution, contrast, and overall quality. For instance, in the FMC scheme, where each transducer channel is fired sequentially for maximum wavefield complexity, the data acquisition and subsequent beamforming are time-intensive processes, limiting the speed of imaging in practical scenarios such as cardiac imaging, in-situ SHM, or in-motion NDE. Sparse transmit aperture modalities, which reduce the number of transmissions and decrease redundancy in multistatic data, present a viable solution for achieving faster SAFT imaging [53]. However, a primary concern with this approach is the reduced transmission power from individual elements, which can lead to a diminished SNR in the received signals and compromise image quality in challenging environments. In NDE applications, this issue becomes particularly pronounced when imaging through highly attenuating materials or across an interposed medium, such as a transducer wedge.

Efforts to improve the poor SNR in sparse SAFT began with medical intravascular imaging. O'Donnell and Thomas first proposed using simultaneous excitation of multiple elements in a circular array [54]. Ylitalo and Ermert applied this idea to linear arrays with monostatic data acquisition [55]. Karaman et al. suggested using time delays to defocus subapertures for wider sector coverage, but the acoustic pressure improvement was limited by beam divergence [56]. Lockwood et al. introduced the concept of Virtual Element (VE) arrays for multistatic modalities, where subapertures are either focused or defocused depending on the virtual element position [57]. Since then, numerous variations of VE modalities have found their applications. Focused VE subapertures in SAFT are advantageous for deeper imaging in highly attenuating tissues [58]-[59],

while defocused beams are useful for nearer regions of interest, such as in echocardiography [60]-[64] or multi-layered medium NDE [7], [65].

The development of active phased array modalities has also been complemented by advances in Plane Wave (PW) imaging, particularly in medical imaging for "ultrafast" applications [66]. Unlike conventional B-mode line scans, PW imaging uses full-aperture transmissions of unfocused plane waves to fully illuminate the ROI [67]. In line with the synthetic aperture approach, multiple beam angles were introduced to be coherently compounded in space, enhancing image quality by improving angular diversity and resolution [68]-[70]. Recently, PW imaging has garnered attention in NDE, with investigations of its use for imaging cracks in steel blocks and complex geometry composite components [71]-[74].

1.2.3 Passive Modalities to Extract Pure Green's Functions

In active sensing for ultrasonic imaging, the excitation signal is typically a Gaussian-windowed tone burst or a square wave, often simplified as a Dirac delta function. However, this simplification becomes problematic when the transducer's transfer function is non-negligible, such as in the tuning effects observed during the actuation and reception of guided waves [75]. Extracting the pure Green's function of active ray paths has been a longstanding challenge in acoustics. For broadband and dispersive ultrasound signals, proper deconvolution between the excitation and reception signals significantly enhances sharpness (signal compression) and thus improves imaging resolution in post-processing.

In recent years, "passive" acoustic sensing has gained attention, inspired by Lobkis and Weaver's work [76]. They demonstrated that if a system is excited by a diffuse wave field — generated either by randomly distributed acoustic sources or a field with energy evenly partitioned among all normal modes — the time-averaged cross-correlation between signals at two receiver

points, I and J, converges to the system's Green's function (IRF) between them. Consequently, the "passively" reconstructed signal between I and J corresponds to the "active" IRF that would be obtained if I acted as a "virtual" source and J as the receiver.

This concept of passive Green's function reconstruction has since been applied across various fields, including ultrasonic, acoustic, and dynamic characterization. Applications include underwater acoustics [77]-[79], seismology [80]-[86], seismic interferometry for civil infrastructure identification [87]-[92], and SHM/NDE defect detection [93]-[106]. From a data acquisition standpoint, passive modalities are especially appealing as they eliminate the need for controlled excitations, thereby reducing transmission channel costs. Passive sensing has also been leveraged for beamforming by utilizing multiple "virtual" transmitters created from an array of receivers. This passive beamforming capability has been demonstrated for damage detection in structures using randomly distributed ultrasonic sources, as well as for SAFT imaging of subsurface defects via a few controlled excitations [103]-[106].

1.2.4 Analogy between Active and Passive Sensing in Match Field Beamformers

Time-delay type beamformers function as matched filters, correlating a delayed reference signal (model) with an unknown signal (measurement) to detect the presence of the reference in the measurement signal [107]. Although the matched filter is proven to be the optimal linear filter for maximizing SNR in the presence of stochastic noise, beamformer performance can be further enhanced using nonlinear techniques. One such method is the temporal minimum variance algorithm introduced in section 1.2.1, which optimizes the weight distribution in DAS beamforming. Alternatively, beamforming in active systems can be approached through matched field beamformers in the frequency domain [2]. These beamformers, akin to matched filters, compute the cross-correlation between a model and a measurement, allowing for more complex

medium propagation modeling. Enhanced imaging performance can be achieved through the decomposition of the transfer matrix or optimization of the replica (or steering) vector.

Within matched field beamformers for active ultrasonic imaging, transfer matrix factorization has garnered significant attention due to its ability to achieve super-resolution imaging beyond the Rayleigh diffraction limit. Specifically, the MUltiple SIgnal Classification (MUSIC) algorithm is extensively studied, relying on a correct separation between signal and noise spaces using singular value decomposition (SVD) of the transfer matrix or the eigen-decomposition of the time reversal operator (TRO). Prada et al. demonstrated that the eigenvectors of the TRO correspond directly to the number of well-resolved point scatterers in the medium [108]-[109], enabling subwavelength physical focusing through time reversal [110]-[112]. When the Green's function of the medium is known, numerical backpropagation can be used to produce super-resolution images (virtual time reversal) without the need for electronic phasing of the transmit array [113]. Since then, SVD-based MUSIC beamformers have been widely applied to imaging in bulk solids [114]-[120], impact and crack detection in waveguide structures [121]-[125], shallow water localization [126]-[127], and breast microcalcification detection [128]-[129].

High-resolution imaging of multistatic data can also be achieved using adaptive beamforming techniques, which focus on replica vector optimization. These techniques have been extensively explored in passive sensing such as the field of underwater acoustics [130]. Prada and Thomas first interpreted the TRO obtained from active FMC as a covariance matrix of a passive array [131], showing that TRO constructed from active transmit elements is analogous to taking "snapshots" in time, which builds the covariance matrix rank. They further demonstrated that for imaging two closely spaced scatterers, the Minimum Variance (MV) beamformer, implemented in the match field context, provided similar azimuth resolution as the MUSIC algorithm.

One significant advantage of treating active sensing within a “passive” framework is the possibility to beamform multitone TRO data coherently across the relevant frequency spectrum, using methods developed within the matched field community. Michalopoulou and Porter proposed a technique that exploits coherence between frequencies by stacking narrowband data into a long “supervector” [132]. Orris et al. introduced a matched-phase algorithm, resolving relative phase differences in cross-frequency terms to handle unknown source spectra [133]. Debever and Kuperman integrated robust adaptive beamformers, such as the white noise constraint (WNC) algorithm [134], into broadband formulations to reduce MV's sensitivity to modeling errors [135]. Despite the rank deficiency of the multitone covariance matrix in experimental acquisitions, the optimization of replica vectors can be stabilized by imposing a white noise gain constraint. Furthermore, WNC positively impacts the SNR output of diagonally loaded MV beamformers by adjusting the bias from small, non-physical eigenvalues, which enhances the dynamic range of the beamformer [136]. Coherent beamforming is highly attractive in the field of SHM and NDE, particularly for imaging complex waveguide structures. This is due to the inherent multimodal and dispersive nature of wave propagation in such environments, which makes conventional time delay beamformers less effective. Coherent adaptive beamforming techniques offer the ability to improve imaging quality by taking advantage of these complexities [137], thus enhancing the detection and characterization of defects in waveguide systems.

1.3 Beyond Imaging: Elastic Moduli Inversion in Composites

In the SHM and NDE of aerospace composite structures, various methods for damage detection have been developed, such as the previously introduced DAS and MUSIC imaging algorithm. As opposed to merely detecting damage, there has been increasing interest in

identifying the elastic moduli of composite components in the field of composite mechanics, because the estimation of residual strength is more directly tied to informed decisions regarding maintenance and continued operation of in-service structures.

Ultrasonic guided waves offer a distinct advantage for identifying elastic constants due to their insensitivity to the part's boundary conditions, allowing for the implementation of guided wave-based SHM/NDE strategies directly on in-service structures [138]-[140]. Guided waves, typically propagating in the frequency range of hundreds of kHz, have been widely employed for defect detection in composite materials [141]-[143]. However, predicting guided wave propagation in laminated composites is challenging due to the multimodal and dispersive nature of these waves. As a result, most guided wave testing has focused on damage detection, with relatively fewer studies addressing the identification of elastic properties.

Elastic property identification using guided waves is an inverse problem that involves forward modeling the multimodal and dispersive wave propagation behavior in the composite waveguide, followed by an optimization process to match the forward model to experimental data. Balasubramaniam [144] was among the first to achieve this by using dispersion relations of the fundamental axial and flexural mode phase velocities, employing a genetic algorithm for optimization and the transfer matrix method for forward modeling. Vishnuvardhan et al. [145] used a single transmitter and multiple receivers to sample the spatial guided wave field in orthotropic plates, successfully inverting nine elastic constants using the narrowband Christoffel equation as the forward model. Glushkov et al. [146] optimized group velocity dispersion curves for the elastic identification of unidirectional and cross-ply laminates, utilizing general elastodynamic theory and Green's function integrals for layered media.

Additionally, other studies have implemented elastic property inversion using ultrasonic guided waves with non-contact methods [147], which is particularly attractive in the field of NDE due to its versatility and efficiency. More recent work in this area has employed either genetic algorithms [148] or convolutional neural networks [149] for dispersion inversion. The pulsed ultrasonic polar scan (P-UPS) method represents another successful ultrasonic-based technique for inverting the viscoelastic properties of composites, achieving this without prior knowledge of the material's symmetry orientation [150].

1.4 Scope of the Dissertation

This dissertation focuses on recent advances in ultrasonic non-destructive evaluation techniques for defect imaging and elastic constant identification.

Chapter 2 discusses the application of sparse Synthetic Aperture Focusing Techniques (SAFT) to bulk wave ultrasonic imaging using a linear array mounted on a transducer wedge. Two subaperture emission modalities, i.e. virtual element and plane wave methods, are examined in the beamforming algorithms with particular considerations for wave refractions and mode conversions occurring at the wedge-medium interface. Techniques of wave mode compounding in SAFT images are presented to increase the array gain without augmenting its physical aperture.

Chapter 3 presents two experimental prototype systems developed for rail flaw imaging based on enhanced ultrasonic SAFT methods. The first system is hosted in a portable and battery powered carry-on size case. A hand-held probe consists of a linear array mounted on a wedge with a position encoder to build 3D point clouds from 2D beamformed images in quasi real-time. Validation results from rail section scans with natural transverse defects and artificial end-drilled hole defects are presented. The second system demonstrates the use of enhanced SAFT imaging

within a roller search unit (RSU), highlighting the high-speed operation of the RSU in generating 3D images and overcoming the challenges of scanning rail head corners, which were difficult to image with a rigid transducer wedge.

Chapter 4 proposes a “ultrasparse” SAFT method that builds a Full Matrix Capture (FMC) set of waveforms from implementation of “passive” ultrasonic sensing and deconvolution between array element pairs. The passive acquisition of the active transfer matrix (FMC dataset) is achieved through (a) the segment-averaged Normalized Cross-Power Spectrum (NCPS) for robust passive reconstruction of transfer function between two receivers, and (b) the use of both causal and acausal portions of the reconstructed transfer function. Beamforming images generated using the standard delay-and-sum (DAS) algorithm demonstrate the elimination of the near-field blind zone and the potential for ultrafast imaging with only a limited number of active sources.

Chapter 5 proposes an adaptive match field beamformer that requires no subspace factorization of the transfer matrix to achieve high resolution imaging of extended targets in bulk solids. Analogy is drawn between active and passive sensing within a broadband transfer matrix formulation to exploit cross-frequency coherence in ultrasound signals. The Coherent White Noise Constraint (C-WNC) algorithm is demonstrated to achieve high focusing ability of extended targets. The resolution cell distribution within the eigen structures of the transfer matrix is studied for the case of using a linear array to image a horizontal extended target. The C-WNC algorithm is shown to effectively track the tips of extended targets, ranging from the size of a wavelength to larger than the physical aperture width.

Chapter 6 extends the use of C-WNC algorithm to the imaging of defects in stringer-skin stiffened composite panels. Experimental Green’s functions between an image pixel and a receiver element are first collected as replica models using deconvolution implemented in NCPS.

Multimodal and dispersive guided wave signals encoded in the replica vectors are then beamformed coherently with new measurement data using the broadband adaptive match field beamformer to localize impacts and defects. The C-WNC algorithm is shown to provide high-resolution, high-contrast imaging of impact locations at different parts of the stiffened panel. For defect localization, eigen structure decomposition of the covariance matrix is employed to perform a null operation, illuminating potential defects acting as secondary sources in active sensing mode.

Chapter 7 presents an ultrasonic scanning system for the inspection of stiffened composite panels based on elastic constant identification. The system utilizes air-coupled ultrasonic transducers to rapidly map impact damage in inaccessible areas of stiffened panels. The inversion of engineering moduli at each line scan is performed by matching phase velocity dispersion curves to Semi-Analytical Finite Element (SAFE) models. An efficient method for extracting experimental dispersion curves is introduced, based on the analysis of phase spectra of the deconvoluted transfer function in a single-input dual-output configuration.

Chapter 8 presents the conclusions and outlines potential directions for future research.

References

[1] J. D. Achenbach, "Quantitative nondestructive evaluation," *Int. J. Solids Struct.*, vol. 37, no. 1–2, pp. 13–27, 2000.

[2] M.V. Felice and Z. Fan, "Sizing of flaws using ultrasonic bulk wave testing: A review," *Ultrasonics*, vol. 88, pp. 26–42, 2018.

[3] P. Cawley, "Non-destructive testing—current capabilities and future directions," *Proc. Inst. Mech. Eng. Part L: J. Mater. Des. Appl.*, vol. 215, no. 4, pp. 213–223, 2001.

[4] R. Halmshaw, *Introduction to the Non-destructive Testing of Welded Joints*. Cambridge, U.K.: Woodhead Publishing, 1996.

[5] J. L. Rose, *Ultrasonic Guided Waves in Solid Media*. Cambridge, U.K.: Cambridge Univ. Press, 2014.

[6] L. W. Schmerr, *Fundamentals of Ultrasonic Nondestructive Evaluation*. New York, NY, USA: Springer, 2016.

[7] C. Huang and F. Lanza di Scalea, “Rail Flaw Imaging Prototype Based on Improved Ultrasonic Synthetic Aperture Focus Method,” *Mater. Eval.*, vol. 82, pp. 51–59, 2024.

[8] B. W. Drinkwater and P. D. Wilcox, “Ultrasonic arrays for non-destructive evaluation: a review,” *NDT&E Int.*, vol. 39, no. 7, pp. 525–541, Oct. 2006.

[9] J. N. Potter, P. D. Wilcox, and A. J. Croxford, “Diffuse field full matrix capture for near surface ultrasonic imaging,” *Ultrasonics*, vol. 82, pp. 44–48, Jan. 2018.

[10] J. A. Jensen, S. I. Nikolov, K. L. Gammelmark, and M. H. Pedersen, “Synthetic aperture ultrasound imaging,” *Ultrasonics*, vol. 44, pp. e5–e15, Dec. 2006.

[11] I. K. Holfort, F. Gran, and J. A. Jensen, "Broadband minimum variance beamforming for ultrasound imaging," *IEEE Trans. Ultrason., Ferroelect., Freq. Control*, vol. 56, no. 2, pp. 314–325, 2009.

[12] C. H. Wang, J. T. Rose, and F. K. Chang, “A synthetic time-reversal imaging method for structural health monitoring,” *Smart Mater. Struct.*, vol. 13, no. 2, pp. 415–423, Mar. 2004.

[13] C. Holmes, B. W. Drinkwater, and P. D. Wilcox, “Post-processing of the full matrix of ultrasonic transmit–receive array data for non-destructive evaluation,” *NDT&E Int.*, vol. 38, no. 8, pp. 701–711, Dec. 2005.

[14] A. Chahbaz and R. Sicard, "Comparative evaluation between ultrasonic phased array and synthetic aperture focusing techniques," in *AIP Conf. Proc.*, vol. 657, no. 1, pp. 769–776, Mar. 2003. American Institute of Physics.

[15] P. D. Wilcox, C. Holmes, and B. W. Drinkwater, "Advanced reflector characterization with ultrasonic phased arrays in NDE applications," *IEEE Trans. Ultrason., Ferroelect., Freq. Control*, vol. 54, no. 8, pp. 1541–1550, 2007.

[16] J. Zhang, B. W. Drinkwater, and P. D. Wilcox, "Defect characterization using an ultrasonic array to measure the scattering coefficient matrix," *IEEE Trans. Ultrason., Ferroelect., Freq. Control*, vol. 55, no. 10, pp. 2254–2265, 2008.

[17] C. Holmes, B. W. Drinkwater, and P. D. Wilcox, "Advanced post-processing for scanned ultrasonic arrays: Application to defect detection and classification in non-destructive evaluation," *Ultrasonics*, vol. 48, no. 6–7, pp. 636–642, 2008.

[18] J. Zhang J, B. W. Drinkwater, P. D. Wilcox, and A. J. Hunter, “Defect detection using ultrasonic arrays: The multi-mode total focusing method,” *NDT&E Int.*, vol. 43, no. 2, pp. 123–133, Mar. 2010.

[19] F. Lanza di Scalea, S. Sternini, and T. V. Nguyen, “Ultrasonic imaging in solids using wave mode beamforming,” *IEEE Trans. Ultrason., Ferroelect., Freq. Control*, vol. 64, no. 3, pp. 602–616, Dec. 2016.

[20] S. Sternini, A. Y. Liang, and F. Lanza di Scalea, “Ultrasonic synthetic aperture imaging with interposed transducer–medium coupling path,” *Struct. Health Monitor.*, vol. 18, no. 5-6, pp. 1543–1556, Nov. 2019.

[21] S. Sternini, A. Pau and F. Lanza di Scalea, “Minimum-variance imaging in plates using guided-wave-mode beamforming,” *IEEE Trans. Ultrason. Ferroelectr. Freq. Control*, vol. 66, no. 12, pp. 1906–1919, Dec. 2019.

[22] J. Camacho, M. Parrilla, and C. Fritsch, "Phase coherence imaging," *IEEE Trans. Ultrason., Ferroelect., Freq. Control*, vol. 56, no. 5, pp. 958–974, 2009.

[23] J. Camacho and C. Fritsch, "Phase coherence imaging of grained materials," *IEEE Trans. Ultrason., Ferroelect., Freq. Control*, vol. 58, no. 5, pp. 1006–1015, 2011.

[24] J. Camacho, D. Atehortua, J. F. Cruza, J. Brizuela, and J. Ealo, "Ultrasonic crack evaluation by phase coherence processing and TFM and its application to online monitoring in fatigue tests," *NDT & E Int.*, vol. 93, pp. 164–174, 2018.

[25] H. Hasegawa and H. Kanai, "Effect of subaperture beamforming on phase coherence imaging," *IEEE Trans. Ultrason., Ferroelect., Freq. Control*, vol. 61, no. 11, pp. 1779–1790, 2014.

[26] H. Hasegawa, "Enhancing effect of phase coherence factor for improvement of spatial resolution in ultrasonic imaging," *J. Med. Ultrason.*, vol. 43, pp. 19–27, 2016.

[27] B. Gauthier, G. Painchaud-April, A. Le Duff, and P. Belanger, "Lightweight and amplitude-free ultrasonic imaging using single-bit digitization and instantaneous phase coherence," *IEEE Trans. Ultrason., Ferroelect., Freq. Control*, vol. 69, no. 5, pp. 1763–1774, 2022.

[28] W. Zhu, Y. Xiang, H. Zhang, M. Zhang, G. Fan, and H. Zhang, "Super-resolution ultrasonic Lamb wave imaging based on sign coherence factor and total focusing method," *Mech. Syst. Signal Process.*, vol. 190, p. 110121, 2023.

[29] X. Li, L. Liu, H. Xu, Z. Hu, Y. Xiang, and F. Z. Xuan, "Lamb wave phased array imaging based on phase-amplitude compounding algorithm," *Mech. Syst. Signal Process.*, vol. 205, p. 110882, 2023.

[30] J. Capon, "High-resolution frequency-wavenumber spectrum analysis," *Proc. IEEE*, vol. 57, no. 8, pp. 1408–1418, 1969.

[31] F. Vignon and M. R. Burcher, "Capon beamforming in medical ultrasound imaging with focused beams," *IEEE Trans. Ultrason., Ferroelect., Freq. Control*, vol. 55, no. 3, pp. 619–628, 2008.

[32] J. F. Synnevag, A. Austeng, and S. Holm, "Benefits of minimum-variance beamforming in medical ultrasound imaging," *IEEE Trans. Ultrason., Ferroelect., Freq. Control*, vol. 56, no. 9, pp. 1868–1879, 2009.

[33] B. M. Asl and A. Mahloojifar, "Eigenspace-based minimum variance beamforming applied to medical ultrasound imaging," *IEEE Trans. Ultrason., Ferroelect., Freq. Control*, vol. 57, no. 11, pp. 2381–2390, 2010.

[34] B. M. Asl and A. Mahloojifar, "Contrast enhancement and robustness improvement of adaptive ultrasound imaging using forward-backward minimum variance beamforming," *IEEE Trans. Ultrason., Ferroelect., Freq. Control*, vol. 58, no. 4, pp. 858–867, 2011.

[35] M. Mozaffarzadeh, A. Mahloojifar, M. Orooji, K. Kratkiewicz, S. Adabi, and M. Nasiriavanaki, "Linear-array photoacoustic imaging using minimum variance-based delay multiply and sum adaptive beamforming algorithm," *J. Biomed. Opt.*, vol. 23, no. 2, p. 026002, 2018.

[36] J. S. Hall and J. E. Michaels, "Minimum variance ultrasonic imaging applied to an in situ sparse guided wave array," *IEEE Trans. Ultrason., Ferroelect., Freq. Control*, vol. 57, no. 10, pp. 2311–2323, Sep. 2010.

[37] J. S. Hall, P. McKeon, L. Satyanarayan, J. E. Michaels, N. F. Declercq, and Y. H. Berthelot, "Minimum variance guided wave imaging in a quasi-isotropic composite plate," *Smart Mater. Struct.*, vol. 20, no. 2, p. 025013, 2011.

[38] J. S. Hall, P. Fromme, and J. E. Michaels, "Guided wave damage characterization via minimum variance imaging with a distributed array of ultrasonic sensors," *J. Nondestruct. Eval.*, vol. 33, pp. 299–308, 2014.

[39] C. Xu, Z. Yang, H. Zuo, and M. Deng, "Minimum variance Lamb wave imaging based on weighted sparse decomposition coefficients in quasi-isotropic composite laminates," *Compos. Struct.*, vol. 275, p. 114432, 2021.

[40] J. Hua, H. Zhang, Y. Miao, and J. Lin, "Modified minimum variance imaging of Lamb waves for damage localization in aluminum plates and composite laminates," *NDT & E Int.*, vol. 125, p. 102574, 2022.

[41] H. Been Lim, N. Thi Tuyet Nhung, E.-P. Li, and N. Duc Thang, "Confocal Microwave Imaging for Breast Cancer Detection: Delay-Multiply-and-Sum Image Reconstruction Algorithm," *IEEE Trans. Biomed. Eng.*, vol. 55, pp. 1697–1704, 2008.

[42] G. Matrone, A.S. Savoia, G. Caliano, and G. Magenes, "The Delay Multiply and Sum Beamforming Algorithm in Ultrasound B-Mode Medical Imaging," *IEEE Trans. Med. Imaging*, vol. 34, pp. 940–949, 2015.

[43] G. Matrone, A. Ramalli, A. S. Savoia, P. Tortoli, and G. Magenes, "High frame-rate, high resolution ultrasound imaging with multi-line transmission and filtered-delay multiply and sum beamforming," *IEEE Trans. Med. Imaging*, vol. 36, no. 2, pp. 478–486, 2016.

[44] G. Matrone, A. S. Savoia, G. Caliano, and G. Magenes, "Depth-of-field enhancement in filtered-delay multiply and sum beamformed images using synthetic aperture focusing," *Ultrasonics*, vol. 75, pp. 216–225, 2017.

[45] T. Su, D. Li, and S. Zhang, "An efficient subarray average delay multiply and sum beamformer algorithm in ultrasound imaging," *Ultrasonics*, vol. 84, pp. 411–420, 2018.

[46] D. Teng, L. Liu, Y. Xiang, and F. Z. Xuan, "An optimized total focusing method based on delay-multiply-and-sum for nondestructive testing," *Ultrasonics*, vol. 128, p. 106881, 2023.

[47] C. C. Shen, "Computationally efficient minimum-variance baseband delay-multiply-and-sum beamforming for adjustable enhancement of ultrasound image resolution," *Ultrasonics*, vol. 112, p. 106345, 2021.

[48] L. Luo, Y. Tan, J. Li, Y. Zhang, and X. Gao, "Wedge two-layer medium ultrasonic plane wave compounding imaging based on sign multiply coherence factor combined with delay multiply and sum beamforming," *NDT & E Int.*, vol. 127, p. 102601, 2022.

[49] M. Spies, H. Rieder, A. Dillhöfer, V. Schmitz, and W. Müller, "Synthetic aperture focusing and time-of-flight diffraction ultrasonic imaging—past and present," *J. Nondestruct. Eval.*, vol. 31, pp. 310–323, 2012.

[50] K. Qin, C. Yang, and F. Sun, "Generalized frequency-domain synthetic aperture focusing technique for ultrasonic imaging of irregularly layered objects," *IEEE Trans. Ultrason., Ferroelect., Freq. Control*, vol. 61, no. 1, pp. 133–146, 2014.

[51] B. Wu, Y. Gao, J. Laviada, M. T. Ghasr, and R. Zoughi, "Time-reversal SAR imaging for nondestructive testing of circular and cylindrical multilayered dielectric structures," *IEEE Trans. Instrum. Meas.*, vol. 69, no. 5, pp. 2057–2066, 2019.

[52] Q. Mao, Y. Chen, M. Chen, W. Shi, C. Lu, and Q. Li, "A fast interface reconstruction method for frequency-domain synthetic aperture focusing technique imaging of two-layered systems with non-planar interface based on virtual points measuring," *J. Nondestruct. Eval.*, vol. 39, pp. 1–10, 2020.

[53] C. R. Cooley and B. S. Robinson, "Synthetic focus imaging using partial datasets," in *Proc. IEEE Ultrason. Symp.*, vol. 3, pp. 1539–1542, 1994.

[54] M. O'Donnell and L. J. Thomas, "Efficient synthetic aperture imaging from a circular aperture with possible application to catheter-based imaging," *IEEE Trans. Ultrason., Ferroelect., Freq. Control*, vol. 39, no. 3, pp. 366–380, May. 1992.

[55] J.T. Ylitalo and H. Ermert, "Ultrasound synthetic aperture imaging: monostatic approach," *IEEE Trans. Ultrason., Ferroelect., Freq. Control*, vol. 41, no. 3, pp. 333–339, May. 1994.

[56] M. Karaman M, P. C. Li, and M. O'Donnell, "Synthetic aperture imaging for small scale systems," *IEEE Trans. Ultrason., Ferroelect., Freq. Control*, vol. 42, no. 3, pp. 429–442, May. 1995.

[57] G. R. Lockwood, J. R. Talman, and S. S. Brunke, “Real-time 3-D ultrasound imaging using sparse synthetic aperture beamforming,” *IEEE Trans. Ultrason. Ferroelectr. Freq. Control*, vol. 45, no. 4, pp. 980–988, Jul. 1998.

[58] C. H. Frazier and W. D. O'Brien, “Synthetic aperture techniques with a virtual source element,” *IEEE Trans. Ultrason., Ferroelect., Freq. Control*, vol. 45, no. 1, pp. 196-207, Jan. 1998.

[59] M. H. Bae and M. K. Jeong, “A study of synthetic-aperture imaging with virtual source elements in B-mode ultrasound imaging systems,” *IEEE Trans. Ultrason., Ferroelect., Freq. Control*, vol. 47, no. 6, pp. 1510-1519, Nov. 2000.

[60] S. I. Nikolov and J. A. Jensen, “Virtual ultrasound sources in high resolution ultrasound imaging,” in *Proc. SPIE*, 2002, vol. 3, pp. 395–405.

[61] S. I. Nikolov and J. A. Jensen, “In-vivo synthetic aperture flow imaging in medical ultrasound,” *IEEE Trans. Ultrason., Ferroelect., Freq. Control*, vol. 50, no. 7, pp. 848–856, Jul. 2003.

[62] N. Oddershede and J. A. Jensen, “Effects influencing focusing in synthetic aperture vector flow imaging,” *IEEE Trans. Ultrason., Ferroelect., Freq. Control*, vol. 54, no. 9, pp. 1811–1825, Sep. 2007.

[63] M. F. Rasmussen and J. A. Jensen, “Comparison of 3-D synthetic aperture phased-array ultrasound imaging and parallel beamforming,” *IEEE Trans. Ultrason., Ferroelect., Freq. Control*, vol. 61, no. 10, pp. 1638–1650, Oct. 2014.

[64] H. Hasegawa and H. Kanai, “High-frame-rate echocardiography using diverging transmit beams and parallel receive beamforming,” *J. Med. Ultrason.*, vol. 38, no. 3, pp. 129-140, Jul. 2011.

[65] E. Hoyle, M. Sutcliffe, P. Charlton, and J. Rees, "Virtual source aperture imaging with auto-focusing of unknown complex geometry through dual layered media," *NDT & E Int.*, vol. 98, pp. 55-62, 2018.

[66] M. Tanter and M. Fink, “Ultrafast imaging in biomedical ultrasound,” *IEEE Trans. Ultrason., Ferroelect., Freq. Control*, vol. 61, no. 1, pp. 102–119, Jan. 2014.

[67] L. Sandrin, S. Catheline, M. Tanter, X. Hennequin, and M. Fink, “Time resolved pulsed elastography with ultrafast ultrasonic imaging,” *Ultrason. Imaging*, vol. 21, no. 4, pp. 259–272, Oct. 1999.

[68] S. K. Jespersen, J. E. Wilhjelm, and H. Sillesen, “Multi-angle compound imaging,” *Ultrason. Imaging*, vol. 20, no. 2, pp. 81–102, Apr. 1998.

[69] M. Tanter, J. Bercoff, L. Sandrin, and M. Fink, “Ultrafast compound imaging for 2-D motion vector estimation: Application to transient elastography,” *IEEE Trans. Ultrason. Ferroelectr. Freq. Control*, vol. 49, no. 10, pp. 1363–1374, Dec. 2002.

[70] G. Montaldo, M. Tanter, J. Bercoff, N. Benech, and M. Fink, "Coherent plane-wave compounding for very high frame rate ultrasonography and transient elastography," *IEEE Trans. Ultrason., Ferroelect., Freq. Control*, vol. 56, no. 3, pp. 489–506, Mar. 2009.

[71] L. Le Jeune, S. Robert, E. L. Villaverde, and C. Prada, "Plane wave imaging for ultrasonic non-destructive testing: Generalization to multimodal imaging," *Ultrasonics*, vol. 64, pp. 128–138, Jan. 2016.

[72] L, Merabet, S. Robert, and C. Prada, "The multi-mode plane wave imaging in the Fourier domain: Theory and applications to fast ultrasound imaging of cracks," *NDT&E Int.*, vol. 110, p. 102171, Mar. 2020.

[73] J. F. Cruza, J. Camacho, and C. Fritsch, "Plane-wave phase-coherence imaging for NDE," *NDT&E Int.*, vol. 87, pp. 31-37, Apr. 2017.

[74] A. J. Brath and F. Simonetti, "Phased array imaging of complex-geometry composite components," *IEEE Trans. Ultrason. Ferroelectr. Freq. Control*, vol. 64, no. 10, pp. 1573-1582, Oct. 2017.

[75] J. Wang and Y. Shen, "An enhanced Lamb wave virtual time reversal technique for damage detection with transducer transfer function compensation," *Smart Mater. Struct.*, vol. 28, no. 8, p. 085017, 2019.

[76] O. I. Lobkis and R. L. Weaver, "On the emergence of the Green's function in the correlations of a diffuse field," *J. Acoust. Soc. Am.*, vol. 110, no. 6, pp. 3011–3017, Dec. 2001.

[77] K. G. Sabra, P. Roux, and W. A. Kuperman, "Emergence rate of the time-domain Green's function from the ambient noise cross-correlation function," *J. Acoust. Soc. Am.*, vol. 118, no. 6, pp. 3524–3531, Dec. 2005.

[78] P. Roux, W. A. Kuperman, and the NPAL Group, "Extracting coherent wave fronts from acoustic ambient noise in the ocean," *J. Acoust. Soc. Am.*, vol. 116, no. 4, pp. 1995–2003, Oct. 2004.

[79] K. G. Sabra, P. Roux, and W. A. Kuperman, "Arrival-time structure of the time-averaged ambient noise cross-correlation function in an oceanic waveguide," *J. Acoust. Soc. Am.*, vol. 117, no. 1, pp. 164–174, Jan. 2005.

[80] M. Campillo and A. Paul, "Long-range correlations in the diffuse seismic coda," *Science*, vol. 299, no. 5606, pp. 547–549, Jan. 2003.

[81] P. Roux, K. G. Sabra, P. Gerstoft, W. A. Kuperman, and M. C. Fehler, "P-waves from cross-correlation of seismic noise," *Geophys. Res. Lett.*, vol. 32, no. 19, pp. 1–4, Oct. 2005.

[82] N. M. Shapiro, M. Campillo, L. Stehly, and M. H. Ritzwoller, "High-resolution surface-wave tomography from ambient seismic noise," *Science*, vol. 307, no. 5715, pp. 1615–1618, Mar. 2005.

[83] K. G. Sabra, P. Gerstoft, P. Roux, W. A. Kuperman, and M. C. Fehler, "Extracting time-domain Green's function estimates from ambient seismic noise," *Geophys. Res. Lett.*, vol. 32, no. 3, pp. 1–5, Feb. 2005.

[84] K. G. Sabra, P. Gerstoft, P. Roux, W. A. Kuperman, and M. C. Fehler, "Surface wave tomography from microseisms in Southern California," *Geophys. Res. Lett.*, vol. 32, no. 14, pp. 1–4, Jul. 2005.

[85] R. Snieder, "Extracting the Green's function from the correlation of coda waves: A derivation based on stationary phase," *Phys. Rev. E*, vol. 69, pp. 0466101-0466108, Apr. 2004.

[86] R. Snieder and K. Wapenaar, "Imaging with ambient noise," *Phys. Today*, vol. 63, no. 9, pp. 44–49, Sept. 2010.

[87] R. Snieder and E. Şafak, "Extracting the building response using seismic interferometry: Theory and application to the Millikan Library in Pasadena, California," *Bull. Seismol. Soc. Am.*, vol. 96, no. 2, pp. 586–598, Apr. 2006.

[88] G. A. Prieto, J. F. Lawrence, A. I. Chung, and M. D. Kohler, "Impulse response of civil structures from ambient noise analysis," *Bull. Seismol. Soc. Am.*, vol. 100, no. 5A, pp. 2322–2328, Oct. 2010.

[89] N. Nakata, R. Snieder, S. Kuroda, S. Ito, T. Aizawa, and T. Kunimi, "Monitoring a building using deconvolution interferometry. I: earthquake-data analysis," *Bull. Seismol. Soc. Am.*, vol. 103, no. 3, pp. 1662–1678, Jun. 2013.

[90] N. Nakata and R. Snieder, "Monitoring a building using deconvolution interferometry. II: ambient vibration analysis," *Bull. Seismol. Soc. Am.*, vol. 104, no. 1, pp. 204–213, Feb. 2014.

[91] A. Mordret, H. Sun, G. A. Prieto, M. N. Toksoz, and O. Büyüköztürk, "Continuous monitoring of high-rise buildings using seismic interferometry," *Bull. Seismol. Soc. Am.*, vol. 107, no. 6, pp. 2759–2773, Dec. 2017.

[92] X. Wu, Z. Guo, L. Liu, Y. J. Chen, C. Zou, and X. Song, "Seismic monitoring of super high-rise building using ambient noise with dense seismic array," *Seismol. Res. Lett.*, vol. 92., no. 1, pp. 396–407, Jan. 2021.

[93] C. R. Farrar and G. H. James, "System identification from ambient vibration measurements on a bridge," *J. Sound Vib.*, vol. 205, no. 1, pp. 1–18, Aug. 1997.

[94] K. G. Sabra, E. S. Winkel, D. A. Bourgoyne, B. R. Elbing, S. L. Ceccio, M. Perlin, and D. R. Dowling, "Using cross correlations of turbulent flow-induced ambient vibrations to estimate the structural impulse response. Application to structural health monitoring," *J. Acoust. Soc. Am.*, vol. 121, no. 4, 1987–1995, Apr. 2007.

[95] J. D. Tippmann, X. Zhu, and F. Lanza di Scalea, "Application of damage detection methods using passive reconstruction of impulse response functions," *Phil. Trans. R. Soc. A*, vol. 373, no. 2035, pp. 1–17, Feb. 2015.

[96] F. Lanza di Scalea, X. Zhu, M. Capriotti, A. Y. Liang, S. Mariani, and S. Sternini, "Passive extraction of dynamic transfer function from arbitrary ambient excitations: Application to high-speed rail inspection from wheel-generated waves," *J. Nondestruct. Eval. Diagn. Progn. Eng. Syst.*, vol. 1, pp. 0110051–01100512, Feb. 2018.

[97] J. E. Michaels and T. E. Michaels, "Detection of structural damage from the local temporal coherence of diffuse ultrasonic signals," *IEEE Trans. Ultrason. Ferroelectr. Freq. Control*, vol. 52, no. 10, pp. 1769–1782, Oct. 2005.

[98] E. Larose, O. I. Lobkis, and R. L. Weaver, "Passive correlation imaging of a buried scatterer," *J. Acoust. Soc. Am.*, vol. 119, no. 6, pp. 3549–3552, Jun. 2006.

[99] K. G. Sabra, A. Srivastava, F. Lanza di Scalea, I. Bartoli, P. Rizzo, and S. Conti, "Structural health monitoring by extraction of coherent guided waves from diffuse fields," *J. Acoust. Soc. Am.*, vol. 123, no. 1, pp. EL8–L13, Jan. 2008.

[100] J. D. Tippmann and F. Lanza di Scalea, "Passive-only damage detection by reciprocity of Green's functions reconstructed from diffuse acoustic fields with application to wind turbine blades," *J. Intell. Mater. Syst. Struct.*, vol. 26, no. 10, pp. 1251–1258, Jul. 2015.

[101] A. Duroux, K. G. Sabra, J. Ayers, and M. Ruzzene, "Extracting guided waves from cross-correlations of elastic diffuse fields: applications to remote structural health monitoring," *J. Acoust. Soc. Am.*, vol. 127, no. 1, pp. 204–215, Jan. 2010.

[102] C. Huang and F. Lanza di Scalea, "An ultrasonic scanning system for the inspection of composite stiffened panels from elastic constant identification via inversion of guided waves," *Compos. Struct.*, vol. 322, p. 117373, Oct. 2023.

[103] L. Chehami, J. De Rosny, C. Prada, E. Moulin, and J. Assaad, "Experimental study of passive defect localization in plates using ambient noise," *IEEE Trans. Ultrason. Ferroelectr. Freq. Control*, vol. 62, no. 8, pp. 1544–1553, Aug. 2015.

[104] J. D. Tippmann and F. Lanza di Scalea, "Passive-only defect detection and imaging in composites using diffuse fields," in *Mechanics of Composite and Multi-functional Materials*, vol. 7, C. Ralph, M. Silberstein, P. R. Thakre, and R. Singh, Eds. USA: Springer, Conference Proceedings of the Society for Experimental Mechanics Series, 2016, pp. 67–72.

[105] J. N. Potter, P. D. Wilcox, and A. J. Croxford, "Diffuse field full matrix capture for near surface ultrasonic imaging," *Ultrasonics*, vol. 82, pp. 44–48, Jan. 2018.

[106] H. Zhang, H. Zhang, J. Zhang, J. Liu, W. Zhu, G. Fan, and Q. Zhu, "Wavenumber imaging of near-surface defects in rails using Green's function reconstruction of ultrasonic diffuse fields," *Sensors*, vol. 19, no. 17, pp. 3744, 2019.

[107] G. Turin, "An introduction to matched filters," *IRE Trans. Inf. Theory*, vol. 6, no. 3, pp. 311-329, 1960.

[108] C. Prada and M. Fink, "Eigenmodes of the time reversal operator: A solution to selective focusing in multiple-target media," *Wave Motion,* vol. 20, pp. 151–163, 1994.

[109] C. Prada, S. Manneville, D. Spoliansky, and M. Fink, "Decomposition of the time reversal operator: Detection and selective focusing on two scatterers," *J. Acoust. Soc. Am.*, vol. 99, pp. 2067–2076, 1996.

[110] C. Prada, J.-L. Thomas, and M. Fink, "The iterative time reversal process: Analysis of the convergence," *J. Acoust. Soc. Am.*, vol. 97, pp. 62–71, 1995.

[111] J.-L. Thomas, and M.A. Fink, "Ultrasonic beam focusing through tissue inhomogeneities with a time reversal mirror: application to transskull therapy," *IEEE Trans. Ultrason., Ferroelect., Freq. Contr.*, vol. 43, pp. 1122–1129, 1996.

[112] M. Fink, D. Cassereau, A. Derode, C. Prada, P. Roux, M. Tanter, J.L. Thomas, and F. Wu, "Time-reversed acoustics," *Rep. Prog. Phys.*, vol. 63, p. 1933, 2000.

[113] S.K. Lehman and A.J. Devaney, "Transmission mode time-reversal super-resolution imaging," *J. Acoust. Soc. Am.*, vol. 113, pp. 2742–2753, 2003.

[114] E. Kerbrat, C. Prada, D. Cassereau, and M. Fink, "Ultrasonic nondestructive testing of scattering media using the decomposition of the time-reversal operator," *IEEE Trans. Ultrason., Ferroelect., Freq. Contr.*, vol. 49, pp. 1103–1113, 2002.

[115] E. Kerbrat, C. Prada, D. Cassereau, and M. Fink, "Imaging in the presence of grain noise using the decomposition of the time reversal operator," *J. Acoust. Soc. Am.* vol. 113, pp. 1230–1240, 2003.

[116] E. Lopez Villaverde, S. Robert, and C. Prada, "Ultrasonic imaging of defects in coarse-grained steels with the decomposition of the time reversal operator," *J. Acoust. Soc. Am.*, vol. 140, pp. 541–550, 2016.

[117] C. Fan, M. Caleap, M. Pan, and B.W. Drinkwater, "A comparison between ultrasonic array beamforming and super resolution imaging algorithms for non-destructive evaluation," *Ultrasonics*, vol. 54, pp. 1842–1850, 2014.

[118] C. Fan, M. Pan, F. Luo, and B. Drinkwater, "Multi-frequency time-reversal-based imaging for ultrasonic nondestructive evaluation using full matrix capture," *IEEE Trans. Ultrason., Ferroelect., Freq. Contr.*, vol. 61, pp. 2067–2074, 2014.

[119] C. Fan, S. Yu, B. Gao, Y. Zhao, and L. Yang, "Ultrasonic time-reversal-based super resolution imaging for defect localization and characterization," *NDT & E Int.*, vol. 131, p. 102698, 2022.

[120] J.B. Elliott, M.J.S. Lowe, P. Huthwaite, R. Phillips, and D.J. Duxbury, "Sizing Subwavelength Defects With Ultrasonic Imagery: An Assessment of Super-Resolution Imaging on Simulated Rough Defects," *IEEE Trans. Ultrason., Ferroelect., Freq. Contr.*, vol. 66, pp. 1634–1648, 2019.

[121] E.A. Marengo, F.K. Gruber, and F. Simonetti, "Time-Reversal MUSIC Imaging of Extended Targets," *IEEE Trans. Image Process.*, vol. 16, pp. 1967–1984, 2007.

[122] W.K. Park and D. Lesselier, "Electromagnetic MUSIC-type imaging of perfectly conducting, arc-like cracks at single frequency," *J. Comput. Phys.*, vol. 228, pp. 8093–8111, 2009.

[123] L. Ambrozinski, T. Stepinski, P. Packo, and T. Uhl, "Self-focusing Lamb waves based on the decomposition of the time-reversal operator using time–frequency representation," *Mech. Syst. Sig. Process.*, vol. 27, pp. 337–349, 2012.

[124] J. He and F.G. Yuan, "Lamb wave-based subwavelength damage imaging using the DORT-MUSIC technique in metallic plates," *Struct. Health Monit.*, vol. 15, pp. 65–80, 2016.

[125] X. Yang, K. Wang, P. Zhou, L. Xu, and Z. Su, "Imaging damage in plate waveguides using frequency-domain multiple signal classification (F-MUSIC)," *Ultrasonics*, vol. 119, p. 106607, 2022.

[126] C. Prada, J. De Rosny, D. Clorennec, J.-G. Minonzio, A. Aubry, M. Fink, L. Berniere, P. Billand, S. Hibral, and T. Folegot, "Experimental detection and focusing in shallow water by decomposition of the time reversal operator," *J. Acoust. Soc. Am.*, vol. 122, pp. 761–768, 2007.

[127] F.D. Philippe, C. Prada, J. De Rosny, D. Clorennec, J.-G. Minonzio, and M. Fink, "Characterization of an elastic target in a shallow water waveguide by decomposition of the time-reversal operator," *J. Acoust. Soc. Am.*, vol. 124, pp. 779–787, 2008.

[128] Y. Labyed and L. Huang, "Ultrasound time-reversal MUSIC imaging with diffraction and attenuation compensation," *IEEE Trans. Ultrason., Ferroelect., Freq. Contr.*, vol. 59, pp. 2186–2200, 2012.

[129] Y. Labyed and L. Huang, "Super-resolution ultrasound imaging using a phase-coherent MUSIC method with compensation for the phase response of transducer elements," *IEEE Trans. Ultrason., Ferroelect., Freq. Contr.*, vol. 60, pp. 1048–1060, 2013.

[130] A.B. Baggeroer, W.A. Kuperman, and P.N. Mikhalevsky, "An overview of matched field methods in ocean acoustics," *IEEE J. Oceanic Eng.*, vol. 18, pp. 401–424, 1993.

[131] C. Prada, and J.L. Thomas, "Experimental subwavelength localization of scatterers by decomposition of the time reversal operator interpreted as a covariance matrix," *J. Acoust. Soc. Am.*, vol. 114, pp. 235–243, 2003.

[132] Z.H. Michalopoulou and M.B. Porter, "Matched-field processing for broad-band source localization," *IEEE J. Oceanic Eng.*, vol. 21, pp. 384–392, 1996.

[133] G.J. Orris, M. Nicholas, and J.S. Perkins, "The matched-phase coherent multi-frequency matched-field processor," *J. Acoust. Soc. Am.*, vol. 107, pp. 2563–2575, 2000.

[134] H. Cox, R. Zeskind, and M. Owen, "Robust adaptive beamforming," *IEEE Trans. Acoust., Speech, Signal Process.*, vol. 35, pp. 1365–1376, 1987.

[135] C. Debever and W.A. Kuperman, "Robust matched-field processing using a coherent broadband white noise constraint processor," *J. Acoust. Soc. Am.*, vol. 122, pp. 1979–1986, 2007.

[136] H. Song, W.A. Kuperman, W.S. Hodgkiss, P. Gerstoft, and J.S. Kim, "Null broadening with snapshot-deficient covariance matrices in passive sonar," *IEEE J. Oceanic Eng.*, vol. 28, pp. 250–261, 2003.

[137] J.B. Harley and J.M. Moura, "Data-driven matched field processing for Lamb wave structural health monitoring," *J. Acoust. Soc. Am.* vol. 135, pp. 1231–1244, 2014.

[138] A. Marzani and L. De Marchi, "Characterization of the elastic moduli in composite plates via dispersive guided waves data and genetic algorithms," *J. Intell. Mater. Syst. Struct.*, vol. 24, no. 17, pp. 2135–2147, Nov. 2013, doi: 10.1177/1045389X12462645.

[139] R. Cui and F. Lanza di Scalea, "On the identification of the elastic properties of composites by ultrasonic guided waves and optimization algorithm," *Compos. Struct.*, vol. 223, p. 110969, Sep. 2019.

[140] R. Cui and F. Lanza di Scalea, "Identification of Elastic Properties of Composites by Inversion of Ultrasonic Guided Wave Data," *Exp. Mech.*, vol. 61, no. 5, pp. 803–816, Jun. 2021.

[141] W. Staszewski, C. Boller, and G. R. Tomlinson, Health Monitoring of Aerospace Structures: Smart Sensor Technologies and Signal Processing. John Wiley & Sons, 2004.

[142] J. L. Rose, Ultrasonic Guided Waves in Solid Media. Cambridge University Press, 2014.

[143] V. Giurgiutiu, "17 - Structural health monitoring (SHM) of aerospace composites," in *Polymer Composites in the Aerospace Industry* (Second Edition), P. Irving and C. Soutis, Eds., in Woodhead Publishing Series in Composites Science and Engineering., Woodhead Publishing, 2020, pp. 491–558.

[144] K. Balasubramaniam, "Inversion of the Ply Lay-up Sequence for Multi-Layered Fiber Reinforced Composite Plates Using Genetic Algorithm," *Nondestruct. Test. Eval.*, vol. 15, no. 5, pp. 311–331, Nov. 1998.

[145] J. Vishnuvardhan, C. V. Krishnamurthy, and K. Balasubramaniam, "Genetic algorithm based reconstruction of the elastic moduli of orthotropic plates using an ultrasonic guided wave single-transmitter-multiple-receiver SHM array," *Smart Mater. Struct.*, vol. 16, no. 5, p. 1639, Aug. 2007, doi: 10.1088/0964-1726/16/5/017.

[146] E. V. Glushkov, N. V. Glushkova, and A. A. Eremin, "Guided wave based nondestructive testing and evaluation of effective elastic moduli of layered composite materials," *Mater. Phys. Mech.*, vol. 40, no. 1, pp. 56–60, 2015.

[147] B. Hosten, M. Castaings, H. Tretout, and H. Voillaume, "Identification of composite materials elastic moduli from Lamb wave velocities measured with single sided, contactless ultrasonic method," AIP Conference Proceedings, vol. 557, no. 1, pp. 1023–1030, Apr. 2001.

[148] P. Kudela, M. Radzienski, P. Fiborek, and T. Wandowski, “Elastic constants identification of woven fabric reinforced composites by using guided wave dispersion curves and genetic algorithm,” *Compos. Struct.*, vol. 249, p. 112569, Oct. 2020.

[149] M. Rautela, A. Huber, J. Senthilnath, and S. Gopalakrishnan, “Inverse characterization of composites using guided waves and convolutional neural networks with dual-branch feature fusion,” *Mech. Adv. Mater. Struct.*, vol. 29, no. 27, pp. 6595–6611, Dec. 2022.

[150] A. Martens, M. Kersemans, J. Daemen, E. Verboven, W. Van Paepegem, S. Delrue, and K. Van Den Abeele, “Characterization of the orthotropic viscoelastic tensor of composites using the Ultrasonic Polar Scan,” *Compos. Struct.*, vol. 230, p. 111499, Dec. 2019.

Chapter 2 Improvements of Synthetic Aperture Focusing Techniques for Ultrasound Imaging in Solids

2.1 Introduction

Synthetic Aperture Focus Techniques (SAFT) for ultrasonic imaging have been established since the late 1960s [1], [2]. The method is widely applied for medical uses [3]-[14], as well as for defect detection and quantification in solids in Non-destructive Testing (NDT) [15]-[25]. In many instances, because of the particular orientation of the reflectors or in cases of test pieces with particular geometries [26]-[31], it is customary to utilize a wedge interposed between the transducer array and the test medium to appropriately direct the ultrasonic waves so as to maximize the target reflections. Some applications of transducer wedges (or, equivalently, inclined transducers in fluid-filled wheels) in ultrasonic imaging are found in pipeline inspections and weld examinations [21], as well as detection of transverse defects in railroad tracks [32]-[36].

The conventional time-backpropagation SAFT approach employs a Full Matrix Capture (FMC) scheme that requires firing each channel of the array sequentially and recording the signals by all channels simultaneously for each of the transmissions [5]. A simple time delay approach such as the total focusing method (TFM) beamforms the interelement response to generate a high-resolution image. The collection and beamforming of FMC data is time-consuming. In several cases (such as cardiac imaging for medical applications or in-motion NDT imaging for industrial applications), there is a need for high frame rates. Sparse transmit aperture modalities [37], with reduced number of transmissions and reduced redundancy in the multistatic data, are a viable option for fast SAFT. One concern, in this case, is the limited transmission power of any single element that may result in poor SNR signal-to-noise ratio of the receptions. This problem is

especially relevant when imaging in highly attenuating materials or through an interposed medium such as a transducer wedge [30]-[33].

Efforts to overcome the problem of poor SNR in sparse SAFT started in medical intravascular imaging. O'Donnell and Thomas [38] first introduced the idea of replacing the single element emission with simultaneous excitation of a multi-element subaperture in a circular array. Ylitalo and Ermert [39] employed the same idea on a linear array with monostatic data acquisition and concluded that as few as 7 elements could be used in each subaperture as a compromise between SNR and lateral resolution. Karaman et al. [40] suggested applying time delays to the subapertures to defocus the transmit beams over a 90º sector in monostatic modalities. However, the radiation pattern diverged from circular waves for a 13-element subaperture, which limited the improvement in the acoustic pressure of each transmit beam. The idea of constructing a Virtual Element (VE) array in multistatic modalities was introduced by Lockwood et al. [41] with intended application to 3D imaging. The positioning of the virtual transmitting element can be either in front of the subaperture (focused beam), or behind the subaperture (defocused beam), and the time delays of each subaperture are simply the times required for the wave to propagate from the virtual element source to the physical elements. Using a focused beam VE subaperture in SAFT is particularly favorable in medical imaging due to an ability to reach a deeper range in highly attenuating tissues in analogy to focused B-modes [13], [14]. The other option is to place the VE array behind the physical array when the Region of Interest (ROI) is closer in range, such as in medical echocardiography [3]-[9] or in multi-layered medium NDT [31]. Despite these works, the use of virtual arrays in SAFT imaging has not been thoroughly investigated in the field of NDT, especially in the case of a transducer wedge setup where beam refractions and mode conversions at the wedge-medium interface play a critical role in the beamforming process.

Hand in hand with the development in the SAFT, Plane Wave (PW) imaging has been investigated in the medical imaging field in search for “ultrafast” capabilities. To improve the conventional B-mode line scans, the simultaneous transmission of the full aperture emits an unfocused plane wave that fully illuminates the ROI. Sandrin et al. [42], [43] experimented the plane wave modality to image transient propagation of shear waves in human tissues with a speed higher than 5000 frames/s. However, the transmission of a single plane wave lacks the angular diversity to characterize the target. The idea of compounding multiple beam angles into a single image was first investigated by Jespersen et al. [44] by steering scan lines of B-mode to reduce grating lobes. Incoherent spatial compounding with different steered plane waves was introduced by Tanter et al. [45] to average the estimations of vector tissue motions. Cheng and Lu [46] proposed a coherent spatial compounding of plane waves in a Fourier imaging framework with limited diffraction beams. Inspired by the dynamic focusing ability of the SAFT approach, Montaldo et al. [10] introduced coherent plane-wave compounding using the synthetic transmit focus of a collection of tilted plane waves. The simplicity and efficiency of spatial-coherent time-delay beamformers have paved the way to apply this ultrafast modality to various clinical applications including shear wave elastography, doppler imaging, and functional ultrasound [11]. Due to the advantage of high acoustic pressure using the full aperture, plane wave imaging is receiving more attention also in the NDT field. Cruza et al. [29] improved the beamforming of multiple PW images using a phase coherence weighting. Le Jeune et al. [26] and Merabet et al. [27] explored PW methods to image crack-type defects in steel blocks using both TFM and wavenumber algorithms in a multi-layered propagation setup. No prior investigation of PW imaging in transducer wedge setups appears in the literature.

One final recent development in SAFT imaging consists of efforts to increase the transducer array gain without increasing its physical aperture by compounding multiple wave modes. This opportunity is particularly applicable to NDT imaging of bulk solids that can support both longitudinal (L-) wave and shear (S-) wave propagations [24], [32], or imaging of dispersive waveguides that can support multiple guided modes (e.g., Lamb modes in plates) [47].

This chapter builds on all these recent developments to propose improvements to ultrasonic SAFT utilized in the field of NDT of materials and structures that require the use of a transducer wedge. The improvements are sought in terms of imaging speed and imaging accuracy. Specifically, the study compares sparse firing SAFT subarrays in both Virtual Element and Plane Wave modalities as they apply to a transducer wedge setup in the presence of wave refractions and mode conversions. It also investigates wave mode compounding in transducer wedges for further contrast improvement. Numerical simulations and experimental tests demonstrate successful implementations of these techniques to transducer-wedge setups. These improvements are also applied to the practical case of imaging transverse defects in rail tracks.

2.2 Sparse Transmit Synthetic Aperture Focus Technique in Transducer-Wedge Setup

This section presents the various steps that are being proposed for high contrast 2D SAFT imaging with fast frame rates via sparse transmit events, considering both the Virtual Element (VE) method and the Plane Wave (PW) method, for cases that require an interposed coupling medium between the transducer array and the test piece. These steps include multi-channel transmission modalities, total focusing method with consideration of refraction ray tracing in the beamforming algorithm, and wave mode compounding for additional contrast improvement.

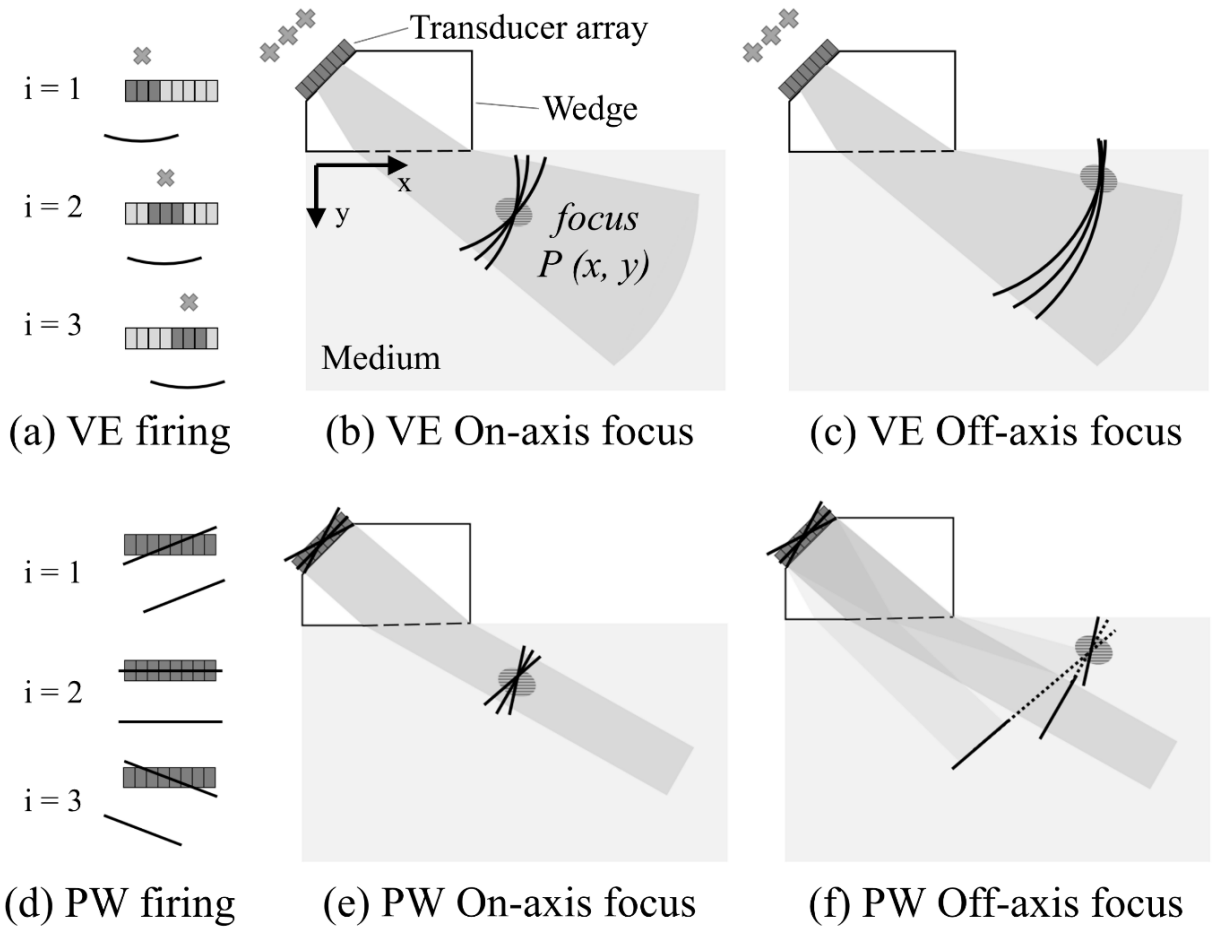

Figure 2.1: Synthetic transmit focus using VE and PW. (a) Three defocused waves defined by the VE subapertures. Beamforming in transmission with synthetic focus at point P(x, y) at on-axis positions (b), and off-axis positions (c). (d) Three unfocused waves defined by the inclined PW full aperture. Synthetic beamforming at on-axis (e) and off-axis (f) positions.

2.2.1 Speed and Contrast Enhancement Methods

A sparse SAFT scheme uses a select set of transmit elements as the active transmit array to increase the frame rate. However, the use of an interposed medium such as an acoustic wedge requires multiple elements in each transmit subarray to overcome the SNR losses of the target reflections. The subarray can be designed to transmit a focused, unfocused, or defocused beam pattern depending on the requirements of the ROI and resulting image quality.

The principle of synthetic transmit focus combined with multi-channel transmission is illustrated in Fig. 2.1. The VE method transmits a defocused circular wave using a phased subaperture in the physical array as shown in Fig. 2.1(a). In each transmit event *i*, the acoustic field of the subaperture elements superimposes to a circular wavefront such that the transmission can be modeled as a virtual element (point source) placed behind the physical array, Fig. 2.1(b). Each transmit beam is properly time delayed by calculating the ray path connecting the virtual element to the focus point $P(x, y)$, so that the transmitted wave fronts are compounded coherently at an on-axis focus. By adjusting the time delays, the synthetic focus can be achieved at any point in the overlapped transmit beam, including an off-axis location as shown in Fig. 2.1(c). For focus locations close to the surface of the medium, the ray path may approach the wedge critical angle, degrading the beam quality. Hence the choice of angular aperture of the VE is important to ensure consistent focusing at multiple locations of the ROI.

Let us now consider the PW imaging method, shown in Fig. 2.1(d), where plane waves at different angles are synthetized by the full array. In each transmit event *i*, the acoustic field of individual elements superimposes to a plane wavefront defined by the incline angle. In analogy to SAFT methods for circular waves, the coherent spatial compounding can be achieved by time delaying the transmit beam considering the ray path connecting the transmit plane to the focus point $P(x, y)$, as shown in Fig. 2.1(e). It is worth emphasizing that the PW method becomes inefficient when the plane waves transmitted at different angles do not overlap in the ROI, as shown in Fig. 2.1(f) for an off-axis focus. Thus, the working distance, angular range, and angular resolution of PW should be carefully examined for a multi-layered medium setup to ensure a consistent focusing ability throughout the ROI.

2.2.2 Total Focusing Method with Interposed Coupling Medium

Fig. 2.2(a) shows a sample *M*-element virtual array located behind the *N*-element physical array using the VE method. The transducer array is attached to a wedge and effectively converts only L-waves propagating to and from the wedge. Assume the physical elements set as (x_e, 0) in a local coordinate system where the *x*-axis is aligned with the array (e = 1, 2, …, N). The location of the virtual element is at (x_c, d_f) and is at the same horizontal location as the center of the active subaperture, Fig. 2.2(a). The transmit delays associated with the active subaperture elements are

$$\tau_e = \frac{\sqrt{(x_e - x_c)^2 + {d_f}^2}}{c_w^L} \tag{2.1}$$

where d_f is the defocal depth, and c_w^L is the speed of the L-wave in the wedge. The angular aperture α is the key feature of the subaperture that approximates the angular range within which the superimposed acoustic field from individual channels can be coherently compounded as a circular wave. The parameter α can be determined by simple geometrical relations

$$\alpha = 2\arctan\frac{D_{act}}{2d_f} \tag{2.2}$$

where D_{act} is the subaperture's size. Typically, for a sector scan where the physical array is directly attached to the test piece, the parameter α is set to $\pi/2$ to ensure sufficient beam spread [6]. However, the angle of view in a transducer wedge setup is restricted by the length of the wedge-medium interface, as shown for example in Fig. 2.1(b). Thus, the main problem here is to determine the angular aperture and the dimension of the subaperture to maximize the image quality.

Fig. 2.2(b) schematizes the VE modality with the transducer wedge. Since there are only *M* subaperture transmission events, the multistatic data acquisition is analogous to an FMC between virtual transmitters i = 1, 2, …, M and physical receivers j = 1, 2, …, N. The usual TFM

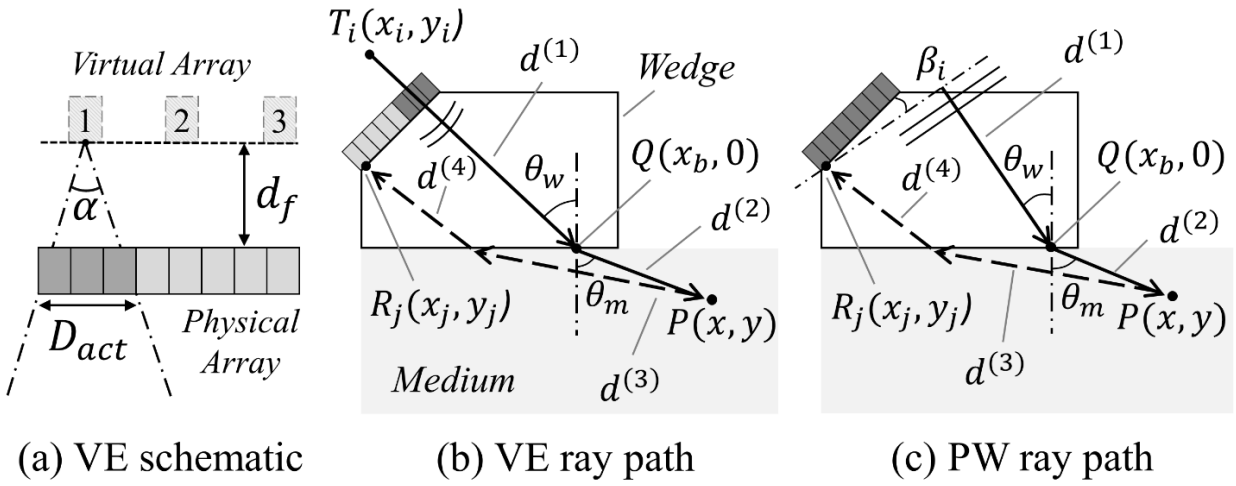

Figure 2.2: (a) The virtual element array defined by the defocal depth z_f and the angular aperture α. Transducer wedge imaging ray paths: (b) VE method: ray tracing connecting virtual transmit element Ti, focal point P(x, y), and receiver element R_j; (c) PW method: ray tracing connecting plane wave transmission with incline angle β_i, focal point P(x, y), and receiver element R_j.

Delay-and-Sum (DAS) algorithm constructs the intensity value at a focus point $P(x, y)$ by summing the amplitudes of received signals that are appropriately backpropagated for each combination of transmitter-receiver pairs

$$I(x,y) = \sum_{i=1}^{M}\sum_{j=1}^{N} A_{ij}(\tau_{ij,xy}) \tag{2.3}$$

where the Time-of-Flight (TOF) $\tau_{ij,xy}$ is the propagation time of a certain ray path from the transmitter $T_i(x_i, y_i)$ to the pixel $P(x, y)$ and back to the receiver $R_j(x_j, y_j)$, and $A_{ij}(t)$ is the amplitude of the received signal.

The wave refractions at the wedge-medium interface, shown in Fig. 2.2(b), need to be taken into account for proper beamforming. Using Snell's law, the ray tracing algorithm extends path identification to multi-layer mediums following Fermat's principle. Given a focus point $P(x, y)$ and a point source $T_i(x_i, y_i)$, there exists a unique point of incidence $Q(x_b, 0)$ at the wedge-medium interface such that Snell's law is best satisfied

$$\frac{c_w^L}{c_m^{L,S}} = \frac{\sin(\theta_w)}{\sin(\theta_m)} = r \tag{2.4}$$

where $c_m^{L,S}$ is the L-wave or S-wave velocities in the test medium, θ_w is the angle of incidence in the wedge, θ_m is the angle of incidence in the medium associated to the wave mode of interest, and r is a constant ratio determined by the wave velocities. Since θ_w and θ_m are functions of x_{trail} for a given set of $P(x, y)$ and $T_i(x_i, y_i)$, the position $(x_{trial}, 0)$ where the ratio of the sines of the two incident angles is closest to the constant r represents the optimum point of incidence $Q(x_b, 0)$. The optimization can be formalized by matching the ratio r as follows

$$x_b(x, y, x_i, y_i) = \arg\min_{x_{trial}} \left| \frac{\sin(\theta_w(x_{trial}))}{\sin(\theta_m(x_{trial}))} - r \right| \tag{2.5}$$

where the value of x_{trial} that minimizes the absolute value on the right-hand side of Eq. 2.5 is taken as x_b. The return ray path connecting a focus point $P(x, y)$ to a point receiver $R_j(x_j, y_j)$ can be calculated in a similar fashion by replacing (x_i, y_i) by (x_j, y_j). With the point of incidence for each ray path identified, the final TOF in Eq. 2.3 can be finally expressed as

$$\tau_{ij,xy}{}^{LSSL,LSLL,LLSL,LLLL} = \frac{d_{i,xy}^{L(1)}}{c_w^L} + \frac{d_{i,xy}^{L,S(2)}}{c_m^{L,S}} + \frac{d_{j,xy}^{L,S(3)}}{c_m^{L,S}} + \frac{d_{j,xy}^{L(4)}}{c_w^L} \tag{2.6}$$

which describes the inter-element wave propagation from the virtual transmit array to the physical receive array. Notice that the selection of wave mode in Eq. 2.6 can result in a total of four wave mode combinations. Since different wave modes in the test piece result in different r (and thus distinct incident angle pairs), each mode combination will have distinct ray paths connecting the same focus point to the array. The calculation of TOFs for the multiple modes in the wedge transducer case is discussed in the next section.

The case of the PW modality with the transducer wedge setup is schematized in Fig. 2.2(c). Again, using the local physical array coordinates (x_e, 0), the transmit delays applied to the full aperture elements are

$$\tau_e = (x_e - x_1)\sin(\beta_i)/c_w^L \tag{2.7}$$

where x_1 is the horizontal position of an arbitrary offset element (here chosen as #1) which has zero phase in all PW transmissions. Notice that in Fig. 2.2(c) the PW incline angle β_i is defined as negative such that the rest of the array actually fires ahead of the offset element. It has to be emphasized that for each wave mode in the medium the selection of β_i has an upper limit beyond which the incident angle θ_w exceeds the critical angle. The range of β_i's define the PW angle of view similarly to the parameter α in VE, so they must be considered carefully to maximize the image resolution at high frame rates.

The multistatic data acquisition now is an FMC scheme between plane transmitters i = 1, 2, …, M and point receivers j = 1, 2, …, N. For a given incline angle β_i, the incident angle θ_w can be determined from geometrical relationships. The angle of incidence θ_m is now as a function of β_i

$$\theta_m(\beta_i) = \arcsin(r\sin(\theta_w)) \tag{2.8}$$

where r is related to the selected wave mode in the medium as in Eq. 2.4. Thus, for PW the optimization of $Q(x_b, 0)$ can be accomplished by matching the value of θ_m as follows

$$x_b(x, y, \beta_i) = \arg\min_{x_{trial}} \left|\arctan\frac{x - x_{trial}}{y} - \theta_m\right|. \tag{2.9}$$

Finally, the TOF of PW-TFM can be calculated in the same way as in Eq. 2.6 and then used in the DAS beamformer of Eq. 2.3. The only difference in calculating the wave distances is the term $d_{i,xy}^{(1)}$, that requires knowledge of the location of the plane wave at time zero, which can be easily found by knowing the location of the offset element. Instead of finding the distance

between two points as in VE-TFM, now $d_{i,xy}^{(1)}$ denotes the distance between the point of incidence $Q(x_b, 0)$ and the planar wavefront at time zero.

2.2.3 Compounding of Multiple Wave Modes

For the transducer wedge setup, the L-wave transmitted in the wedge can be refracted as both an L-wave and an S-wave in the test piece. Wave mode conversion can also exist in the scattering from discontinuities in the medium, resulting a total of four wave mode combinations in the test piece (LSSL, LSLL, LLSL, and LLLL). It is worth stating that since the wedge angle is typically designed to refract S-waves in structural materials, the angle of view (angular position of the transmitted beam) of the L-wave refraction is limited due to the critical angle. Thus, the SNR of the three mode combinations involving L-wave can be expected to be much poorer than the dominant SS combination. In addition, since the wavelength of the L-mode is twice as large as that of the S-mode, its resolution is also poorer.

The feasibility of wave mode compounding using VE or PW sparse transmissions is shown in Fig. 2.3. For the VE modality, although the angle of view of the L-wave is limited there are still sufficient regions of overlap with the refracted S-wave. Coherent spatial compounding is possible by considering the appropriate delays for the S-wave and the L-wave at a given focus point. For the PW modality, wave mode compounding is less efficient since the unfocused waves have a fixed lateral beam spread that does not change with increasing range, as shown in Fig. 2.3(b). Since there is no overlap in the illuminated region of the two wave modes, the two transmitted beams cannot be coherently compounded.

Incoherent wave compounding can be achieved as follows

$$I_{TOT}(x,y) = \sum_{MC} I_{MC}(x,y) = \sum_{MC}\sum_{i=1}^{M}\sum_{j=1}^{N} A_{ij}\left(\tau_{ij,xy}{}^{MC=LSSL,LSLL,LLSL,LLLL}\right) \tag{2.10}$$

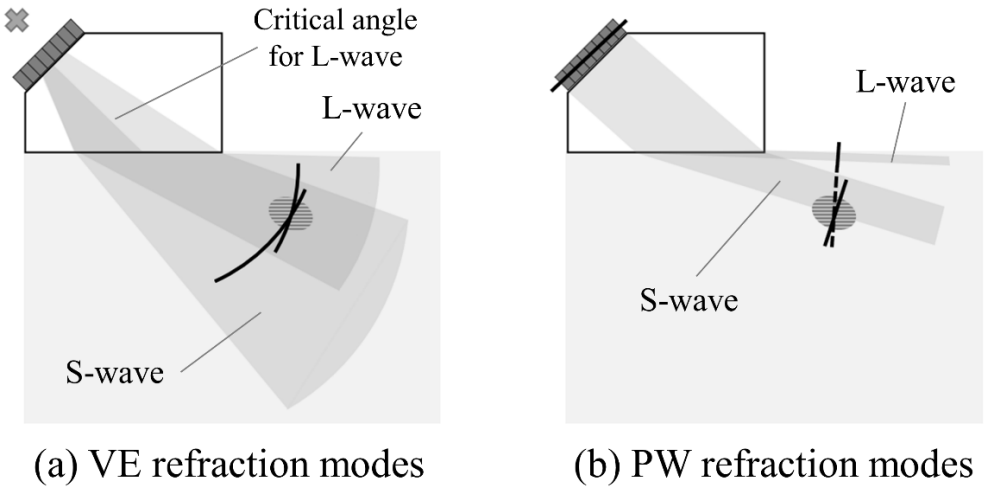

Figure 2.3: Wave mode compounding in transmission using different sparse firing modalities. Beam spread overlapping from a single transmission in VE (a) and in PW (b).

where the compounded image $I_{TOT}(x, y)$ is a summation of TFM images beamformed by individual wave modes $I_{MC}(x, y)$ obtained using Eq. 2.3 with the corresponding time delays. The compounding thus increases the effective array aperture without increasing the array physical size.

2.3 Numerical Analyses

Numerical studies of the sparse SAFT with a wedge were carried out with the k-wave module in MATLAB in a 2-D (plane strain) scenario. The simulation modeled the propagation of the transmitted beam in a 110 mm × 120 mm (length by depth) grid, with the upper half as the transducer wedge and the lower half as the inspected test piece (assumed to be aluminum). The wedge could only propagate L-wave with a speed of 2350 m/s, while the aluminum piece allowed both L-wave and S-wave to propagate with a speed of 6300 m/s and 3100 m/s, respectively. The spatial grid was subdivided with a 0.1 mm spacing, and the time step was set to 5 ns to enable sufficient sampling of all possible wave mode propagations in both media. The ultrasonic array consisted of 64 transmitting channels, with an element width of 0.6 mm. As shown in the schematic

drawings in Fig. 2.4, the array was positioned at an inclined 54 deg angle from the y-axis and the depth of the first element (on the lower left side of the array) was -15 mm. The excitation of each element was simulated by applying a unidirectional displacement perpendicular to the array (hereon referred as the 0º broadside direction of the array) across the width of the element. The applied displacement was a 2.5 MHz tone burst enveloped by a Gaussian window.

For the different transmit modalities, the acoustic pressure fields $\Phi_i(\hat{x}, \hat{y}, t)$ were recorded for each transmission beam in the ROI. Synthetic focus in transmission was performed by first aligning the time delay needed for each transmission to propagate to the focus point $P(x, y)$

$$\tilde{\tau}_{i,xy}{}^{S,L} = \tau_{i,xy}{}^{S,L} - \min_i(\tau_{i,xy}{}^{S,L}) \tag{2.11}$$

where $\tau_{i,xy}{}^{S,L}$ is the propagation time from the source to the focus point for a given wave mode in the medium, and $\tilde{\tau}_{i,xy}{}^{S,L}$ is the offset time delay by subtracting the minimum value of $\tau_{i,xy}{}^{S,L}$ in all transmission events. Then the acoustic field from each transmission was added synthetically with the proper time alignment of individual transmit beams

$$\Phi_{xy}{}^{S,L}(\hat{x}, \hat{y}, t) = \sum_{i=1}^{M} \Phi_i\left(\hat{x}, \hat{y}, t + \tilde{\tau}_{i,xy}{}^{S,L}\right) \tag{2.12}$$

where $\Phi_{xy}(\hat{x}, \hat{y}, t)$ is the synthetic transmit pressure field with spatial compounding on $P(x, y)$. Note that $\hat{x}$ and $\hat{y}$ are variables denoting the coordinates of the ROI, to differentiate from the specific focus point $P(x, y)$. Finally, the beam pattern of the synthetic transmit field $\Phi_{beam,xy}(\hat{x}, \hat{y})$ was taken as the maximum amplitude in the time history $\Phi_{xy}(\hat{x}, \hat{y}, t)$. A simple compounding of the synthetic transmit field of the two wave modes in transmission is a direct sum:

$$\Phi_{beam,xy}{}^{TOT}(\hat{x}, \hat{y}) = \sum_{MC} \Phi_{beam,xy}{}^{MC=S,L}(\hat{x}, \hat{y})\,. \tag{2.13}$$

Note that there were only two wave modes existing in the transmit field simulation, whereas for a pulse-echo signal a total of four wave mode combinations are available for compounding.

The purpose of simulating the synthetic transmit pressure field was to quantitively evaluate the performance of the different SAFT modalities in the designated transducer wedge setup. The line spread function (LSF) was estimated from the beam pattern $\Phi_{beam,xy}(\hat{x}, \hat{y})$ by extracting the intensity values along an arc that denotes the snapshot of the wavefront with the same propagation time from the center element of the array when passing through the focus point $P(x, y)$, as illustrated in the schematics of Fig. 2.4. The performance metrics of interest included: the dynamic range (defined as the mean dB level in the illuminated angular range), the sidelobe level (defined as the dB level of the strongest side lobe), and the lateral resolution (defined as the -6 dB full width of the LSF main lobe for linear beamformers such as DAS). The lateral resolution, or main lobe half width (MLHW), was calculated by multiplying the angular range of the main lobe in the LSF with the ray transmission distance. Two focus points were tested to evaluate the synthetic transmit beam performance at both an on-axis position (70 mm, 27 mm) and an off-axis position (70 mm, 5 mm). Notice that the notation "on-axis" corresponds to the broadside of the S-wave refraction in the test piece. The broadside transmission in the wedge cannot refract L-wave in the aluminum since the transmission angle is beyond the critical angle.

2.3.1 Configurations of Virtual Element Modality

The configurations of VE-SAFT can be classified in two levels. The first level is the parameters required to define a single subaperture. This includes the angular aperture α and the number of elements (dimension) of the subaperture. The angular aperture determines the angle of view of each transmission beam, and the subaperture size is critical to improve the SNR of the coherent wavefronts of the phased subarray. The second level is the parameters that define the

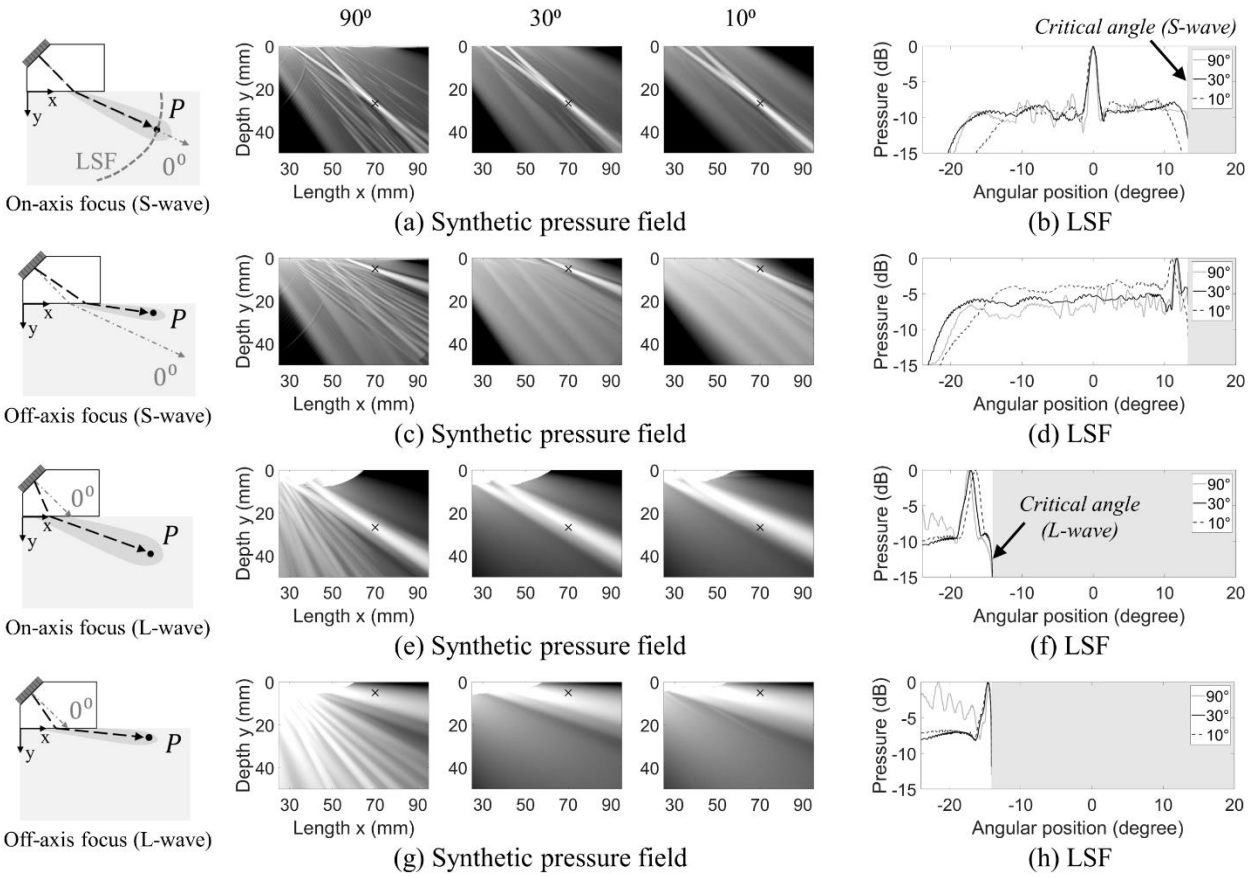

Figure 2.4: Synthetic transmit pressure field for three VE angular apertures. Spatial compounding of S-wave at on-axis P(70 mm, 27 mm): (a) synthetic pressure and (b) lateral LSF; at off-axis position P(70 mm, 5 mm): (c) and (d). Spatial compounding of L-wave at on-axis: (e) and (f); at off-axis: (g) and (h). All images are displayed in 15 dB dynamic range.

synthetic aperture (virtual transmit array). This includes the number of transmissions and the pitch of the virtual array. The number of transmissions should be restricted to achieve fast frame rates. The pitch of the virtual array is related to the resolution of the synthetic transmit beam.

The comparison of different angular apertures in the synthetic transmit field in the aluminum piece is shown in Fig. 2.4. Three VE transmissions with a virtual pitch of 12 mm and a subaperture of 21 elements were simulated. First, the field of S-wave was examined. For the on-axis focus, Fig. 2.4(a) shows the normalized synthetic pressure field ${\Phi_{beam,xy}}^{S}(\hat{x},\hat{y})$ with the variation of α, with the corresponding LSFs in Fig. 2.4(b). The LSFs are plotted as a function of

angular positions that is measured as the transmit angles from the 0º broadside direction of the array. The critical angle at 13.8º in the LSF means that the transmit beam cannot refract S-waves beyond that angular position. For the on-axis focus, the 90º aperture results in numerous side lobes due to the low SNR. As seen in the LSFs these side lobes are reduced by a smaller angular aperture. As α becomes smaller the transmit beam is more focused on the broadside at the cost of lateral resolution.

The steering capability of the synthetic transmit aperture is examined in the case of off-axis focus in Fig. 2.4(c) and (d). The focusing ability of the 3-transmission synthetic field is poor judging from the limited dynamic range. The 10º aperture loses the correct angular direction on the focus because of the poor steering ability with a small α. Thus, a small angular aperture should be avoided to ensure good beam steering near the critical angle.

The comparison of different angular apertures in the synthetic transmit field of L-wave is shown in Fig. 2.4(e)-(h). The synthetic pressure field ${\Phi_{beam,xy}}^{L}(\hat{x}, \hat{y})$ was obtained using the same 3-transmission modality as in Fig. 2.4(a)-(d), but the L-waves were additionally windowed in each individual beam $\Phi_i(\hat{x}, \hat{y}, t)$ to eliminate the disturbance of the S-waves. Fig. 2.4(e) shows the normalized synthetic pressure field ${\Phi_{beam,xy}}^{L}(\hat{x}, \hat{y})$ with the variation of α and their corresponding LSFs in Fig. 2.4(f) when the focus point is on-axis. The uniform white region on the upper left in the images is a contamination of the S-wave that is hard to eliminate because the two modes are closely spaced in time near the wedge-medium interface. As previously stated, due to the inclination of the wedge only a limited angular extent of the beam can refract L-waves in the aluminum, resulting in a critical angle of -14.1º. As a result, beam steering and coherent compounding for L-wave refraction is much more challenging than for the S-wave. For a wide beam spread (α = 90º), the intensity of the side lobes is unacceptably high due to the low SNR. As

the parameter α becomes smaller, the L-wave synthetic transmit aperture cannot capture the correct focus direction. The errors in the lateral position of the focused beams are 1.0 mm and 3.8 mm, for $\alpha = 30^{\circ}$ and 10°, respectively. For an off-axis focus that is close to the critical angle position, the low performance of L-wave is more problematic. As shown in Fig. 2.4(g), none of the angular apertures can generate a focused beam at the correct angular position. A smaller α ensures a strong main lobe though slightly off the focus.

To summarize, an optimum α should be smaller than a typical "half-sector" to ensure sufficient enhancement in the acoustic power, but the α value should not be too small so that the beam steering ability is compromised.

Fig. 2.5 shows the synthetic pressure field at an on-axis focus P(70 mm, 27 mm) as a function of the size of the VE subaperture. The angular aperture was kept at 45° with a varying defocal depth to match the dimension of each subaperture. As shown in Fig. 2.5(a), the transmit pressure of both S-wave and L-wave increases with the number of elements. The curve of S-wave is similar to the case in a single medium setup as predicted in [12]. However, the limited angular range of the refracted L-wave beams does not benefit from enlarging the subaperture. Even using as many as half of the array (33 elements) can only obtain twice the pressure of a 1 channel emission for the L-wave. The resolution of the synthetic transmit beam, quantified by the MLHW (main lobe half width, i.e. -6 dB full width of the LSF main peak), decreases with larger subapertures, as shown in Fig. 2.5(b). This implies that a small number of elements should be used to achieve a resolution similar to the "golden standard" 1 element FMC SAFT. Besides, using a large subaperture limits the maximum pitch achievable by the virtual array, which restricts the angular diversity of transmission beams. A transmit subaperture of approximately 19~21 elements seem like a good tradeoff to obtain a high intensity without sacrificing the resolution.

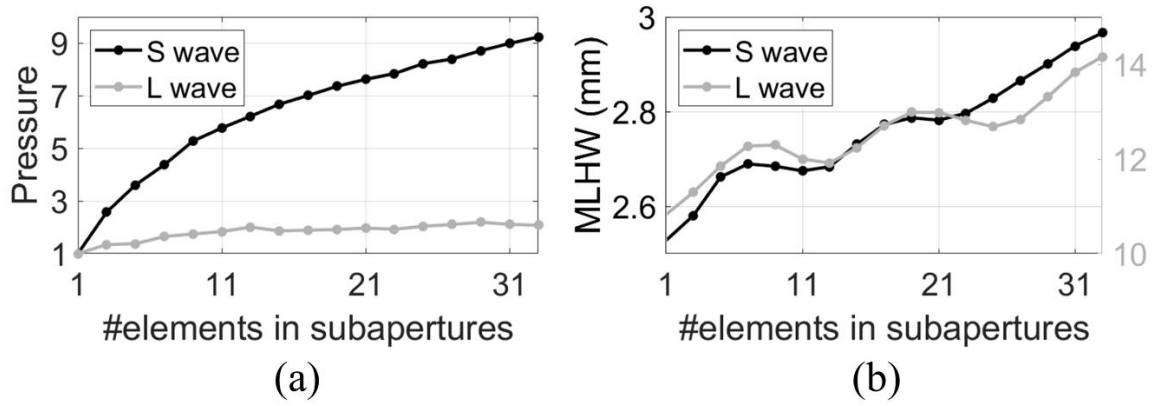

Figure 2.5: Synthetic transmit pressure field of three virtual elements with an angular aperture of 45º for an increasing number of elements in the subapertures. (a) Normalized maximum synthetic pressure and (b) associated resolution.

Fig. 2.6 represents the synthetic transmit pressure field obtained by three different virtual array pitches. Eight VE transmissions with an angular aperture of 45º and a subaperture of 21 elements were simulated. Coherent summation was performed at the same on-axis and off-axis positions using the S-wave refraction. In addition to the maximum 3.6 mm pitch achievable for an 8 × 21 subaperture combination in the 64-element array, a pseudo 5.4 mm pitch was also tested. In the 5.4 mm pitch setup, the required subaperture of some of the virtual elements exceeded the physical aperture. For example, the center of the first subaperture is at the 1st element with a theoretical 21-channel subaperture from element #-9 to #11. However, the available physical aperture is #1 to #11 so roughly half of the subaperture can be fired. The reason to expand the virtual pitch is to increase the beam resolution as much as possible. As shown in Fig. 2.6(a), the lateral resolution increases with the virtual pitch. The main lobe width is seen as 5.0 mm, 2.6 mm, and 2.0 mm for the 1.8 mm, 3.6 mm, and 5.4 mm virtual pitches, respectively. Also, the side lobe levels are reduced with a larger virtual pitch. The only drawback comparing 5.4 mm and the full transmitted 3.6 mm is that the dynamic range of the 5.4 mm version is 2.7 dB smaller due to reduced synthetic pressure. The same observations apply to off-axis focus as shown in Fig. 2.6(c).

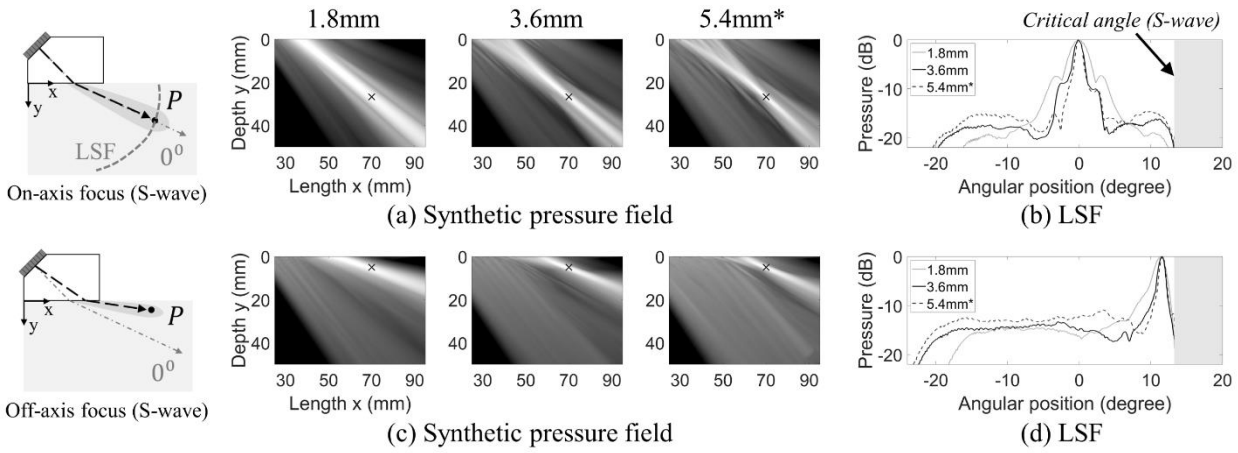

Figure 2.6: Synthetic transmit pressure field of S-wave for three virtual pitches. Spatial compounding at on-axis position: (a) synthetic pressure and (b) lateral LSF; at off-axis position: (c) synthetic pressure and (d) lateral LSF. All images are displayed in 25 dB dynamic range.

The 5.4 mm pitch shows a 2.3 mm resolution beam, which is 0.4 mm thinner than the 3.6 mm pitch. The left-hand side of the main lobe is thinner with the 5.4 mm pitch, giving a more accurate angular coverage of the main lobe, as confirmed in Fig. 2.6(d).

Thus, the widest virtual element array should be used to maximize the resolution and the steering ability. Instead of positioning all subapertures within the physical aperture, the constraint is instead to position the center of the subapertures within the physical aperture so that each transmission has more than half of the elements needed to compose the "ideal" subaperture.

2.3.2 Comparison between Plane Wave and Virtual Element Modalities

The configuration of PW transmission is simpler than the VE transmission since only the angle of view needs to be determined once the frame rate is fixed. The angle of view is defined by the angular range that the tilted angle β_i covers $\alpha \approx |\beta_M - \beta_1|$. As discussed in the critical angular positions of the refracted wave field, the transducer wedge setup considered in this paper can only refract S-waves at angles smaller than 13.8º and L-waves at angles smaller than -14.1º. It is useless to transmit plane waves with β_i < -14.1º since the refracted beams are propagating out of the ROI

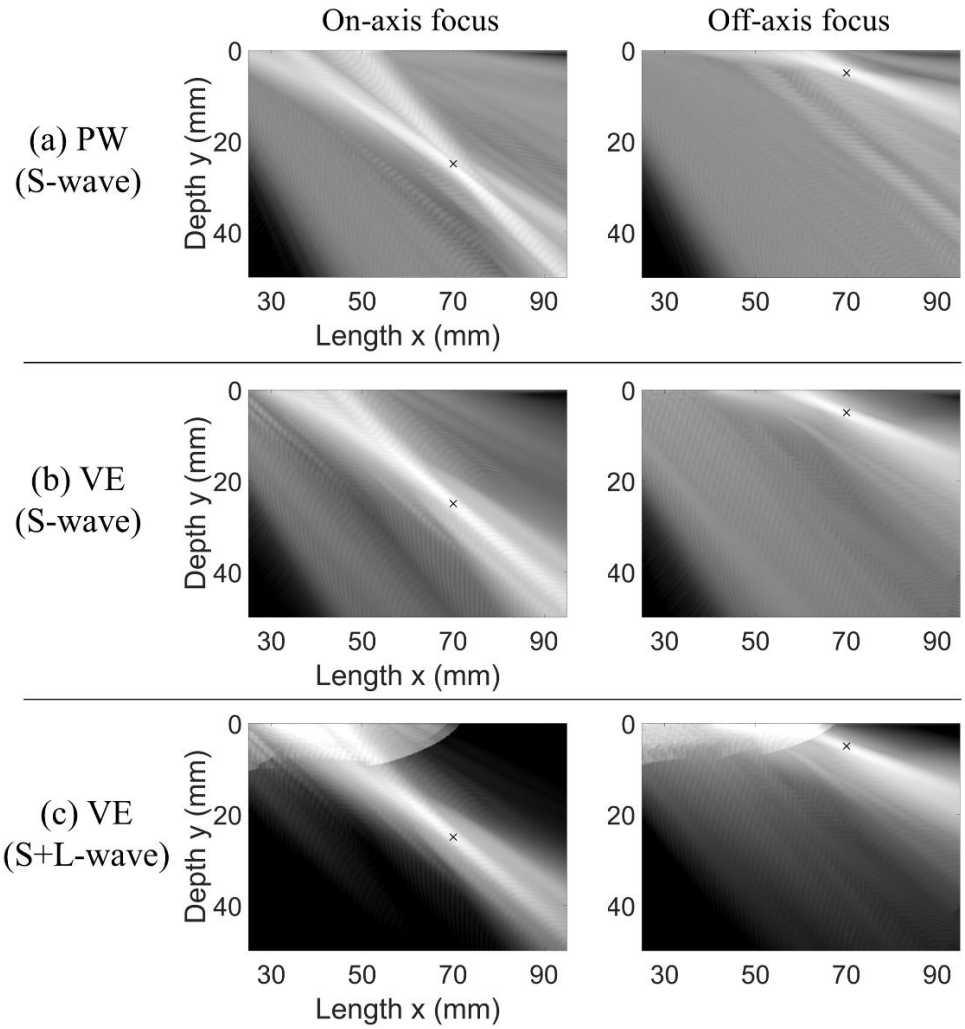

Figure 2.7: Synthetic transmit pressure field using 16 transmissions with different modalities focused on-axis and off-axis. (a) 16 PW transmissions beamforming using S-wave. In comparison, 16 VE transmissions beamforming using (b) S-wave only and (c) compounded S-wave and L-wave.

and the lateral coverage is limited. The range of β_i is finally set to -13º to 13º to cover the ROI using the dominant S-wave.

To show that PW and VE are similar with sufficient transmissions, the synthetic pressure field using the two modalities was simulated using 16 transmissions, as shown in Fig. 2.7. Comparing Fig. 2.7(a) and (b), the transmitted S-wave fields exhibit similar beam width and dynamic range. However, the VE modality can use the L-wave to "virtually" increase the transmit

aperture size through wave mode compounding using Eq. 2.13. As shown in Fig. 2.7(c), the compounded wave field shows a dramatic improvement in the dynamic range, especially for an on-axis focus. The resolution beams of both focus locations seem unchanged, since the resolution of the L-wave is much larger than that of the S-wave.

Thus, the addition of the L-wave in mode compounding beamforming tends to suppress the noise floor in the S-wave image while preserving the main lobe structure.

Clearly, the overall number of transmissions directly impacts the imaging frame rate. Fig. 2.8 shows the role of the number of transmissions on the synthetic transmit focus. The PW modalities were transmitted in a β_i range of -13º to 13º, and the VE modalities were transmitted with an angular aperture of 45º, a subaperture of 21 elements, and a maximum virtual pitch. The number of transmissions was varied by increasing the sampling of β_i in PW and decreasing the virtual pitch for VE. For the PW modalities with S-wave beamforming in Fig. 2.8(a), the improvement in dynamic range is most significant above 8 transmissions for both on-axis and off-axis focus. With a number of transmissions equal or smaller than 8, the shape of the main lobe cannot be clearly identified, and noise floors are too high. The transmit focus cannot find the correct angular position at 3 transmissions for both on-axis and off-axis focus due to the lack of overlapping regions to realize spatial compounding when the mesh of β_i is too sparse. On the contrary, the VE modalities with S-wave beamforming in Fig. 2.8(b) show a consistent improvement with an increasing number of transmissions. Only the off-axis focus of 3-transmission VE has larger side lobes than the correct lobe response. This can be attributed to the truncated transmission of the pseudo 5.4 mm virtual array in an extreme case (31% of the 3 × 21 subaperture combination was not emitted).

To compare the PW and VE S-wave fields, the pressure level of the off-axis focus was

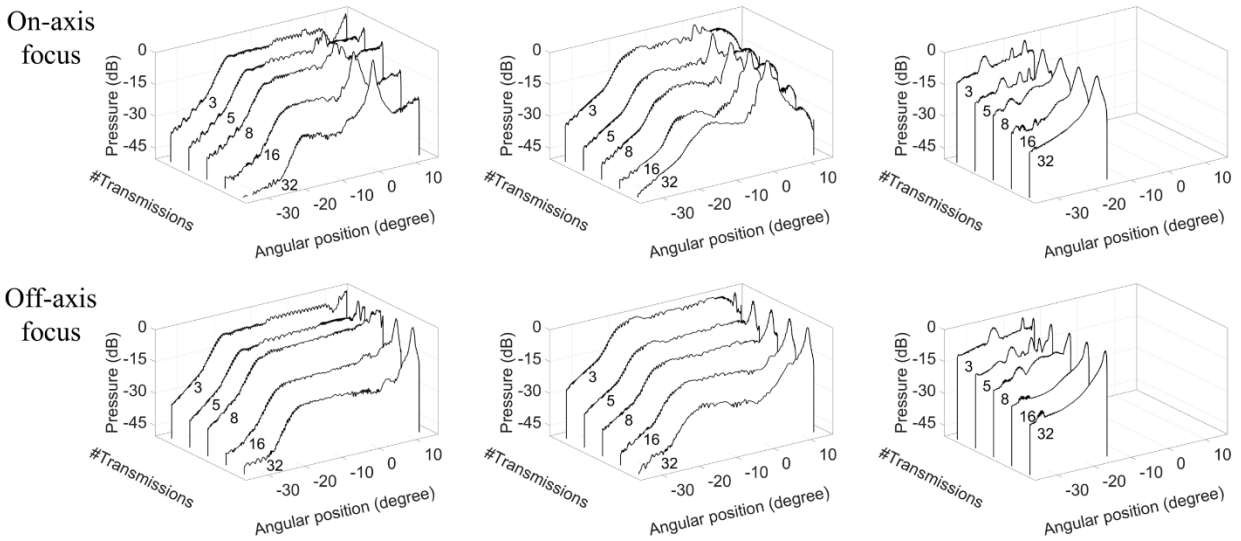

(a) PW (S-wave) (b) VE (S-wave) (c) VE (L-wave)

Figure 2.8: Normalized synthetic pressure field LSF focused on-axis and off-axis compounded with 3, 5, 8, 16, and 32 diverging waves using different modalities. (a) PW transmission beamformed using S-wave propagation in the test piece. VE transmission beamformed using (b) S-wave and (c) L-wave propagation in the test piece.

evaluated at broadside. For 3, 5, 8, 16, and 32 transmissions, the pressure levels are -5.1, -7.0, -7.3, -17.2, and -26.5 dB for PW and -2.0, -8.8, -12.8, -21.8, and -28.3 dB for VE. The two modalities show similar dynamic range at large number of transmissions, but the performance of VE is more stable than that of PW at fewer transmissions, i.e. high frame rates. Similar conclusions can be made for the two L-wave focuses using the same VE modalities in Fig. 2.8(c). As for the L-waves, the side lobes are largely suppressed with 8 transmissions, and focusing is progressively improved with increasing number of transmissions.

2.4 Experimental Results

2.4.1 Sparse Transmit Aperture Imaging Performance

Fig. 2.9 shows the setup of the first set of experimental tests on an aluminum block. The transducer was a 64-element linear array (Olympus NDT 2.25L64-A12) with central frequency at 2.25 MHz, 38.4 mm total active aperture with 10 mm elevation, and 0.6 mm element pitch. The array was attached to a 55-degree Rexolite wedge (Olympus NDT SA12-N55S) to generate directional S-wave in the target aluminum block. The block had three side drilled holes as targets for imaging. The diameter of the drilled holes was 0.5 mm so they can be considered as subwavelength scatterers (given the S-wave wavelength of 1.4 mm and the L-wave wavelength of 2.8 mm in aluminum at 2.25 MHz).

The image quality was examined by two metrics: the main lobe half width (MLHW) (defined previously in Section 3.A). The CNR is computed as [48]

$$CNR = \frac{\mu_s - \mu_n}{\sqrt{{\sigma_s}^2 + {\sigma_n}^2}} \tag{2.14}$$

where μ_s and μ_n are the mean gray levels in the scatterer and the noise floor, and σ_s and σ_n are their respective standard deviations. The scatterer is distinguished by a -15 dB threshold, and the rest of the pixels are treated as noise with a minimum of -60 dB.

The performance of the different sparse transmit imaging modalities is compared in Fig. 2.10, considering only the LSSL mode combination. Fig. 2.10(a) shows the PW-TFM image of the drilled hole at 12 mm in depth and 68 mm in length. Five PW transmissions were emitted covering incident angles from -13º to 13º. Each LSF was extracted along the cross-range direction shown as a dashed line. Significant side lobes are seen around the scatterer at high frame rate due to the lack of overlap region of the transmitted beams. The effect of suppressing the side lobes is

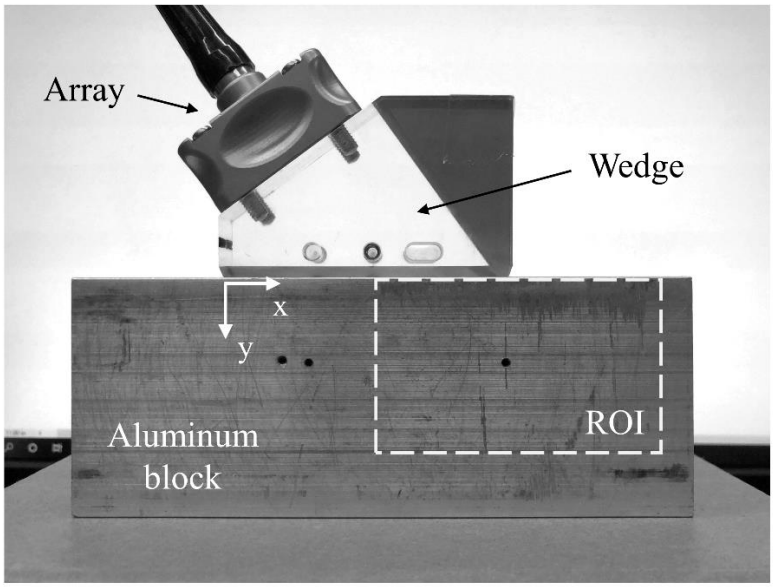

Figure 2.9: Experimental setup: the 64-element linear transducer array fixed to a plastic wedge scanning the aluminum block with drilled holes as imaging targets.

seen in the comparison of LSF between the faster 5-transmission and the slower 32-transmission PW-TFM images, shown in Fig. 2.10(b) with an average of 10 dB increase in dynamic range. Besides the improvement in side lobes, the lateral resolution is also higher seen from a shrinking of the main lobe width.

The VE-TFM image of the same hole scatterer is shown in Fig. 2.10(c). Five VE transmissions with an angular aperture of 45º and a subaperture of 21 elements were used with the maximum virtual pitch. Contrarily to PW, no significant side lobe is observed using the sparse transmissions of VE. The comparison of 5-transmission and 32-transmission VE-TFM images in Fig. 2.10(d) also shows better image quality at reduced frame rates. The most distinguishable improvement in the dynamic range is seen around 70 to 75 mm in length where the side lobes are suppressed by -10 dB. This denotes the improved steering ability of the VE beamformer to distinguish off-axis targets close to the surface of the aluminum block that is hard to illuminate with limited number of transmissions.

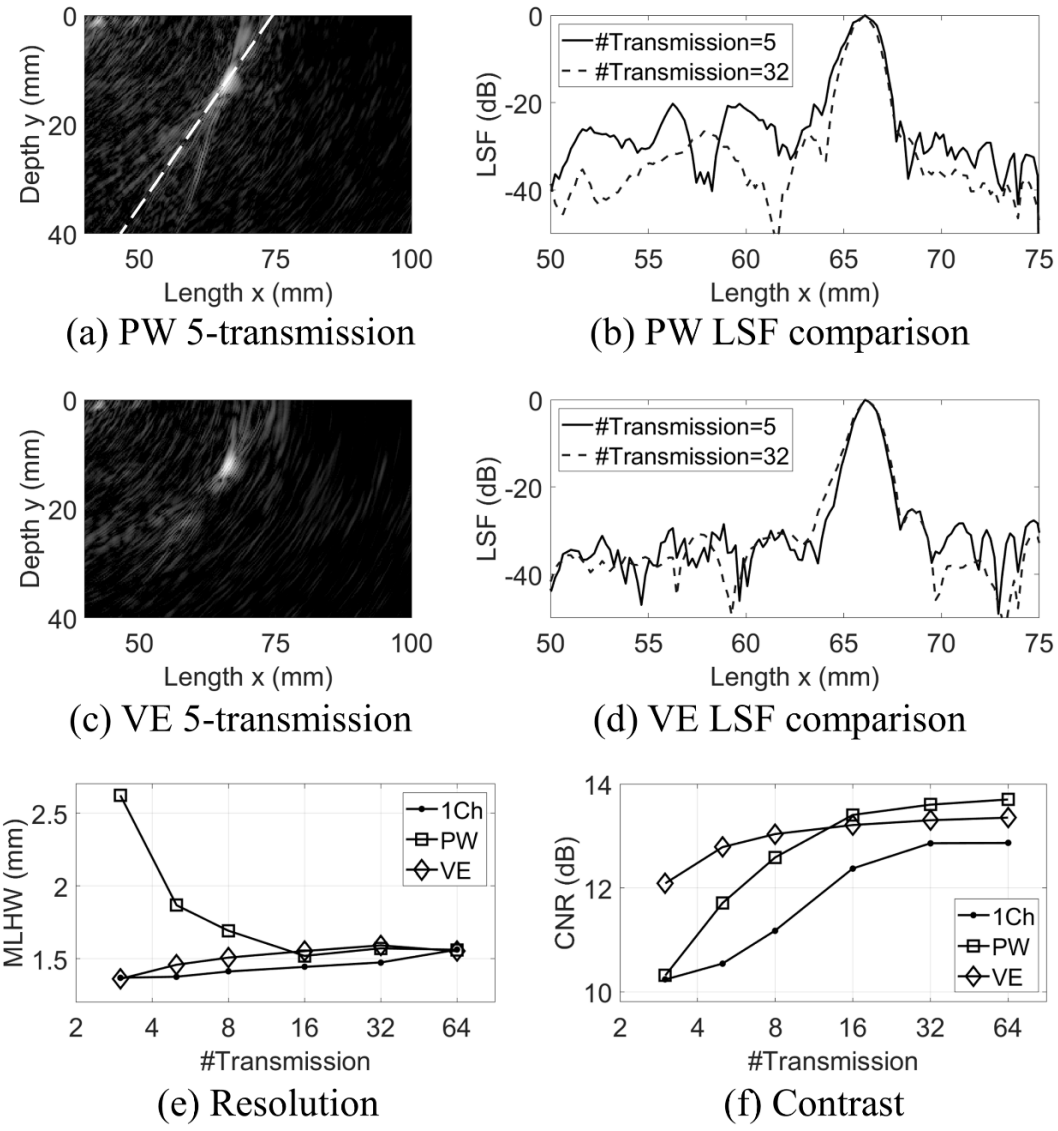

Figure 2.10: (a) TFM image of a drilled hole using 5-transmission PW modality. (b) LSF comparison of PW-TFM images. (c) TFM image using 5-transmission VE modality. (d) LSF comparison of VE-TFM images. Comparison of TFM images quantified by (e) MLHW and (f) CNR as a function of the number of transmissions.

Fig. 2.10(e) and (f) show the image quality of PW and VE at different numbers of transmissions, with 1 element transmission as benchmark in comparison. The CNR starts to degrade rapidly at 16-transmisson using only 1 element transmission due to the lack of synthetic acoustic power. PW-TRM images have the highest CNR at large number of transmissions, but

both CNR and resolution of PW-TFM are poorer when using few transmissions, as predicted in the numerical simulations of the previous section. In comparison, the CNR of the VE-TFM images is similar for all numbers of transmissions, and the MLHW is only 0.1 mm wider than the sparse SAFT at 5, 8, 16, and 32 transmissions. The resolution is interestingly slightly poorer with a larger number of transmissions as a result of saturation in the transmit field at high SNR.

2.4.2 Optimum Configuration of Virtual Element Modality

Fig. 2.11 discusses the choice of parameters in the VE modality with a transducer wedge. For this study, the number of transmissions was set to 8 and only the LSSL mode combination was beamformed. Comparing VE-TFM images of different angular apertures in Fig. 2.11(a), the smaller 20º VE results in higher image contrast but wider lateral lobes. Shown in Fig. 2.11(b), different angular apertures were tested in the range between 10º and 90º. It is observed that using angular apertures larger than 40º cannot achieve improvements in resolution due to the unique geometry in the transducer wedge setup. The wide beam spread is constrained by the limited angle of view in the wedge. In addition, angular apertures larger than 13.8º exceed the critical angle of S-wave in aluminum as explained earlier. The improvement in CNR is seen with a smaller angular aperture as expected, but the smallest angular aperture does not result in the highest CNR since the narrow beam spread does not result in a strong spatial coherence. The role of the subaperture size is examined in Fig. 2.11(c). The smallest MLHW is seen at 19-element subapertures as a tradeoff between transmit power and beam resolution. The improvement in CNR with larger subaperture sizes is not obvious, since the SNR is high when imaging strong scatterers. A more significant difference is expected when the target is acoustically weaker. Note that although these parameters need to be re-evaluated for different wedge angles or sizes, the general trend found in this study is still valid.

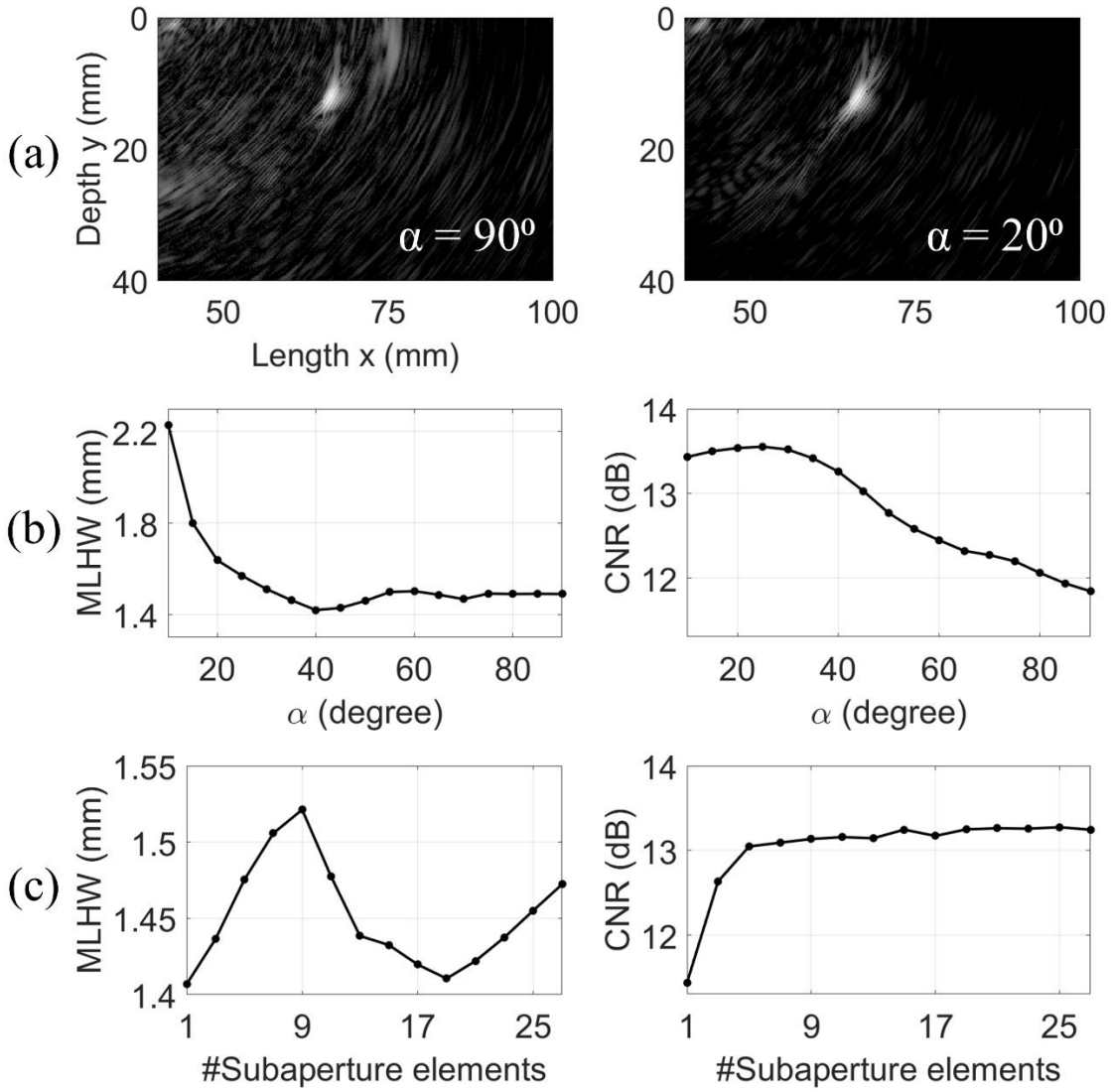

Figure 2.11: (a) VE-TFM images of a drilled hole in an aluminum block using two different angular apertures (90º and 20º), plotted in 40 dB dynamic range. (b) VE-TRM image quality as a function of angular aperture. The number of elements in each subaperture is 21. (c) VE-TRM image quality as a function of subaperture size. The angular aperture is 40º.

2.4.3 Demonstration of Wave Mode Compounding

Additional experimental tests were performed to illustrate the improvement in image quality using wave mode compounding. For this study, two 0.5-mm-diameter drilled holes in the aluminum block were imaged, located at 12.5 mm in the vertical dimension, and 56 mm and 68

mm in the horizontal dimension, respectively. The 8-transmission TFM images of the VE and PW modalities using different wave modes are shown in Fig. 2.12. Notice that different wave modes are displayed in different dynamic ranges to illuminate the focus. Again, due to the lack of modal spatial coherence in PW transmission beams, only two wave modes are available to beamform in reception. As shown in Fig. 2.12(a), for the PW-TFM image beamformed using the LSLL mode combination, a clear focus is seen at the hole closer to the array (on the left). The contrast of the LSLL mode combination is poorer than LSSL combination as predicted in the numerical simulations. The lobe sizes are also larger than LSSL combination since the L-mode wavelength is roughly twice that of the S-wave. The effect of wave mode compounding of the LSSL and LSLL mode combinations shows significant improvement in contrast compared to the images of an individual combination.

Similar behaviors are seen in the VE-TFM images shown in Fig. 2.12(b). VE transmissions were emitted with the optimum 40º, 19-element, maximum virtual pitch setup. For a defocused beam, compounding S-waves and L-waves in transmission is possible for VE-SAFT. This results in a maximum of four mode combinations, and the three mode combinations that have a good focus are displayed in Fig. 2.12(b). For the additional LLLL mode combination, the lobe sizes are the largest since both transmitted and received beams involve lower resolution L-waves. The compounding of the three wave mode combinations in VE-TFM shows significant contrast gains compared with the two-mode compounding of PW-TFM. In addition, all the side lobes are suppressed below the -50 dB visible dynamic range.

The line profiles showing comparison of wave mode compounding are shown in Fig. 2.12(c) and (d), respectively. Each plot was sampled at 12.5 mm in depth along the dashed line in Fig. 2.12(a). The compounded line profiles show that wave mode compounding lowers the noise

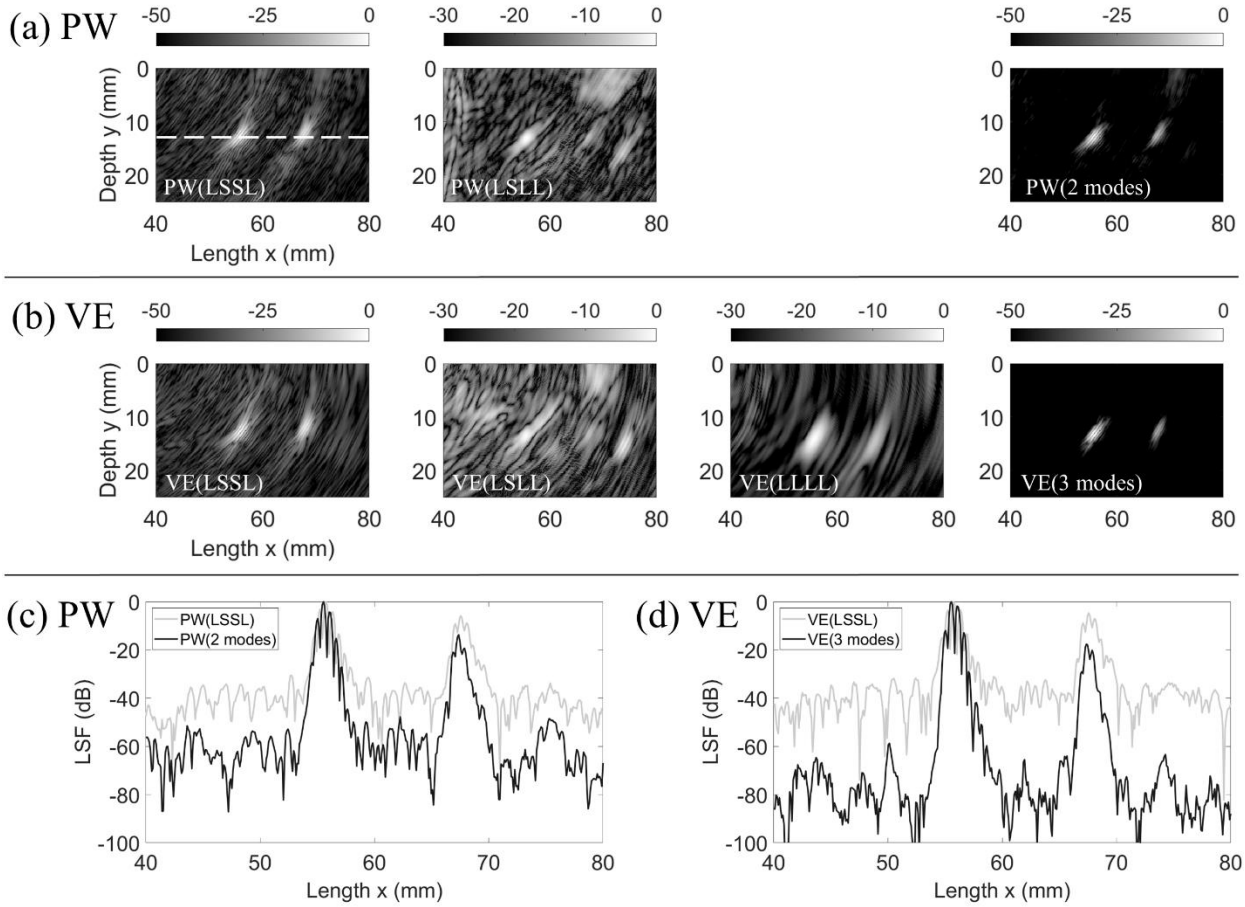

Figure 2.12: (a) PW-TFM images of two drilled holes beamformed using different wave mode combinations: LSSL, LSLL, and compounding two modes. (b) VE-TFM images of the same targets: LSSL, LSLL, LLLL, and compounding all three modes. Line profile comparison along the same depth at y = 12.5 mm for (c) PW and (d) VE.

floor and narrows the main lobes compared to the SS mode combination alone. Specifically, the average improvement in dynamic range is 20 dB for PW-TFM and 40 dB for VE-TFM. Besides, the compounded image does not lose focus on the drilled hole on the right. The second main lobe is only reduced by 8 dB and 13 dB from the LSSL mode counterparts, for PW-TFM and VE-TFM respectively. This suggests that wave mode compounding can be applied to extended targets without losing focus on the acoustically weaker targets.

2.4.4 Application to Imaging Transverse Defects in Rails

Transverse defects in the rail head are notorious causes of severe train accidents, if not detected early [49]. For this reason rails are routinely inspected by ultrasonic testing and other NDT techniques to detect and quantify these defects. Imaging of the flaws, beyond simple detection, is a particularly challenging task. Because of the importance to perform the imaging in a scanning mode (whether for manual scanning or in-motion scanning), any improvements to the speed of imaging technologies for this application (such as the sparse SAFT) is highly desirable. This section applies the strategies discussed above to the imaging of transverse defects in the railhead which, because of their orientation, require the use of a wedge transducer for manual scanning (or a wheel transducer for in-motion scanning). These defects represent extended targets, with sizes typically larger than one wavelength.

The first case examined is an end-drilled hole in a rail test section with an inclined angle of 10 degrees (Fig. 2.13) that is often used to simulate transverse rail defects for ultrasonic calibration tests. The 55-deg transducer wedge was positioned on the top of the railhead above the flaw. Since the SAFT image was generated in the x-y plane, the objective was then to image a vertical line in the ROI. The ground truth result is a 10-degree inclined line from y-axis with a length of 19 mm (the bottom of the drilled hole), as marked by the bracket in Fig. 2.13(b). Fig. 2.13(a) shows the VE-TFM image using 8-transmission beamformed using different wave mode combinations. The dynamic range of the LSSL combination is set to 30 dB while the other three combinations are set to 15 dB in order to highlight the focus region. As expected, the LSSL combination has the best imaging result in both defect shape and contrast. The LSLL and LLLL combinations can partially “see” the defect with limited contrast due to low SNR. The LLSL combination has no energy and the image is simply replicas of the dominant LSSL modes with incorrect location (from erroneous TOF).

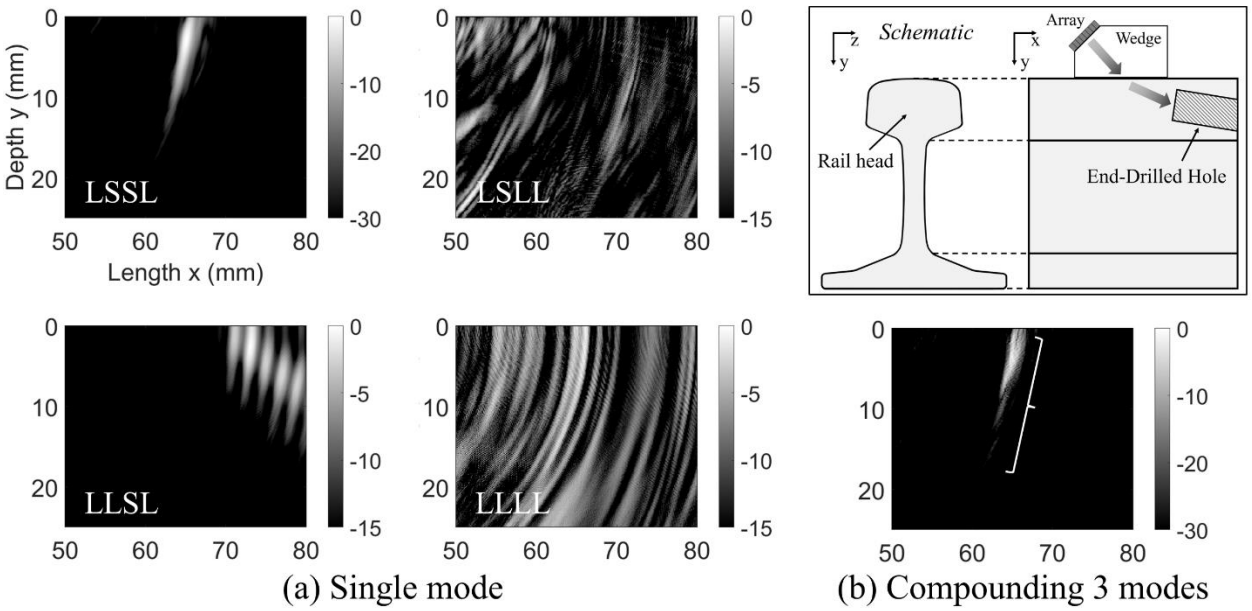

Figure 2.13: Imaging of an end-drilled hole in a rail head using 8-transmission VE method with a wedge transducer. (a) Comparison of all wave mode combinations, and (b) compounded image using three combinations. The actual size and orientation of the defect is marked in (b).

The compounded image using the LSSL, LSLL and LLLL mode combinations is shown in Fig. 2.13(b). Compared with the ground truth, it can be seen that the LSSL combination alone provides an accurate estimation of the defect size and orientation. However, due to the limited angular range of L-wave propagation in the transducer-wedge setup, the images involving L-modes have poor SNR and inhomogeneous distribution on the extended target (large defect).

The final set of experimental tests were conducted on a natural transverse defect in a rail section, as shown in Fig. 2.14, provided by MxV Rail of Pueblo, CO (formerly Transportation Technology Center, Inc.). Following the ultrasonic testing, the rail section was broken to reveal the true shape and size of the defect (ground truth), as shown in Fig. 2.15(a). The ground truth size of the defect was thus determined as 4 mm to 30 mm in depth in the scanned x-y plane, as marked by the arrow in Fig. 2.14(a). All TFM images are displayed in 30 dB dynamic range.

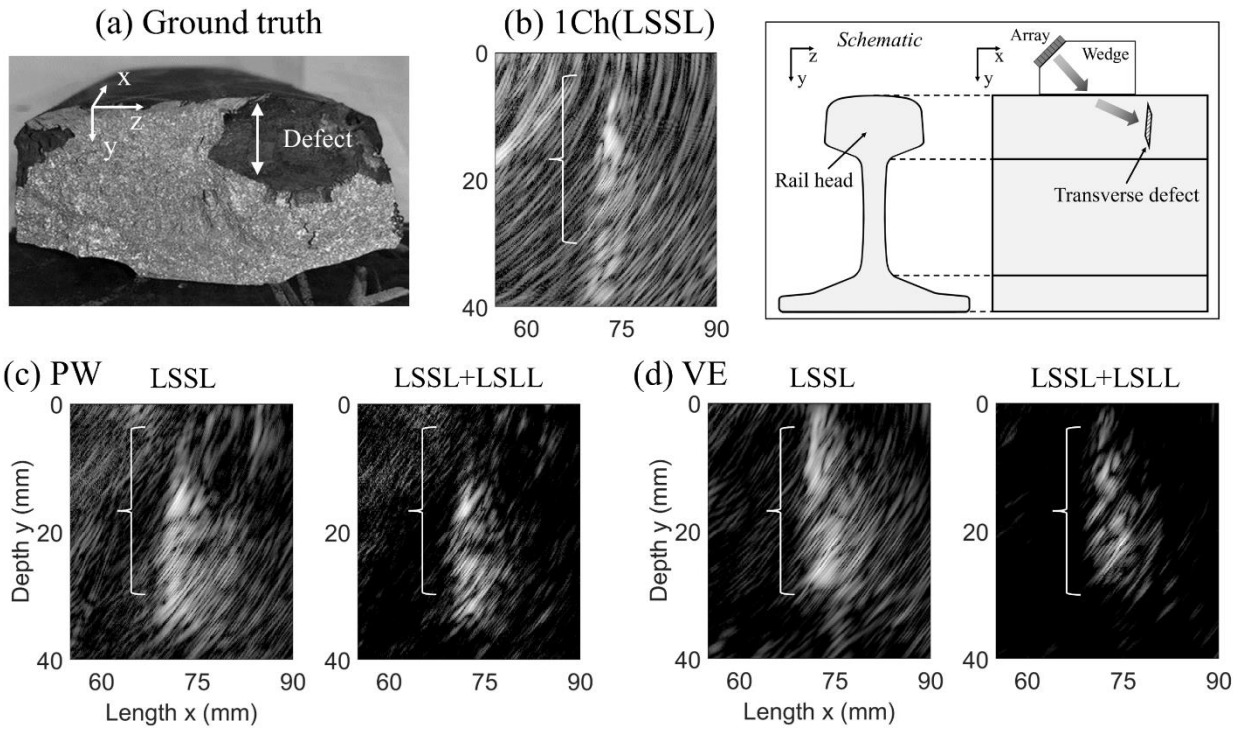

Figure 2.14: Imaging of a natural transverse defect in a rail head with a wedge transducer by comparing different modalities. (a) Ground truth picture of the defect. TFM images beamformed using (b) 1 element emission LSSL (benchmark), (c) PW LSSL and compounded LSSL + LSLL combinations, and (d) VE LSSL and compounded LSSL + LSLL combinations.

The benchmark 1 element emission 8-transmission TFM image, beamformed using the LSSL mode combination, is shown in Fig. 2.14(b) with the ground truth marked by the bracket. Compared with the drilled hole's flat reflectors of the previous section, due to its particular surface morphology the natural defect has a lower reflectivity resulting in a lower SNR of the sparse SAFT images. The main lobe response extends to the bottom of the ROI which leads to an overestimation of the defect size. A noticeable ghost image appears on the left of the image resulting from the internal reflections of the L-wave reverberating in the wedge.

The TFM image using the PW modality is shown in Fig. 2.14(c). The image contrast of the LSSL combination using PW is slightly improved compared to 1 element emission, and no distinguishable side lobe occurs. Additionally, wave mode compounding using the reflected L-

wave from the defect (LSLL combination) further improves the contrast. However, the depth indication of the defect using PW-TFM (10-37 mm) still deviates from the ground truth (3-31 mm). This angular shift of the image (in depth) is due to the limited steering ability of the PW transmission.

The best result is seen in the VE-TFM images shown in Fig. 2.14(d), with the highest contrast and a reasonable defect size estimation even using a single LSSL mode combination. Finally, the compounded image (LSSL and LSLL combination) shows that most of the side lobes are suppressed below -30 dB, with the main lobe indicating the correct size of the defect. Most interestingly, the elongation of the main lobe around 31-40 mm in depth, seen in the benchmark 1 element image, is suppressed in this case. This result confirms that the sparse VE method with wave mode compounding in wedge-transducer applications can provide satisfactory images of weak-reflection targets.

2.5 Discussions and Conclusions

This article has investigated the implementation of sparse SAFT for high frame rate ultrasonic imaging of internal discontinuities in solids when using a transducer wedge setup. This case requires particular consideration of the wave refractions and mode conversions at the wedge-medium interface. In particular, the Virtual Element (VE) method and the Plane Wave (PW) method were examined in order to find appropriate combinations of the operational parameters that yield fast frame rates with strong image contrast.

This paper also explored the opportunity to compound the S-wave and the L-wave propagating in the test medium through the interposed wedge to further increase the array gain. For the VE method, the circular wavefront of the two wave modes from a single transmission can

be focused synthetically at any point in the ROI. Since the beam directions of each of the two wave modes are distinct, compounding the S-wave and the L-wave is equivalent to doubling the array aperture. For the PW method, the incident angle for each transmission beam is fixed, resulting in the beam of different wave modes diverging in different directions with no overlap. Moreover, since mode conversions also occurs at the target reflectors, a total of four wave mode combinations are generally possible with the VE method, while only two mode combinations are available with the PW method.

Proof-of-principle numerical simulations of sparse SAFT transmissions for the transducer wedge setup were carried out in a 2-D case. Different configurations of the VE method were compared to determine the focusing ability of the array as a function of angular aperture, subaperture size, and virtual array pitch. A moderate angular aperture was found appropriate to ensure sufficient beam steering capability for the wedge setup while maximizing the SNR of each transmission. A formulation to identify appropriate positions of the virtual array was proposed to improve lateral resolution and steering ability of the synthetic focus. The PW method was compared to the VE method at various frame rates. While possible instability was found for PW at ultrafast frame rates, it was also confirmed that both methods can benefit from wave mode compounding in transmission.

Experimental tests were also performed using a 64-element linear ultrasonic array mounted on a 55-degree Rexolite wedge probing an aluminum block containing drilled holes as targets. The tests confirmed the stability of the VE method with appropriate operational configurations to operate at ultrafast frame rates. The performance of PW was found less satisfactory at extremely high imaging speeds, although its focusing capability was still found better than the single-channel emission when a sufficient number of transmissions were used. The validation of the wave mode

compounding, considering refractions and mode conversions due to the wedge, was also carried out experimentally on the hole targets, with clearly improved contrast compared to a traditional single mode imaging. The last set of experimental tests was performed on an artificial and a natural transverse defect in a rail section that typically require a wedge transducer for detection. The opportunities for fast and accurate imaging using VE and PW methods and mode compounding are also demonstrated in this practical application.

Acknowledgements

This research was funded by the U.S. Federal Railroad Administration under contract no. 693JJ619C000008 (Dr. Robert Wilson, Program Manager). The test rail sections presented for the final part of the paper, as well as the result of the rail break for the natural defect case, were provided by Dr. Anish Poudel of former Transportation Technology Center (now MxV Rail) in Pueblo, CO. The authors would also like to acknowledge Mr. Gavin Dao of Advanced OEM Solutions (West Chester, OH, USA) for providing technical advice on SAFT hardware solutions and valuable insights on the use of the multiplexer currently adopted in the prototype.

Chapter 2, in full, is a reprint of the material as it appears in C. Huang and F. Lanza di Scalea, "Application of sparse synthetic aperture focusing techniques to ultrasound imaging in solids using a transducer wedge," *IEEE Transactions on Ultrasonics, Ferroelectrics, and Frequency Control,* vol. 71, no. 2, pp. 280-294, 2024. The dissertation author was the primary investigator and author of this paper.

References

[1] J. J. Flaherty, K. R. Erikson, and V. M. Lund, "Synthetic aperture ultrasound imaging systems," *U.S. Patent* 3548642, 1967.

[2] C.B. Burckhardt, P-A. Grandchamp, and H. Hoffmann, “An experimental 2MHz synthetic aperture sonar system intended for medical use,” *IEEE Trans. Son. Ultrason.*, vol. 21, no. 1, pp. 1-6, Jan. 1974.

[3] S. I. Nikolov and J. A. Jensen, “Virtual ultrasound sources in high resolution ultrasound imaging,” in *Proc. SPIE,* 2002, vol. 3, pp. 395–405.

[4] S. I. Nikolov and J. A. Jensen, “In-vivo synthetic aperture flow imaging in medical ultrasound,” *IEEE Trans. Ultrason., Ferroelect., Freq. Control*, vol. 50, no. 7, pp. 848–856, Jul. 2003.

[5] J. A. Jensen, S. I. Nikolov, K. L. Gammelmark, and M. H. Pedersen, “Synthetic aperture ultrasound imaging,” *Ultrasonics*, vol. 44, pp. e5–e15, Dec. 2006.

[6] N. Oddershede and J. A. Jensen, “Effects influencing focusing in synthetic aperture vector flow imaging,” *IEEE Trans. Ultrason., Ferroelect., Freq. Control*, vol. 54, no. 9, pp. 1811–1825, Sep. 2007.

[7] M. F. Rasmussen and J. A. Jensen, “Comparison of 3-D synthetic aperture phased-array ultrasound imaging and parallel beamforming,” *IEEE Trans. Ultrason., Ferroelect., Freq. Control*, vol. 61, no. 10, pp. 1638–1650, Oct. 2014.

[8] H. Hasegawa and H. Kanai, “High-frame-rate echocardiography using diverging transmit beams and parallel receive beamforming,” *J. Med. Ultrason.*, vol. 38, no. 3, pp. 129-140, Jul. 2011.

[9] L. Tong, H. Gao, H. F. Choi, and J. D'hooge, “Comparison of conventional parallel beamforming with plane wave and diverging wave imaging for cardiac applications: A simulation study,” *IEEE Trans. Ultrason., Ferroelect., Freq. Control*, vol. 59, no. 8, pp. 1654–1663, Sep. 2012.

[10] G. Montaldo, M. Tanter, J. Bercoff, N. Benech, and M. Fink, “Coherent plane-wave compounding for very high frame rate ultrasonography and transient elastography,” *IEEE Trans. Ultrason., Ferroelect., Freq. Control*, vol. 56, no. 3, pp. 489–506, Mar. 2009.

[11] M. Tanter and M. Fink, “Ultrafast imaging in biomedical ultrasound,” *IEEE Trans. Ultrason., Ferroelect., Freq. Control*, vol. 61, no. 1, pp. 102–119, Jan. 2014.

[12] C. Papadacci, M. Pernot, M. Couade, M. Fink, and M. Tanter, “High-contrast ultrafast imaging of the heart,” *IEEE Trans. Ultrason., Ferroelect., Freq. Control*, vol. 61, no. 2, pp. 288–301, Jan. 2014.

[13] C. H. Frazier and W. D. O'Brien, “Synthetic aperture techniques with a virtual source element,” *IEEE Trans. Ultrason., Ferroelect., Freq. Control*, vol. 45, no. 1, pp. 196-207, Jan. 1998.

[14] M. H. Bae and M. K. Jeong, "A study of synthetic-aperture imaging with virtual source elements in B-mode ultrasound imaging systems," *IEEE Trans. Ultrason., Ferroelect., Freq. Control*, vol. 47, no. 6, pp. 1510-1519, Nov. 2000.

[15] C. H. Wang, J. T. Rose, and F. K. Chang, "A synthetic time-reversal imaging method for structural health monitoring," *Smart Mater. Struct.*, vol. 13, no. 2, pp. 415–423, Mar. 2004.

[16] C. Holmes, B. W. Drinkwater, and P. D. Wilcox, "Post-processing of the full matrix of ultrasonic transmit–receive array data for non-destructive evaluation," *NDT&E Int.*, vol. 38, no. 8, pp. 701–711, Dec. 2005.

[17] B. W. Drinkwater and P. D. Wilcox, "Ultrasonic arrays for non-destructive evaluation: a review," *NDT&E Int.*, vol. 39, no. 7, pp. 525–541, Oct. 2006.

[18] A. J. Hunter, B. W. Drinkwater, and P. D. Wilcox, "The wavenumber algorithm for full-matrix imaging using an ultrasonic array," *IEEE Trans. Ultrason., Ferroelect., Freq. Control*, vol. 55, no. 11, pp. 2450-2462, Nov. 2008.

[19] J. Zhang J, B. W. Drinkwater, P. D. Wilcox, and A. J. Hunter, "Defect detection using ultrasonic arrays: The multi-mode total focusing method," *NDT&E Int.*, vol. 43, no. 2, pp. 123–133, Mar. 2010.

[20] C. Fan, M. Caleap, M. Pan, and B. W. Drinkwater, "A comparison between ultrasonic array beamforming and super resolution imaging algorithms for non-destructive evaluation," *Ultrasonics*, vol. 54, no. 7, pp. 1842–1850, Sep. 2014.

[21] N. Budyn, R. L. Bevan, J. Zhang, A. J. Croxford, and P. D. Wilcox, "A model for multiview ultrasonic array inspection of small two-dimensional defects," *IEEE Trans. Ultrason., Ferroelect., Freq. Control*, vol. 66, no. 6, pp. 1129-1139, Apr. 2019.

[22] J. S. Hall and J. E. Michaels, "Minimum variance ultrasonic imaging applied to an in situ sparse guided wave array," *IEEE Trans. Ultrason., Ferroelect., Freq. Control*, vol. 57, no. 10, pp. 2311–2323, Sep. 2010.

[23] J. S. Hall and J. E. Michaels, "Multipath ultrasonic guided wave imaging in complex structures," *Struct. Health Monitor.*, vol. 14, no. 4, pp. 345–358, Jul. 2015.

[24] F. Lanza di Scalea, S. Sternini, and T. V. Nguyen, "Ultrasonic imaging in solids using wave mode beamforming," *IEEE Trans. Ultrason., Ferroelect., Freq. Control*, vol. 64, no. 3, pp. 602–616, Dec. 2016.

[25] E. A. Marengo, F. K. Gruber and F. Simonetti, "Time-reversal MUSIC imaging of extended targets," *IEEE Trans. Image Process.*, vol. 16, no. 8, pp. 1967-1984, Aug. 2007.

[26] L. Le Jeune, S. Robert, E. L. Villaverde, and C. Prada, "Plane wave imaging for ultrasonic non-destructive testing: Generalization to multimodal imaging," *Ultrasonics*, vol. 64, pp. 128–138, Jan. 2016.

[27] L, Merabet, S. Robert, and C. Prada, “The multi-mode plane wave imaging in the Fourier domain: Theory and applications to fast ultrasound imaging of cracks,” *NDT&E Int.*, vol. 110, p. 102171, Mar. 2020.

[28] T. Lukomski, “Full-matrix capture with phased shift migration for flaw detection in layered objects with complex geometry,” *Ultrasonics*, vol. 70, pp. 241–247, Aug. 2016.

[29] J. F. Cruza, J. Camacho, and C. Fritsch, “Plane-wave phase-coherence imaging for NDE,” *NDT&E Int.*, vol. 87, pp. 31-37, Apr. 2017.

[30] H. Hu, J. Du, N. Xu, H. Jeong, and X. Wang, “Ultrasonic sparse-TFM imaging for a two-layer medium using genetic algorithm optimization and effective aperture correction,” *NDT&E Int.*, vol. 90, pp. 24-32, Sep. 2017.

[31] E. Hoyle, M. Sutcliffe, P. Charlton, and J. Rees, “Virtual source aperture imaging with auto-focusing of unknown complex geometry through dual layered media,” *NDT&E Int.*, vol. 98, pp. 55-62, Sep. 2018.

[32] S. Sternini, A. Y. Liang, and F. Lanza di Scalea, “Ultrasonic synthetic aperture imaging with interposed transducer–medium coupling path,” *Struct. Health Monitor.*, vol. 18, no. 5-6, pp. 1543–1556, Nov. 2019.

[33] S. Sternini, A. Y. Liang, and F. Lanza di Scalea, “Rail Defect Imaging by Improved Ultrasonic Synthetic Aperture Focus Techniques,” *Mater. Eval.*, vol. 77, no. 7, pp. 931–940, Jul. 2019.

[34] F. Lanza di Scalea, “Ultrasonic testing applications in the railroad industry,” in *Non-destructive testing handbook*, P. O. Moore, Ed., 3rd ed. Columbus, OH, USA: American Society for Nondestructive Testing, 2007, pp. 535–552.

[35] G. Garcia and J. Zhang, “Application of ultrasonic phased arrays for rail flaw inspection,” Fed. Railroad Admin., DC, USA, No. DOT/FRA/ORD-06/17, July 2006.

[36] M. Witte and A. Poudel, “High-speed rail flaw detection using phased-array ultrasonics,” Transp. Tech. Centr., Pueblo, CO, USA, *Tech. Digest* TD-16-030, July 2016.

[37] C. R. Cooley and B. S. Robinson, “Synthetic focus imaging using partial datasets,” in *Proc. IEEE Ultrasonics Symp.*, 1994, vol. 3, pp. 1539–1542.

[38] M. O’Donnell and L. J. Thomas, “Efficient synthetic aperture imaging from a circular aperture with possible application to catheter-based imaging,” *IEEE Trans. Ultrason., Ferroelect., Freq. Control*, vol. 39, no. 3, pp. 366–380, May. 1992.

[39] J.T. Ylitalo and H. Ermert, “Ultrasound synthetic aperture imaging: monostatic approach,” *IEEE Trans. Ultrason., Ferroelect., Freq. Control*, vol. 41, no. 3, pp. 333–339, May. 1994.

[40] M. Karaman M, P. C. Li, and M. O'Donnell, "Synthetic aperture imaging for small scale systems," *IEEE Trans. Ultrason., Ferroelect., Freq. Control*, vol. 42, no. 3, pp. 429–442, May. 1995.

[41] G. R. Lockwood, J. R. Talman, and S. S. Brunke, "Real-time 3-D ultrasound imaging using sparse synthetic aperture beamforming," *IEEE Trans. Ultrason. Ferroelectr. Freq. Control*, vol. 45, no. 4, pp. 980–988, Jul. 1998.

[42] L . Sandrin, S. Catheline, M. Tanter, X. Hennequin, and M. Fink, "Time resolved pulsed elastography with ultrafast ultrasonic imaging," *Ultrason. Imaging*, vol. 21, no. 4, pp. 259–272, Oct. 1999.

[43] L . Sandrin, M. Tanter, S. Catheline, and M. Fink, "Shear modulus imaging using 2D transient elastography," *IEEE Trans. Ultrason. Ferroelectr. Freq. Control*, vol. 49, no. 4, pp. 426–435, Apr. 2002.

[44] S. K. Jespersen, J. E. Wilhjelm, and H. Sillesen, "Multi-angle compound imaging," *Ultrason. Imaging*, vol. 20, no. 2, pp. 81–102, Apr. 1998.

[45] M. Tanter, J. Bercoff, L. Sandrin, and M. Fink, "Ultrafast compound imaging for 2-D motion vector estimation: Application to transient elastography," *IEEE Trans. Ultrason. Ferroelectr. Freq. Control*, vol. 49, no. 10, pp. 1363–1374, Dec. 2002.

[46] J. Cheng and J. Y. Lu, "Extended high frame rate imaging method with limited diffraction beams," *IEEE Trans. Ultrason. Ferroelectr. Freq. Control*, vol. 53, no. 5, pp. 880–899, Jun. 2006.

[47] S. Sternini, A. Pau and F. Lanza di Scalea, "Minimum-variance imaging in plates using guided-wave-mode beamforming," *IEEE Trans. Ultrason. Ferroelectr. Freq. Control*, vol. 66, no. 12, pp. 1906–1919, Dec. 2019.

[48] M. S. Patterson and F. S. Foster, "The improvement and quantitative assessment of B-mode images produced by an annular array/cone hybrid," *Ultrason. Imaging*, vol. 5, no. 3, pp. 195–213, Jul. 1983.

[49] "FRA Safety Data & Reporting," Fed. Railroad Admin., DC, USA [Online]. Available: https://railroads.dot.gov/safety-data, Accessed on Sep. 19, 2023.

Chapter 3 Rail Flaw Imaging Systems Based on Improved Ultrasonic Synthetic Aperture Focusing Techniques

3.1 Introduction

Internal rail flaws are a significant cause of train accidents. According to FRA's Safety Statistics data shown in Fig. 3.1, in the past five years (2018-2022) "Detail Fractures" were responsible for as many as 222 derailments and damage cost of $79M (the highest cost of any other cause within the category of Track, Roadbed and Structures). "Transverse/Compound Fissures" (TF) were responsible for 77 derailments and $21M in damage costs, and "Vertical Split Head" (VSH) defects caused 83 derailments and ~$20M in damage cost. These three defects combined therefore caused as many as ~80 derailments per year and ~$25M in damage cost per year. The detection and quantification of these flaws is clearly of importance to railroad safety and efficiency.

The current manual verification of detected flaws consists of a simple ultrasonic pulse-echo test conducted using a hand-held ultrasonic transducer with a wedge that is manually moved around the flaw in attempt to estimate the flaw size through a -6 dB threshold technique [1]. This process yields rail flaw sizing results that are highly subjective to the operator's judgement. An improved flaw verification would allow to generate 3D ultrasound images of the internal flaw for an objective determination of flaw size and orientation. Knowledge of the correct flaw size can inform the most appropriate remedial actions, which can largely reduce the cost of rail maintenance and improve safety.

Current OEM portable systems exist for manual flaw imaging in structural components using ultrasonic techniques. These systems are based on Phased-Array (PA) technology [2]. As schematized in Fig. 3.2, in PAs transmission signals are sent to all channels that are appropriately

TRAIN ACCIDENTS BY CAUSE FROM FORM FRA F 6180.54

MAJOR CAUSE= Track

Selections: Railroad - ALL
Region - All Regions
State - ALL, County - ALL
Derailment / All TRACK TYPES / T-ALL-Track, Roadbed and Structures
Time Frame: Jan 2018 To Dec 2022

Specific causes:	Total		Type of Accident	Reportable Damage		Casualty	
	Cnt	%	Der	Amount	%	Kld	Nonf
T001- Roadbed settled or soft	99	4.5	99	32,194,952	6.9	0	0
T002- Washout/rain/slide/etc. dmg -track	19	0.9	19	20,796,111	4.5	0	8
T099- Other roadbed defects	8	0.4	8	1,153,547	0.2	0	0
T101- Cross level of track irregular(joints)	45	2.1	45	3,541,392	0.8	0	0
T102- Cross level track irreg.(not at joints)	58	2.7	58	10,996,036	2.4	0	1
⋮							
T207- Detail fracture - shelling/head check	222	10.2	222	78,938,028	16.9	0	0
T220- Transverse/compound fissure	77	3.5	77	21,390,579	4.6	0	0
T221- Vertical split head	83	3.8	83	19,269,929	4.1	0	0

(a)

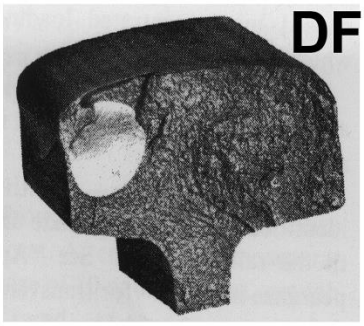

(b)

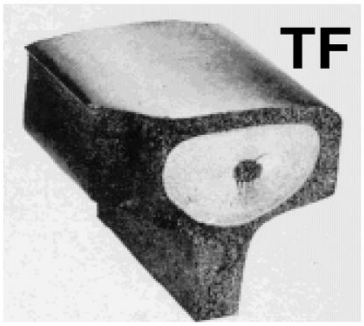

(c)

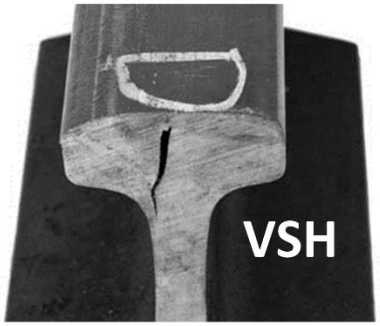

(d)

Figure 3.1: (a) FRA safety statistics data for all track, roadbed and structures (2018-2022). Examples of (b) Detail Fracture (DF), (c) Transverse Fissure (TF), and (d) Vertical Split Head (VSH).

delayed for physical focusing and steering at various depths. This means that (a) the PA hardware is fairly complicated because of the multiple D/A output channels required, (b) the PA imaging speed is limited by the need to physically focus at different locations in the medium, and (c) the classical PA beamforming is only achieved in transmission through focused beams which limits the lateral resolution.

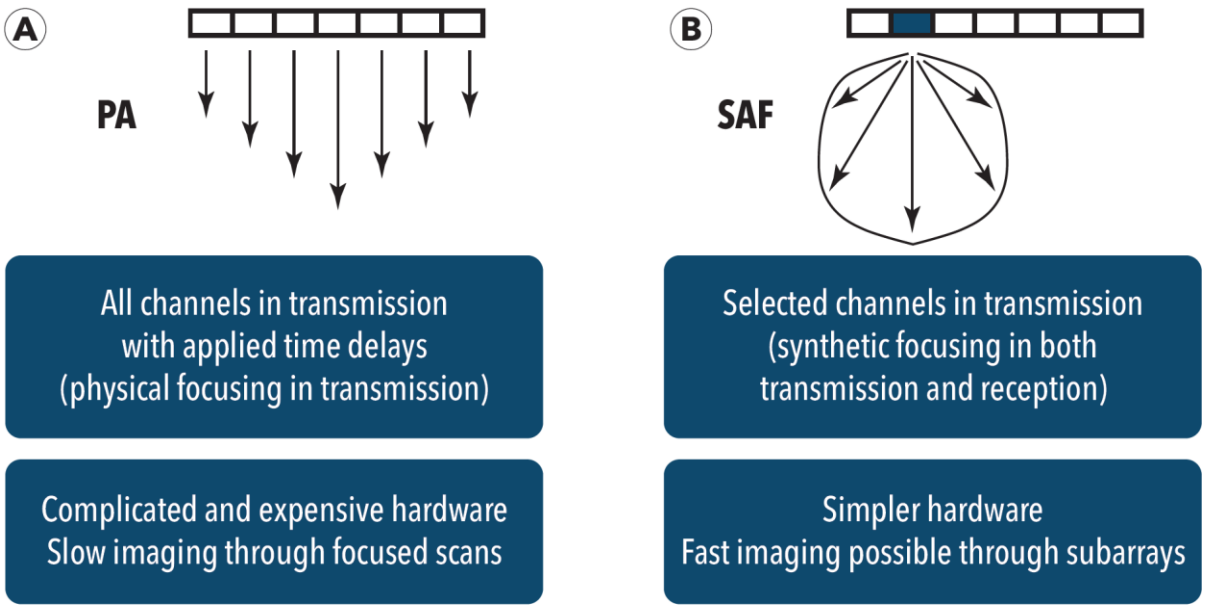

Figure 3.2: Ultrasound imaging technology: conventional Phased-Arrays (left) vs. Synthetic Aperture Focusing (right).

Conversely, Synthetic Aperture Focus Techniques (SAFT) have been considered for defect imaging for various benefits over the PA methods [3]. In a traditional SAFT scheme, the transmission is sent to a single channel at a time, and the focusing is done in post-processing both in transmissions and in receptions (two-way synthetic focusing) [4]. This means that (a) the SAFT hardware can be much simpler since only a few D/A output channels are required, (b) the SAFT imaging speed can be increased by limiting the output channels, and (c) the SAFT focusing is achieved in both transmission and reflection leading to better resolution in a large inspection area.

The objective of this chapter is to present the capabilities of SAFT methods developed in chapter 2 applied to rail flaw imaging with an ultimate goal of automatic defect size estimation. The first part of the chapter introduces a field deployable prototype system for 3D imaging of internal rail flaws using ultrasonic SAFT techniques in a transducer-wedge setup. The improved SAFT beamforming scheme proposed in chapter 2 provides high contrast images in quasi real-

time [5]. A sophisticated post-processing routine is developed to enable automatic rail flaw quantification without the user's judgement. The prototype's hardware is packaged in a battery-powered Pelican case for portability and ruggedness. Validation tests were performed on a number of flawed rail sections from the FRA rail defect library managed by MxV Rail. The flaw images generated by the imaging prototype showed a good match compared to the ground truth established from rail break tests, especially in the case of natural transverse-type defects.

The second part of the chapter explores the performance of the developed enhanced SAFT imaging methods applied to a Roller Search Unit (RSU) setup with a smaller aperture size. A substantial improvement can be obtained when the ultrasonic inspection is implemented with a rolling wheel using an architecture similar to the RSUs utilized by conventional ultrasonic rail inspections. Enhancements to SAFT are implemented to tackle issues with limited signal-to-noise ratio (SNR) and to accelerate the imaging frame rate for the RSU setup. The aperture is angled to generate both longitudinal and shear wave beams, optimizing reflections from transverse defects as well as increasing the effective Region of Interest (ROI). Validation tests were carried out with the RSU imaging system on both artificial and natural rail flaws at the UCSD rail defect farm.

3.2 The SAFT Imaging System with a Wedge Transducer

A portable imaging prototype system was designed, assembled and tested to enable hand-held ultrasound imaging of rail flaws based on an enhanced SAFT technique [6]. As shown in Fig 3.3(a), the hardware components of the imaging prototype were a multiplexer, a 12V battery, a host computer, and a probe comprised of a transducer array, a wedge and an encoder wheel. All the hardware components were screw-fixed inside a carry-on size Pelican case. The multiplexer (OEM-PA Mini 64/64 by Advanced OEM Solutions, West Chester, OH, USA) that allowed multi-

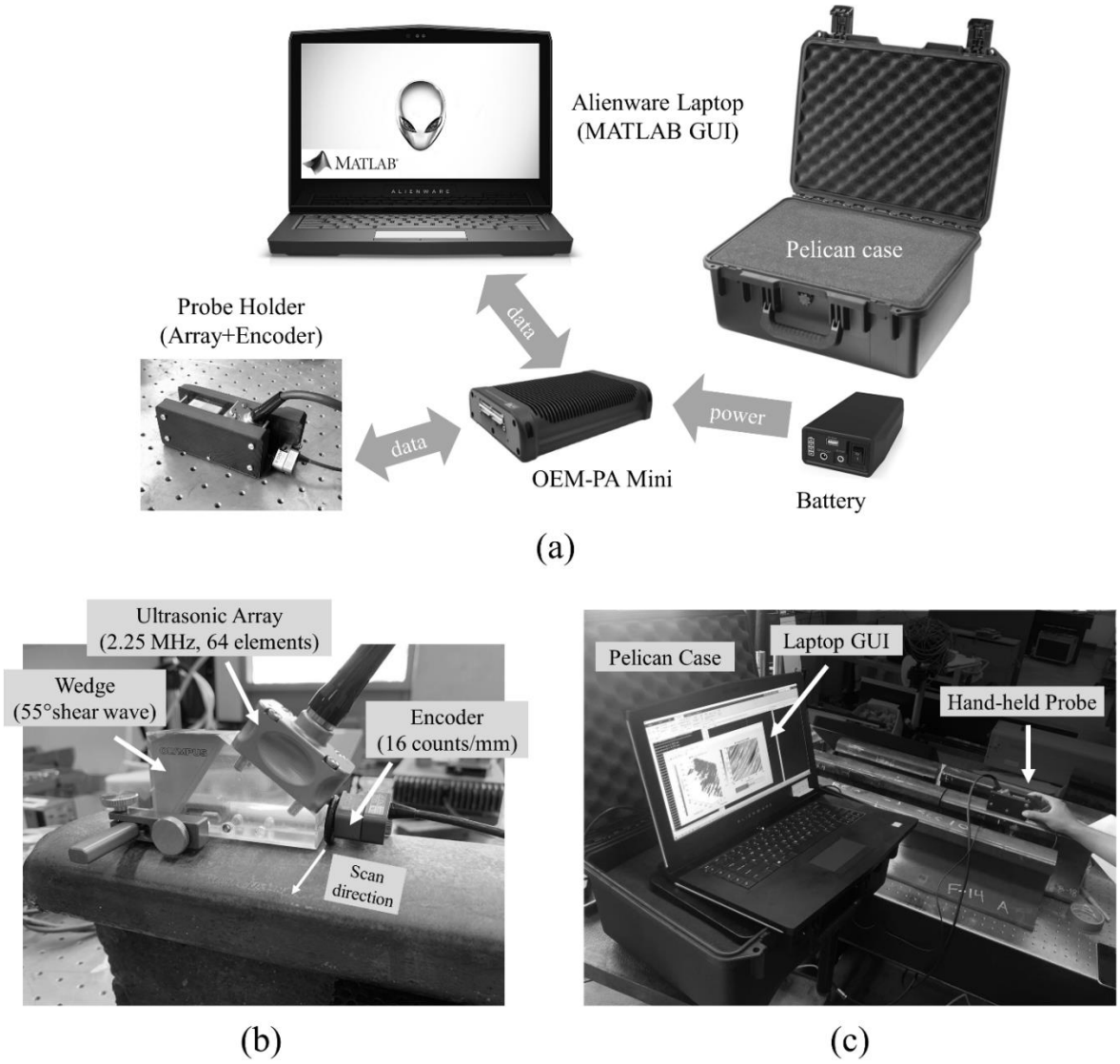

Figure 3.3: (a) Main components of the portable imaging prototype. (b) Array-wedge probe. (c) The prototype during scanning of a rail section in the laboratory.

channel data acquisition controlled the pulsed emission and reception to/from the array. A 12V battery was used to support the multiplexer for up to 8 hours of autonomous operation. The probe was composed of a transducer array, a shear wedge, and an encoder, as shown in Fig. 3.3(b). The transducer was a 64-element longitudinal (L-) wave linear array (Olympus NDT 2.25L64-38.4X10-A12-P-2.5-OM) with a central frequency at 2.25 MHz. The array was attached to a 55-degree wedge (Olympus NDT SA12-N55S) to generate directional shear (S-) waves in the rail

steel. The encoder recorded the transverse position of the probe when scanned on the rail surface, with a resolution of 16 counts/mm. The encoder allowed the system to create 3D images from the individual 2D scans. The array was coupled to the wedge using conventional ultrasonic gel couplant. The couplant was also applied at the wedge/rail interface to compensate for the impedance mismatch. A Guided User Interface (GUI) platform was developed on a CUDA enabled Alienware R13 Laptop with a NVIDIA GeForce GTX 1070 GPU. All steps of the signal processing algorithms were programmed and automated in the GUI platform which enabled flexible configuration and result analysis for the user's convenience. As shown in Fig. 3.3(c), during testing the user simply moves the probe on the surface of the rail section, and 3D images of the scanned area are displayed in quasi real-time in the GUI. Specific features of the image reconstruction algorithms that were developed and implemented in the prototype are discussed in detail in the following subsections.

3.2.1 Time Back-propagation Beamforming with a Transducer Wedge

The time backpropagation algorithm (also known as Delay-And-Sum or DAS algorithm) is widely used in SAFT imaging [7]. Dynamic focus is achieved both in transmission and in reception by considering the ray path connecting the transmitting transducer element, the focus point, and the receiving transducer element. An image is built by summing the backpropagated signals through all transmitter-receiver pairs of the transducer array. Considering transmitters i = 1, 2, …, M and receivers j = 1, 2, …, N, the DAS beamformed SAFT image is constructed as:

$$I(y,z) = \sum_{i=1}^{M}\sum_{j=1}^{N} A_{ij}\left(\tau_{ij,yz}\right) \tag{3.1}$$

where the Time-of-Flight (TOF) $\tau_{ij,yz}$ is the propagation time of the ray path from the transmitter $T_i(y_i, z_i)$ to the focus pixel $P(y, z)$ and back to the receiver $R_j(y_j, z_j)$. Notice that the transmitter i can

be a virtual source instead of a physical element if a subarray emission is considered [8]. When a wedge is interposed between the transducer array and the test piece (as in the present case of the rail flaw imaging prototype), the wave path in the wedge must be taken into account in the beamforming algorithm. Referring to Fig. 3.4, following Snell's law, the new backpropagation TOF can be calculated by finding the point of refraction at the wedge-medium interface [9], [10]. Considering the fact that, in general, both L-waves and S-waves can propagate in the test medium, where only L-waves can be considered in the wedge, there exist in general up to four wave mode combinations that can be theoretically utilized for imaging. Accordingly, the backpropagation time $\tau_{ij,yz}$ for each of the possible wave mode combinations can be calculated as:

$$\tau_{ij,yz}{}^{LLLL,LLSL,LSLL,LSSL} = \frac{d_{i,yz}^{L(1)}}{c_w^L} + \frac{d_{i,yz}^{L,S(2)}}{c_m^{L,S}} + \frac{d_{j,yz}^{L,S(3)}}{c_m^{L,S}} + \frac{d_{j,yz}^{L(4)}}{c_w^L} \tag{3.2}$$

where: *LLLL* is <L-wave transmitted in wedge + L-wave refracted in medium + L-wave reflected in medium + L-wave received in wedge>, *LLSL* is <L-wave transmitted in wedge + L-wave refracted in medium + S-wave reflected in medium + L-wave received in wedge>, *LSLL* is <L-wave transmitted in wedge + S-wave refracted in medium + L-wave reflected in medium + L-wave received in wedge>, and *LSSL* is <L-wave transmitted in wedge + S-wave refracted in medium + S-wave reflected in medium + L-wave received in wedge>. In addition, $c_m^{L,S}$ is the L-wave or S-wave velocity in the medium, c_w^L is the L-wave velocity in the wedge, and $d_{i,yz}^{L(1)}$, $d_{i,yz}^{L,S(2)}$, $d_{j,yz}^{L,S(3)}$, and $d_{j,yz}^{L(4)}$ are the corresponding propagation distances of each ray path segment as identified in Fig. 3.4. It was previously shown that the compounding of multiple wave modes can dramatically increase the array gain [11]. In this paper, only S-waves are considered in the rail steel because of the use of the shear wedge that maximizes S-wave refractions.

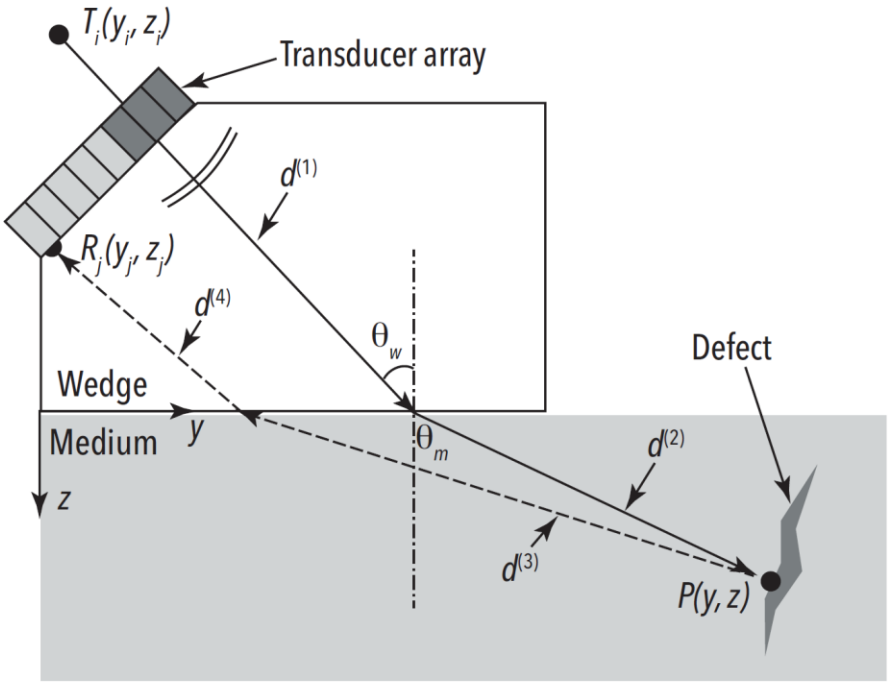

Figure 3.4: Ray tracing scheme connecting one virtual transmit element T_i, the focal point P, and one receiver element R_j.

In order to generate the final image, the raw waveforms are analyzed via their Hilbert Transform (analytical representation) as customary in SAFT [12]. Specifically, each waveform is decomposed into its in-phase and phase-quadrature components, and the final image is built by computing the modulus of these two contributions at each pixel $P(y, z)$.

3.2.2 Sparse SAFT and Subarray Emission

The general SAFT scheme in Full Matrix Capture (FMC) mode requires emitting from each individual elements of the transducer array sequentially (1 channel at a time) with the full aperture acting in reception for each transmission. However, utilizing all possible transmissions slows down the imaging process and increases computational burden. That is why, particularly so in the medical imaging field, "sparse" transmission schemes are being considered to increase imaging speed without sacrificing image quality [13]. Since imaging speed is inversely

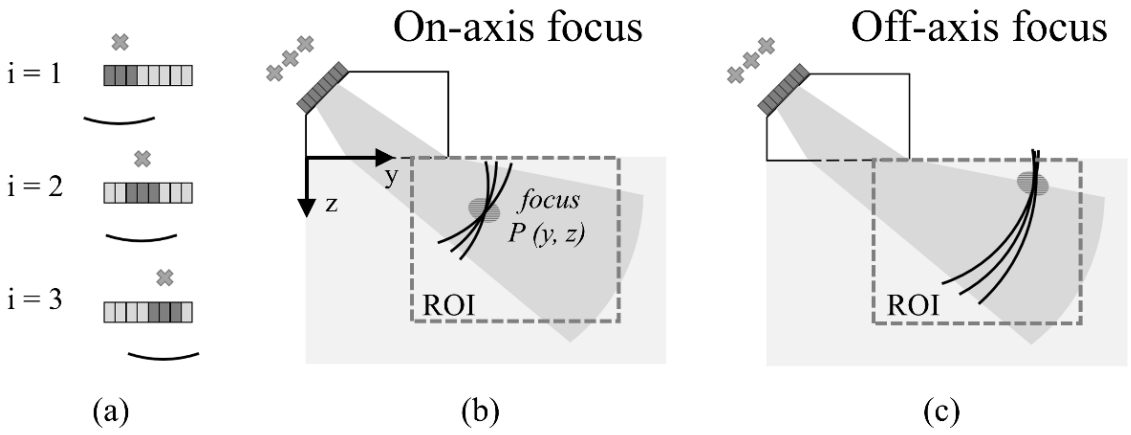

Figure 3.5: Subarray SAFT technique for faster and more accurate images. (a) Three defocused waves defined by the virtual elements are emitted independently by subarrays. Beamforming in transmission is performed by applying time delays corresponding to a synthetic focus on point *P* either at (b) on-axis positions or (c) off-axis positions.

proportional to the number of transmissions, the sparse SAFT technique utilized in the rail flaw imaging prototype employs only a subset of all possible transmission events. In order to compensate for the limited energy transmissible by a single element at high frame rates, multiple elements (a subarray) are fired at once [8]. As shown in Fig. 3.5(a), for example, an 8-element array only transmits 3 defocused circular waves using 3-element subapertures to replace 8 consecutive firing of each element. In each transmit event *i*, the acoustic field of the phased subaperture elements superimposes a circular wavefront such that the transmission of the 3-element subaperture can be modeled as a virtual element (point source) placed behind the physical array. In the transmit beamforming, a virtual element array substitutes the physical transmit subapertures in the consideration of the DAS ray paths. As shown in Fig. 3.5(b), each transmit beam can be properly time delayed by calculating the ray path connecting the virtual array element and the focus point *P*, so that the three transmitted wave fronts are compounded coherently at an on-axis focus. By adjusting the time delays, the synthetic focus can be achieved at any point in the region-of-interest (ROI), such as an off-axis location in Fig. 3.5(c). The ability to dynamically

focus the defocused beams at various locations ensures an acceptable resolution of the SAFT images throughout the ROI. This is particularly important for the imaging of rail flaws since the size of the transverse-type defects can be fairly large compared to the physical aperture of the array thus occupying the full height of the ROI. For the 64 element array in the imaging prototype, the authors have found that using eight, 17-element subarray with a 9-element-wide pitch between virtual elements (the first and last firings have to discard part of the subaperture that is beyond the physical array element numbers) is a reasonable compromise between imaging speed and image quality (resolution and SNR).

3.2.3 Quasi Real-time Rail Flaw Image Display in 3D

The prototype includes a Graphic User Interface (GUI) that has been specifically designed for the rail flaw imaging application. After the setup configuration of the multiplexer, the user starts the scanning process by moving the probe along the transverse direction of the rail (perpendicularly to the imaging y-z plane). The parallel computation capability of GPU in the host computer achieves quasi real-time beamforming of the SAFT images with a frame rate of ~25 Hz using an 8-transmission modality [14]. The frame rate limit in the system comes from the data transmission and conversion hardware. The theoretical frame rate limit is much higher. As shown in Fig. 3.6, the quasi real-time 3D point cloud display is created by compounding the beamformed 2D images at each transverse position tracked by the encoder. The raw 2D SAFT image slices are displayed using a -30 dB threshold while the 3D display highlights only the pixels with intensity above the -15 dB threshold. To distinguish image slices of different signal strengths in the volumetric compounding, each 2D image is normalized by the maximum intensity value in the total collection of 3D pixels. Such a normalization process calibrates the decibel levels of “noised” image slices to those images with a strong reflection, suppressing any noise-only pixels between

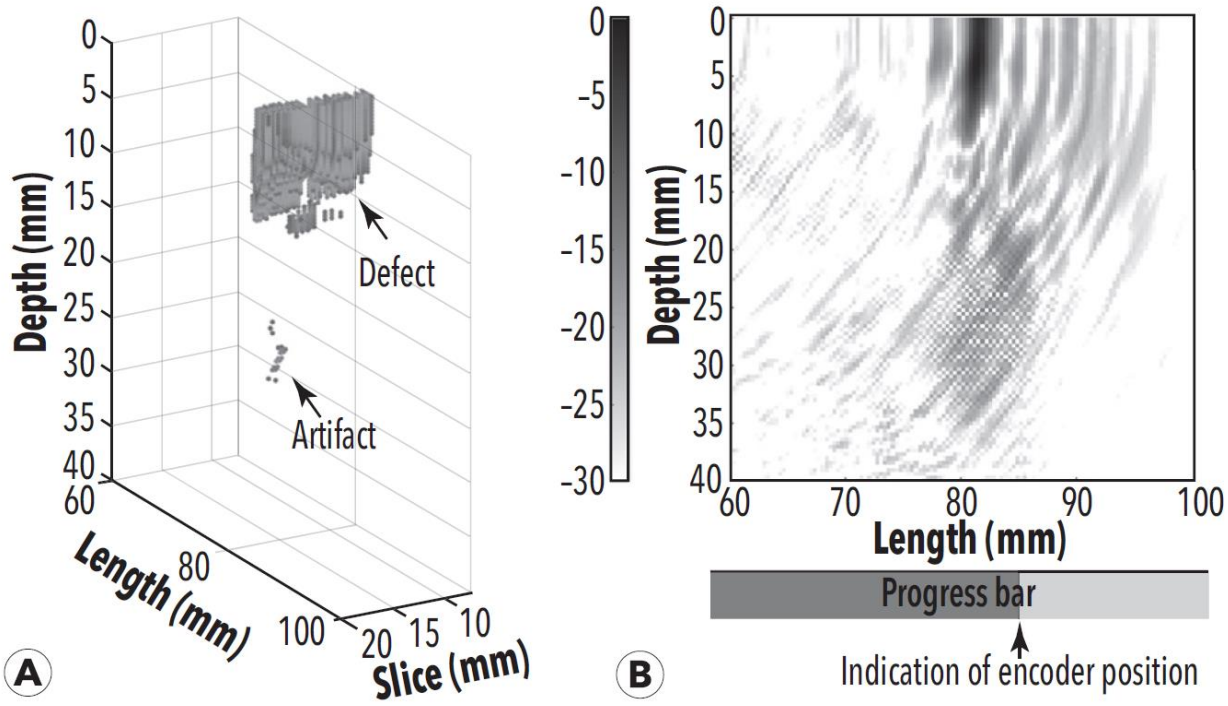

Figure 3.6: GUI runtime window displaying both compounded 3D point cloud (left) and raw 2D SAFT image (right). The refreshing rate is 25 Hz using the improved SAFT technique.

different image slices. In the 3D display, the algorithm performs this normalization adaptively by retaining the maximum intensity value from the previous 2D image and updating it if a larger maximum value is obtained. Notice that the temporary display of 3D point cloud is only for an initial visualization of any strong reflections, including artifacts that could affect the final size estimation. A post-processing algorithm is needed to extract accurate quantitative information regarding a possible internal flaw.

3.2.4 Postprocessing of Volumetric SAFT Images

Post-processing algorithms have been developed to further analyze the volumetric SAFT images in order to extract the final size and shape of the flaw. The flowchart illustrating the steps taken in post-processing is shown in Fig. 3.7. Referring to the schematic on the upper right, the SAFT image slices are beamformed in the vertical plane, while the final plane of interest is the

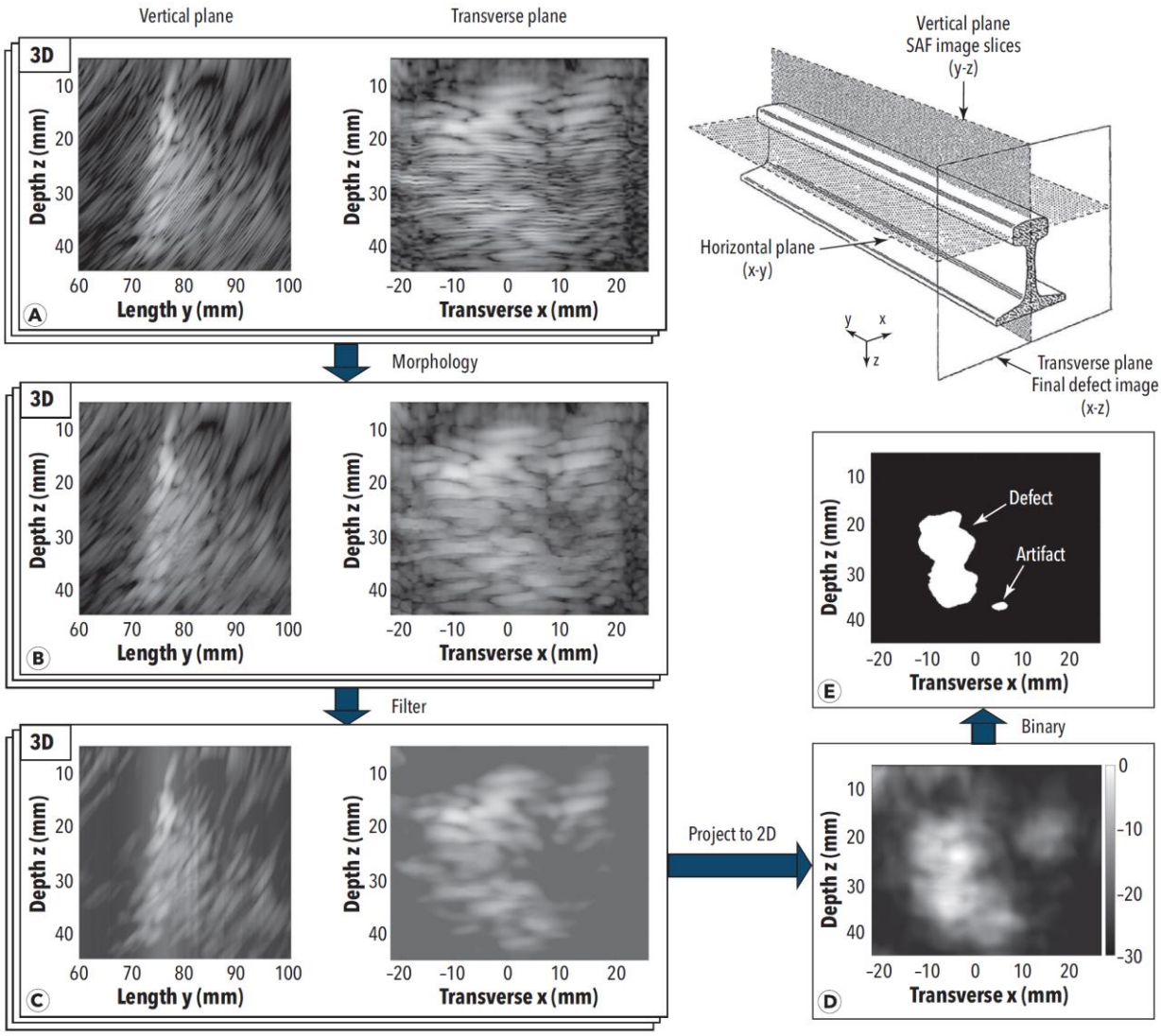

Figure 3.7: Volumetric image post-processing flowchart.

transverse plane. To prepare for image processing, the point cloud is first resized to high resolution through bilinear interpolation and converted from the decibel level (-40 dB to 0 dB) to an 8-bit grayscale, as shown in Fig. 3.7(a) with two sample slices both in the vertical plane and the transverse plane. The volumetric image first goes through a coupled dilation-erosion operation, where the intensity of each pixel is first increased and then decreased based on the intensity distribution of the neighboring pixels in 3D. As shown in Fig. 3.7(b), the coupled morphology process blurs the void between the grating lobes that are caused by Rayleigh diffraction limit of

the beamformed ultrasonic waves. Following the dilation and erosion operation, the volumetric image is flattened to an identified noise level through filtering techniques, as shown in Fig. 3.7(c). Each transverse plane slice is low pass filtered and then subtracted from the original slice to flatten the noise "phantoms". From the sample slice in the vertical plane, the smoothing process does not change the intensity of the main lobe response. Since the noise floor is identified in each transverse plane, the volumetric intensity map can finally be projected onto the transverse plane such that the high intensity pixels are coherently added up, while the lower intensity pixels remain at their intensity levels. Shown in Fig. 3.7(d), after converting gray scale image to decibel levels, the example transverse defect is finally identified with a high contrast.

At this point of the processing, it is necessary to isolate the flaw from the background image. The critical step to highlight the edge of the flaw is to apply a decibel level threshold and convert the intensity map into a binary map. Typically, the threshold is chosen as -15 dB for a ~30 dB dynamic range SAFT image, but the value should be adaptive to various circumstances such as defect orientation, reflectivity, SNR, etc. In this paper a dynamic threshold level is determined through the following empirical equation

$$Threshold = a + b * \cos(\theta_{defect}) + c * noise \tag{3.3}$$

where {a, b, c} are empirical constants calibrated from ground truth results from known flaws, θ_{defect} is the incident angle of the acoustic beams on the flaw, and *noise* is the decibel level of the background phantom determined in the flattening process. To find the incident angle θ_{defect}, the algorithm first approximates the tilted angle φ of the flaw using the initial 3D visualization by projecting the 3D cluster on arbitrary inclined transverse planes and finding the angle of the tentative plane that results in the maximum area of the defect. The incident angle is then computed by considering the geometric relationship between the broadside of the refracted acoustic beams

and the defect inclination φ. As an example, consider a 30 dB dynamic range tomography of a sample transverse defect with an estimated inclination $\varphi = 20^{\circ}$. The resulting incident angle θ_{defect} using the 55º shear wedge is 15º. A reasonable set of empirical constants is therefore $a = 1.5$, $b = -2$, and $c = 0.5$ to obtain a threshold of -15.4 dB. When the incident angle is small, it is appropriate to increase the search range in the decibel levels since the defect gives a good reflection to the array (higher contrast image), which results in a negative value of b. The additional consideration of noise level gives a second chance of energy level adjustment according to the image SNR.

The final binary defect image is shown in Fig. 3.7(e). Typically, for a single flaw present in the scanner area, a good SNR in SAFT imaging results in only one cluster of pixels. However, as in the case of Fig. 3.7(e) a less than ideal SNR may result in artifacts that still need to be segmented out before the final estimation of the flaw size. For this purpose, the algorithm further segments the 3D point cloud using the k-means clustering algorithm by calculating a minimum Euclidean distance between pixels to form identified clusters. The minimum Euclidean distance is set to 1.4 mm (S-wave resolution in steel) to differentiate between different clusters of pixels, and the clusters are arranged in descending order per area. To account for cases of multiple separate flaws within the same scanned area, the GUI includes the possibility to investigate each individual cluster if the secondary clusters are worthy of attention.

3.2.5 Experimental Results

Validation of the rail flaw SAFT imaging prototype was performed on flawed rail sections from the FRA Defect Library managed by former TTCI (now MxV Rail). Some of the test sections contained natural rail defects, while others contained artificial defects. Following the scanning by the prototype at UCSD Experimental Mechanics & NDE Laboratory, each test rail section with natural defects was broken by TTCI personnel to establish the “ground truth” from visual

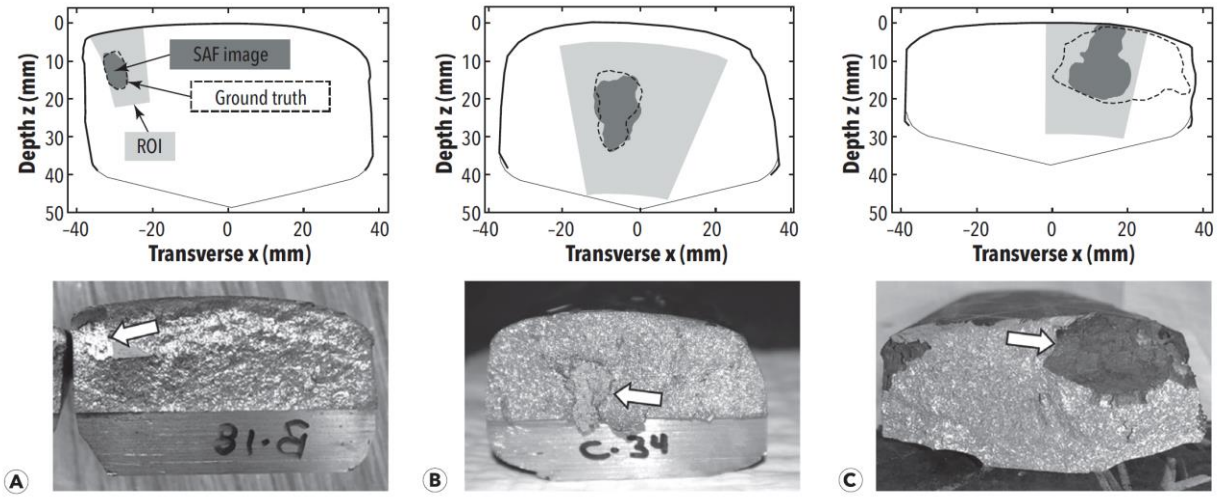

Figure 3.8: Validation tests: SAFT images of natural rail flaws and their corresponding ground truth pictures. (a) A Transverse Defect in a weld, (b) a void in a weld, and (c) a Transverse Defect in the rail head corner.

observation of the flaws. Following the initial validation, some parameters in the SAFT post-processing algorithms were optimized to better match the ground truth.

Fig. 3.8 shows the final images obtained by the SAFT imaging prototype for three natural defects from three FRA rail sections compared to the corresponding ground truth pictures after the rail breaks. Fig. 3.8(a) shows the case of a natural Transverse Defect (TD) in a weld. In this case, the size and shape of the defect are perfectly imaged by the SAFT system, with a size error as low as -2.3%. This example therefore shows an ideal case of a strong reflector (large SNR of the ultrasonic reflections) and located in a region that allowed good contact between the wedge and the rail surface during manual scanning. Fig. 3.8(b) shows the case of a void defect in the welded region of another rail section. The ground truth picture shows a clear indication of the void with the oxidized boundary. However, compared to the first case of the TD, the void defect is a slightly weaker reflector of ultrasound. In the raw SAFT images for this case, the noise level is as high as -25 dB, and some areas of the reflection from the weld may be mistaken for the defect in the initial

3D point cloud display. However, as shown in Fig. 3.8(b), the post-processing routine described in the previous section successfully isolate the void reflector with a final defect area estimation only differing from the ground truth by 3%, with a similarly good match in defect shape. Fig. 3.8(c) shows the case of a natural TD located in the upper right corner of the rail head. This case highlights the difficulty in scanning defects located under highly curved surfaces such as the head corners. In this case, it is impossible to maintain good wedge-rail contact throughout the entire scan. As a consequence, the SNR of the SAFT reflections degrades close to the head corners making these regions effectively "blind" to the scanning. Due to the contact limitation, the final image of Fig. 3.8(c) only detects about half of the defect, resulting in a severe underestimation of the defect size.

The next Fig. 3.9 shows the validation results for four cases of artificial flaws (End Drilled Holes -EDHs) in the FRA Defect Library. In these cases, the ground truth is obtained from CAD drawings of the holes. Fig. 3.9(a) shows an EDH in the rail head corner. Due to the aforementioned difficulty to maintain a good wedge-rail contact, the ROI cannot fully cover the corner defect resulting in the expected size underestimation. When the EDH is in the middle of the rail head as in Fig 3.9(b), the SAFT imaging results in a good match to the ground truth. In the absence of other explanations, the "leakage" of SAFT image at the bottom of the EDH is likely to be a secondary crack growing from the corner of the drill bit. Fig. 3.9(c) shows an EDH in a heavily worn rail section. In this case, the wedge-rail contact is further compromised by the highly curved surface resulting in a severe underestimation of the defect size. Finally, Fig. 3.9(d) shows an EDH in a worn section with a sharp corner on the head surface. This is an extremely unideal case, since the scanning process has to stop before the probe reaches the corner to avoid complete loss of signal. It is comforting to see that even in cases of reduced ROI due to the rail corner curvature,

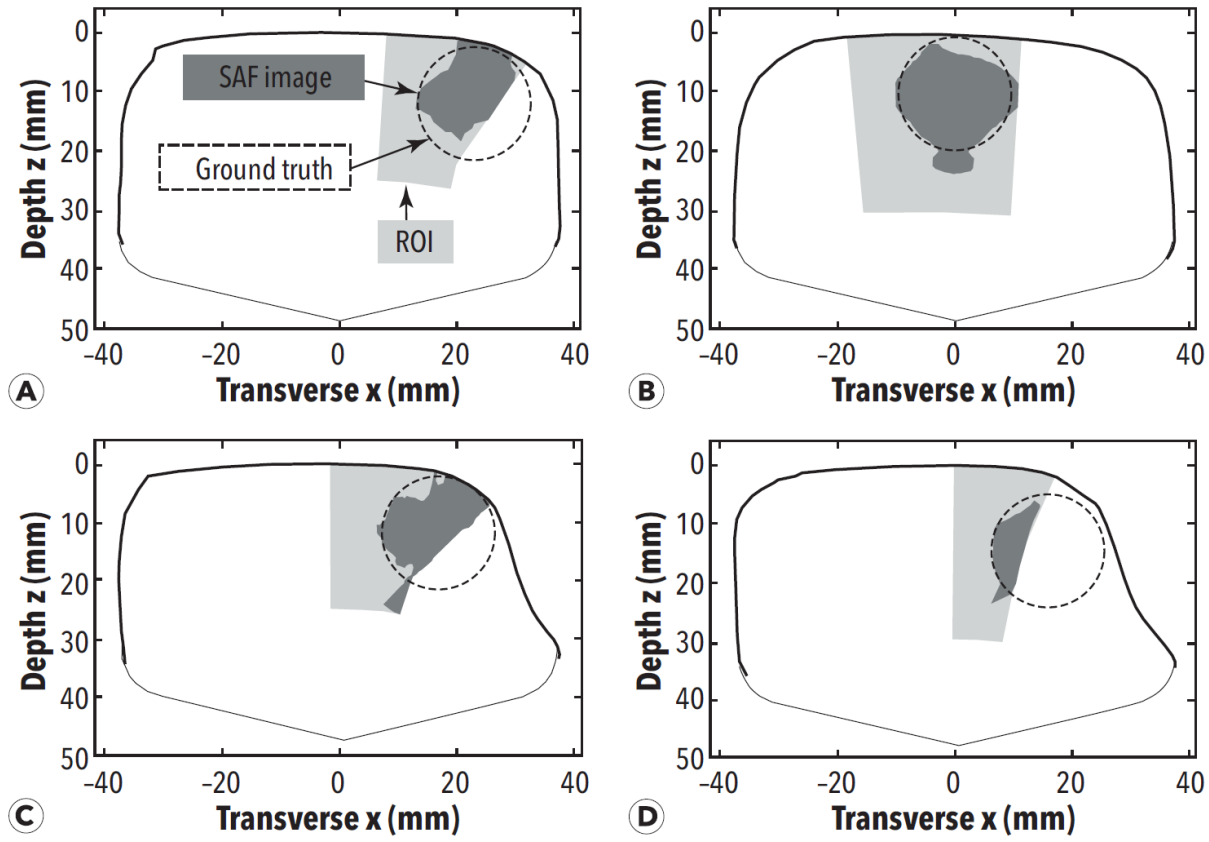

Figure 3.9: Validation tests: SAFT images of artificial rail flaws (End-Drilled Holes) and their corresponding ground truth circles: (a) EDH in rail head corner, (b) EDH in middle of rail head, (c) and (d) EDH in heavily worn rail head corner.

the portion of the defect that is successfully scanned shows a good match with the corresponding portion of the ground truth holes.

3.3 SAFT Imaging Capabilities with a Roller Search Unit

The prior wedge probe introduced in section 3.2 requires manual scanning with gel couplant and has difficulty conforming to curved surfaces such as the railhead corners, for example shown in Fig. 3.9. A wheel implementation of the SAFT imaging capability can lead to a more practical and accurate test for quantifying rail flaws, with examples shown in Fig. 3.10. Section

Figure 3.10: In-motion ultrasonic rail inspections using Rolling Search Units (RSUs).

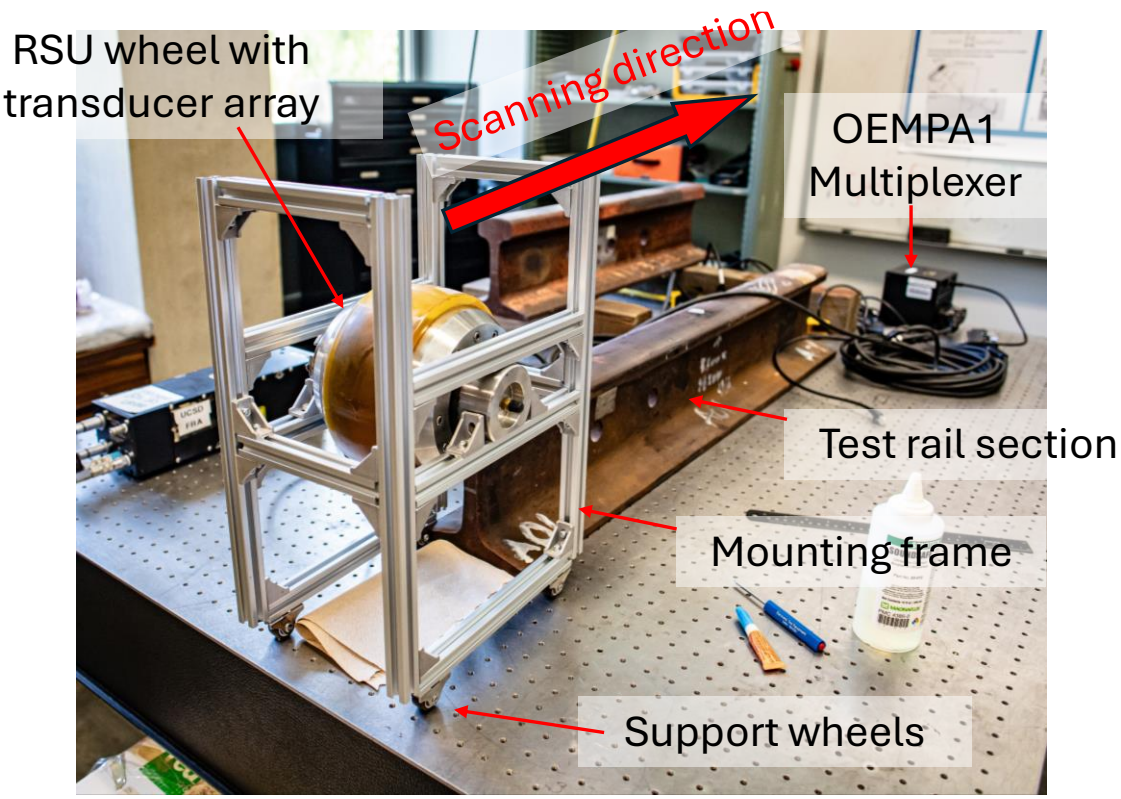

Figure 3.11: The RSU with the mounting frame and positioned on a test rail section in the laboratory.

3.3 is therefore aimed at building on this prior experience to develop a laboratory prototype for in-motion, wheel-based imaging of rail flaws. Once completed, this effort is expected to contribute to an innovative and practical solution for accurate quantification of safety-critical rail flaws.

3.3.1 Laboratory Setup of the RSU Imaging Unit

The investigated RSU system is a rubber wheel with conventional water-based coupling hosting various ultrasonic array transducers that were previously used by MxV Rail in a Phased-Array imaging configuration [2]. As shown in Fig. 3.11, the RSU wheel was mounted on a test rail section in the UCSD Laboratory by designing an aluminum frame that allowed longitudinal movement for scanning along the rail. The design of the frame enabled not only to adjust the vertical position of the RSU by applying different amount of pressure in the vertical direction, but also to rotate the orientation of the transducer in order to create inclined transmission/reception directions so as to maximize the reflections from TDs.

The reason for inclining the orientation of the transducer array inside the RSU is illustrated in Fig. 3.12. The RSU setup works in a similar manner as a transducer wedge by adding an interposed medium (water inside the wheel) between the transducer array and the rail. Let us focus on TDs as the primary targets of the inspection. If the array is positioned horizontally (Fig. 3.12-left), only the top of the TD will reflect the beams, hence the defect would be greatly underestimated. Conversely, by positioning the array at an appropriate inclined angle (Fig. 3.12-right), the entirety of the defect will reflect the beams allowing for imaging the full defect size. As a rule of thumb, an optimum angle for full ultrasonic reflection from a TD is generally considered 70-degree from the vertical plane (resulting in normal incidence on the TD that is generally oriented at 20-degrees from the vertical). Additional discussion on the aspect of transducer orientation is provided later in section 3.3.4.

3.3.2 Rail Profile Recovery Using RSU

Before applying the SAFT imaging scheme developed in section 3.2, it is important to recognize that the relative position of the transducer array and the water/steel interface needs to be

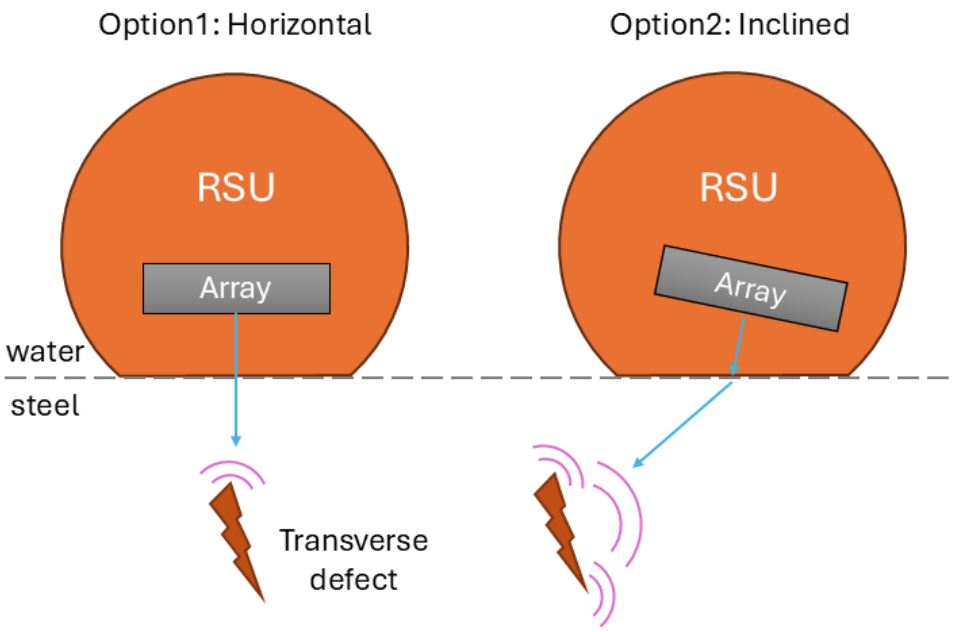

Figure 3.12: Horizontal vs. inclined transducer array orientation inside the RSU wheel for ultrasonic imaging a Transverse Defect (TD) in the rail.

calibrated each time the RSU is used. This is because the pressure applied to enlarge the contact area between the tire and the railhead can change the position of the RSU. In addition, considering the 1.5D Matrix Transducer (MT) that was mounted inside the RSU wheel, each row (treated as a linear array in this section) has a different height with respect to the railhead surface due to the unknown rail profile. Thus, it is essential to establish the precise position of the array (height and angle) to allow for accurate TOF estimations as detailed in section 3.2.1. These exact positions can be determined by reading the ultrasound reflections from the water/tire or the tire/steel interface.

Consider a pulse-echo signal collected by an arbitrary element of the transducer array, as shown in Fig. 3.13(a). The reflections from the inner side of the tire (water/tire interface) and the outer side of the tire (tire/rail interface) are the most significant wave arrivals in this plot. By combining these pulse-echo signals across a row of the MT (hereafter simplified as a linear array), a B-scan “heat map” can be generated as shown in Fig. 3.13(b). The TOF of these two reflections

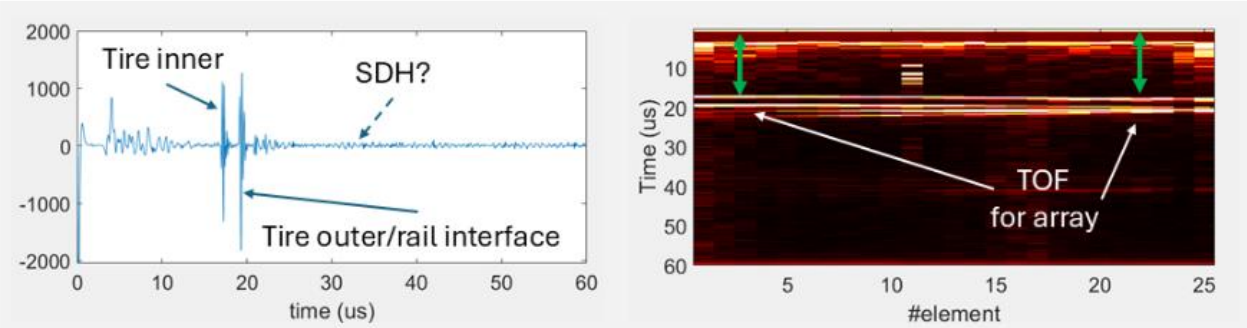

Figure 3.13: (a) A typical pulse-echo waveform recorded by one element of the transducer array in the RSU wheel on a rail. (b) B-scan image combining pulse-echo waveforms from a row of elements showing variations of arrival times of the tire reflections across the array.

can be now automatically tracked to recover the height and angle of the linear array with respect to the railhead surface. By performing the same estimation for all row components of the MT, the rail head profile can be recovered to enable full 3D image reconstruction of any internal flaw with high accuracy.

Fig. 3.14 shows a typical SAFT image obtained by placing the RSU with the transducer array in a horizontal orientation probing a rail section with an 8 mm Side Drilled Hole (SDH). Since only one row in the MT is considered (25 elements), the generated SAFT image is 2D in the x-y plane (x - longitudinal direction of the rail and y - vertical direction). The identified height of the array from the tire/rail interface is 16 mm. The estimated positions of the RSU, the array, and the rail head surface are shown in Fig. 3.14(b). With this horizontal orientation, the refracted L-wave is the dominant wave mode in the rail since the incident beam is normal to the interface. Thus, it is reasonable to set the region of interest (ROI) to form a SAFT image directly below the array. Fig. 3.14(a) shows the 2D SAFT image by performing a conventional 25x25 FMC using L-wave TOF for back propagation. The most significant response is seen near the tire/rail interface, which corresponds to the strong reflections seen in the raw signal of Fig. 3.13(a). There also exist

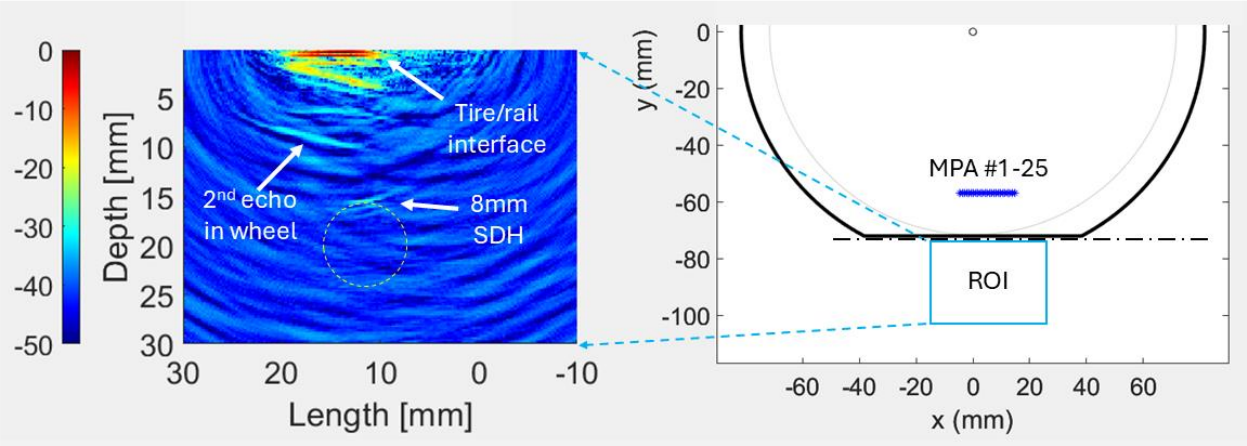

Figure 3.14: An example of SAFT imaging of a Side-Drilled Hole in the rail using a horizonal transducer orientation. (a) The SAFT image in decibels, and (b) the schematic showing the positions of array, wheel, rail and ROI.

multiple other reflections inside the RSU that are incorrectly back propagated in the ROI as "false positives." Only the top surface of the SDH is imaged, since the limited aperture size (20 mm for the 25-element linear array) is only able to illuminate a small angle of view. It is therefore clear from these results that orienting the transducer horizontally can generate false positives in the ROI. This confirms the necessity to incline the transducer for better imaging performance.

3.3.3 Use of Angled Beams and Analysis of Wave Modes

As illustrated in section 2.3, the ROI of the SAFT image is constrained by the quality of the synthetic ultrasonic transmit beams that can build up a high-resolution focus through beamforming. Orienting the transducer array in the RSU in an inclined position can dramatically increase the effective ROI in the inspected railhead while maximizing the sensitivity to TDs. A comprehensive study of the ROI is important because it determines the highest speed the RSU can travel along a rail track without compromising image quality. This section is focused on finding a suitable orientation of the transducer array to achieve strong imaging performance.

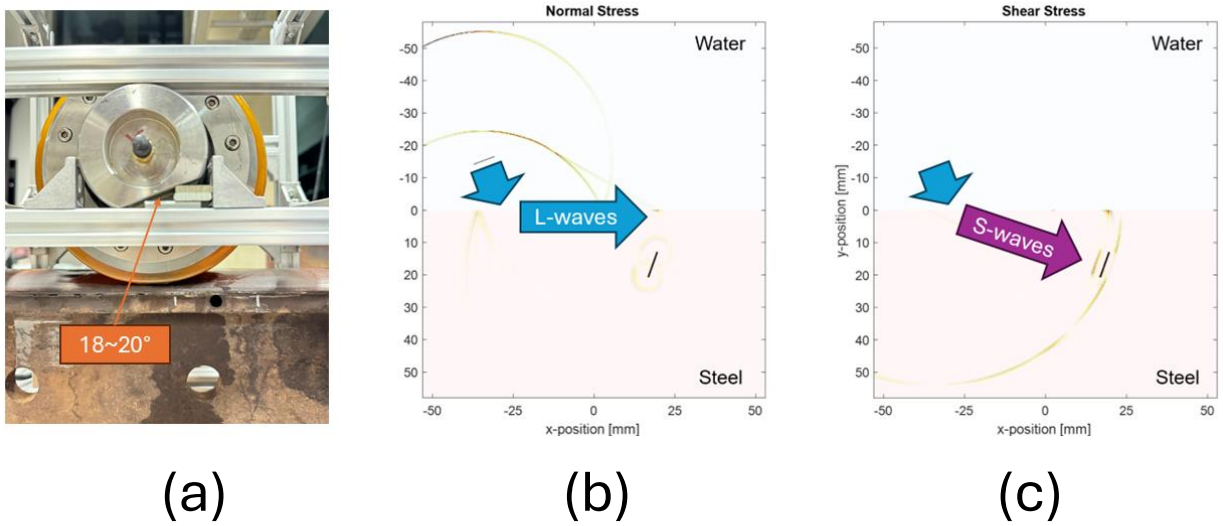

Figure 3.15: Angled beam setup for RSU. (a) The RSU holder oriented at an inclined angle of 18~20-degrees. MATLAB simulations of the wave propagation considering (b) L-waves refracted in the rail and (c) S-waves refracted in the rail.

Despite the differences in wave speed for L-wave and S-wave SAFT images, their effective ROI can be highly different due to the difference in wave refraction [15]. Fig. 3.15 shows the angle beam RSU setup with the array positioned at an 18~20-degree inclination from the horizontal direction. Fig. 3.15(a) shows a picture of the RSU oriented for this case in the UCSD laboratory setup. Figs. 3.15(b) and (c) present the results of a simulation performed using MATLAB's k-wave toolbox. Specifically, the simulation analyzed a TD illuminated by L-waves (Fig. 3.15(b)) and S-waves (Fig. 3.15(c)), respectively. The transducer array is placed in water as the first layer, and the second medium is set as steel. The simulated defect is an 8 mm slit oriented at 20-degree from vertical as typical of TDs in rails. As shown in the figures, the refracted L-wave in steel is beyond the first critical angle, whereas the refracted S-wave propagates at ~40 degrees generating strong reflections from the TD. This situation is highly beneficial for imaging purposes, where the TD can be therefore best imaged using the refracted S-wave in the rail without confusion with any

L-wave reflections. The same scenario, in fact, is desired in traditional RSU detection of TDs that also rely on the refracted S-waves in the rail steel.

Although theory and simulations suggest that the refracted S-wave is the best candidate to generate high quality SAFT image of TDs in a large ROI, there is a certain angular range where L-wave images may work better. Fig. 3.16 shows both L-wave and S-wave images when an SDH is placed directly at the bottom of the RSU. The two images are beamformed using the same FMC dataset but with different TOF corresponding to each of the wave modes. The CNR of the L-wave image is -15 dB while that of the S-wave image is only -10 dB. The lower SNR of the S-wave image is caused by the fact that the S-wave "misses" the SDH that is placed directly below the RSU. It is also interesting to observe that there is a phantom of S-wave reflection in the L-wave image located at -15 ~ -20 mm in length. This is because the S-mode wave speed is slower than L-mode in steel but incorrectly beamformed using L-mode wave speed. Therefore, as a rule of thumb, we can conclude that when the target flaw is located directly below the RSU, it is reasonable to consider the refracted L-wave to build the image.

Fig. 3.17 shows the same comparison of L-wave and S-wave images, where now the SDH is located ahead of the RSU. In this case, the S-wave image shows superior CNR of -25 dB, while the L-wave image has much less contrast and poor resolution. Comparing the results in Fig. 3.16 and Fig. 3.17, for L-wave images there is a consistent side lobe located around 10 ~ 12 mm in depth at the upper left corner of the image. Similarly to the findings in Fig. 3.14(a), this side lobe is the result of reverberations within the wheel and can be eliminated by performing a baseline subtraction.

From these results it therefore appears that when the target flaw is located ahead of the RSU, the S-wave angled beam provides the best images. The L-wave beam can however provide

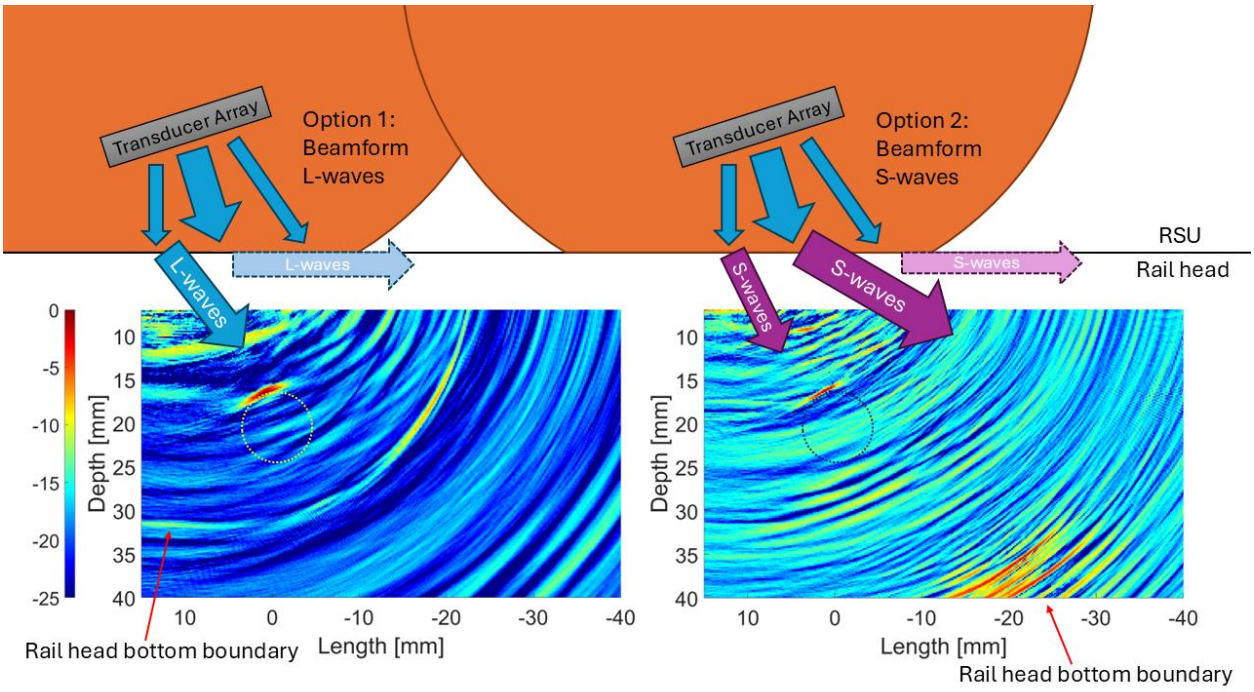

Figure 3.16: Comparison of SAFT images of an SDH using L-waves (left) or S-waves (right). The position of the SDH is directly *below* the RSU.

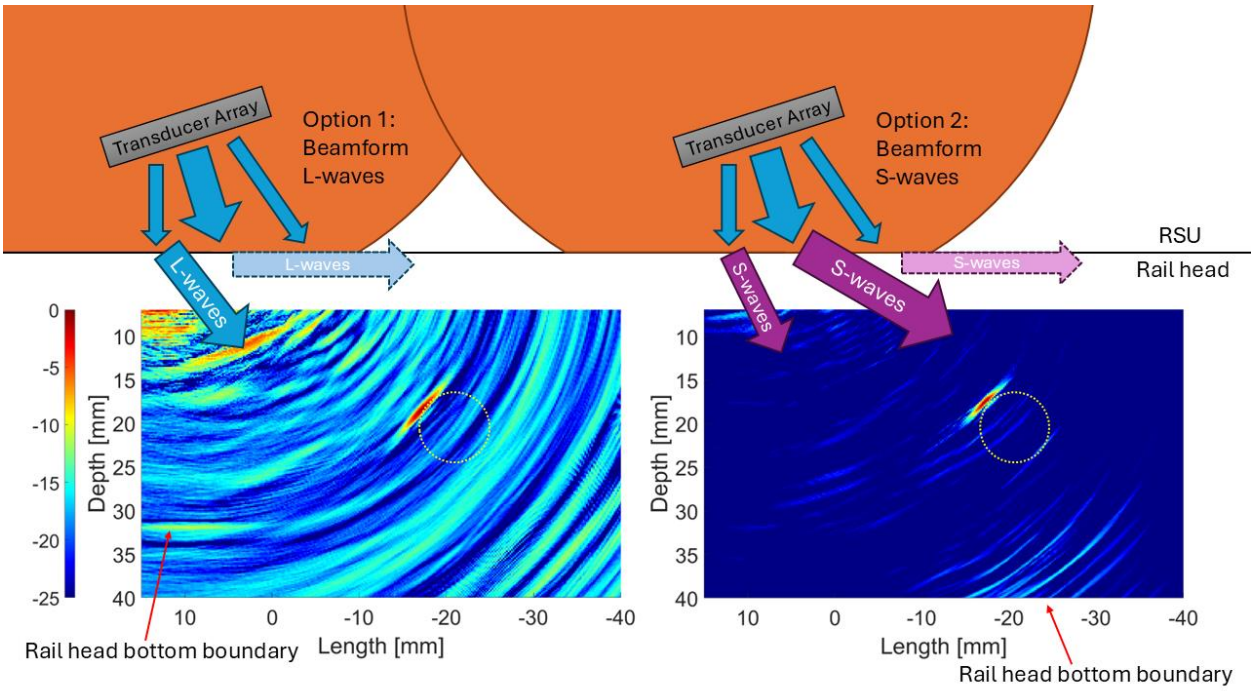

Figure 3.17: Comparison of SAFT images of an SDH using L-waves (left) or S-waves (right). The position of the SDH is *ahead of* the RSU.

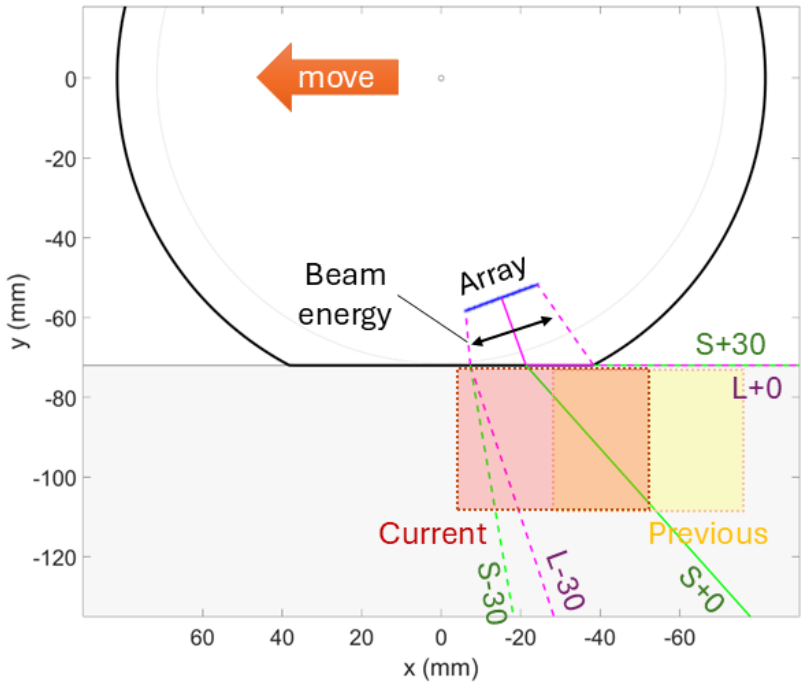

Figure 3.18: ROI of the RSU imaging for estimating possible test speeds.

additional information when the flaw is located directly below the RSU. This opens an opportunity to combine L-waves and S-waves to image different regions of the rail and thus enlarging the ROI.

3.3.4 Estimates of RSU Moving Speed

Once the ROI area is set in accordance with the angle beam profile, it is appropriate to estimate potential test speeds using the proposed SAFT imaging modalities. As shown in the schematic of Fig. 3.18, it is reasonable to consider an ROI with a length of 50 mm. Let us also enforce a 50% overlap during the scanning (i.e. the same portion of rail is imaged by at least two frames). Considering the current capabilities of the multiplexer hardware available at UCSD (OEM-PA1 model from Advanced OEM Solutions, West Chester, OH), using a 50x50 FMC for the first two rows in the 5x25 MT and only firing 4 sparse transmissions in one frame, the framerate is restricted to 25 Hz due to limited multiplexer/computer communication bandwidth. Thus, the speed of the RSU can be as fast as 25 mm × 25 Hz = 625 mm/s = 1.4 mph.

Figure 3.19: Field test at UCSD's Rail Defect Farm.

This initial analysis therefore suggests that with the available hardware capabilities the 3D imaging test can only be implemented in a slow scanning mode, perhaps following a traditional flaw detection at higher speeds. To further increase imaging speed, the number of transmissions needs to further decrease or hardware with faster data communication needs to be procured. These and other options to further increase test speed while keeping an acceptable image quality will be considered further in the continuation of this study.

3.3.5 Testing of Imaging System at UCSD Rail Defect Farm

UCSD's Rail Defect Farm (Fig. 3.19) is a 250-ft Class I track using 136RE rail constructed in 2010 under FRA funding and support of BNSF. It consists of a 125-ft tangent portion and a 125-ft 8-deg curved portion, both containing a number of artificial and natural rail flaws including several TDs. This track enables to test the RSU imaging system under conditions representative of the field. The RSU mounted on the aluminum frame was moved along the track by hand. The OEM-PA1 multiplexer processed the first 2 rows of the MT transducer array hosted in the RSU and positioned over the rail gage side. The host computer displayed the SAFT images in quasi-real time using parallel computation capabilities in the GPU [10].

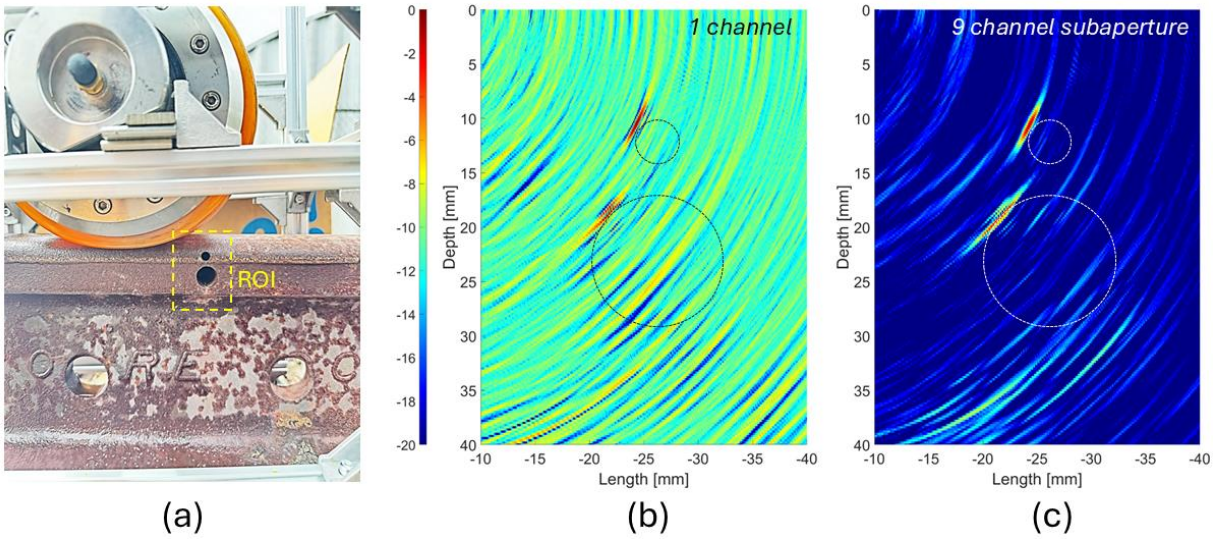

Figure 3.20: Results from two SDHs at UCSD Rail Defect Farm. (a) The RSU positioned above the defects. (b) SAFT image using a traditional 1-channel transmission. (c) SAFT image using the enhanced 9-channel subaperture transmission showing much better contrast.

The RSU system was first tested on two SDH artificial defects. Shown in Fig. 3.20(a), the two SDHs (diameters of 3 mm and 12 mm, respectively) were drilled at the gage side of the railhead. The RSU was mounted such that the transducer array was oriented at an 18-degree inclination from the horizontal. For these tests the conventional SAFT method was compared with the subaperture transmission SAFT. Both modalities were implemented in a full 25 firings (instead of sparse firing) to compare the highest imaging quality. Only the S-wave was considered in this case. For the 1 channel 25x25 FMC scheme in Fig. 3.20(b), the image CNR is as low as -8 dB, which is unimpressive. A 9-element subaperture transmission, Fig. 3.20(c) shows a much better performance with greatly improved CNR of -20 dB. Hence it is confirmed that a sufficient number of elements is required in SAFT subaperture transmissions to achieve a satisfactory image quality.

The RSU system was then tested on one of the natural TDs present in the UCSD test track. Fig. 3.21(a) shows the RSU positioned on the rail for this case. The TD was first imaged using the wedge-based imaging system described in section 3.2 as the “ground-truth.” That system used a

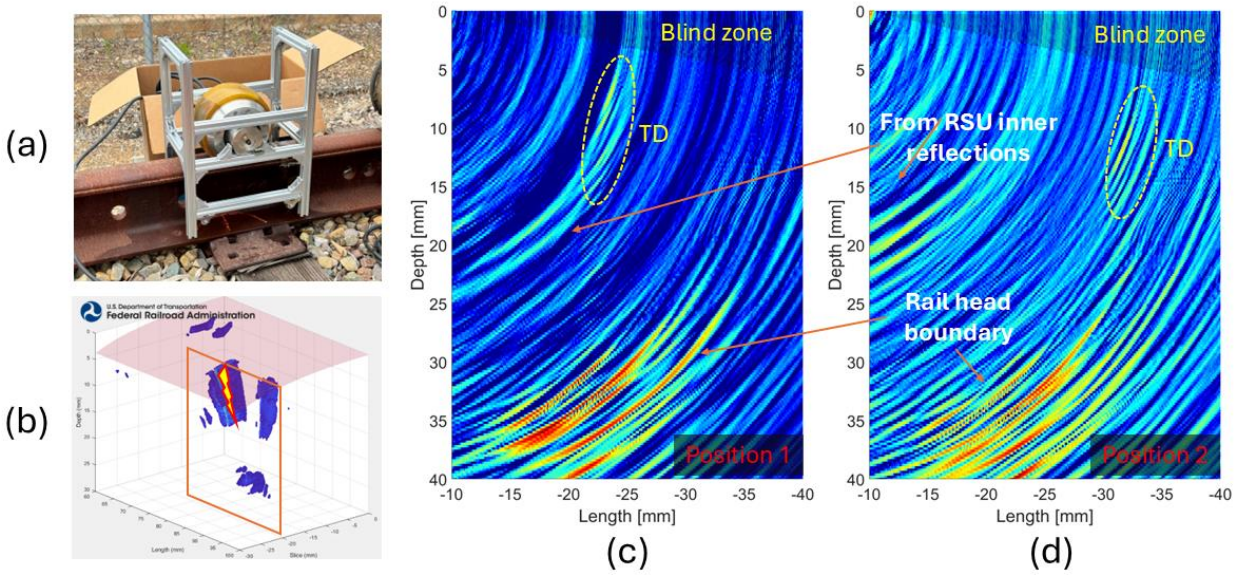

Figure 3.21: Results from a natural TD at UCSD Rail Defect Farm. (a) The RSU positioned above the defect. (b) Ground truth of the TD obtained from the wedge-based imaging system. (c) SAFT image using the enhanced 9-channel subaperture when the TD is in the center of the ROI. (d) same as (c) when the TD is to the right of the ROI.

64-element linear transducer on a plastic wedge that was scanned across the railhead to construct 3D images from 2D slices. This final "ground truth" result is shown as a point cloud in the 3D image of Fig. 3.21(b). From this image, a 2D slice in the vertical plane (orange contour in the figure) indicates that the TD is oriented 20-degree from the vertical and initiates from the rail head surface up to a depth of ~12 mm. The RSU imaging result using the 9-channel subaperture transmission SAFT is shown in Fig. 3.21(c) and (d) for two different RSU positions along the track. In the case of Fig. 3.21(c) where the TD is located at the center of the ROI, the SAFT image matches well with the ground truth, with the exception of a small underestimation of the defect size in the area close to the rail head surface. This small error is due to the "blind zone" that exists very close to the rail surface due to the finite contact interface between the tire and the rail (also shown in the figure). No ultrasonic beam is allowed to propagate in this zone. When the TD is located further ahead in the ROI, Fig. 3.21(d), the SAFT image has lower contrast and results in

an underestimation of the TD size. This error is again related to the blind zone that is extended for targets located ahead of the ROI.

In the continuation of this study, the problem of the "blind zone" will be addressed in at least two ways. First, several images of the same TD for different positions of the RSU could be combined and fused to obtain the true size of the flaw. Second, the extent of the blind zone itself could be reduced by redesigning the position of the transducer array inside the RSU in order to obtain a wider angular range of the ultrasonic beams propagating through the tire/rail interface.

3.4 Discussions and Conclusions

SAFT techniques are the new front in ultrasonic imaging of internal discontinuities because of their potential for accurate and fast imaging. This chapter has presented two prototype systems based on improved SAFT techniques applied to the 3D imaging of rail flaws. These tools can improve the outcome of the manual verification of rail flaws by resulting in objective flaw size and shape that can then inform the most appropriate remedial actions.

The first field-deployable prototype is hosted in a ruggedized carry-on size case and is battery powered for autonomous operation. The sensing probe consists of a linear ultrasonic array that is mounted on a wedge and includes a position encoder to build 3D images from 2D SAFT slices. The beamforming algorithm tracks the ray paths of the ultrasonic waves through the wedge and utilizes sophisticated subarray sparse firing to increase imaging speed. Currently high-contrast images can be obtained at a frame rate of 25 Hz, although higher speeds can be obtained (if necessary) by further reducing the number of firings at the expense of image quality. Special post-processing algorithms are utilized to reduce the 3D point cloud into a result that can lead to the final size and shape of one (or multiple) flaws present in the scanned Region of Interest.

The transducer-wedge based imaging prototype was tested on rail sections containing both natural and artificial flaws. The testing allowed the authors to refine control parameters of the imaging system to find the best match to the ground truth. Good results, in terms of both flaw size and flaw shape, were obtained in the presence of natural TDs and EDHs if the defects were located aways from the curved rail head corners. When instead the defects were located underneath the head corners (and particularly so in the presence of heavy head wear), the curvature of the surface adversely affected the wedge-rail contact effectively reducing the scanned ROI. In these cases, therefore, only a portion of the rail flaw could be successfully scanned resulting in an underestimation of flaw size.

The second imaging system utilized a Roller Search Unit (RSU) that hosted various ultrasonic transducer arrays. A multiplexer and a computer were interfaced with a subset of the arrays for full control of transmissions and receptions at the applicable transducer elements. A mounting frame was built to position the RSU above the rail. The ultimate envisaged implementation would be a rolling wheel hosting the ultrasonic transducer arrays and operated either by a walking operator or by a high-speed rail vehicle. Many elements seen in the first imaging system, including ray-tracing beamforming with an interposed path, multi-mode imaging with L-waves and S-waves and subaperture sparse transmissions, are being now implemented in the current in-motion RSU probe. Promising results have been shown for the imaging of Side-Drilled Holes as well as natural Transverse Defects in rail sections tested in the laboratory and at UCSD's Rail Defect Farm.

While the results have demonstrated the potential to obtain good image quality of the flaws with the SAFT-RSU implementation, several aspects deserve further attention and will be addressed in the continuation of this research. These include: 1) Further investigations of the sparse

transmission modality and hardware communication options to increase achievable test speed. 2) Further investigations of the multi-mode (L-wave plus S-wave) beamforming to extend the effective Region-Of-Interest (ROI) hence increase rail coverage. 3) Further investigations of the "blind zone" ahead of the RSU to improve defect sizing in the region close to the rail head surface. Finally, additional development work will be needed for a field-deployable system. For example, the currently available multiplexer has only allowed access to one or two rows of the 5x25 Matrix Transducer Array available in the MxV Rail RSU. If all the 5x25 array channels can be accessed, the true performance limits of the system can be assessed.

Acknowledgements

This research was funded by the U.S. Federal Railroad Administration under contract No. 693JJ619C000008 (Dr. Robert Wilson, Program Manager) and by MxV Rail under the "AAR University Programs – Grand Challenges in Railroad Technology," contract No. 24-0312-008622. The test rail sections presented for section 3.2, as well as the result of the rail break for the natural defect case, were provided by Dr. Anish Poudel of former Transportation Technology Center (now MxV Rail) in Pueblo, CO. The authors acknowledge the technical support and the RSU on loan provided by Dr. Anish Poudel and Mr. Brian Lindeman of MxV Rail The authors would also like to acknowledge Mr. Gavin Dao of Advanced OEM Solutions (West Chester, OH, USA) for providing technical advice on SAFT hardware solutions and valuable insights on the use of the multiplexer currently adopted in the prototype systems.

Chapter 3, in part, is a reprint of the material as it appears in C. Huang and F. Lanza di Scalea, "Rail Flaw Imaging Prototype Based on Improved Ultrasonic Synthetic Aperture Focus Method," *Materials Evaluation*, vol. 82, no. 1, pp. 51-59, 2024. Chapter 3 also contains

unpublished material coauthored with F. Lanza di Scalea and A.Z. Hosseinzadeh in "Towards Efficient 3D Imaging of Internal Rail Flaws in Motion," *Mid-year Report to MxV Rail AAR University Programs* (24 pages), MxV Rail contr. 24-0312-008622, August 2024. The dissertation author was the primary investigator and author of this chapter.

References

[1] F. Lanza di Scalea, "Ultrasonic testing applications in the railroad industry," Chapter 15: *Special Applications of Ultrasonic Testing*, in *Non-destructive Testing Handbook*, 3rd edition, P.O. Moore, ed., American Society for Nondestructive Testing, pp. 535-552, 2007.

[2] M. Witte and A. Poudel, "High-speed rail flaw detection using phased-array ultrasonics," *Technology Digest TD-16-030*, Transportation Technology Center, July, 2016.

[3] B.W. Drinkwater and P.D. Wilcox, "Ultrasonic arrays for non-destructive evaluation: a review," *NDT&E Int.*, vol. 39, no. 7, pp. 525–541, 2006.

[4] J.J. Flaherty, K.R. Erikson, and V.M. Lund, "Synthetic aperture ultrasonic imaging systems," *U.S. Patent* 3,548,642, 1967.

[5] C. Huang and F. Lanza di Scalea, "High Resolution Real Time Synthetic Aperture Imaging in Solids Using Virtual Elements," in *Proc. ASME*, vol. 86717, p. V009T14A001, 2022.

[6] C. Huang, and F. Lanza di Scalea, "Development of Rail Flaw Imaging Technology Based on Ultrasonic Tomography," Final Technical Report to the Federal Railroad Administration (47 pages), FRA contr. 693JJ619C000008, December 2022.

[7] J.A. Jensen, S.I. Nikolov, K.L. Gammelmark, and M. H. Pedersen, "Synthetic aperture ultrasound imaging," *Ultrasonics*, vol. 44, Suppl. 1, pp. e5-e15, 2006.

[8] G.R. Lockwood, J.R. Talman, and S.S. Brunke, "Real-time 3-D ultrasound imaging using sparse synthetic aperture beamforming," *IEEE Trans. Ultrason., Ferroelect., Freq. Control*, vol. 45, no. 4, pp. 980–988, 1998.

[9] S. Sternini, A. Y. Liang, and F. Lanza di Scalea, "Ultrasonic synthetic aperture imaging with interposed transducer–medium coupling path," *Struct. Health Monitor.*, vol. 18, no. 5-6, pp. 1543–1556, 2019.

[10] S. Sternini, A. Y. Liang, and F. Lanza di Scalea, "Rail Defect Imaging by Improved Ultrasonic Synthetic Aperture Focus Techniques," *Mater. Eval.*, vol. 77, no. 7, pp. 931–940, 2019.

[11] F. Lanza di Scalea, S. Sternini, and T.V. Nguyen, “Ultrasonic imaging in solids using wave mode beamforming.” *IEEE Trans. Ultrason., Ferroelect., Freq. Control,* vol. 64, no. 3, pp. 602-616, 2017.

[12] C.H. Frazier and W.D. O’Brien, “Synthetic aperture techniques with a virtual source element,” *IEEE Trans. Ultrason., Ferroelect., Freq. Control*, vol. 45, no. 1, pp. 196-207, 1998.

[13] M. Karaman, P.C. Li, and M. O’Donnell, “Synthetic aperture imaging for small scale systems,” *IEEE Trans. Ultrason., Ferroelect., Freq. Control*, vol. 42, no. 3, pp. 429–442, 1995.

[14] C.J. Martin-Arguedas, D. Romero-Laorden, O. Martinez-Graullera, M. Perez-Lopez, and L. Gomez-Ullate, “An ultrasonic imaging system based on a new SAFT approach and a GPU beamformer,” *IEEE Trans. Ultrason., Ferroelect., Freq. Control,* vol. 59, no. 7, pp. 1402-1412, 2012.

[15] C. Huang, and F. Lanza di Scalea, “Application of sparse synthetic aperture focusing techniques to ultrasound imaging in solids using a transducer wedge.” *IEEE Trans. Ultrason., Ferroelect., Freq. Control*, vol. 71, no.2, pp. 280-294, 2024.

Chapter 4 Ultrasparse Synthetic Aperture Imaging by Passive Ultrasonic Sensing

4.1 Introduction

The ultrasonic Synthetic Aperture Focus Technique (SAFT) has gained increasing interest in recent years in multiple applications ranging from medical imaging to industrial Non-Destructive Testing (NDT). Compared to traditional B-scan imaging modalities (e.g. Phased-Arrays or PAs) that require simultaneous active excitations by multiple transmitters with controlled time delays for physical beam steering and focusing in transmission, SAFT can achieve the same or better focus by transmitting with individual elements at a time [1], [2]. The image is then obtained by post-processing the data using beamforming algorithms that create a synthetic focus in both transmission and reception. The best SAFT image quality is obtained when using the full aperture of an N-element array. This is known as Full-Matrix Capture (FMC) or Total Focusing Method (TFM) [3], [4]. In FMC, each array element is used as a transmitter at a time, with all elements used as receivers for each transmission, resulting in an $N \times N$ matrix of collected waveforms. Compared to PA imaging, SAFT offers the advantages of simpler hardware (by eliminating multiple simultaneous transmissions with controlled time delays) and better image contrast (by theoretically achieving perfect focus exploiting the full array aperture in both transmission and reception).

Several improvements have been proposed to increase the performance of SAFT ultrasonic imaging, in terms of both image quality and test speed. In terms of image quality, the SAFT results can be degraded by the limited energy that is injected into the test medium by each single transmitter. This is a larger issue in medical imaging because of the highly attenuating materials, or when using a wedge in industrial NDT applications [5]-[8]. The limited transmitted energy can

be overcome by the use of transmission subarrays, where multiple elements contribute to a single transmission. These subarrays can be shaped to generate planar or circular wavefronts to illuminate the region of interest with varying degrees of performance [9]-[18]. In terms of imaging speed, the prime need for "fast" or "ultrafast" imaging has been the medical field, in applications requiring transient elastography for breast cancer diagnosis, functional imaging of brain activity, imaging blood motion or contrast agents, and many other applications, as summarized in [19]. Other studies have further improved the performance of high-frame-rate medical imaging via coherent and incoherent image processing [20], [21]. In NDT, fast imaging can also benefit applications of in-motion scanning of solids such as imaging of defects in railroad tracks using moving inspection vehicles. Regardless of the application, the most effective way to increase the speed of a SAFT method is to decrease the number of transmissions (whether using single-element transmitters or multi-element subarray transmitters). This is known as "sparse" array firing. An added advantage of sparse firing is the simplification of the multiplexer hardware because of the reduced number of high-voltage digital-to-analog output channels. Unfortunately, decreasing the number of transmissions generally degrades the quality of the image since the Signal-to-Noise Ratio (*SNR*) of a SAFT image is given by $SNR = \sqrt{\#\text{transmissions} \times \#\text{receptions}}$.

One technique proven effective to increase the array gain without increasing its physical array aperture when imaging solid materials is the compounding of multiple wave modes. This concept exploits the simultaneous existence of various wave modes, whether longitudinal and shear waves in bulk 3D solids [8], [9], [22], or multiple guided waves in dispersive waveguides [23]. The wave paths from these modes can be compounded either coherently or incoherently to significantly improve image focus compared to a single-wave mode image.

This chapter demonstrates a technique for "ultrasparse" array imaging that uses as few as one, and as many as four individual single-element transmissions for fast SAFT imaging without sacrificing image quality. This important result is achieved by implementing revised concepts of "passive sensing" to effectively reconstruct a virtual FMC (or TFM) set of waveforms with a minimum number of physical transmissions.

The field of "passive" ultrasonic (or acoustic) sensing has gained increasing interest in recent years following the seminal work of Lobkis and Weaver [24]. These authors demonstrated that if a closed or open system is excited by a diffuse wave field (e.g. generated by acoustic sources randomly distributed in space and time, or a field with equi-partitioned energy among all normal modes), the time-averaged cross-correlation of the signals collected at two receiver points *I* and *J* converges to the Green's function (or the Impulse Response Function - *IRF*) of the system between the two receivers. Hence the "passively" reconstructed signal between receivers *I* and *J* corresponds to the "active" *IRF* that would be collected if *I* was the source (hence acting as a "virtual" source) and *J* was the receiver. This concept of passive Green's function reconstruction has since been used in several applications of ultrasonic, acoustic or dynamic characterization of a test medium where the excitations can be provided by either the natural environment or by a few controlled sources. Several useful applications of this "passive" approach have been demonstrated in underwater acoustics [25]-[27], seismology [28]-[34], seismic interferometry for dynamic identification of civil infrastructure [33], [35]-[40], as well as structural health monitoring and NDT defect detection [41]-[53]. Some applications of passive sensing have included beamforming imaging by taking advantage of the multiple "virtual" sources that could be created by an array of only receivers. This kind of passive beamforming imaging was demonstrated to visualize surface waves on the earth's surface by using ocean-generated ambient excitations [34], map geological

features for oil and gas exploration using ambient micro-earthquakes [34], image damage in structures using randomly distributed ultrasonic sources [43], [46], and perform SAFT-TFM imaging of subsurface defects using conventional ultrasonic arrays to reconstruct the "virtual" responses via cross-correlations of delayed reverberating waveforms [54], [55].

It was in seismic interferometry that Snieder and Şafak [35] highlighted the advantages of performing a deconvolution between the two receiver responses, instead of a cross-correlation, for passive *IRF* reconstructions. In that paper, they noted the fact that the cross-correlation is affected by the frequency spectrum of the excitation source, that instead is eliminated by the deconvolution process. The idea that an output-input deconvolution, rather than a cross-correlation, provides a robust estimate of a system's transfer function (i.e. the frequency-domain version of the *IRF*) was actually first remarked in the 1970's by Roth [56] in the context of electrical systems. In particular, he showed how a specific implementation of the deconvolution operations (i.e. an averaged Normalized Cross-Power Spectrum - *NCPS*) should be performed to eliminate the distortions caused by the shape and/or the randomness of the input, with very important consequences for the estimation of an accurate transfer function. Another very important factor addressed in that paper by Roth is the importance of the *segmental averages* of the *NCPS* operation to appropriately reconstruct the coherent transfer function and eliminate the incoherent portion of the signal (e.g. noise). Accordingly, robust reconstruction of the passive transfer function requires *ensemble averaging* that can be practically achieved by multiple overlapping segments, as also implemented in the 1960's and 1970's by Carter et al. [57] for the estimation of the magnitude-squared coherence function and by Welch [58] and Nuttall [59] for the estimation of power spectra. This aspect of segmental averaging is often neglected in many studies of passive *IRF* reconstruction

even when using cross-correlation, where the time average inherent in the cross-correlation operation is mistakenly considered equivalent to an ensemble average of multiple segments.

The objective of this chapter is to demonstrate the robust and accurate implementation of "passive" ultrasonic sensing to achieve "ultrasparse" SAFT array imaging requiring a minimum number of single-element physical transmissions (one to four elements) to generate an entire FMC set of waveforms. Compared to a traditional "active" FMC capture, the extreme sparsity of the "passive" array brings unique advantages of speed (less physical transmissions) and simplicity of hardware (less high voltage digital-to-analog channels). Despite the extreme sparsity of transmissions, the proposed method can obtain images of good quality without requiring long time windows. This result is obtained by implementing several key analysis steps including: (a) the use of carefully designed segment-averaged normalized cross-power spectrum for passive *IRF* reconstruction, (b) the use of both the causal and acausal portions of the reconstructed *IRF*, and (c) the compounding of multiple wave modes. After presenting theoretical considerations of passive ultrasonic sensing at two receivers, experimental results are shown for ultrasparse SAFT imaging of drilled holes in an aluminum block.

4.2 Passive Reconstruction of Impulse Response Function Between Two Receivers

4.2.1 Dual-Output Model

Consider a linear dynamical system (test medium) as shown in Fig. 4.1(a). It is easier to work in the frequency domain. Assume the medium subjected to an excitation spectrum $E(f)$ and whose response is measured at two receiver points I and J using transducers whose frequency responses are $R_i(f)$ and $R_j(f)$, respectively. Let us also consider the presence of noise in the

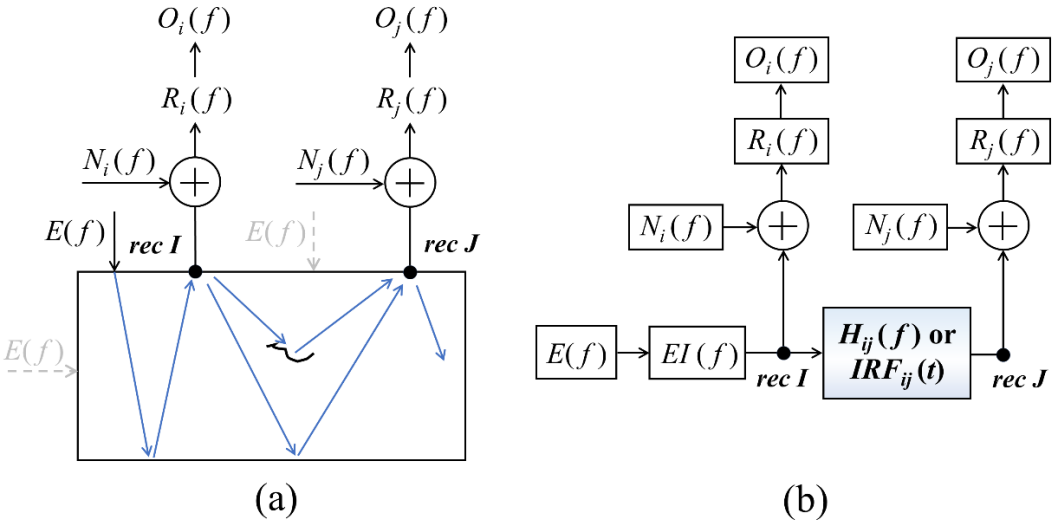

Figure 4.1: Reconstruction of a structural system's transfer function between two receivers *I* and *J*. (a) Physical system. (b) Schematic system. The figure shows the key components contributing to the two outputs.

receptions, $N_i(f)$ and $N_j(f)$, assumed zero-DC and uncorrelated with itself and with the excitation. These noise terms generally represent incoherent arrivals or system nonlinearities. Using the convolution theorem, and considering the schematic system in Fig. 4.1(b), the two receiver outputs $O_i(f)$ and $O_j(f)$ can be written as:

$$O_i(f) = E(f)\, EI(f)\, R_i(f) + N_i(f)\, R_i(f)\,, \qquad receiver\ I, \tag{4.1}$$

$$O_j(f) = E(f)\, EI(f)\, H_{ij}(f)\, R_j(f) + N_j(f)\, R_j(f)\,, \qquad receiver\ J, \tag{4.2}$$

where $EI(f)$ is the transfer function of the medium from the excitation to receiver *I* and $H_{ij}(f)$ is the transfer function of the medium between receiver *I* and receiver *J* (the quantity of interest here). Similarly to what remarked by Roth [56] in a single-input/single-output case, the dual-output schematic system of Fig. 4.1(b) only defines a general linear dependence between the two outputs even in cases where the transfer function is not a physical transmission path. Therefore, the specific position of the excitation relative to the receivers in this discussion does not matter as long as there is sufficient energy reaching the two receivers and a linear dependence between

the two responses exists. The objective of this analysis is to compute the transfer function $H_{ij}(f)$. The time-domain Impulse Response Function $IRF_{ij}(t)$ can be then simply obtained by the inverse Fourier-Transform of $H_{ij}(f)$:

$$IRF_{ij}(t) = \frac{1}{2\pi}\int_{-\infty}^{+\infty} H_{ij}(f)e^{i2\pi f}df\,. \tag{4.3}$$

4.2.2 Cross-Correlation versus Deconvolution (as Normalized Cross-Power Spectrum)

For this comparison let us neglect the noise terms in eqs. (1) and (2). The cross-correlation operation between the two responses O_i and O_j can be computed in the frequency domain by the following cross-power spectrum:

$$\begin{aligned} Xcorr_{ij}(f) = O_i^*(f)\,O_j(f) &= E^*(f)\,EI^*(f)\,R_i^*(f)\,E(f)\,EI(f)\,H_{ij}(f)\,R_j(f) \\ &= |E(f)|^2\,|EI(f)|^2\,R_i^*(f)\,R_j(f)\,H_{ij}(f) \end{aligned} \tag{4.4}$$

where * means conjugate (i.e. time-reversed) and $|\ |^2$ are auto-correlations, which physically correspond to the energy spectra of the functions. If the two receiving transducers have the same frequency response, $R(f) = R_i(f) = R_j(f)$, Eq. 4.4 simplifies to:

$$Xcorr_{ij}(f) = |E(f)|^2\ |EI(f)|^2\,|R(f)|^2 H_{ij}(f). \tag{4.5}$$

Therefore, the cross-correlation operation computes the desired transfer function $H_{ij}(f)$ but colored by (a) the energy spectrum of the excitation $|E(f)|^2$, (b) the energy spectrum of the transfer function from the excitation to receiver I, $|EI(f)|^2$ and (c) the energy spectrum of the transducer response $|R(f)|^2$. When moving to the time domain, therefore, the cross-correlation retrieves the $IRF_{ij}(t)$ convolved, or distorted, by the autocorrelations of the excitation, of the excitation-to-receiver-I transfer function, and of the transducer response:

$$\begin{aligned} Xcorr_{ij}(t) = O_i(t) \otimes O_j(t) &= \int_{-\infty}^{+\infty} O_i(\tau)\,O_j(\tau+t)\,d\tau \\ = Acorr(E(t)) \circledast\ Acorr(EI(t)) &\circledast Acorr(R(t)) \circledast IRF_{ij}(t) \end{aligned} \tag{4.6}$$

where the symbol "⊗" means cross-correlation and the symbol "⊛" means convolution. These convolutions would simply result in a harmless scale factor if the autocorrelation functions were a Dirac delta (i.e. the energy spectra $|E(f)|^2$, $|EI(f)|^2$ and $|R(f)|^2$ were constants), which can only come from white Gaussian content. In general, however, and specifically in ultrasonic testing, $|E(f)|^2$, $|EI(f)|^2$ and $|R(f)|^2$ are not constants but always band-limited signals. Therefore, the distortions introduced in the retrieval of the system's transfer function $H_{ij}(f)$ in Eq. 4.5, or its time-domain $IRF_{ij}(t)$ in Eq. 4.6, are quite relevant and constitute a deterministic error.

Many researchers have attempted to improve the performance of the cross-correlation by computing the so called "normalized" cross-correlation where the normalization is done by the square root of the product of the two autocorrelations *at time zero*, i.e.

$$NormXcorr_{ij}\,(t) = \frac{O_i(t) \otimes O_j(t)}{\sqrt{Acorr_i(0)Acorr_j(0)}} = \frac{O_i(t) \otimes O_j(t)}{\sqrt{\sum_t O_i^2(t) \sum_t O_j^2(t)}} \tag{4.7}$$

Therefore, in this case the cross-correlation is normalized by the mean value of the signal energy at *I* and *J* (a constant scale factor, not dependent on frequency or shape of the signals). This metric simply scales the cross-correlation to bound it to the interval [-1,1]. It only makes quantitative sense at ±1 (full correlation between O_i and O_j) and 0 (no correlation). Besides these values, the normalized cross-correlation of Eq. 4.7 does not provide a more quantitative comparison of the signals than the traditional cross-correlation of Eqs. 4.7 or 4.6 and therefore leads to the same distortions of the pure $IRF_{ij}(t)$ that is being reconstructed.

A better reconstruction of the pure $H_{ij}(f)$ (and therefore $IRF_{ij}(t)$) can be obtained by using a deconvolution operation, implemented as the cross-power spectrum of the two responses at *I* and *J*, normalized by the auto-power spectrum of the response at *I* (Normalized Cross-Power Spectrum or *NCPS*):

$$Deconv_{ij}(f) = \frac{O_j(f)}{O_i(f)} = NCPS_{ij}(f) = \frac{O_i^*(f)O_j(f)}{O_i^*(f)O_i(f)} \tag{4.8}$$

By using eqs. (1) and (2), again neglecting the noise terms and assuming the same frequency response for the two receivers, $R(f)$, this metric becomes:

$$NCPS_{ij}(f) = \frac{O_i^*(f)O_j(f)}{O_i^*(f)O_i(f)} = \frac{|E(f)|^2\ |EI(f)|^2\ |R(f)|^2\ H_{ij}(f)}{|E(f)|^2|EI(f)|^2|R(f)|^2} = H_{ij}(f). \tag{4.9}$$

Hence in an ideal case (no noise) the normalized cross-power spectrum *NCPS* results in the reconstruction of the system's pure transfer function without any distortions.

4.2.3 Noise Mitigation

Only the coherent and linear portion of the signals recorded at receivers *I* and *J* is of interest to reconstruct $H_{ij}(f)$ and $IRF_{ij}(t)$. The "noise" terms $N_i(f)$ and $N_j(f)$ in eqs. (1) and (2), containing incoherent arrivals or system nonlinearities, should therefore be minimized or eliminated. For this purpose, ensemble averages of the numerator and the denominator of the *NCPS* metric must be taken to exploit the fact that the expectation of the cross-power spectrum of two uncorrelated, zero-DC signals S_1 and S_2 is zero, or:

$$\langle S_1^*(f)\ S_2(f)\rangle = 0. \tag{4.10}$$

Considering the general output expressions in eqs. (1) and (2), and assuming the two receivers having the same frequency response $R(f) = R_i(f) = R_j(f)$, the ensemble averaged Numerator and Denominator of the *NCPS* from Eq. 4.9 in the presence of noise become:

$$\begin{aligned} Num = \langle O_i^*(f)\ O_j(f)\rangle &= \langle |E(f)|^2\ |EI(f)|^2\ |R(f)|^2\ H_{ij}(f)\rangle + \langle E^*(f)\ EI^*(f)\ |R(f)|^2\ N_j(f)\rangle \\ &+\langle E(f)\ EI(f)\ |R(f)|^2\ H_{ij}(f)\ N_i^*(f)\rangle + \langle N_i^*(f)\ N_j(f)\ |R(f)|^2\rangle \\ &= |E(f)|^2\ |EI(f)|^2\ |R(f)|^2\ H_{ij}(f), \end{aligned} \tag{4.11}$$

$$\begin{aligned} Den = \langle O_i^*(f)\ O_i(f)\rangle &= \langle |E(f)|^2\ |EI(f)|^2\ |R(f)|^2\rangle + \langle E^*(f)\ EI^*(f)\ |R(f)|^2\ N_i(f)\rangle \\ &+\langle E(f)\ EI(f)\ |R(f)|^2\ N_i^*(f)\rangle + \langle |N_i(f)|^2\ |R(f)|^2\rangle \\ &= |E(f)|^2\ |EI(f)|^2\ |R(f)|^2 + |N_i(f)|^2\ |R(f)|^2 \end{aligned} \tag{4.12}$$

In the above expressions, the terms $\langle E^*(f)\, EI^*(f)\, |R(f)|^2 N_j(f)\rangle$, $\langle E(f)\, EI(f)\, |R(f)|^2\, H_{ij}(f)\, N_i^*(f)\rangle$, $\langle E^*(f)\, EI^*(f)\, |R(f)|^2 N_i(f)\rangle$, and $\langle E(f)\, EI(f)\, |R(f)|^2\, N_i^*(f)\rangle$ vanish since the noise terms $N_i(f)$ and $N_j(f)$ are uncorrelated with $E(f)$, $EI(f)$ or $H_{ij}(f)$, and the term $\langle N_i^*(f)\, N_j(f)\, |R(f)|^2\rangle$ vanishes since $N_i(f)$ and $N_j(f)$ are uncorrelated with one another. Also, the $|\ |^2$ terms in eqs. (11)-(12) now represent power spectra, rather than energy spectra, because averaged. These simplifications result in the following ensemble averaged *NCPS*:

$$NCPS_{ij}(f) = \frac{\langle\, O_i^*(f) O_j(f)\rangle}{\langle\, O_i^*(f) O_i(f)\rangle} = \frac{Num}{Den} = \frac{|E(f)|^2\, |EI(f)|^2\, H_{ij}(f)}{|E(f)|^2\, |EI(f)|^2 + |N_i(f)|^2}. \tag{4.13}$$

This result shows that, in the most general case that includes uncorrelated noise at the two receivers, even the ensemble averaged *NCPS* cannot exactly isolate the pure transfer function $H_{ij}(f)$ because of the presence of the power spectrum of the noise at receiver *I*, $|N_i(f)|^2$. If this noise is negligible, then $NCPS_{ij}(f) = H_{ij}(f)$ and the pure transfer function is retrieved. If instead this noise is not negligible but rather white Gaussian, then $|N_i(f)|^2$ is a constant (and equal to the noise variance). Interestingly, in this case this constant term helps to stabilize the *NCPS* metric by avoiding extremely small values in the autocorrelation term at the denominator. This stabilization is in fact purposely added in many applications of the *NCPS* for passive transfer function extraction, particularly in the seismic interferometry field (e.g. [35]-[37] and many others). In these works, the transfer function is in fact computed using an operator similar to a Wiener filter:

$$H_{ij}(f) = \frac{\langle\, O_i^*(f) O_j(f)\rangle}{\langle\, O_i^*(f) O_i(f)\rangle + \alpha\langle\, O_i^*(f) O_i(f)\rangle} \tag{4.14}$$

where the "regularization term" α is artificially introduced as a small percentage (e.g. 0.5%) of the averaged power spectrum at receiver *I* to "stabilize the deconvolution", analogously to what recommended as early as the 1970's for the deconvolution analysis of seismic waves [60]. The interesting result of Eq. 4.13 is that the incoherent noise at receiver *I* can serve naturally as such

regularization parameter to stabilize the *NCPS* transfer function extraction. Following the $H_{ij}(f)$ computation, the time-domain $IRF_{ij}(t)$ can then be computed from the inverse Fourier Transform of Eq. 4.3.

4.2.4 Segmental Averages versus Long Time Averages

In much literature on the passive extraction of a system's transfer function (whether using cross-correlations of diffuse ultrasonic fields or deconvolutions of seismic interferometry waves) the averaging is performed by simply relying on an integral over a long recording time windows. On the contrary, the necessity to perform segmental averaging using windowed overlapping segments to properly minimize incoherent noise has been established since the 1960s for FFT-based spectral estimations [57]-[59]. This procedure, schematized in Fig. 4.2, involves (a) dividing the entire time recording window into multiple overlapping time segments, (b) zero-padding and windowing each time segment, (c) computing the Fast-Fourier Transforms (FFTs) for each segment, and finally (d) averaging the FFTs for the Numerator and the Denominator of the *NCPS* metric per Eq. 4.13. Fig. 4.3 demonstrates the importance of the segmental averages on synthetically produced "passive" signals affected by noise. Fig. 4.3(a) simulates the arrivals of a 1 MHz, 5-cycle Hanning-windowed toneburst at two receivers *I* and *J* separated by an 8 μs delay. White Gaussian noise at a level of 10% of the tonebursts' Root Mean Square has been artificially added to the signals. Fig. 4.3(b) compares the reconstructed $IRF_{ij}(t)$, computed as the inverse Fourier Transform of the $NCPS_{ij}(f)$, when using segmental averages (50 μs-wide Hamming-windowed segments with 50% overlap) according to Eq. 4.13, or when using no averages according to Eq. 4.9. The coherent $IRF_{ij}(t)$ arrival is clearly seen at the 8 μs delay, but the incoherent noise following the arrival is only suppressed when using the segmental averaging. In an imaging application, the later signal contamination may of course result in an increased noise floor for the image and even artifacts. A similar result for the same synthetic

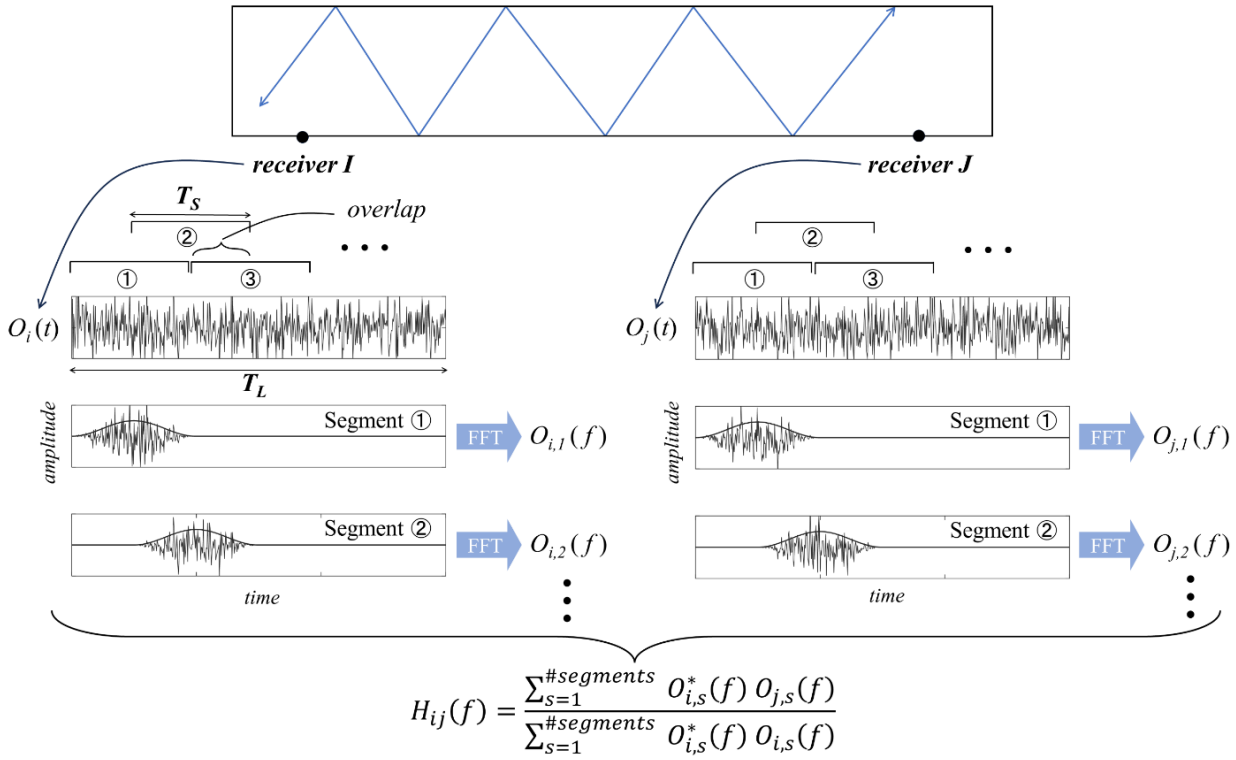

Figure 4.2: Segmental averaging for the computation of the normalized cross-power spectrum for passive transfer function reconstruction in a manner that is robust against incoherent noise and nonlinearities. The final transfer function expression is shown at the bottom as the averaged sum of each segment.

tone burst signals is obtained in Fig. 4.3(c) when comparing the reconstructed $IRF_{ij}(t)$ from the segmental averaged $NCPS_{ij}(f)$ of Eq. 4.13 to the result from the Normalized Cross-Correlation $NormXcorr_{ij}(t)$ of Eq. 4.7 that only relies on the cross-correlation integral over the entire signal duration. Noise suppression is again best achieved with the segmental averaged $NCPS_{ij}(f)$.

The control parameters in the ensemble segmental averaging process are (1) the width of each time segment (T_S in Fig. 4.2), (2) the segment overlap and (3) the length of the total recording time window (T_L in Fig. 4.2). Regarding parameter (1) (segment width), decreasing T_S results in increased averages, theoretically leading to better transfer function estimations (since the *SNR* is related to $\sqrt{\#averages}$). However, the segment width must be large enough to include the same coherent arrivals at both of the receivers *I* and *J* for both causal and acausal times, an important aspect that

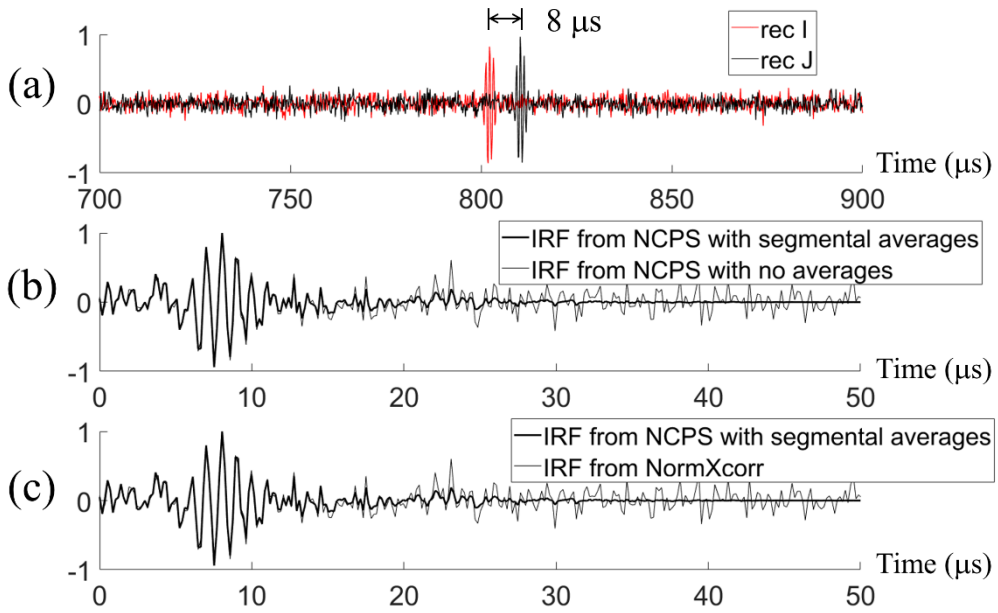

Figure 4.3: (a) Synthetic tone burst arrivals at receivers *I* and *J* with an 8 μs delay and noise added. (b) Reconstructed $IRF_{ij}(t)$ from $NCPS_{ij}(f)$ using segmental averages (Eq. 4.13) and no averages (Eq. 4.9). (c) Reconstructed $IRF_{ij}(t)$ from segment-averaged $NCPS_{ij}(f)$ (Eq. 4.13) and from $NormXcorr_{ij}(t)$ (Eq. 4.7).

applies solely to the present dual-output reconstruction. Since there is no guarantee that a given segment will actually fall in a perfect time window that simultaneously includes the two coherent arrivals, and also given the window function is applied to the segment, it seems reasonable to set the segment width T_S equal to 3 to 5 times the largest expected arrival time difference at the two receivers. For the subject ultrasonic imaging application, this time difference can be estimated, for example, by the time of flight of the backwall reflection expected at receiver *J* when receiver *I* acts as the virtual source. Regarding parameter (2) (segment overlap), Carter et al. [57] showed that the improvement in Magnitude-Squared Coherence (MSC) estimation stabilizes after a certain amount of overlap, with a 62.5% overlap reaching the limit of improvement that is already mostly achieved with a 50% overlap. Hence a 50% segment overlap seems like a practical choice. Regarding parameter (3) (total recording time length), it has been long known in passive transfer function reconstruction that a longer recording window improves the estimation. In underwater acoustic applications (e.g. [26]), the *SNR* of the

passively reconstructed Green's function from cross-correlations of diffuse fields was found proportional to $\sqrt{T_L}$. A similar relationship has been established in *IRF* reconstruction from *NCPS* of reverberating waves in seismic interferometry for buildings (e.g. [33]). Clearly, in the application at hand of sparse-transmission ultrasonic imaging with a goal for high-speed performance, the recording time must be kept reasonably small. As the results that follow will show, if the segmental averaging process described above is applied appropriately, the total recording time window can be kept surprisingly small for a satisfactory reconstruction of the virtual FMC set of *IRF*s.

4.2.5 Causal versus Acausal Impulse Response Function Reconstruction

Whether using cross-correlations or normalized cross-power power spectrum for dual-output passive *IRF* reconstruction, it is possible to extract both the causal signal (equivalent to a virtual excitation at *I* and reception at *J*) found in the positive times of IRF_{ij}, and the acausal signal (equivalent to a virtual excitation at *J* and reception at *I*) found in the negative times of IRF_{ij}:

$$IRF_{ij}(t) + IRF_{ij}(-t) = causal + acausal = IRF_{ij}(t) + IRF_{ji}(t). \qquad (4.15)$$

For reciprocity, in the absence of nonlinearities, the causal and acausal signals should be the same, hence $IRF_{ij}(t) = IRF_{ji}(t)$. This theoretical equality has been employed in the past for various purposes, whether to determine the convergence of the passively reconstructed transfer function in seismic interferometry [35], [52], or to eliminate half of the FMC matrix in ultrasonic imaging with diffuse fields [54], [55].

While the causal-acausal equality holds for the theoretical "pure" *IRF*, in a practical measurement scenario, however, the passively reconstructed causal IRF_{ij} and acausal IRF_{ji} are generally different for various reasons. One reason is the incoherent noise content that can affect differently the $I \rightarrow J$ wave path and the $J \rightarrow I$ wave path. Another reason, that was also noticed in underwater acoustics [61], SHM [53] and seismology [34], is the non-isotropic or directional excitation

sources that cause an "imbalance" between IRF_{ij} and IRF_{ji} because of the preferred wave propagation direction. Reference [61], for example, dealing with cross-correlation passive reconstructions of underwater acoustic responses using linear arrays, conclude that only the "on-axis" sources ("within ±20º of the array endfire direction") contribute to the long-time averaged *IRF* while the "off-axis" sources create only the incoherent fluctuations in the reconstruction. A third reason why the reconstructed causal and acausal responses in a practical dual-output measurement may be different are the different frequency responses of the two receiving transducers. In fact, using the framework of Fig. 4.1, and assuming receiver responses $R_i(f) \neq R_j(f)$ and no noise, the *IRF* calculated for $I \rightarrow J$ will be different from that calculated for $J \rightarrow I$ because of the different normalization at the denominator of the *NCPS*:

$$IRF_{ij}(t) = F^{-1}(NCPS_{ij}(f)) = F^{-1}\left(\frac{O_i^*(f)O_j(f)}{O_i^*(f)O_i(f)}\right) = F^{-1}(H_{ij}(f)\frac{R_j(f)}{R_i(f)}), \qquad I \rightarrow J, \quad (4.16)$$

$$IRF_{ji}(t) = F^{-1}(NCPS_{ji}(f)) = F^{-1}\left(\frac{O_j^*(f)O_i(f)}{O_j^*(f)O_j(f)}\right) = F^{-1}(H_{ji}(f)\frac{R_i(f)}{R_j(f)}), \qquad J \rightarrow I, \quad (4.17)$$

where F^{-1} means inverse Fourier Transform. Hence the "pure" $H_{ij}(t)$ is convolved with $R_j(f)/R_i(f)$, whereas the "pure" $H_{ji}(t)$ is convolved with $R_i(f)/R_j(f)$. These ratios are not just constant scale factors, but filters on the *IRF*s that are a function of frequency. Hence the causal (positive times) portion of $IRF_{ij}(t)$ will not be equal to the acausal portion of $IRF_{ji}(t)$ (negative times), and vice versa.

In summary, all of these considerations lead to the following conclusion that applies in general to passive reconstruction of *IRF*'s, and especially when the sources are anisotropic or directional (which happens in almost all realistic cases where the wavefield is not perfectly "diffuse"): each of the four reconstructions, i.e. positive and negative times of $IRF_{ij}(t)$ from Eq. 4.16, and positive and negative times of $IRF_{ji}(t)$ from Eq. 4.17, are different "colored" versions of the "pure" *IRF* between *I* and *J*.

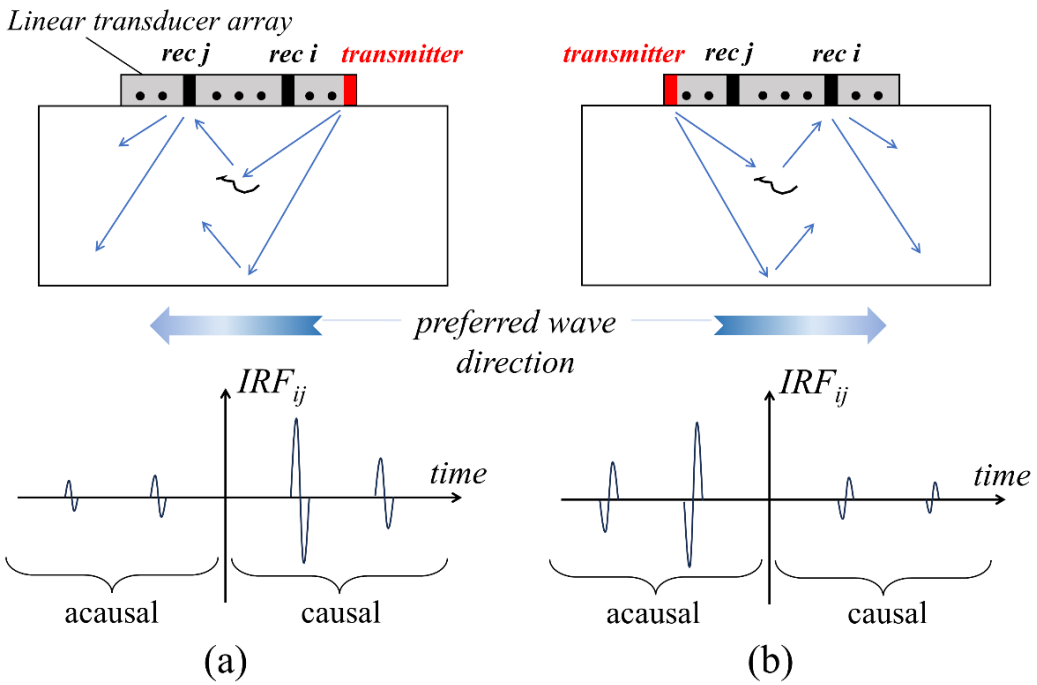

Figure 4.4: Effect of directional excitation in passive *IRF* reconstruction at two receiver elements (*i* , *j*) of a transducer array. (a) Physical excitation at right-edge of the array causes predominantly causal IRF_{ij} response. (b) Physical excitation at left-edge of the array causes predominantly acausal IRF_{ij} response.

In the ultrasonic imaging application at hand, the excitation from any single element of the transducer array will be necessarily highly anisotropic or directional for some (or most) of the receiving element pairs (see Fig. 4.4). It is therefore wise to average in postprocessing all four of these *IRF*s so as to maximize image quality while keeping a minimum number of excitations. This means, for each transducer element pair (*i* , *j*) considered as the two receivers, computing independently $NCPS_{ij}$ and $NCPS_{ji}$, each *NCPS* being normalized by a different auto-power spectrum (of the *i* response and of the *j* response). By combining all four signals, we are sure to include in the beamforming process the stronger of the *IRF* that can be reconstructed from *all* (*i* , *j*) element pairs, regardless of the relative strength of the transducer frequency responses and regardless of the preferred direction of the coherent waves generated by the individual excitations.

4.3 Application of Passive IRF Reconstruction to Ultrasparse SAFT Imaging

4.3.1 Experimental Procedure and Beamforming Algorithm

This section will apply the considerations made in section II to demonstrate ultrasparse ultrasonic SAFT with FMC image quality performance. For this study, a 5 MHz linear 64-element transducer array (Olympus model #NDT 5L64-A12, 0.6 mm interelement spacing) was utilized to image in 2D artificial reflectors in two 56 mm thick aluminum blocks. An OEM-PA Mini 64×64 by Advanced OEM Solutions (West Chester, OH, USA) was used as the signal multiplexer. The reflectors were, respectively: (a) a single 2 mm-diameter hole at a depth of 12.5 mm from the first block's surface, (b) another single 2 mm-diameter hole at a depth of 20 mm from the second block's surface, and (c) two closely spaced 2 mm-diameter holes spaced at a lateral distance of 6 mm at a depth of 11 mm from the first block's surface.

The beamforming algorithm utilized was the classical time back-propagation method implemented in the FMC mode. Crucially, the "virtual" FMC was here obtained by employing a minimum number of physical transmitters (as few as a single element and as many as four elements, hence "ultra-sparse" transmit modality), and exploiting the passively-reconstructed IRF_{ij} from each of the possible (i, j) combinations of elements used solely as receivers. More specifically, according to the discussion in Section II-E, for each receiver pair (i, j) the $IRF_{ij}(t)$ for $i \rightarrow j$ and the $IRF_{ji}(t)$ for $j \rightarrow i$ were computed separately, i.e. with different auto-power spectra in the denominator of the segment-averaged NCPS of Eq. 4.13. A traditional Hanning window was used as an apodization weight on the reception array.

After averaging for each physical transmission, k, the image was then formed as the following 64×64 "virtual" full matrix:

$$I(x,y) = \sum_{\substack{i=1 \\ \uparrow \\ rec.}}^{64} \sum_{\substack{j=1 \\ \uparrow \\ rec.}}^{64} \sum_{\substack{k=1 \\ \uparrow \\ trans.}}^{1,2,3\ or\ 4} w_{ij} IRF_{ij,k}\left(\tau_{ij,xy}\right). \tag{4.18}$$

In the above equation, w_{ij} are the apodization weights and $\tau_{ij,xy}$ are the backpropagation times, i.e. the travel times of the wave from the "virtual" transmitter i positioned at (x_i , y_i) to the focus point positioned at (x , y) and back to the receiver j positioned at (x_j , y_j). These travel times can be written as:

$$\tau_{ij,xy} = \frac{\sqrt{(x_i - x)^2 + (y_i - y)^2}}{v_{L,S}} + \frac{\sqrt{\left(x_j - x\right)^2 + \left(y_j - y\right)^2}}{v_{L,S}}. \tag{4.19}$$

Each beamformed image was computed from the analytical signal representation of the IRF_{ij}(t) waveforms. Hence each reconstructed waveform was Hilbert transformed to compute its in-phase (I) and quadrature-phase (Q) components, and the final image envelope was constructed as the modulus $\sqrt{I^2 + Q^2}$.

In Eq. 4.19 the velocity of the longitudinal wave mode (v_L) and that of the shear wave mode (v_S) have been explicitly separated to consider images created from multiple wave mode combinations. As discussed in Section I, wave mode compounding has been recently proposed when imaging solid media to significantly increase dynamic range without increasing the array's physical aperture. In general, up to four wave mode combinations can be compounded: (1) *L*-wave transmitted and *L*-wave reflected (*LL* combination), (2) *L*-wave transmitted and *S*-wave reflected from mode conversion (*LS* combination), (3) *S*-wave transmitted and *L*-wave reflected from mode conversion (*SL* combination), and (4) *S*-wave transmitted and *S*-wave reflected (*SS* combination). Mode compounding was here implemented by incoherent addition of each of the individual images according to:

$$I_{comp}(x,y) = \sum_{MC=LL,LS,SL,SS} I^{MC}(x,y) \tag{4.20}$$

where $I^{MC}(x,y)$ (dB normalized by the respective maxima) are the individual mode combination images. As it will be shown in the next sections, mode compounding is particularly beneficial when attempting "ultrasparse" transmissions. Among other advantages, for example, since a point source excitation (similarly to a single element of the transducer array) will generate *L*-waves preferentially on-axis and *S*-waves preferentially off-axis, combining both wave modes provides a better coverage of the entire field of view.

4.3.2 Active IRF vs. Passive Cross-correlation IRF vs. Passive NCPS IRF

Fig. 4.5 compares the *IRF*s obtained when probing the 12.5 mm deep single hole reflector in the aluminum block using two transducer array elements i = #28 and j = #37 located symmetrically with respect to the center of the 64-element array, in the cases of (a) conventional "active" excitation, (b) passive reconstruction using the cross-correlation $Xcorr_{ij}(t)$ of Eq. 4.6, and (c) passive reconstruction using the inverse Fourier Transform of the normalized cross-power spectrum with segmental averages $NCPS_{ij}(f)$ of Eq. 4.13. For the last two cases of passive reconstruction, the physical excitation was provided by either a transmitter element in the center of the array (k = #32) or a transmitter element at the right edge of the array (k = #1). Also, for the passive reconstructions the total recording window was of length T_L = 400 μs with a start time of 2 μs after firing to limit the initial electronic crosstalk. The segment window width for the averaging of the *NCPS* was T_S = 60 μs which was selected between 3 and 4 times the arrival time of the first *L*-wave backwall reflection expected at ~18 μs for source (active or virtual) at element #28 and receiver at element #37. The segment overlap was 50%.

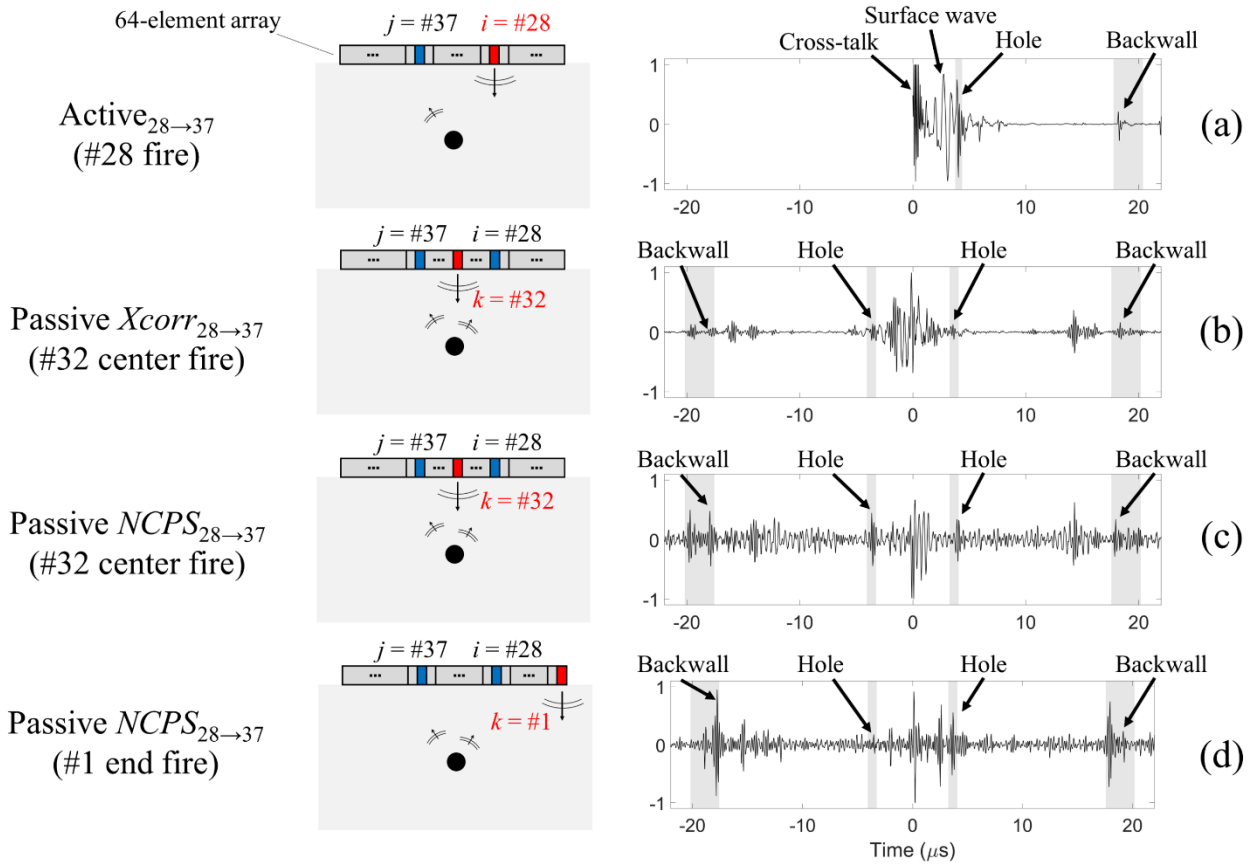

Figure 4.5: Impulse Response Functions for the drilled block obtained using two transducer array elements i = #28 and j = #37 for (a) conventional "active" excitation (#28 fires), (b) passive reconstruction using the cross-correlation (#32 fires), (c) passive reconstruction using the segment-averaged NCPS (#32 fires), and (d) same as (c) but with #1 fire.

The active 28 → 37 *IRF* waveform is shown in Fig. 4.5(a) for only the available causal domain (positive times). The active signal shows the hole reflection at the expected ~4 μs but merged with a significant early surface-wave arrival and following the initial crosstalk. The backwall reflection is also seen at ~18 μs. The passive waveform computed from the cross-correlation $Xcorr_{28\rightarrow37}(t)$ using the central element #32 as the excitation is shown in Fig. 4.5(b) in both causal and acausal domains. The cross-correlation reconstruction does not show clearly either the hole reflection or the backwall reflection, in part due to the limited recording time window of 400 μs that was purposely kept rather short with fast imaging performance in mind. The passive $IRF_{28\rightarrow37}(t)$

computed from the segment-averaged $NCPS_{28\rightarrow37}(f)$ for the same element #32 excitation is shown in Fig. 4.5(c). In this case, the hole reflection at ~4 μs is clearly visible, the initial crosstalk is suppressed, and the spurious early surface wave is eliminated. This result is quite remarkable considering that a single excitation was utilized. The elimination of the surface wave has to do with the fact that this wave does not reverberate as much as the hole reflection, hence losing the benefits of the ensemble averaging process that instead reinforces the hole signature. A comparison of the causal and acausal signals in Fig. 4.5(c) shows that both portions contain both hole and backwall reflections, although the two contributions are not exactly the same. The causal-acausal differences indicate that the field is not perfectly diffuse (given the single transmitter and the observation time window kept short). Fig. 4.5(d) shows the passive $IRF_{28\rightarrow37}(t)$, again computed from the segment-averaged $NCPS_{28\rightarrow37}(f)$, but using the end element #1 as the physical excitation. Also, in this case the hole and backwall reflections are quite visible, highlighting the remarkable fact that valuable reconstruction results can be obtained with a single transmission regardless of the position of the physical transmitter. As expected, the reconstruction for the element #1 excitation shows more unbalance between the causal and acausal signals, with the hole for example mostly visible only in the causal portion. This unbalance is the result of the preferential "right-to-left" wave propagation direction induced by the end element excitation as presented in Fig. 4.4. Hence the necessity discussed earlier in Section II-E to average the causal and acausal portions of the reconstructed *IRF*s, regardless of the excitation position, so as to utilize the relevant information present in either of the two portions to form the final image.

4.3.3 Active FMC (all firings) vs. Passive Cross-correlation FMC (single firing) vs. Passive NCPS FMC (single firing)

Fig. 4.6 shows the images of the block with the 12.5 mm deep single hole using (a) the conventional active FMC where all elements are in turn physically transmitting, and (b)-(e) the passive reconstructions using a single element as the physical transmission (total recording window length T_L = 400 μs with a start time of 20 μs after firing). Each image is normalized in dB to the louder reflector. Zoomed-in versions of the images around the target hole are shown below each of the full images. For this comparison, the single *L*-wave mode was used for beamforming (no mode compounding). The conventional active FMC capture, using all 64 transmissions and 64 receptions (64×64 waveforms) is shown in Fig. 4.6(a). The hole and the backwall are clearly visible here. However, there is also a blind zone in the near-field at the top of the image extending for ~9 mm caused by the inter-element crosstalk and spurious surface wave arrivals as seen in the individual waveform analysis of the previous Fig. 4.5(a). In addition, the zoomed-in image of the active FMC shows a hole position that is slightly off from the ground truth, due to the difficulty in establishing the correct time zero for the actively emitted signals. Fig. 4.6(b) and (c) show the "passive" images resulting, respectively, from the cross-correlation $Xcorr_{ij}(t)$ of Eq. 4.6, and from the normalized cross-power spectrum with segmental averages $NCPS_{ij}(f)$ of Eq. 4.13, both obtained using the center array element as the physical transmitter (k = #32). In the segmental averages, the segment window was T_S = 60 μs with the usual 50% overlap. The "virtual" FMCs were therefore obtained by extracting the passive *IRF*s for all possible element combinations (i , j) under the single-element physical transmission according to Eq. 4.18. The causal and acausal passive reconstructions for each of the element pairs were averaged. Compared to the "active" image of Fig. 4.6(a), the two passive images of Fig. 4.6(b) and (c) show a significant reduction in the near-field blind zone at the top because of the suppression of the initial crosstalk and the surface waves. In addition, the zoomed-in

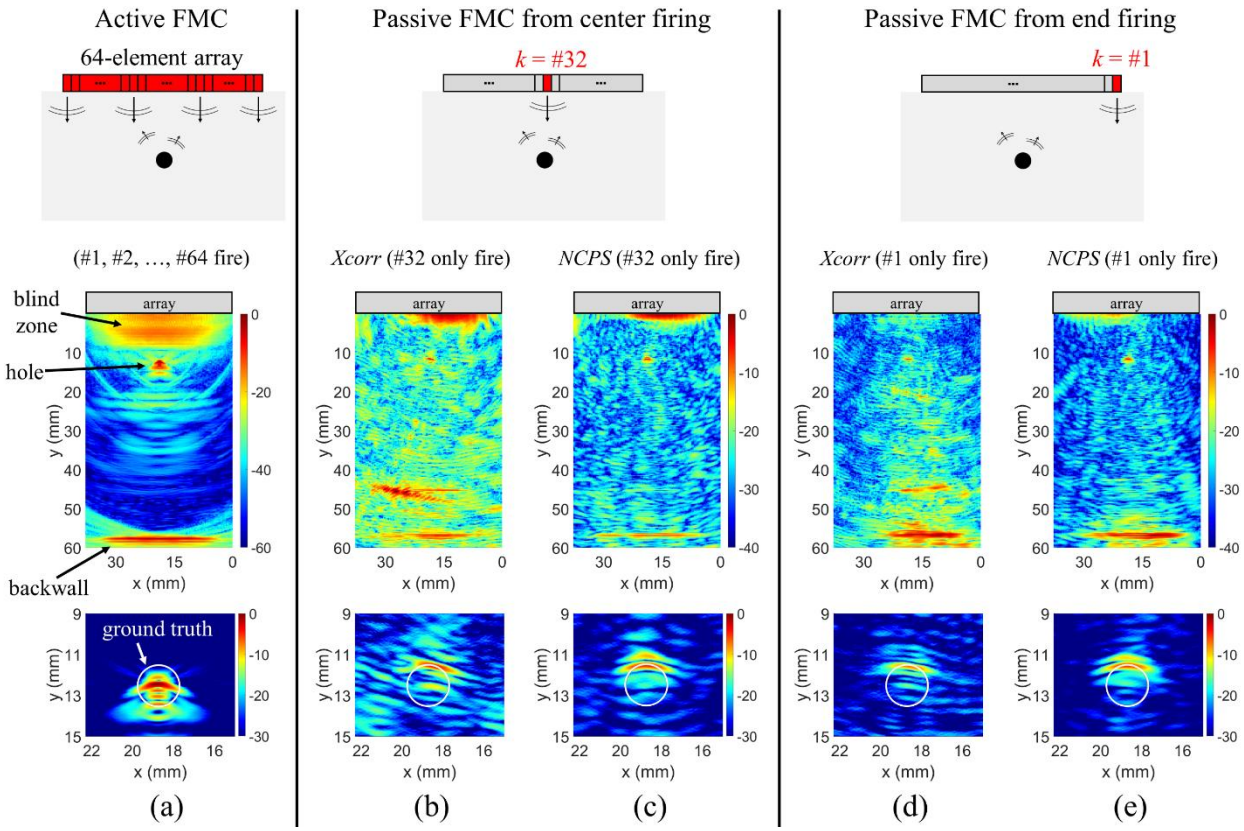

Figure 4.6: Full Matrix Capture images of the drilled block in (a) conventional active FMC (all elements fire in turn), (b) virtual FMC with cross-correlation passive reconstruction (#32 only fires), (c) virtual FMC with segment-averaged normalized cross-power spectrum (#32 only fires), (d) same as (b) but with #1 only fire, and (e) same as (c) but with #1 only fire.

passive images show the correct position of the hole reflection. The *Xcorr* image of Fig. 4.6(b) does show several artifacts and a higher noise floor compared to the *NCPS* image of Fig. 4.6(c). The zoomed-in images of the hole confirm the superior performance of the *NCPS* compared to the *Xcorr*, with a ~3 dB stronger contrast and a more extended coverage of the hole's curved top surface. The reduction of the blind zone and the accurate image of the hole in the "passive" *NCPS* approach is surprisingly remarkable considering that this was obtained with a single-element transmission. Interestingly, a similar performance of the passive image is obtained when changing the transmitting element to the right-edge of the array (k = #1), as shown in Fig. 4.6(d) and (e). The *NCPS* does a better job than the *Xcorr* with increased contrast and more extended coverage of the hole's surface.

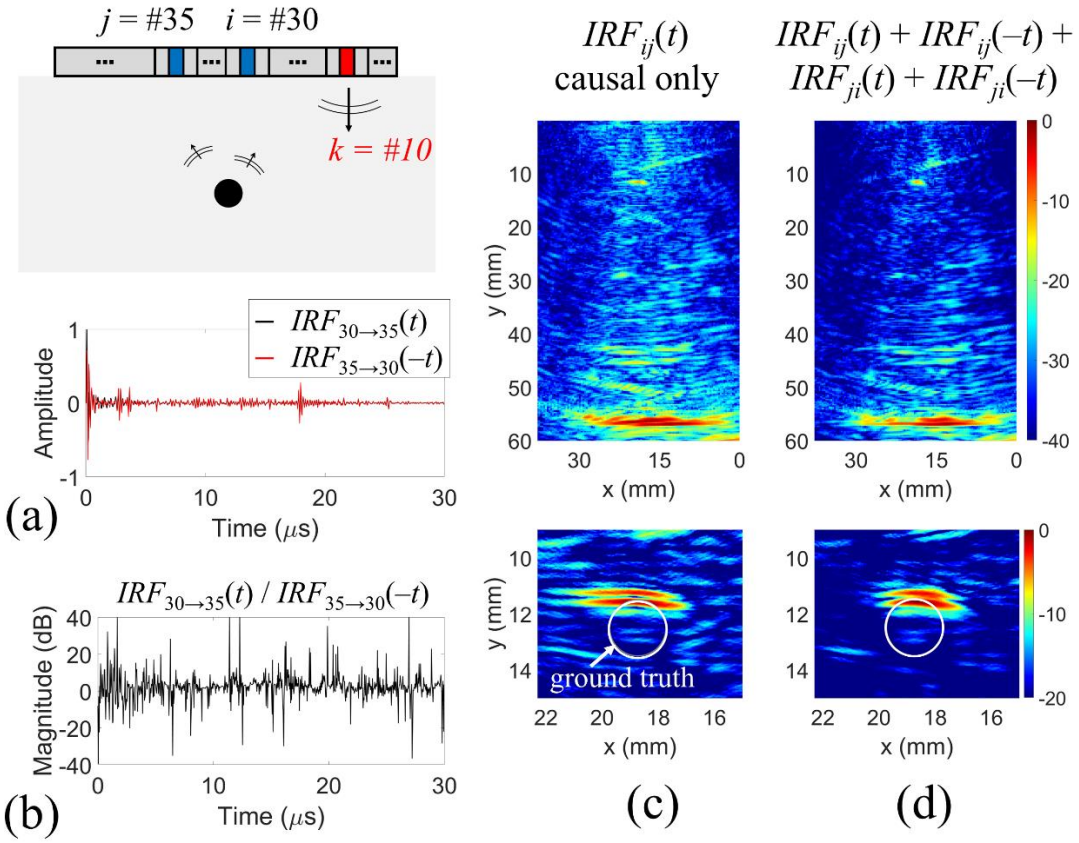

Figure 4.7: (a) *NCPS* reconstructed causal $IRF_{30\rightarrow35}(t)$ and acausal $IRF_{35\rightarrow30}(-t)$ with element #10 firing. (b) Ratio $IRF_{30\rightarrow35}(t)$ / $IRF_{35\rightarrow30}(-t)$. (c) Passive FMC image of drilled block using only causal $IRF_{ij}(t)$. (d) Passive FMC image combining causal and acausal portions of $IRF_{ij}(t)$ and $IRF_{ji}(t)$.

4.3.4 Averaging Causal and Acausal Portions of NCPS Passively Reconstructed IRFs

Fig. 4.7 demonstrates the opportunity to add causal and acausal information for best image quality from the passive *NCPS* reconstructions. A single excitation from element #10 was used with a short recording time length T_L = 120 μs for this figure. Fig. 4.7(a), for the two receivers i = #30 and j = #35, compares the causal $IRF_{ij}(t)$ from Eq. 4.16 with the acausal $IRF_{ji}(-t)$ from Eq. 4.17 showing appreciable differences, particularly in the near field at < 3 μs. These differences are better highlighted by the ratios $IRF_{ij}(t)$ / $IRF_{ji}(-t)$ plotted in Fig. 4.7(b). It was discussed in Section II-E how the difference is the result of the anisotropic or directional excitation (the case for an imperfectly

diffuse field) and the different frequency responses of the receiving elements. Hence in a sparse transmission array it is important to consider all four "passive" contributions when beamforming the image with a short recording time length. Fig. 4.7(c) shows the image of the hole reflector when using the virtual FMC using only the causal part of $i \rightarrow j$, hence $IRF_{ij}(t)$. Fig. 4.7(d) shows the same image when averaging $IRF_{ij}(t) + IRF_{ij}(-t) + IRF_{ji}(t) + IRF_{ji}(-t)$. The averaging further reduces the near-field blind zone, improves image contrast and focusing on the hole.

4.3.5 Passive FMC with Multiple Firings

This section considers multiple firing elements for the creation of the passive FMC from the segmental-averaged *NCPS* of Eq. 4.13. In this case, the final image is created by averaging all "virtual" FMC *IRF*s obtained for each transmission per Eq. 4.18. For these results, the recording window length was $T_L = 120$ μs and the segment width $T_S = 60$ μs with 50% overlap, with averaging of the causal and acausal responses. We first examine the position of the transmitters, comparing two transmitters located asymmetrically at the right end of the array (k = #1 and #2) shown in Fig. 4.8(a), with two transmitters located symmetrically at the two ends of the array (k = #1 and #64) shown in Fig. 4.8(b). The images show that both sets of transmitters provide a good image of the hole and the backwall, indicating again the robustness of the proposed passive method against changes in the physical transmitter positions. At the same time, the symmetric firings of Fig. 4.8(b) provide a slight improvement compared to the asymmetric firings of Fig. 4.8(a) in terms of increased contrast and decreased spatial resolution, as best seen in the vertical line profiles shown in Fig. 4.8(c) drawn across the middle of the images.

The next analysis examines the effect of increasing the number of transmitters beyond only two. For this study we used the Contrast-to-Noise Ratio (CNR) metric computed as [62]:

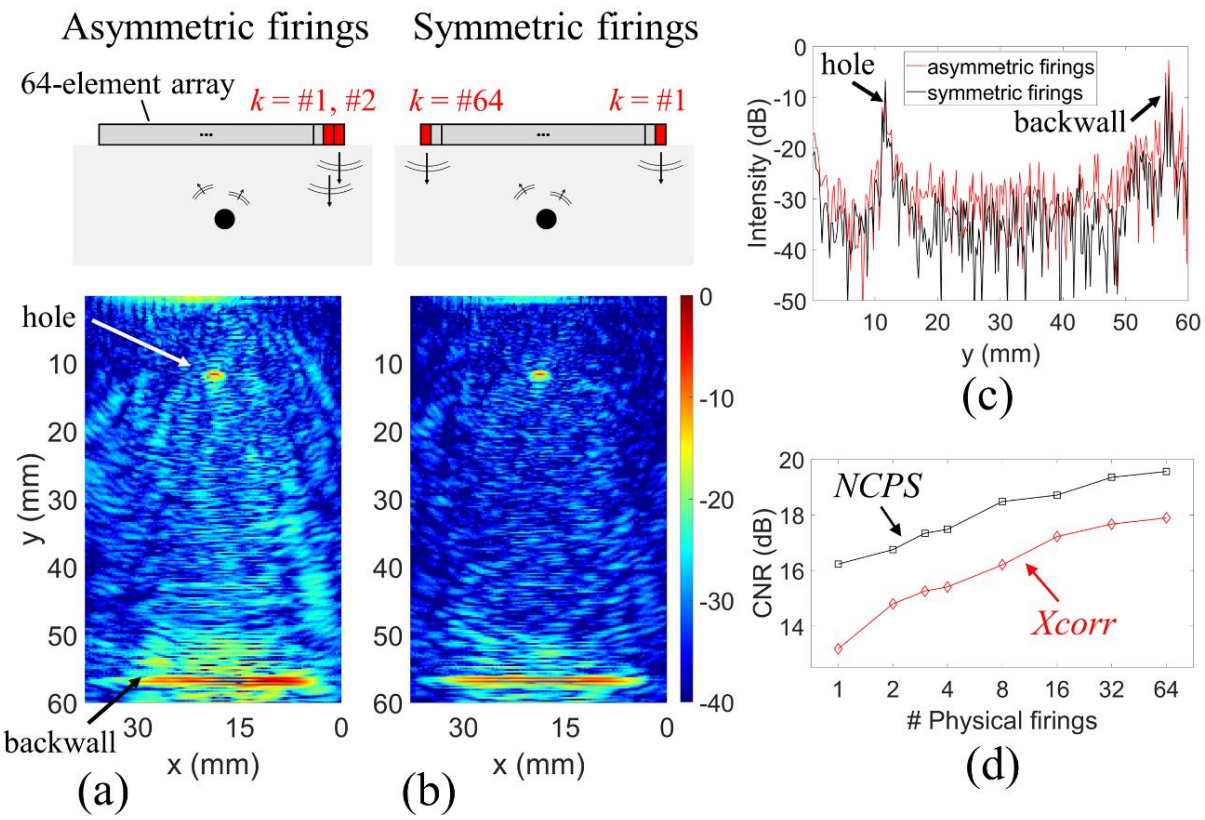

Figure 4.8: Passive imaging with multiple firings. (a) Passive FMC image of drilled block using *NCPS* and two transmitters located asymmetrically. (b) Same as (a) but using two symmetrically located transmitters. (c) Vertical line profiles in (a) and (b). (d) CNR of passive *Xcorr* images and passive *NCPS* images as a function of the number of physical firings.

$$CNR = \frac{\mu_S - \mu_N}{\sqrt{\sigma_S^2 + \sigma_N^2}}, \tag{4.21}$$

where μ_S and μ_N are the mean image magnitude in the hole scatterer and the noise floor, respectively, and σ_S and σ_N their respective standard deviations. Given that the noise floor is -20 to -30 dB below the hole reflection in our beamformed images, the pixels below -15 dB between 0 and 40 mm in depth are regarded as noise floor, to isolate the CNR computation of the drilled hole. Fig. 4.8(d) plots the *CNR* for the passive FMC images obtained from the *Xcorr* of Eq. 4.6 and the *NCPS* of Eq. 4.13. In both cases, the performance clearly improves when increasing the number of firings. However, the *NCPS* has a consistently higher performance, and especially for small number of

firings. For example, as few as 4 transmissions (ultrafast imaging capability) with *NCPS* offer a *CNR* comparable to as many as 64 transmissions (the entire array) with *Xcorr*.

4.3.6 NCPS Segment Width, Recording Time Delay and Recording Time Length

The role of segment width T_S and recording time length T_L in passively reconstructed *IRF*'s from segment-averaged *NCPS*'s was discussed theoretically Section II-D. It was proposed then to use a T_S = 3 to 5 times the expected *IRF* arrival of the target reflection as a reasonable compromise between a large number of averages and the need to include the coherent arrivals at the two receivers within each segment. Fig. 4.9 compares the passive FMC images of the drilled block using the averaged *NCPS* with segment widths T_S = 30 μs, 60 μs and 120 μs. The images were obtained by averaging three firings from elements # 1, #32 and #64 and using a total recording window T_L = 120 μs. When T_S = 120 μs, therefore, a single segment was used (i.e. no segmental averaging). Considering solely the *L*-mode for this comparison, the hole reflection is expected at ~4 μs and the backwall reflection at ~18 μs. Hence, according to our rule of thumb T_S = 3 to 5 times the expected arrival, T_S = 30 μs is appropriate for the hole but too short for the backwall. Accordingly, the backwall reflection is found to be weak in the image of Fig. 4.9(a). Increasing the segment width to T_S = 60 μs improves the backwall contrast as seen in the image of Fig. 4.9(b). A further increase to T_S =120 μs, however, increases the noise floor and creates artifact line reflections (e.g. at a depth of ~45 mm) as seen in Fig. 4.9(c). The vertical line profiles of the three images are plotted in Fig. 4.9(d), which confirm that the shorter T_S = 30 μs increases the contrast for the hole but decreases the contrast for the backwall. Vice versa, the longer T_S = 60 μs increases the contrast for the backwall at the expense of a slightly smaller contrast for the hole because of the reduced averages. T_S = 120 μs is too large, increasing noise because of the absence of averages. In summary, the results of Fig. 4.9 confirm the rule of thumb proposed in Section II-D for a reasonable segment width.

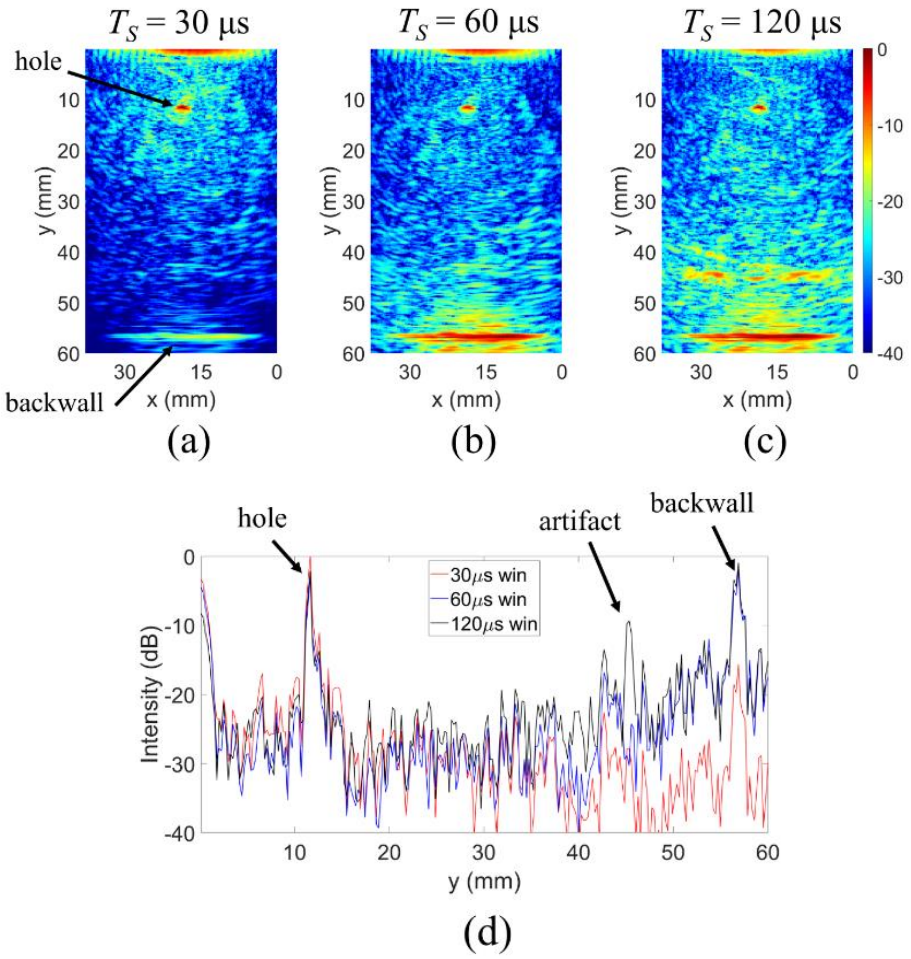

Figure 4.9: Role of segment width T_S in passive imaging using segment-averaged *NCPS*. Passive FMC images of the drilled block obtained with three firings for (a) T_S = 30 µs, (b) T_S = 60 µs, and (c) T_S = 120 µs. (d) Vertical line profiles across the middle of the images in (a), (b), and (c).

Regarding the recording time length T_L, it is quite customary in passive reconstruction of *IRF*s in underwater acoustics, structural monitoring (e.g. [53]) and even ultrasonic imaging [54], [55] to apply a significant initial time delay, T_i to the recordings in order to eliminate the initial strong arrivals. This delay is imposed in an effort to avoid the initial strong arrivals disproportionately affecting the passively reconstructed *IRF* at the expense of finding the diffuse field in the "coda" of the signals, as schematized in Fig. 4.10(a). This effort may be worthwhile when long recording times are allowed by the application and/or when the active transmissions are remote from the reflectors

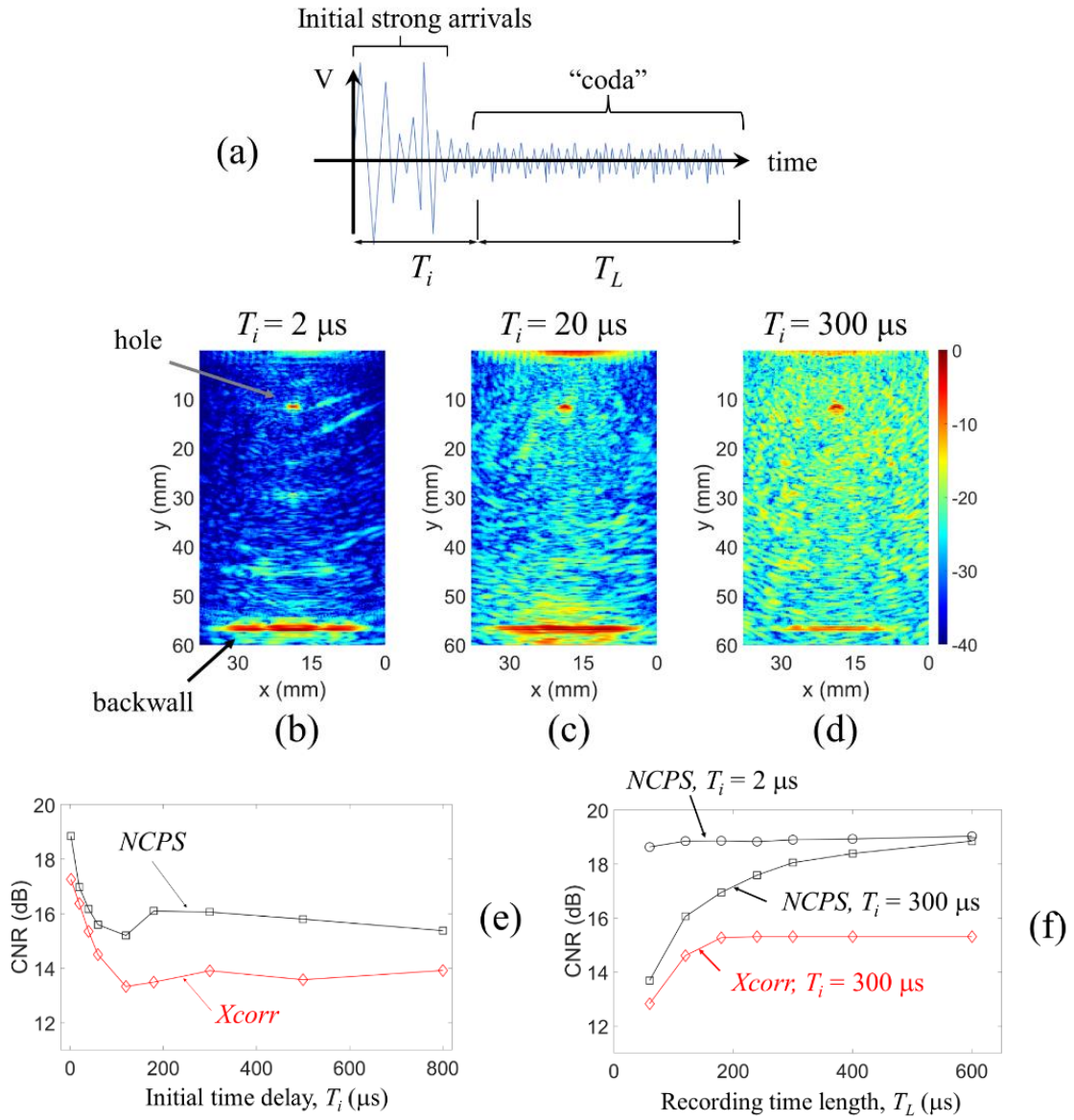

Figure 4.10: Role of initial time delay T_i and recording time length T_L in passive imaging. (a) Initial arrivals and coda waves. Passive FMC images of drilled block from averaged *NCPS* for (b) T_i = 2 µs, (c) T_i = 20 µs, and (d) T_i = 300 µs. (e) CNR of *Xcorr* images and *NCPS* images as a function of initial time delay. (f) Same as (e) but as a function of recording time length.

of interest. In the present effort, however, the requirement for "diffuse" fields is greatly relaxed because all that is needed for imaging is a few coherent arrivals between the two receivers *i* and *j* that have interacted with the target reflectors. This requirement for passive fields is further relaxed by the averaging of the causal and acausal portions of the reconstructed signals, as discussed above.

Our results therefore do not require monitoring a long coda of the waveforms (it was discussed how keeping a short T_L is of interest for fast imaging). Actually, in our case cutting out the initial strong arrivals is detrimental because it eliminates useful coherent information, as demonstrated in the results of Fig. 4.10. In this figure we compare three images obtained with increasing initial time delays, for the segmental averaged *NCPS* reconstruction of the virtual FMC for the single hole drilled block. Specifically, the following delays are examined: T_i = 2 μs (i.e. suppressing some of the initial crosstalk but including the first hole reflection) in Fig. 4.10(b), T_i = 20 μs (i.e. eliminating the first hole reflection) in Fig. 4.10(c), and T_i = 300 μs (i.e. considering solely the wave coda) in Fig. 4.10(d). For all cases, the total recording time following the delay was T_L = 120 μs, the segment width was T_S = 60 μs with 50% overlap, and the physical excitation was again provided by firing elements #1, #32 and #64. The images show that the shortest T_i = 2 μs produces the highest contrast and focus for both the hole and the backwall, while also suppressing the near field blind zone. The intermediate delay T_i = 20 μs significantly raises the noise floor of the image and does not suppress the near-field blind zone as well. The longest delay T_i = 300 μs results in the worst performance, with significant noise added to the image. Hence for the passive imaging configuration proposed, where the few physical transmitters are elements of the same receiving transducer array, the best results are obtained by retaining the initial reflections with a minimum initial delay.

An additional analysis is presented in Fig. 4.10(e) where the *CNR* of the images is plotted as a function of the initial time delay for both the *Xcorr* reconstruction and the averaged *NCPS* reconstruction. As expected, the latter operation yields overall improved results regardless of T_i. The plots also show that field stabilization occurs after T_i ~120 μs for both methods. However, the best *CNR* performance is obtained with the shortest T_i that includes the first hole reflection hence without requiring field stabilization. Fig. 4.10(f) examines the role of the total recording time length, T_L, on

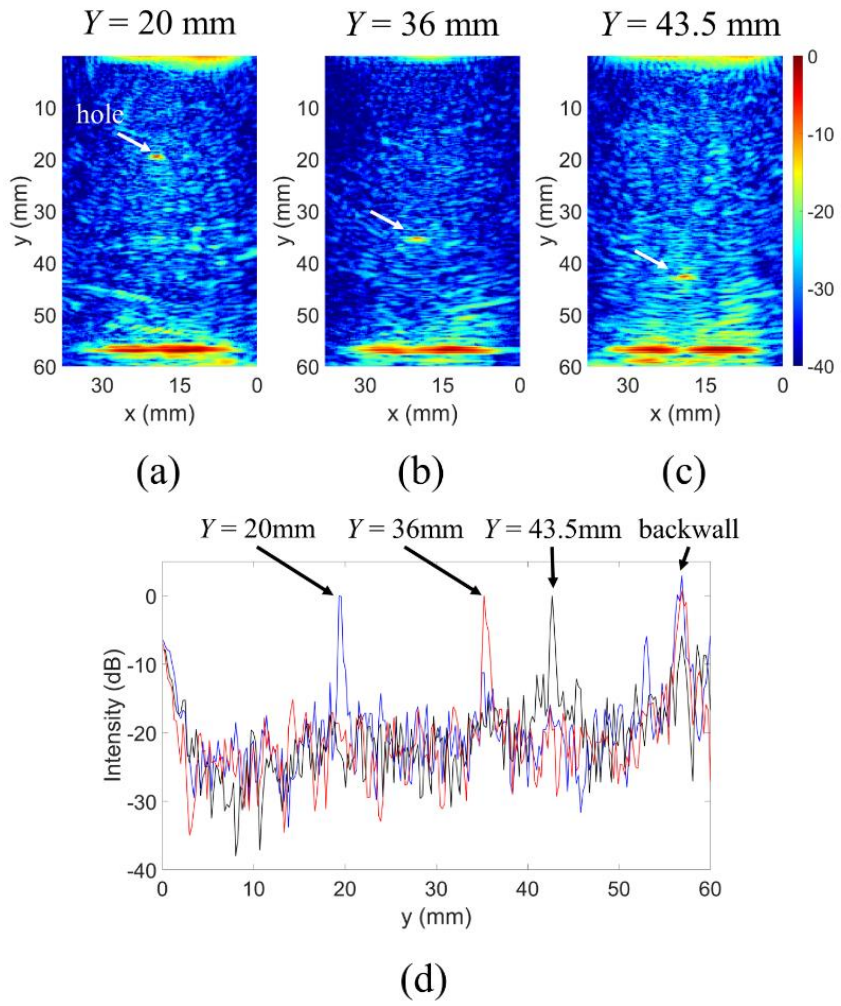

Figure 4.11: Effect of the depth of a single drilled hole on image quality. Tested holes drilled at (a) Y = 20 mm, (b) Y = 36 mm, (c), Y = 43.5 mm. (d) Vertical line profiles by normalizing with respect to maximum intensity of the hole reflections in (a), (b), and (c).

the *CNR*. The plots compare the *Xcorr* and averaged *NCPS* reconstructions with T_i = 2 μs (including first arrivals) and T_i = 300 μs (coda waves only). When using coda waves only, the performance improves with increasing total recording time, but the improvement saturates for the *Xcorr* because the time averaging is not as effective as the segmental averaging of the *NCPS* to suppress the incoherent information. The *CNR* for the short T_i = 2 μs has always the best performance independently of the total recording time, and even for recording times as short as 60 μs. Hence the potential, again, for fast imaging by keeping a short recording window.

Fig. 4.11 shows the passive FMC images when the hole reflector is located at different depths. Specifically, the image in Fig. 4.11(a) for the hole depth of 20 mm was obtained from the second aluminum block, that was then flipped to obtain the image in Fig. 4.11(b) for the hole depth of 36 mm. The image in Fig. 4.11(c) for the hole depth of 43.5 mm was obtained by flipping the first block with the 12.5 mm deep hole. The *NCPS* parameters were the same as in Fig. 4.10(c) with T_i = 20 μs, T_L = 120 μs, T_S = 60 μs with 50% overlap, and physical excitation provided by three firing elements #1, #32 and #64. The image quality in Fig. 4.11 is fundamentally similar regardless of the depth of the drilled hole. Note that the magnitude of each image is normalized by the maximum intensity in the region of interest. To better evaluate the signal-to-noise, Fig. 4.11(d) shows a vertical line profile cut through the holes where the values are normalized to the hole reflection maxima. The comparison shows similar signal-to-noise levels for all hole depths. As expected, the intensity of the backwall decreases for the deeper holes because of the hole shadow effect that is also visible in the images of Fig. 4.11 (b) and (c).

4.3.7 Wave Mode Compounding

It was discussed in Section III-A that there exist up to four wave mode combinations that can be exploited for ultrasonic imaging of solids, here referred to as *XY* combinations, where *X* is the transmitted mode (either *L* or *S* wave) and *Y* is the target-reflected mode (either *L* or *S* wave). In the subject case of passive imaging, the "transmission" from element *i* is of course "virtual". The images for each of the individual mode combinations are created by using the appropriate wave velocities in the time backpropagation algorithm of Eqs. (18) and (19). Fig. 4.12 demonstrates the significant improvements that can be obtained by compounding multiple wave modes in the passive *NCPS* FMC imaging of the drilled hole in the aluminum block. For these images, the segment width was T_S = 60 μs (50% overlap) with firing elements #1, #21, #42 and #64. The passive images are shown for: the

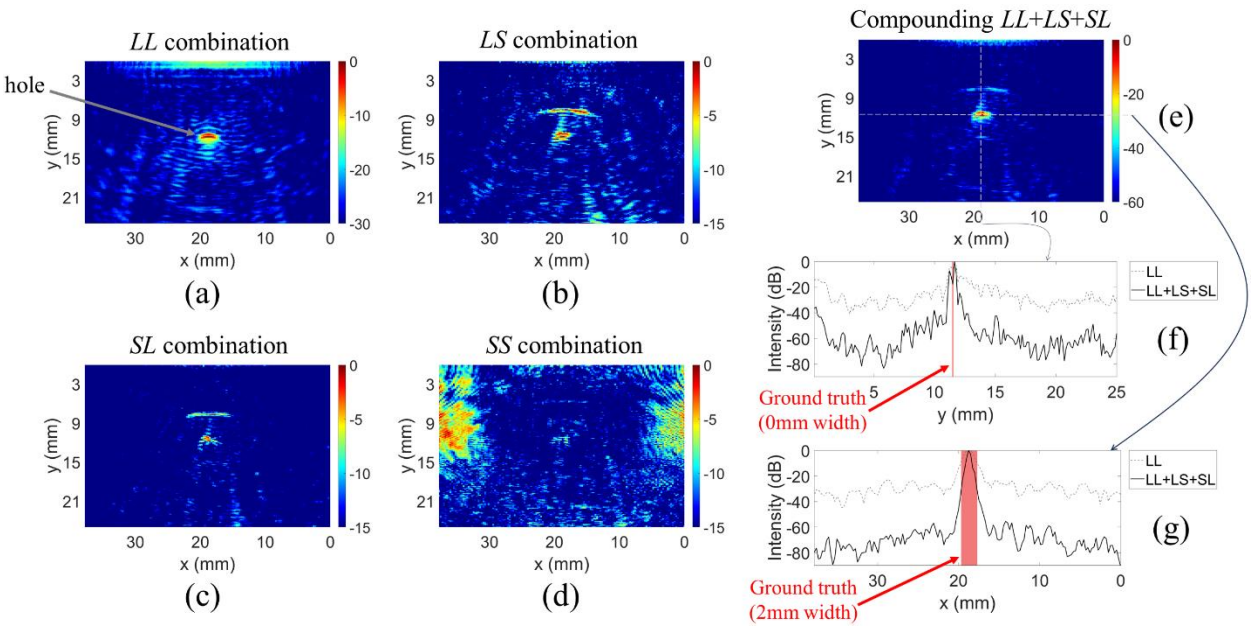

Figure 4.12: Wave mode compounding in passive *NCPS* imaging of the single drilled hole in the aluminum block. (a) *LL* mode combination. (b) *LS* mode combination. (c) *SL* mode combination. (d) *SS* mode combination. (e) *LL*+*LS*+*SL* mode compounding. Vertical (f) and horizontal (g) line profiles through the hole for the *LL* image and for the *LL*+*LS*+*SL* image.

LL combination in Fig. 4.12(a), the *LS* combination in Fig. 4.12(b), the *SL* combination in Fig. 4.12(c), and the *SS* combination in Fig. 4.12(d). Since the *L*-wave is dominant in this case both in transmission and in reflection, *LL* provides the best image of the hole in Fig. 4.12(a). However, the *S*-wave also provides valuable information on the hole through the *LS* and *SL* combinations. Since the *S*-wave transmission is predominantly at 45º from the direction of a point-wise excitation (and similarly the *S*-wave mode-converted reflection is predominantly at 45º from the direction of an incoming *L*-wave on a point-wise reflector), the *SS* combination in Fig. 4.12(d) is not very effective in imaging the central hole providing a response mostly on the sides of the image. When compounding the images *LL*+*LS*+*SL* according to Eq. 4.20, shown in Fig. 4.12(e), a significant improvement is obtained in both contrast and focus (notice that Fig. 4.12(e) is plotted with a larger 60 dB dynamic range to show the noise floor). The compounded image also eliminates the near-field blind zone that is instead still present (although not severely) in the *LL* image. A more quantitative

comparison of the compounded *LL*+*LS*+*SL* image versus the single *LL* image is provided by the line profiles cut through the hole vertically and horizontally shown in Fig. 4.12(f) and (g), respectively. Consider that the ideal profiles (ground truths) will have a main lobe of zero width for the vertical line profile of Fig. 4.12(f) (the sharp top surface of the hole), and a main lobe of width equal to 2 mm for the horizontal profile of Fig. 4.12(g) (the hole diameter). The results clearly show that that the compounded *LL*+*LS*+*SL* image produces a contrast improvement of ~40 dB and a spatial resolution improvement of ~two-fold for the hole compared to the single *LL* image.

4.3.8 Two Closely-Spaced Holes

The last set of experiments was performed to image two, 2 mm-diameter holes spaced at a distance of 6 mm and at a depth of 11 mm from the aluminum block's surface. Fig. 4.13 shows the IRF_{ij} waveforms passively reconstructed between array elements i = #28 and j = # 37, with the physical excitation located either at the center of the array (k = #32) in Fig. 4.13(a) and (b), or at the right end of the array (k = #1) in Fig. 4.13(c) and (d). The reconstructions are compared using the $Xcorr_{28\rightarrow37}(t)$ from Eq. 4.6 or the segmental averaged $NCPS_{28\rightarrow37}(f)$ from Eq. 4.13. For these results, T_i = 2 μs, T_S = 60 μs with 50% overlap, and T_L = 400 μs. Using the central element firing, the *Xcorr* result in Fig. 4.13(a) shows initial low frequency large fluctuations in both the causal and acausal portions, likely from cross-talks and surface waves, that results in a significant blind zone with no indication of the two-hole reflectors. The *NCPS* result in Fig. 4.13(b), instead, greatly compresses the initial blind zone to < 1 μs and shows an appreciable detection of the hole reflectors in both the causal and acausal portions. This result reaffirms the fact that the *NCPS* does not need the large initial delay that may otherwise be needed using *Xcorr* to focus on coda arrivals. Similar comparative performances are obtained using the end element firing. In this case, the *Xcorr* in Fig. 4.13(c) is still contaminated by the large low frequency fluctuations mostly affecting the causal times, with little

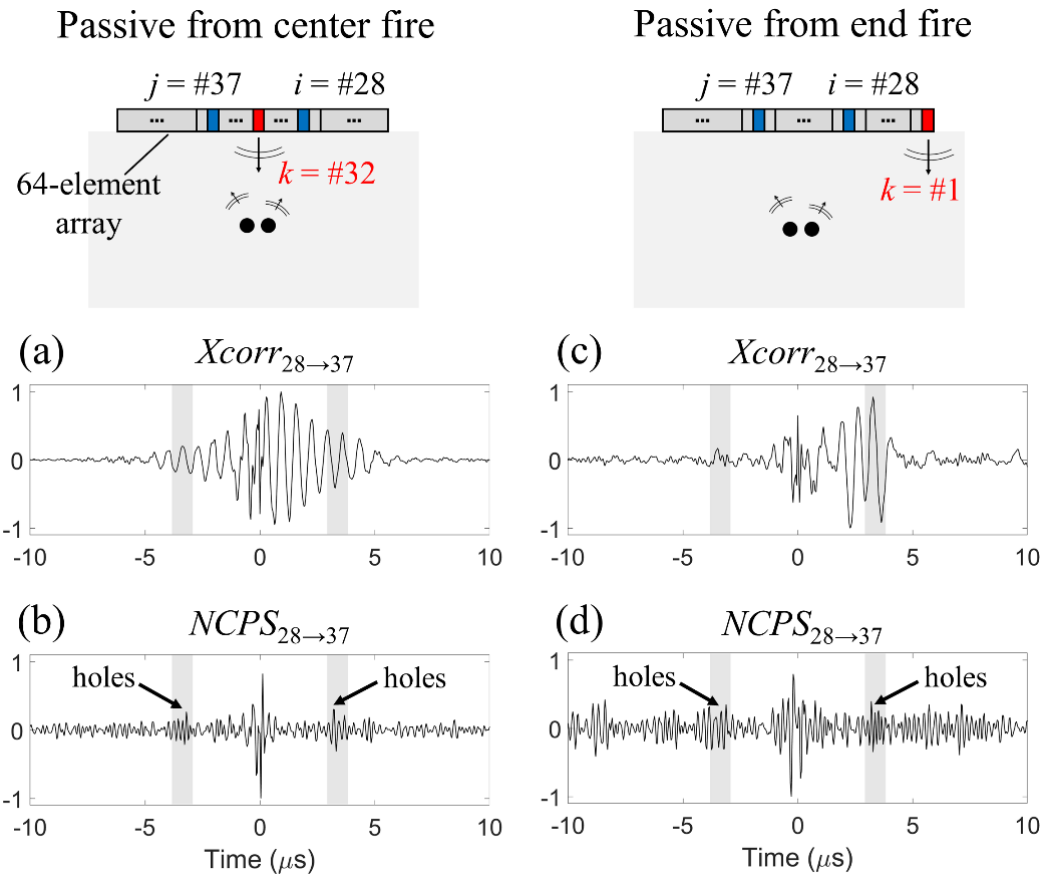

Figure 4.13: Passive Impulse Response Functions for the two, closely-spaced drilled holes in the aluminum block obtained using two transducer array elements i = #28 and j = #37 for (a) cross-correlation (#32 fires), (b) segment-averaged normalized cross-power spectrum (#32 fires), (c) same as (a) but with #1 fire, and (d) same as (b) but with #1 fire.

chance to see the holes. The *NCPS* of Fig. 4.13(d) suppresses the large fluctuations and shows the hole reflections.

Finally, Fig. 4.14 presents the imaging results for the two holes comparing (a) the conventional active FMC where all elements are in turn physically transmitting (*LL* mode combination), (b) the passive reconstruction using *Xcorr* (*LL* mode combination), (c) the passive reconstruction using segmental-averaged *NCPS* (*LL* mode combination), and (d) same as (c) but with *LL*+*LS*+*SL* mode compounding. For the passive reconstructions, again T_i = 2 μs, T_S = 60 μs with 50% overlap, T_L = 400 μs, and physical transmissions provided by elements #1, #21, #42 and #64.

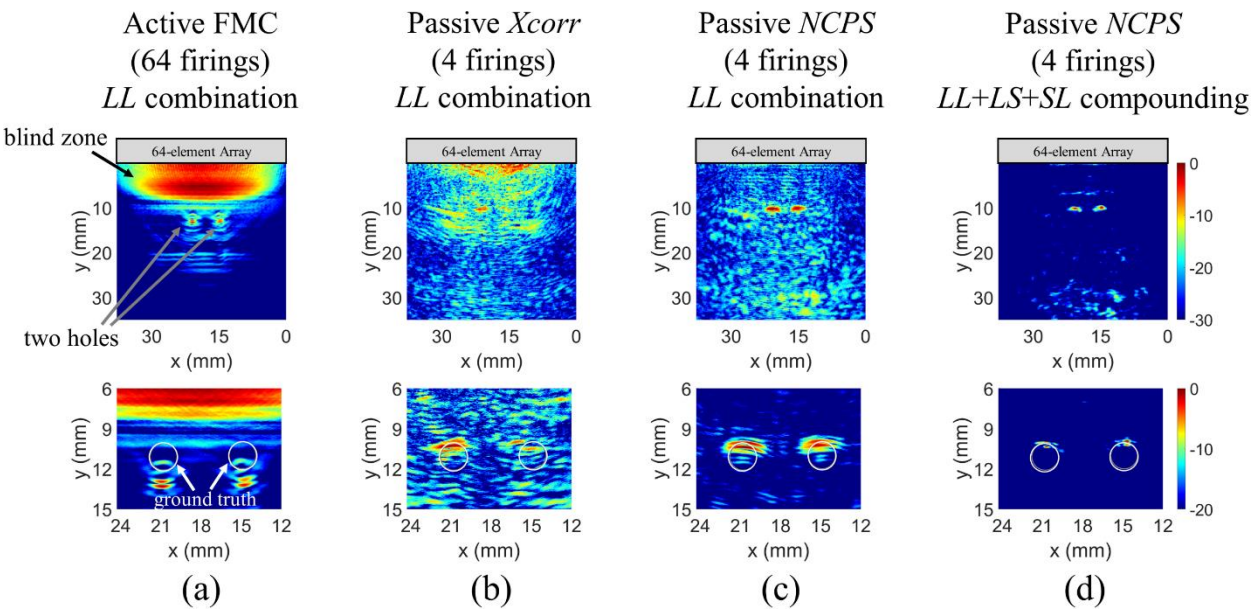

Figure 4.14: Full Matrix Capture images of the two closely spaced holes in the aluminum block from (a) conventional active FMC (*LL* combination only), passively reconstructed virtual FMC with (b) *Xcorr* (*LL* combination only), (c) segment-averaged *NCPS* (*LL* combination only), and (d) same as (c) but compounding the *LL*+*LS*+*SL* combinations.

As seen previously in the single-hole images of Fig. 4.6, the active FMC image of Fig. 4.14(a) presents a large blind zone extending for ~10mm in depth. It also shows the two holes at offset positions from the true locations (as seen in the zoomed-in image) due to the complicated initial signal affecting the time zero calculations. The *Xcorr* image of Fig. 4.14(b) misses the hole on the right. The *NCPS* image of Fig. 4.14(c) provides an excellent detection of the two holes, with their correct positions and clear separation. It also practically eliminates the near-field blind zone. Finally, the compounded *NCPS* image adding *LL*+*LS*+*SL* modes in Fig. 4.14(d) further improves the contrast and focusing on the two holes. In summary, the results obtained for the two holes confirm the conclusions reached earlier for the single hole.

4.4 Discussions and Conclusions

This paper proposes an "ultrasparse" SAFT imaging technique that uses passive reconstruction of the ultrasonic Impulse Response Functions (*IRF*s) between two receivers. A virtual Full Matrix Capture (FMC) matrix is constructed by interrogating all elements of a transducer array used primarily as receivers. The physical excitation is provided by an extremely small number of elements (from one to four) used as transmitters. This kind of ultrasparse transmission has the potential for high imaging speeds and simplified multiplexer hardware due to the reduction in the number of high-voltage digital-to-analog channels required, compared to a conventional "active" FMC scheme where all transducer elements are in turn used as transmitters. In order to keep a high image quality, the sparse transmissions are compensated by a robust algorithm to ensure the most accurate passive reconstructions. An added advantage of the proposed approach is the elimination of the blind zone in the near-field of the transducer array that potentially enables near-field imaging.

In particular, it is demonstrated theoretically and experimentally how an overlapped segment-averaged Normalized Cross-Power Spectrum (*NCPS*) is the best algorithm to estimate the IRF between two receivers with large Signal-to-Noise Ratios. The cross-correlation operation is often used in passive ultrasonic sensing, conversely, distorts the *IRF* by convolving it with the autocorrelations of the excitation, of the excitation-to-receiver transfer function, and of the receiver response function.

The paper demonstrates how time averaging does not equate to ensemble segmental averaging for noise suppression (where "noise" includes incoherent arrivals and/or nonlinear responses). Interestingly, the segment-averaged *NCPS* does not completely eliminate the noise at the first receiver, but in the case of white Gaussian noise this term helps to stabilize the metric by

avoiding close-to-zero values at the denominator. Care must be taken to choose the width of the segments in the ensemble averaging process, in order to strike a good compromise between obtaining a large number of averages and ensuring that the same coherent event at both receivers is included in the same segment for both causal and acausal times. It is therefore proposed to use a segment width equal to 3 to 5 times the expected difference in arrivals of a target reflection at the two receivers, that can be estimated by considering one of the receivers as the "virtual" source. The paper also shows how, in the imaging application at hand, it is appropriate (and actually desired) to consider the initial large arrivals at the receivers, rather than eliminating them by applying a significant initial time delay to focus on the "coda" portion of the waves, as instead done in many other applications of passive ultrasonic sensing. In fact, the application at hand does not require fully diffused fields (which are anyways very difficult to obtain in practice, and especially so when few physical transmissions are used).

In the quest for ultrasparse transmission performance, where the few transmitters create excitation fields that are generally anisotropic or directional, it is also important to average both causal and acausal portions of the passively reconstructed $IRFi \rightarrow j$ and $IRFj \rightarrow i$ for the generation of the virtual FMC. This step also helps to ensure that the quality of the final image is rather independent of the location of the few physical transmitters. Since this approach is not based on monitoring coda waves during long recording times, it allows to create passive images by keeping the total recording time rather short, which again is important for fast imaging performance.

One final step that significantly aids in the generation of high-quality images is implementing wave mode compounding in the construction of the passive FMC from the ultrasparse transmit array. This step exploits the simultaneous existence of the L-wave and S-wave modes when imaging solid media. Combining images beamformed with different mode

combinations (up to four) ultimately improves contrast and focus without increasing the array's physical aperture. The fact that S-waves (both in excitation and in reflection) tend to propagate at oblique directions (e.g. 45º) with respect to the predominant L-wave also improves the overall coverage of the region of interest when compounding the images.

These conclusions are demonstrated for the imaging of hole reflectors in an aluminum block probed by a linear transducer array. For the case of different reflections, for example defects of arbitrary orientations and/or located at arbitrary positions, the quality of the images should follow general rules of SAFT beamforming. A worthwhile extension of this study would be the imaging of targets located off-axis at the edges of the region of interest, where the role of the S-wave mode would probably be more significant. The results of the paper were obtained with a simple static Hanning apodization window applied to the array. This window was sufficient for the parametric and comparative analyses that were carried out. The overall quality of the images could be likely further improved if using more sophisticated windows such as wave structure weights [22]-[23], Minimum-Variance Distortionless Response (MVDR) adaptive weights [22], [23], [63]-[68], or weights based on amplitude decays and wave scattering patterns [67]-[70].

Clearly, the computation of the segmental averages adds complexity to the data processing. Specific metrics for computational and acquisition times will depend on the specific software and hardware employed. In this study, the imaging algorithms were implemented on a CUDA enabled host computer with a NVIDIA GeForce GTX 3060 GPU running MATLAB. Under these conditions, the reconstruction of a 64 by 64 FMC dataset from a single firing using a 60 msec segmented *NCPS* of 120 msec time signals sampled at 25 MHz took ~ 45 seconds. Faster performances will require changing the processing software to a more efficient language (e.g. C or C++) and utilizing optimized hardware and signal acquisition architectures.

The recommendations given in the paper for the design of a robust segment-averaged *NCPS*, including the choice of the segment width, total recording time, and causal/acausal reconstructions, can be helpful to other applications of passive sensing besides ultrasonic imaging, for example seismic interferometry for health monitoring of civil infrastructure.

Acknowledgements

This research was funded by the U.S. Federal Railroad Administration under contract no. 693JJ619C000008 (Dr. Robert Wilson, Program Manager). The authors would also like to acknowledge Mr. Gavin Dao of Advanced OEM Solutions (West Chester, OH, USA) for providing technical advice on SAFT hardware solutions and valuable insights on the use of the multiplexer currently adopted in the prototype.

Chapter 4, in full, is a reprint of the material as it appears in C. Huang, A.Z. Hosseinzadeh, and F. Lanza di Scalea, "Ultrasparse Ultrasonic Synthetic Aperture Focus Imaging by Passive Sensing," *IEEE Transactions on Ultrasonics, Ferroelectrics, and Frequency Control*, vol. 71, no. 5, pp. 518-535, 2024. The dissertation author was the primary investigator and author of this paper.

References

[1] J. J. Flaherty, K. R. Erikson, and V. M. Lund, "Synthetic aperture ultrasound imaging systems," U.S. Patent 3 548 642, Dec. 22, 1970.

[2] C. B. Burckhardt, P-A. Grandchamp, and H. Hoffmann, "An experimental 2 MHz synthetic aperture sonar system intended for medical use," *IEEE Trans. Son. Ultrason.*, vol. 21, no. 1, pp. 1–6, 1974.

[3] C. Holmes, B. W. Drinkwater, P. D. Wilcox, "Post-processing of the full matrix of ultrasonic transmit-receive array data for non-destructive evaluation," *NDT&E Int.*, vol. 38, pp. 701–711, 2005.

[4] J. A. Jensen, S. I. Nikolov, K. L. Gammelmark, and M. H. Pedersen, "Synthetic aperture ultrasound imaging," *Ultrasonics*, Vol. 44, Suppl. 1, pp. e5–e15, 2006.

[5] H. Hu, J. Du, N. Xu, H. Jeong, and X. Wang, "Ultrasonic sparse-TFM imaging for a two-layer medium using genetic algorithm optimization and effective aperture correction," *NDT&E Int.*, vol. 90, pp. 24–32, Sep. 2017.

[6] E. Hoyle, M. Sutcliffe, P. Charlton, and J. Rees, "Virtual source aperture imaging with auto-focusing of unknown complex geometry through dual layered media," *NDT&E Int.*, vol. 98, pp. 55–62, Sep. 2018.

[7] S. Sternini, A. Y. Liang, and F. Lanza di Scalea, "Ultrasonic synthetic aperture imaging with interposed transducer–medium coupling path," *Struct. Health Monit.*, vol. 18, no. 5-6, pp. 1543–1556, Nov. 2019.

[8] S. Sternini, A. Y. Liang, and F. Lanza di Scalea, "Rail defect imaging by improved ultrasonic synthetic aperture focus techniques," *Mater. Eval.*, vol. 77, no. 7, pp. 931–940, Jul. 2019.

[9] C. Huang and F. Lanza di Scalea, "Application of sparse synthetic aperture focusing techniques to ultrasound imaging in solids using a wedge transducer," *IEEE Trans. Ultrason. Ferroelectr. Freq. Control*, vol. 71, no. 2, pp. 280–294, Feb. 2024.

[10] G. Montaldo, M. Tanter, J. Bercoff, N. Benech, and M. Fink, "Coherent plane-wave compounding for very high frame rate ultrasonography and transient elastography," *IEEE Trans. Ultrason. Ferroelectr. Freq. Control*, vol. 56, no. 3, pp. 489–506, Mar. 2009.

[11] M. O'Donnell and L. J. Thomas, "Efficient synthetic aperture imaging from a circular aperture with possible application to catheter-based imaging," *IEEE Trans. Ultrason. Ferroelectr. Freq. Control*, vol. 39, no. 3, pp. 366–380, May. 1992.

[12] J.T. Ylitalo and H. Ermert, "Ultrasound synthetic aperture imaging: monostatic approach," *IEEE Trans. Ultrason. Ferroelectr. Freq. Control*, vol. 41, no. 3, pp. 333–339, May. 1994.

[13] M. Karaman M, P. C. Li, and M. O'Donnell, "Synthetic aperture imaging for small scale systems," *IEEE Trans. Ultrason. Ferroelectr. Freq. Control*, vol. 42, no. 3, pp. 429–442, May. 1995.

[14] G. R. Lockwood, J. R. Talman, and S. S. Brunke, "Real-time 3-D ultrasound imaging using sparse synthetic aperture beamforming," *IEEE Trans. Ultrason. Ferroelectr. Freq. Control*, vol. 45, no. 4, pp. 980–988, Jul. 1998.

[15] L. Sandrin, S. Catheline, M. Tanter, X. Hennequin, and M. Fink, "Time resolved pulsed elastography with ultrafast ultrasonic imaging," *Ultrason. Imaging*, vol. 21, no. 4, pp. 259–272, Oct. 1999.

[16] L. Sandrin, M. Tanter, S. Catheline, and M. Fink, "Shear modulus imaging using 2D transient elastography," *IEEE Trans. Ultrason. Ferroelectr. Freq. Control*, vol. 49, no. 4, pp. 426–435, Apr. 2002.

[17] S. K. Jespersen, J. E. Wilhjelm, and H. Sillesen, "Multi-angle compound imaging," *Ultrason. Imaging*, vol. 20, no. 2, pp. 81–102, Apr. 1998.

[18] M. Tanter, J. Bercoff, L. Sandrin, and M. Fink, "Ultrafast compound imaging for 2-D motion vector estimation: Application to transient elastography," *IEEE Trans. Ultrason. Ferroelectr. Freq. Control*, vol. 49, no. 10, pp. 1363–1374, Dec. 2002.

[19] M. Tanter and M. Fink, "Ultrafast imaging in biomedical ultrasound," *IEEE Trans. Ultrason. Ferroelectr. Freq. Control*, vol. 61, no. 1, pp. 102–119, Jan. 2014.

[20] J-Y. Lu, "High frame rate imaging system," U. S. Patent, 8 496 585, Jul. 30, 2013.

[21] J-Y. Lu, "Improving quality of high-frame-rate imaging with coherent and incoherent processing," in *2018 IEEE International Ultrasonics Symposium (IUS)*, Kobe, Japan, Oct. 22-25, 2018, pp. 1–4.

[22] F. Lanza di Scalea, S. Sternini, and T. V. Nguyen, "Ultrasonic imaging in solids using wave mode beamforming," *IEEE Trans. Ultrason. Ferroelectr. Freq. Control*, vol. 64, no. 3, pp. 602–616, Mar. 2017.

[23] S. Sternini, A. Pau and F. Lanza di Scalea, "Minimum-variance imaging in plates using guided-wave-mode beamforming," *IEEE Trans. Ultrason. Ferroelectr. Freq. Control*, vol. 66, no. 12, pp. 1906–1919, Dec. 2019.

[24] O. I. Lobkis and R. L. Weaver, "On the emergence of the Green's function in the correlations of a diffuse field," *J. Acoust. Soc. Am.*, vol. 110, no. 6, pp. 3011–3017, Dec. 2001.

[25] K. G. Sabra, P. Roux, and W. A. Kuperman, "Emergence rate of the time-domain Green's function from the ambient noise cross-correlation function," *J. Acoust. Soc. Am.*, vol. 118, no. 6, pp. 3524–3531, Dec. 2005.

[26] P. Roux, W. A. Kuperman, and the NPAL Group, "Extracting coherent wave fronts from acoustic ambient noise in the ocean," *J. Acoust. Soc. Am.*, vol. 116, no. 4, pp. 1995–2003, Oct. 2004.

[27] K. G. Sabra, P. Roux, and W. A. Kuperman, "Arrival-time structure of the time-averaged ambient noise cross-correlation function in an oceanic waveguide," *J. Acoust. Soc. Am.*, vol. 117, no. 1, pp. 164–174, Jan. 2005.

[28] M. Campillo and A. Paul, "Long-range correlations in the diffuse seismic coda," *Science*, vol. 299, no. 5606, pp. 547–549, Jan. 2003.

[29] P. Roux, K. G. Sabra, P. Gerstoft, W. A. Kuperman, and M. C. Fehler, "P-waves from cross-correlation of seismic noise," *Geophys. Res. Lett.*, vol. 32, no. 19, pp. 1–4, Oct. 2005.

[30] N. M. Shapiro, M. Campillo, L. Stehly, and M. H. Ritzwoller, "High-resolution surface-wave tomography from ambient seismic noise," *Science*, vol. 307, no. 5715, pp. 1615–1618, Mar. 2005.

[31] K. G. Sabra, P. Gerstoft, P. Roux, W. A. Kuperman, and M. C. Fehler, "Extracting time-domain Green's function estimates from ambient seismic noise," *Geophys. Res. Lett.*, vol. 32, no. 3, pp. 1–5, Feb. 2005.

[32] K. G. Sabra, P. Gerstoft, P. Roux, W. A. Kuperman, and M. C. Fehler, "Surface wave tomography from microseisms in Southern California," *Geophys. Res. Lett.*, vol. 32, no. 14, pp. 1–4, Jul. 2005.

[33] R. Snieder, "Extracting the Green's function from the correlation of coda waves: A derivation based on stationary phase," *Phys. Rev. E*, vol. 69, pp. 0466101-0466108, Apr. 2004.

[34] R. Snieder and K. Wapenaar, "Imaging with ambient noise," *Phys. Today*, vol. 63, no. 9, pp. 44–49, Sept. 2010.

[35] R. Snieder and E. Şafak, "Extracting the building response using seismic interferometry: Theory and application to the Millikan Library in Pasadena, California," *Bull. Seismol. Soc. Am.*, vol. 96, no. 2, pp. 586–598, Apr. 2006.

[36] N. Nakata, R. Snieder, S. Kuroda, S. Ito, T. Aizawa, and T. Kunimi, "Monitoring a building using deconvolution interferometry. I: earthquake-data analysis," *Bull. Seismol. Soc. Am.*, vol. 103, no. 3, pp. 1662–1678, Jun. 2013.

[37] N. Nakata and R. Snieder, "Monitoring a building using deconvolution interferometry. II: ambient vibration analysis," *Bull. Seismol. Soc. Am.*, vol. 104, no. 1, pp. 204–213, Feb. 2014.

[38] X. Wu, Z. Guo, L. Liu, Y. J. Chen, C. Zou, and X. Song, "Seismic monitoring of super high-rise building using ambient noise with dense seismic array," *Seismol. Res. Lett.*, vol. 92., no. 1, pp. 396–407, Jan. 2021.

[39] A. Mordret, H. Sun, G. A. Prieto, M. N. Toksoz, and O. Büyüköztürk, "Continuous monitoring of high-rise buildings using seismic interferometry," *Bull. Seismol. Soc. Am.*, vol. 107, no. 6, pp. 2759–2773, Dec. 2017.

[40] G. A. Prieto, J. F. Lawrence, A. I. Chung, and M. D. Kohler, "Impulse response of civil structures from ambient noise analysis," *Bull. Seismol. Soc. Am.*, vol. 100, no. 5A, pp. 2322–2328, Oct. 2010.

[41] C. R. Farrar and G. H. James, "System identification from ambient vibration measurements on a bridge," *J. Sound Vib.*, vol. 205, no. 1, pp. 1–18, Aug. 1997.

[42] K. G. Sabra, E. S. Winkel, D. A. Bourgoyne, B. R. Elbing, S. L. Ceccio, M. Perlin, and D. R. Dowling, "Using cross correlations of turbulent flow-induced ambient vibrations to estimate the structural impulse response. Application to structural health monitoring," *J. Acoust. Soc. Am.*, vol. 121, no. 4, 1987–1995, Apr. 2007.

[43] J. D. Tippmann, X. Zhu, and F. Lanza di Scalea, "Application of damage detection methods using passive reconstruction of impulse response functions," *Phil. Trans. R. Soc. A*, vol. 373, no. 2035, pp. 1–17, Feb. 2015.

[44] F. Lanza di Scalea, X. Zhu, M. Capriotti, A. Y. Liang, S. Mariani, and S. Sternini, "Passive extraction of dynamic transfer function from arbitrary ambient excitations: Application to high-speed rail inspection from wheel-generated waves," *J. Nondestruct. Eval. Diagn. Progn. Eng. Syst.*, vol. 1, pp. 0110051–01100512, Feb. 2018.

[45] J. E. Michaels and T. E. Michaels, "Detection of structural damage from the local temporal coherence of diffuse ultrasonic signals," *IEEE Trans. Ultrason. Ferroelectr. Freq. Control*, vol. 52, no. 10, pp. 1769–1782, Oct. 2005.

[46] E. Larose, O. I. Lobkis, and R. L. Weaver, "Passive correlation imaging of a buried scatterer," *J. Acoust. Soc. Am.*, vol. 119, no. 6, pp. 3549–3552, Jun. 2006.

[47] K. G. Sabra, A. Srivastava, F. Lanza di Scalea, I. Bartoli, P. Rizzo, and S. Conti, "Structural health monitoring by extraction of coherent guided waves from diffuse fields," *J. Acoust. Soc. Am.*, vol. 123, no. 1, pp. EL8–L13, Jan. 2008.

[48] J. D. Tippmann and F. Lanza di Scalea, "Passive-only defect detection and imaging in composites using diffuse fields," in *Mechanics of Composite and Multi-functional Materials*, vol. 7, C. Ralph, M. Silberstein, P. R. Thakre, and R. Singh, Eds. USA: Springer, Conference Proceedings of the Society for Experimental Mechanics Series, 2016, pp. 67–72.

[49] J. D. Tippmann and F. Lanza di Scalea, "Passive-only damage detection by reciprocity of Green's functions reconstructed from diffuse acoustic fields with application to wind turbine blades," *J. Intell. Mater. Syst. Struct.*, vol. 26, no. 10, pp. 1251–1258, Jul. 2015.

[50] A. Duroux, K. G. Sabra, J. Ayers, and M. Ruzzene, "Extracting guided waves from cross-correlations of elastic diffuse fields: applications to remote structural health monitoring," *J. Acoust. Soc. Am.*, vol. 127, no. 1, pp. 204–215, Jan. 2010.

[51] L. Chehami, J. De Rosny, C. Prada, E. Moulin, and J. Assaad, "Experimental study of passive defect localization in plates using ambient noise," *IEEE Trans. Ultrason. Ferroelectr. Freq. Control*, vol. 62, no. 8, pp. 1544–1553, Aug. 2015.

[52] J. Salvermoser, C. Hadziioannou, and S. C. Stähler, "Structural monitoring of a highway bridge using passive noise recordings from street traffic," *J. Acoust. Soc. Am.*, vol. 138, no. 6, pp. 3864–3872, Dec. 2015.

[53] C. Huang and F. Lanza di Scalea, "An ultrasonic scanning system for the inspection of composite stiffened panels from elastic constant identification via inversion of guided waves," *Compos. Struct.*, vol. 322, p. 117373, Oct. 2023.

[54] J. N. Potter, P. D. Wilcox, and A. J. Croxford, "Diffuse field full matrix capture for near surface ultrasonic imaging," *Ultrasonics*, vol. 82, pp. 44–48, Jan. 2018.

[55] H. Zhang, H. Zhang, J. Zhang, J. Liu, W. Zhu, G. Fan, and Q. Zhu, "Wavenumber imaging of near-surface defects in rails using Green's function reconstruction of ultrasonic diffuse fields," *Sensors*, vol. 19, no. 17, pp. 3744, 2019.

[56] P. R. Roth, "Effective measurements using digital signal analysis," *IEEE Spectr.*, vol. 8, no. 4, pp. 62–70, Apr. 1971.

[57] G. C. Carter, C. H. Knapp, and A. H. Nuttall, "Estimation of the magnitude-squared coherence function via overlapped Fast Fourier Transform processing," *IEEE Trans. Audio Electroacoust.*, vol. AU-21, no. 4, pp. 337–344, Aug. 1973.

[58] P. D. Welch, "The use of Fast Fourier Transform for the estimation of power spectra: A method based on time averaging over short, modified periodograms," *IEEE Trans. Audio Electroacoust.*, vol. AU-15, no. 2, pp. 70–73, Jun. 1967.

[59] A. H. Nuttall, "Spectreal estimation by means of overlapped Fast Fourier Transform processing of windowed data," Naval Underwater Systems Center, New London, CT, USA, Tech. Rep. 4169, Oct. 1971.

[60] R. W. Clayton and R. A. Wiggins, "Source shape estimation and deconvolution of teleseismic bodywaves," *Geophys. J. Int.*, vol. 47, no. 1, pp. 151–177, Oct. 1976.

[61] K. F. Woolfe and K. G. Sabra, "Variability of the coherent arrivals extracted from low-frequency dep-ocean ambient noise correlations," *J. Acoust. Soc. Am.*, vol. 138, no. 2, pp. 521–532, Aug. 2015

[62] M. S. Patterson and F. S. Foster, "The improvement and quantitative assessment of B-mode images produced by an annular array/cone hybrid," *Ultrason. Imaging*, vol. 5, no. 3, pp. 195–213, Jul. 1983.

[63] F. Arabshahi, S. Monajemi, H. Sheikhzadeh, K. Raahemifar, and R. Faraji-Dana, "A frequency domain MVDR beamformer for UWB microwave breast cancer imaging in dispersive mediums," in *IEEE International Symposium on Signal Processing and Information Technology*, Athens, Greece, Dec. 12-15, 2013, pp. 000362–000367.

[64] J. F. Synnevag, A. Austeng, and S. Holm, "Adaptive beamforming applied to medical ultrasound imaging," *IEEE Trans. Ultrason., Ferroelectr., Freq. Control*, vol. 54, no. 8, pp. 1606–1613, Aug. 2007.

[65] A. M. Deylami, J. A. Jensen, and B. M. Asl, "An improved minimum variance beamforming applied to plane-wave imaging in medical ultrasound," in *2016 IEEE International Ultrasonics Symposium (IUS)*, Tours, France, Sept. 18-21, 2016, pp. 1-4.

[66] K. Diamantis, A. Greenaway, T. Anderson, J. A. Jensen and V. Sboros, "Experimental performance assessment of the sub-band minimum variance beamformer for ultrasound imaging," *Ultrasonics*, vol. 79, pp. 87–95, Aug. 2017.

[67] J. S. Hall, P. Fromme and J. E. Michaels, "Guided wave damage characterization via minimum variance imaging with a distributed array of ultrasonic sensors," *J. Nondestruct. Eval.*, vol. 33, no. 3, pp. 299–308, Sept. 2014.

[68] J. S. Hall and J. E. Michaels, "Minimum variance ultrasonic imaging applied to an in situ sparse guided wave array," *IEEE Trans. Ultrason. Ferroelectr. Freq. Control*, Vol. 57, no. 10, pp. 2311–2323, Oct. 2010.

[69] J. S. Hall and J. E. Michaels, "Multipath ultrasonic guided wave imaging in complex structures," *Struct. Health Monit.*, vol. 14, no. 4, pp. 345–358, Jul. 2015.

[70] J. Zhang, B. W. Drinkwater, and P. D. Wilcox, "Defect characterization using an ultrasonic array to measure the scattering coefficient matrix," *IEEE Trans. Ultrason. Ferroelectr. Freq. Control*, vol. 55, no. 10, pp. 2254–2265, Oct. 2008.

Chapter 5 High Resolution Ultrasonic Imaging of Extended Targets in Solids via Combined Match Field and Time Delay Beamforming

5.1 Introduction

Ultrasound imaging using active sensing modalities has received wide interest in medical imaging, nondestructive evaluation (NDE), and underwater acoustics. Regardless of its steering or focusing capabilities, the ultrasound transmitter-receiver array system can be characterized in the frequency domain by the transfer matrix that contains the interelement responses between each transmitter and receiver [1]. Practically the transfer matrix can be approximated by sequentially isolating the emission of each transmitter element and recording with the full receiver array in parallel, termed full matrix capture (FMC), to construct the multistatic dataset.

Robust beamforming algorithms have been developed in the time domain to achieve fast imaging of the broadband transfer matrix of the FMC dataset. The synthetic aperture focus technique has been proven as the benchmark method to beamform the FMC dataset. The delay-and-sum (DAS) algorithm has been applied in numerous modalities including single element transmission [2]-[6], plane wave transmission [7]-[8], and subaperture transmission [9]-[12]. With the boost of computational power, recent DAS frameworks have been extended to the delay-multiply-and-sum (DMAS) algorithm by coupling each transmitter-receiver pair to obtain higher resolution and contrast [13]-[16]. However, the linear time-delay type beamformers cannot achieve resolution beyond the Rayleigh diffraction limit.

In parallel with time-delay type beamformers, numerous methods have been developed in the frequency domain to obtain high resolution images from the transfer matrix, with particular interest in super-resolution imaging capabilities beyond the Rayliegh diffraction limit. A popular

algorithm is the multiple signal classification (MUSIC) based on the Singular Value Decomposition (SVD) or eigen decomposition to achieve subwavelength resolution in the cross-range (azimuth) direction. Prada et al. found that the eigenvectors of the time reversal operator (TRO, that is an outer product of the transfer matrix) have a one-to-one correspondence with the number of well-resolved point scatterers in the interrogated medium [17]-[18], which allowed physical focusing with subwavelength resolution [19]-[21]. When the Green's function of the test medium is available, the backpropagation can be computed numerically to form a super resolution image without the need of electronically phasing the transmit array [22]. Since then, the SVD based MUSIC type beamformers have seen numerous applications in imaging defects in bulk solids [23]-[29], cracks in waveguide structures [30]-[34], localization in shallow water [35]-[36], and detecting breast microcalcifications [37]-[38].

In most medical diagnostics or industrial NDT applications, the size of the target is usually larger than the wavelength at the central frequency of a transducer array [39]. The imaging of these extended targets using MUSIC type beamformers is challenging in several aspects. First, the one-to-one correspondence in SVD based factorization is not available when the scatterers are finite sized or not well resolved in the transfer matrix. Chambers and Gautesen found that there could be up to four eigenfunctions associated to one small sphere due to compressibility and density contrast [40]. To resolve multiple scatterers, the Foldy-Lax model was used for better estimation of target scattering strengths [41]-[42]. Robert and Fink pointed out that the eigenvectors of the TRO for an extended target are prolate spheroidal wave functions instead of superposition of point scatterers [43]. Second, the dimension of the signal subspace can be larger than the dimension of the transfer matrix when either there are too many scatterers, or the size of the scatterer is too large. To avoid saturation of the signal subspace, Labyed and Huang achieved high resolution imaging of many

glass spheres in tissue-mimicking phantom by dividing the imaging plane into subregions and applied MUSIC on the time-windowed multistatic data corresponding to these subregions [37]. Another drawback of MUSIC is that standard algorithms are formulated as narrowband beamformers that expand to broadband only by incoherently averaging the ambiguity surfaces of each narrowband output [23]. Another way, termed phase-coherent MUSIC, is to retain phase information of the MUSIC magnitude squared output by multiplying transpose instead of Hermitian transpose of the transfer matrix [27] [28] [38] [44] [45]. The phase coherent approach greatly increases the axial resolution of MUSIC in case of low signal-to-noise ratio (SNR), but neither the azimuth focus nor the dynamic range is improved. Moreover, these methods neglect the fact that the eigenfunctions can vary significantly across the spectrum of interest, which inevitably reduces the coherence in wideband signals. Finally, the high-resolution characteristic of MUSIC comes from separating the eigen space into signal and noise subspaces. Pierri and Soldovieri worked out the theoretical signal space dimension of a planar aperture in Fresnel zone as a function of aperture width, target lateral size, target axial range, and wavelength [46]. However, the use of this theoretical subspace dimension requires prior knowledge of the extended target. Hou et al. approximated the signal space dimension by comparing the variation in the singular value structure [47]. Up to now, most work on MUSIC finds the threshold based on trial and error testing of the experimental data.

Another way to achieve high resolution imaging of multistatic data is by using adaptive beamforming techniques that have been extensively studied in passive sensing. Prada and Thomas first interpreted the TRO acquired using active FMC as a covariance matrix of a passive array [48]. They showed that the TRO constructed from the active transmit elements is analogous to taking “snapshots” in time to build the rank of the covariance matrix in match field processing. They

reported that for the case of imaging two closely separated point-like scatterers, the minimum variance distortionless response (MVDR) beamformer performed similarly as MUSIC in azimuth resolution. With the tools developed in match field community, it is possible to beamform multitone TRO coherently. Michalopoulou and Porter demonstrated a way to exploit the coherence between each frequency in the magnitude squared inner products by stacking each narrowband data vector to a long "supervector" [49]. Orris et al. developed a matched-phase algorithm by searching for the relative phase differences in cross-frequency terms to deal with unknown source spectrum [50]. Debever and Kuperman cooperated robust adaptive beamformers (the white noise constraint algorithm, or WNC) into broadband formulation to reduce the sensitivity of MVDR algorithms to modeling mismatch [51]. They found that although the multitone covariance matrix is naturally rank deficient in experimental acquisition, the optimization of replica vectors can be stabilized by constraining the maximum possible white noise gain. Another advantage of the WNC algorithm is that it influences the SNR output of the diagonally loaded MVDR by altering the variation of small non-physical eigenvalues that results in a beneficial bias in the dynamic range of the beamformer output [52].

This chapter proposes a high-performance ultrasonic imaging scheme by combining coherent adaptive match field beamforming with robust time-delay type beamforming. The goal is to achieve high resolution and high contrast imaging of extended targets placed parallel to a linear array in both azimuth and axial range directions. This objective was previously shown possible in imaging point scatterers by exploiting the invariance of an active array system using a similar combined match field and time-delay beamforming scheme [53]. Specifically, the coherent broadband match field formulation developed in [49] is analogously applied to active FMC scheme to form a multitone TRO. The adaptive WNC algorithm is used to beamform the multitone TRO

with high azimuth resolution. The WNC algorithm also takes advantage of the rank deficiency in the multitone TRO to obtain high contrast indication of resolution cells due to the dynamic range bias. The coherent WNC algorithm is compared with the MUSIC algorithm to demonstrate its advantage in imaging extended targets. The DMAS beamformer is added to provide stable imaging of the continuous surfaces of the extended targets with high axial resolution. Both simulation and experiments show the superior performance of the proposed combined imaging scheme when targeting extended scatterer in sizes ranging from a wavelength to the physical aperture of the ultrasonic array.

5.2 High Lateral Resolution Imaging via Match Field Beamformers

5.2.1 Formulation of Transfer Matrix and Analogy to Passive Sensing

Consider and array of M transmitters and N receivers as shown in Fig. 5.1(a). Assuming linearity and time invariance, the received signal on the nth element $r_n(t)$ can be described as the convolution between the emitted signal $e_m(t)$ on the mth element and the interelement response $k_{nm}(t)$, summed over all transmissions:

$$r_n(t) = \sum_{m=1}^{M} k_{nm}(t) \circledast e_m(t) + b_n(t) \tag{5.1}$$

where $\circledast$ denotes convolution, and $b_n(t)$ is the noise at the nth receiver. The interelement response is typically measured by transmitting with each element individually in the Full Matrix Capture (FMC) scheme such that it $k_{nm}(t)$ can be estimated from the received signal $k_{nm}(t) \approx r_n(t)$. As shown in Fig. 5.1(a), such an active sensing modality can detect a scatterer by measuring the reflections from a point P in the transmitter-receiver ray path. However, assuming a delta function for the emitted signal $e_m(t)$ inevitably leads to undesired phase lag in $k_{nm}(t)$ for ultrasonic applications.

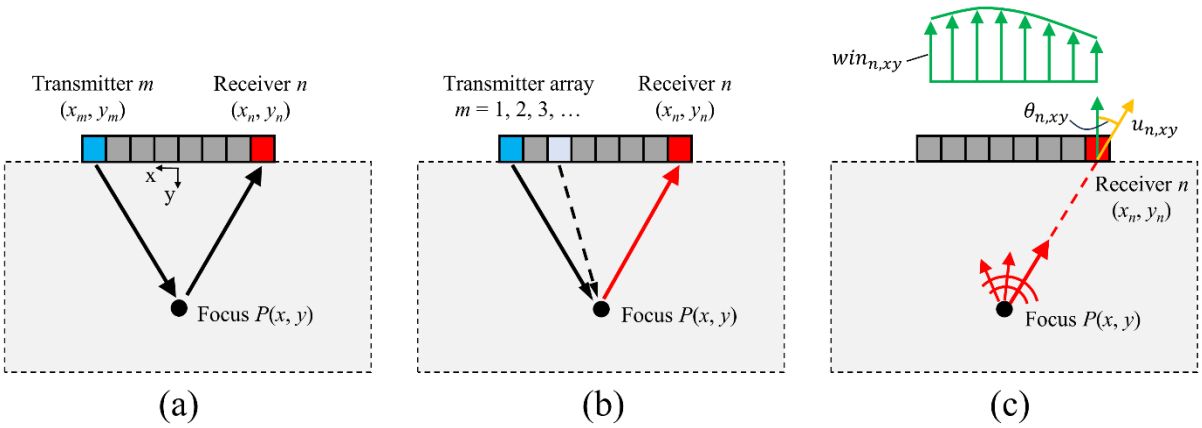

Figure 5.1: (a) Schematic of the active sensing mode of an array. (b) Coherent wave path from the scatterer to a receiver element by only considering passive reception and averaging the transmissions. (c) Modeling longitudinal wave reception by considering the angle between particle displacement and the normal direction to the transducer.

Deconvolution of ultrasonic signals is not a trivial task because $r_n(t)$ is colored by the spectrum response of the transducers in both transmission and reception. The authors have developed a dual-output strategy to eliminate the contamination of the source spectrum in the reconstruction of interelement transfer function $k_{nm}(t)$ using normalized cross power spectrum [54] of the form:

$$K_{nm}(\omega) = \frac{R_n(\omega)E_m{}^*(\omega)}{|E_m(\omega)|^2 + \alpha\sigma^2} \tag{5.2}$$

where $K_{nm}(\omega)$, $R_n(\omega)$, and $E_m(\omega)$ are the Fourier transforms of $k_{nm}(t)$, $r_n(t)$, and $e_m(t)$, respectively, α is regularization parameter, and σ^2 is the noise variance estimated from the root mean square of $r(t)$ for simplicity. It is worth stating that this band-limited frequency domain operation cannot perfectly capture the transient features in the time domain.

To start the discussions on match field beamformers, it is helpful to rewrite Eq. 5.1 in the frequency domain and in its vector form:

$$\hat{R}(\omega) = \hat{K}(\omega)\hat{E}(\omega) + \hat{B}(\omega) \tag{5.3}$$

where the dimension of $\hat{R}(\omega)$ and $\hat{B}(\omega)$ are N×1, $\hat{E}(\omega)$ is M×1, and $\widehat{K}(\omega)$ is N×M. Much research has been devoted to exploiting the singular value decomposition (SVD) of the multistatic response matrix $\widehat{K}(\omega)$ that characterizes the interelement responses between the transmission array to the reception array. For example, the widely used MUSIC algorithm is based on separating the signal and noise space in the SVD of the transfer matrix $\widehat{K}(\omega)$:

$$\widehat{K}(\omega) = \widehat{U}(\omega)\hat{\Sigma}(\omega)\hat{V}^{\mathrm{H}}(\omega) = [\widehat{U}_{\mathrm{S}}(\omega) \quad \widehat{U}_{\mathrm{N}}(\omega)] \begin{bmatrix} \widehat{\Sigma_{\mathrm{S}}}(\omega) & 0 \\ 0 & \widehat{\Sigma_{\mathrm{N}}}(\omega) \end{bmatrix} \begin{bmatrix} \widehat{V_{\mathrm{S}}}^{\mathrm{H}}(\omega) \\ \widehat{V_{\mathrm{N}}}^{\mathrm{H}}(\omega) \end{bmatrix} \tag{5.4}$$

where $\widehat{U}(\omega)$ and $\widehat{V}(\omega)$ are matrices whose columns are the left and right singular vectors, and $\hat{\Sigma}(\omega)$ is a diagonal matrix containing singular values. These singular vectors contain the phase information across the reception or transmission array to focus on the scatterers, if there is any. The subscript H denotes Hermitian conjugate, and the subscripts S and N represent the signal and noise subspace, respectively. The SVD operation provides an opportunity to focus solely on the existing scatterers using the signal subspace while discarding the noise subspace. Theoretically, the singular values in $\widehat{\Sigma_{\mathrm{S}}}(\omega)$ are significantly larger than those in $\widehat{\Sigma_{\mathrm{N}}}(\omega)$ so that the separation between the signal and noise can be determined from the variation in the energy levels. However, as shown later in this paper, such a threshold can be hard to determine for near field imaging of extended targets because the SVD structure is highly dependent on the sampled frequency and the size and location of the target.

Another interpretation of the response matrix $\widehat{K}(\omega)$ is to consider the active sensing modality as passive source detection, so that various beamformers developed in the match field community can be applied to the multistatic data. As shown in Fig. 5.1(b), if only the reception array is considered, the ray paths from different transmit elements is coherent from the focus point P to a receive element n. Analytically, one can rewrite the transfer matrix $\widehat{K}(\omega)$ into a collection

of columns, where each column is a data vector $\widehat{D}_m(\omega)$ that characterizes the signal across the reception array under transmission by element *m*

$$\widehat{K}(\omega) = \left[\widehat{D}_1(\omega), \widehat{D}_2(\omega), \dots, \widehat{D}_m(\omega), \dots, \widehat{D}_M(\omega)\right] \tag{5.5}$$

$$\widehat{D}_m(\omega) = [K_{1m}(\omega), K_{2m}(\omega), \dots, K_{nm}(\omega), \dots, K_{Nm}(\omega)]^{\mathrm{T}}. \tag{5.6}$$

It is natural to find the covariance matrix that characterizes the cross-power spectrum between the elements in the reception array. Prada et al. showed that the outer product of the multistatic matrix (equivalent to the time reversal operator matrix, or monotone TRO) is analogous to the covariance matrix $\hat{C}(\omega)$ in a match field processing context [48], hence

$$\hat{C}(\omega) = \widehat{K}(\omega)\widehat{K}^{\mathrm{H}}(\omega) = \sum_{m=1}^{M} \widehat{D}_m(\omega)\widehat{D}_m{}^{\mathrm{H}}(\omega) \tag{5.7}$$

which shows that the covariance matrix is an average of the transmission ray path and coherently sums the reception ray path connecting a scatterer and a receiver element.

5.2.2 Considerations on Modeling Replica Vectors

The match field beamformers require accurate modeling of the expected wave field. Thus, it is important to properly model the reception ray path that forms a replica of the column vector $\widehat{D}_m(\omega)$ as in Eq. 5.6, that is

$$\widehat{w}(x, y, \omega) = [w(x, y, x_1, y_1, \omega), w(x, y, x_2, y_2, \omega), \dots, w(x, y, x_N, y_N, \omega)]^{\mathrm{T}} \tag{5.8}$$

where the location of a focus pixel *P* is at (*x*, *y*) and the location of a receiver *n* is at (x_n, y_n). An option is to use a free field Green's function that captures the phase difference of a spherical wave across the reception array, as seen in numerous literature [27].

To achieve a better focus, a spatial window across the array can be added based on the amplitude distribution of the received wave mode [6]. This concept uses the fact that typical ultrasonic transducers are sensitive to normal (out-of-plate) displacements. As seen in Fig. 5.1(c),

considering longitudinal mode propagation, the particle motions in the test medium $u_{n,xy}$ (shown in yellow) are in line with the ray path. The measured amplitude distribution, shown in green, is simply a cosine function determined by the angle of incidence $\theta_{n,xy}$ between the longitudinal mode particle motion and the surface normal direction. Also considering geometrical spreading effect, the weighted Green's function can now be rewritten as

$$w(x, y, x_n, y_n, \omega) = \frac{1}{d} \cdot \frac{|y_n - y|}{d} \cdot \frac{i}{4} \mathrm{H}_0^1(kd) \tag{5.9}$$

where the first term shows the geometrical spreading of a sphere, and the second term is the cosine window from the wave mode structure in reception, H_0^1 is the Hankle function of the first kind, k is the wavenumber, and d is the distance between the focus pixel P and the receiver.

With the construction of the replica vector, a linear Bartlett beamformer can be formulated as [55]

$$I^{\mathrm{BAR}}(x, y, \omega) = \widehat{w}^{\mathrm{H}}(x, y, \omega) \hat{C}(\omega) \widehat{w}(x, y, \omega) \tag{5.10}$$

where the replica vectors $\widehat{w}(x, y, \omega)$ is normalized to unity norm for all results in this paper. For a collection of frequencies $\Omega = \{\omega_1, \omega_2, \ldots, \omega_L\}$, the broadband match field beamformer output can be an incoherent (IC) averaging of the narrowband ambiguity surfaces [56]

$$I^{\mathrm{IC-BAR}}(x, y, \Omega) = \sum_{l=1}^{L} I^{\mathrm{BAR}}(x, y, \omega_l)\,. \tag{5.11}$$

5.2.3 SVD Based Multiple Signal Classification (MUSIC) Algorithm

The MUSIC algorithms utilize the orthogonality in the SVD of the transfer matrix $\widehat{K}(\omega)$ as seen in Eq. 5.4 or, equivalently, the eigen decomposition of monotone TRO $\hat{C}(\omega)$. Consider a pitch-catch mode as in Fig. 5.1(a) where the transmission and reception array share the same physical aperture. In this case the left and right singular vectors are identical due to reciprocity.

Using the left singular vectors in the signal space, the incoherent broadband MUSIC algorithm is given by an averaging of narrowband outputs over the spectrum of interest Ω

$$I^{\mathrm{MUSIC}}(x, y, \Omega) = \frac{1}{1 - \frac{1}{L}\sum_l A_{\mathrm{S}}(x, y, \omega_l)} \tag{5.12}$$

where for each frequency ω_l,

$$A_{\mathrm{S}}(x, y, \omega) = \hat{w}^{\mathrm{H}}(x, y, \omega)\hat{U}_{\mathrm{S}}(\omega)\widehat{U_{\mathrm{S}}}^{\mathrm{H}}(\omega)\hat{w}(x, y, \omega). \tag{5.13}$$

The term $A_S(x, y, \omega)$ can be interpreted as a narrowband Bartlett beamformer where the covariance matrix is the outer product of the signal subspace of the left singular matrix $\hat{U}_{\mathrm{S}}(\omega)\widehat{U_{\mathrm{S}}}^{H}(\omega)$. The MUSIC beamformers are beneficial to image extended targets because they discard the magnitude of the singular values in the subspaces when composing the "covariance matrix". Thus, all resolution cells in the signal space can be illuminated, giving a higher weight to those weaker singular modes that are invisible to linear beamformers.

The high-resolution characteristic of the MUSIC algorithm comes from the nonlinear subspace "cut" in the SVD of the transfer matrix $\hat{K}(\omega)$. For the imaging of extended targets, the threshold in the singular values is hard to determine since the nonzero components can occupy the entire $\hat{\Sigma}(\omega)$, as seen in numerous examples [28] [31].

Besides the difficulty of experimentally finding the subspace dimension for MUSIC beamformers, it was found that the theoretical dimension of the signal subspace for a linear array is related to the lateral size and range of the target [43] [46]. The number of nonzero singular values N_s is proportional to the following:

$$N_s \propto DW/(\lambda Y) \tag{5.14}$$

where D is the full width of the array, W and Y are the lateral width and range of the extended target, and λ is the wavelength. This shows that the subspace dimension N_s can change dramatically

across the broad frequency band Ω if the extended target is wide (large W) and located in the near field (small Y). The problem is most severe when the dimension N_s is comparable to the dimension of the reception array N where the MUSIC algorithms fail to work due to the inseparable subspaces.

5.2.4 Broadband Formulation of Transfer Matrix and Adaptive Beamforming

Another strategy to improve the resolution of imaging the matrix $\widehat{K}(\omega)$ is to use adaptive beamformers that increase focusing abilities through varying the replica vectors according to the measured data vectors. The ability to exploit coherence across frequencies is often desired due to the broadband nature of ultrasonic signals. In this respect, coherent, rather than incoherent broadband beamformers can provide additional array gains. These can be created by stacking the narrowband data vectors into broadband "supervectors" as demonstrated in underwater acoustics [49]. This arrangement exploits the cross-frequency coherence across the array for increased gains.

5.2.4.1 Using supervector formulation in active sensing

Inspired by the idea of broadband "supervector", a broadband formulation of the transfer matrix for active sensing is introduced as follows. Eq. 5.3 is rewritten by stacking the L narrowband components:

$$\begin{aligned}\tilde{R}(\Omega) &= \left[\hat{R}(\omega_1)^{\mathrm{T}}, \hat{R}(\omega_2)^{\mathrm{T}}, \dots, \hat{R}(\omega_L)^{\mathrm{T}}\right]^{\mathrm{T}} \\ &= [R_1(\omega_1), R_2(\omega_1), \dots, R_N(\omega_1), R_1(\omega_2), \dots, R_N(\omega_L)]^{\mathrm{T}}\end{aligned} \tag{5.15}$$

$$\begin{aligned}\tilde{E}(\Omega) &= \left[\hat{E}(\omega_1)^{\mathrm{T}}, \hat{E}(\omega_2)^{\mathrm{T}}, \dots, \hat{E}(\omega_L)^{\mathrm{T}}\right]^{\mathrm{T}} \\ &= [E_1(\omega_1), E_2(\omega_1), \dots, E_M(\omega_1), E_1(\omega_2), \dots, E_M(\omega_L)]^{\mathrm{T}}\end{aligned} \tag{5.16}$$

where $\tilde{R}(\Omega)$ and $\tilde{E}(\Omega)$ are $N{\cdot}L{\times}1$ and $M{\cdot}L{\times}1$, respectively. From these supervectors, the multi-tone transfer matrix of size $N{\cdot}L{\times}M{\cdot}L$ can be constructed as

$$\tilde{R}(\Omega) = \tilde{K}(\Omega)\tilde{E}(\Omega) + \tilde{B}(\Omega) \tag{5.17}$$

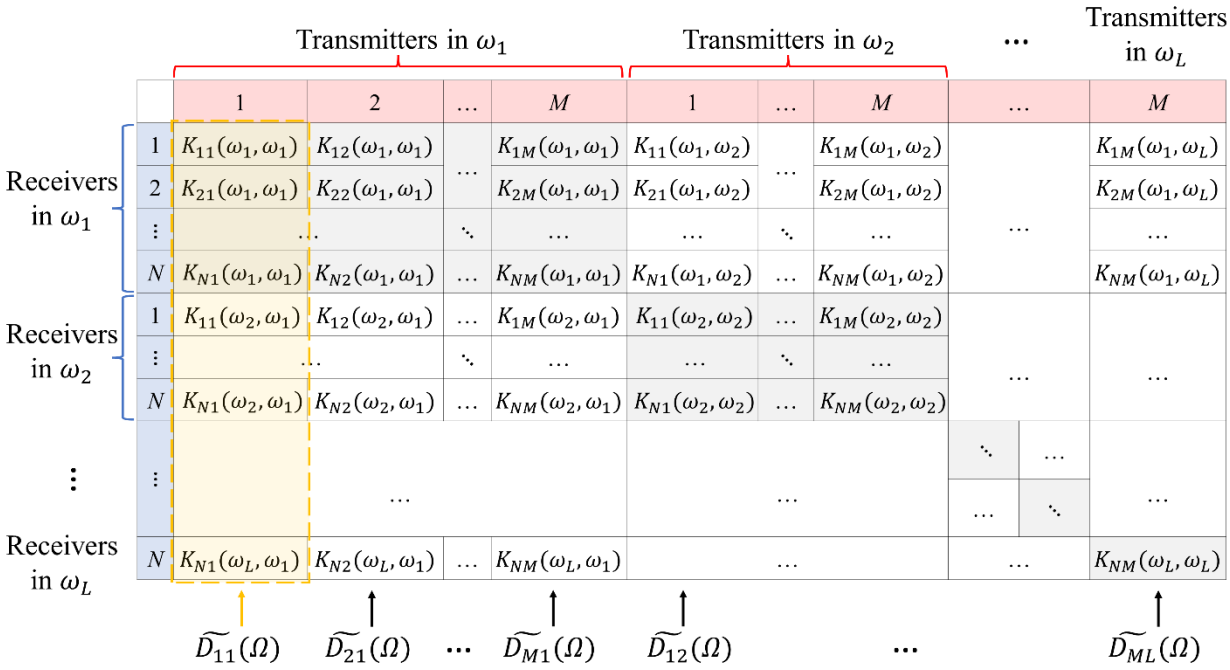

Figure 5.2: Formulation of broadband transfer matrix for coherent multi-frequency processing of active sensing. Each column is analogous to the "supervector" formulation in passive sensing.

where $\tilde{B}(\Omega)$ is the supervector form of noise. The multitone transfer matrix $\widetilde{K}(\Omega)$ is the interelement responses between multi-tone receiver array and multitone transmitter array. As shown in Fig. 5.2, each entry in $\widetilde{K}(\Omega)$ defines the transfer function between a transmitter at one frequency and a receiver at one or another frequency. The diagonal monotone blocks (colored in gray) are the same as $\widehat{K}(\omega)$ in Eq. 5.3. The off diagonal cross frequency terms track the cross-frequency coherence. Similarly to the decomposition as in Eq. 5.5, the multitone transfer matrix can be interpreted as a combination of column "supervectors", as pointed out in Fig. 5.2,

$$\widetilde{K}(\Omega) = \left[\widetilde{D_{11}}(\Omega), \widetilde{D_{21}}(\Omega), \dots, \widetilde{D_{M1}}(\Omega), \widetilde{D_{12}}(\Omega), \dots, \widetilde{D_{mu}}(\Omega), \dots, \widetilde{D_{ML}}(\Omega)\right] \tag{5.18}$$

where the subscripts of $\widetilde{D_{mu}}(\Omega)$ denotes the index of transmit element for m and the index of sampled transmitting frequency for u respectively. Then each of the supervector $\widetilde{D_{mu}}(\Omega)$ is analogous to those seen in passive sensing as a stack of monotone data vectors received at different frequencies ω_v.

The analogy between the TRO in active time reversal and the covariance matrix in passive sensing is still valid in the "supervector" formulation. This analogy can be easily found by using the column decomposition in Eq. 5.18:

$$\tilde{C}(\Omega) = \widetilde{K}(\Omega)\widetilde{K}^{\mathrm{H}}(\Omega) = \sum_{m=1}^{M}\sum_{u=1}^{L} \widetilde{D_{mu}}(\Omega)\widetilde{D_{mu}}^{\mathrm{H}}(\Omega) \tag{5.19}$$

which shows that the multitone TRO in "supermatrix" form is a summation of the covariance matrices of the reception supervectors over all transmit elements and at all sampled frequencies. The dimension of the multitone TRO $\tilde{C}(\Omega)$ is now $N{\cdot}L \times N{\cdot}L$ that only accounts for the correlation between broadband-augmented reception array.

Experimentally, the elements of $\widetilde{K}(\Omega)$ can be measured by a modification of Eq. 5.3 into cross-frequency:

$$\widetilde{K_{pq}} = \frac{R_n(\omega_u){E_m}^*(\omega_v)}{|E_m(\omega_v)|^2 + \alpha\sigma^2} \tag{5.20}$$

where $p = (u\text{-}1){\cdot}N{+}n$ and $q = (v\text{-}1){\cdot}M{+}m$ are the row and column number in $\widetilde{K}(\Omega)$, respectively. Note that although the rank of the monotone TRO illustrated in Eq. 5.7 is built by the "snapshots" taken in the different locations (and thus arrival times) of the transmit elements, for multitone TRO the matrix is likely to be rank deficient since the sampling in multiple frequencies in transmission does not provide additional information to the $\tilde{C}(\Omega)$ supermatrix. Considering for example a Dirac delta as an ideal emitted signal $E(\omega)$ = constant, there would be repetitive columns at the same transmit element in $\widetilde{K}(\Omega)$. This means that the rank of $\tilde{C}(\Omega)$ as seen in Eq. 5.19 is still governed by the number of transmit elements M instead of being augmented by the number of sampled frequencies L.

5.2.4.2 White noise constraint beamformer to resolve rank deficiency in adaptive beamforming

The maximum likelihood method (MVDR algorithm) for high resolution imaging in active sensing [48] requires the covariance matrix to be full rank, which cannot be satisfied in broadband TRO formulation. The white noise constraint (WNC) algorithm is a modified version of the MVDR processor that utilizes an inequality constraint on the gain against the spatial white noise in the covariance matrix [57].

The WNC replica supervector $\widetilde{w_{\mathrm{WNC}}}(x, y, \Omega)$ is found using an optimization approach by finding the minima of the function $F(x, y, \Omega)$ using a Lagrange multiplier γ:

$$F = \widetilde{w_{\mathrm{WNC}}}^{\mathrm{H}}(x, y, \Omega)\left(\tilde{C}(\Omega) + \varepsilon(x, y)I\right)\widetilde{w_{\mathrm{WNC}}}(x, y, \Omega) + \gamma(\widetilde{w_{\mathrm{WNC}}}^{\mathrm{H}}(x, y, \Omega)\widetilde{w_{\mathrm{BAR}}}(x, y, \Omega) - 1) \tag{5.21}$$

where $\varepsilon(x, y)$ is the amount of spatial white noise added to enable the inversion of $\tilde{C}(\Omega)$. The solution to Eq. 5.21 can be found by first determining the white noise gain G_{W} in dB that constrains the norm of the WNC replica:

$$\widetilde{w_{\mathrm{WNC}}}^{\mathrm{H}}(x, y, \Omega)\widetilde{w_{\mathrm{WNC}}}(x, y, \Omega) \leq {G_{\mathrm{W}}}^{-1} = S \tag{5.22}$$

where S denotes the sensitivity to errors. When the constraint G_{W} is 0 dB, which means $\widetilde{w_{\mathrm{WNC}}}(x, y, \Omega)$ is the same as Bartlett with unity norm, the algorithm puts large diagonal loading $\varepsilon(x, y)$ everywhere that makes $\tilde{C}(\Omega)$ similar to the identity matrix I. When the constraint G_{W} is small (e.g. -5 dB) or equivalently with high sensitivity S, the output approaches an ideal MVDR beamformer. The solution to Eq. 5.21 involves equalizing its derivatives to zero that leads to

$$\widetilde{w_{\mathrm{WNC}}}(x, y, \Omega, G_{\mathrm{W}}) = \frac{(\tilde{C}(\Omega) + \varepsilon(x, y)I)^{-1}\widetilde{w_{\mathrm{BAR}}}(x, y, \Omega)}{\widetilde{w_{\mathrm{BAR}}}^{\mathrm{H}}(x, y, \Omega)(\tilde{C}(\Omega) + \varepsilon(x, y)I)^{-1}\widetilde{w_{\mathrm{BAR}}}(x, y, \Omega)} \tag{5.23}$$

In practice, for a given constraint G_{W}, the diagonal loading $\varepsilon(x, y)$ at each pixel (x, y) in the image is found by computing $\widetilde{w_{\mathrm{WNC}}}(x, y, \Omega)$ from Eq. 5.23 and varying the values of $\varepsilon(x, y)$ until

Eq. 5.22 is satisfied. Finally, the broadband coherent WNC (C-WNC) beamformer is written as the magnitude squared output:

$$I^{\mathrm{C-WNC}}(x, y, \Omega, G_{\mathrm{W}}) = \widetilde{w_{\mathrm{WNC}}}^{\mathrm{H}}(x, y, \Omega, G_{\mathrm{W}})\tilde{C}(\Omega)\widetilde{w_{\mathrm{WNC}}}(x, y, \Omega, G_{\mathrm{W}}). \tag{5.24}$$

5.3 High Axial Resolution Imaging via Time Delay Beamformers

Although the match field beamformers can provide high resolution images in the lateral direction (cross-range), these beamformers are less sensitive to axial resolution since the transient features of the ultrasonic signals cannot be captured in the frequency domain. The time-backpropagation algorithm (delay-and-sum or DAS) is widely used for fast and robust imaging in the time domain. The DAS type algorithms achieve high resolution in axial range by extracting the properly delayed amplitude in each interelement response $k_{nm}(t)$. The delay-multiply-and-sum (DMAS) algorithm extends the array gain of DAS by exploiting the correlation between different transmitter-receiver pairs [13]. An image is built by combinatorial multiplication of the backpropagated signals extracted through the interelement responses, that is

$$I^{\mathrm{DMAS}}(x, y) = \sum_{u=1}^{S-1} \sum_{v=u+1}^{S} \mathrm{sign}(k_u(\tau_{u,xy})k_v(\tau_{v,xy}))\sqrt{\left|k_u(\tau_{u,xy})k_v(\tau_{v,xy})\right|} \tag{5.25}$$

where each *u*th combination, or similarly *v*th, is formed by a unique transmitter-receiver pair (*m*, *n*), and the total number of interelement response is $S = M \cdot N$. The "sign" operator preserves the sign of the correlation between the *u*th and *v*th extracted amplitudes before feeding them to the square root. The multiplication of all possible signal pair combinations exploits the correlation between recorded signals belonging to not only the same transmit element but also different element firings, thus increasing the overall array gain compared to a traditional DAS beamforming.

Referring to Fig. 5.1(a), the time of flight (TOF) $\tau_{mn,xy}$ for each transmitter-receiver pair (m, n) can be easily found as

$$\tau_{mn,xy}(x,y) = (\sqrt{(x_m - x)^2 + (y_m - y)^2} + \sqrt{(x_n - x)^2 + (y_n - y)^2})/c \qquad (5.26)$$

where c is the longitudinal mode wave speed considered in this work.

Recall that the inverse Fourier transform of the operation in Eq. 5.2 cannot capture a clean transient feature of the interelement response $k_{nm}(t)$. In this work, the time domain $k_{nm}(t)$ first goes through data compression processing using wavelet decomposition to cleanse the undesired ringing in the waveforms as in [58]. The time domain DMAS imaging is then computed from the analytical signal representation utilizing known Hilbert transform considerations [6] [16].

The complete flowchart of the proposed beamforming strategy is schematized in Fig. 5.3. The DMAS beamformer provides robust and stable images with high resolution in the axial range. For narrowband beamformers, the MUSIC obtains high resolution by performing SVD on the transfer matrix $\widehat{K}(\omega)$. If the transfer matrix is interpreted as a passive modality where all transmissions are summed in the outer product as $\hat{C}(\omega)$, incoherent beamforming can be performed either linearly (IC-BAR) or adaptively (IC-WNC). It is worth stating that though the WNC algorithm can be used in narrowband to provide high azimuth resolution as in [57], there is no dynamic range bias in the beamformer output because the covariance matrix $\hat{C}(\omega)$ is full rank. The three narrowband beamformers (in blue boxes) are expanded to broadband by incoherent averaging of each narrowband output. For broadband beamformers, both the covariance matrix and the replica vector are assembled in the "supervector" formation to take advantage of the signal coherence in cross-frequency terms. Using the WNC optimization, a significant dynamic range bias is expected because the supermatrix $\tilde{C}(\Omega)$ is rank deficient [51]. The final image can be a conditional summation of the DMAS image and the C-WNC image that features high resolution

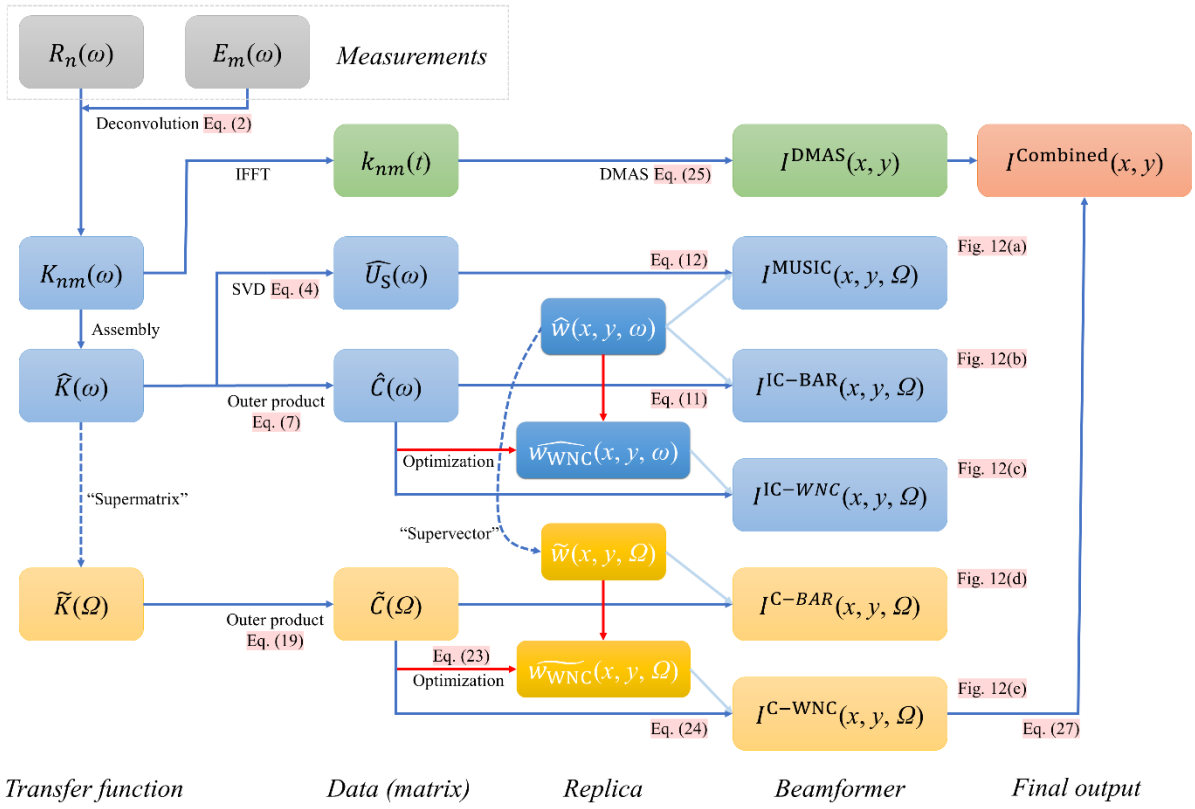

Figure 5.3: The beamforming strategy discussed in this paper. Green, blue, and yellow boxes correspond to time domain, narrowband, and broadband variables, respectively. Examples of match field beamformers are given in Fig. 5.12 by experimentally scanning two side-drilled holes in an aluminum block.

in both axial and azimuth range as the proposed imaging strategy in this chapter. The details of this summation scheme are to be introduced in section 5.4.2.2.

5.4 Simulation Results

The performance of the various imaging algorithms discussed above was first validated using numerical simulations from MATLAB k-wave toolbox in a 2D (plane strain) scenario [59]. The simulation modeled a 30 mm wide × 40 mm deep aluminum square with a simulated ultrasonic array consisting of 32 elements with a 0.6 mm pitch. The excitation $e_m(t)$ was a 5 MHz tone burst signal with 2 cycles and a Gaussian envelope. The transducer transmission/reception was modeled

as vertical displacement perpendicular to the array-medium interface. The size of a grid was set to 0.05 mm that is sufficiently smaller than the L-mode wavelength λ = 1.2 mm calculated from the center frequency. The scatterers/reflectors were modeled as hard inclusions with a sound speed and density that were 20 times larger than the propagation medium. The time step was carefully selected as 0.2 ns to satisfy the desired bandwidth.

The replica vectors used in the model were free field Green's function. The improvement of scaling the amplitude in the replica vectors to match the 3D measurements will be shown in the experimental results in section 5.5.

5.4.1 Simulation of Matched Field Beamforming

5.4.1.1 Point spread function and closely-spaced point scatterers

Before looking at the performance of matched field beamformers on extended targets, it is beneficial to check their Point Spread Functions (PSFs) to compare the resolution. Fig. 5.4 shows the comparison of MUSIC and proposed C-WNC algorithm when the imaged scatterers are point-like. The size of the model point scatter is 0.05 mm (one pixel in the simulation grid), which is considerably smaller than the wavelength λ of 1.2 mm. For both beamformers the transfer function is sampled at 4, 5.25, and 6.5 MHz. For MUSIC the beamformer is an average of narrowband outputs as in Eq. 5.12 with an estimated dimension of subspace N_S = 2, while for C-WNC the beamformer involves a supervector formulation as in Eq. 5.24. Fig. 5.4(a) shows the comparison of the PSFs when the scatterer is at a range of 15 mm (12.5 λ). Both algorithms form a single resolution cell, but the dynamic range bias of C-WNC suppresses the noise floor to -160 dB making the image high contrast. The cause of the output power bias for rank deficient covariance matrix has been thoroughly discussed in [52].

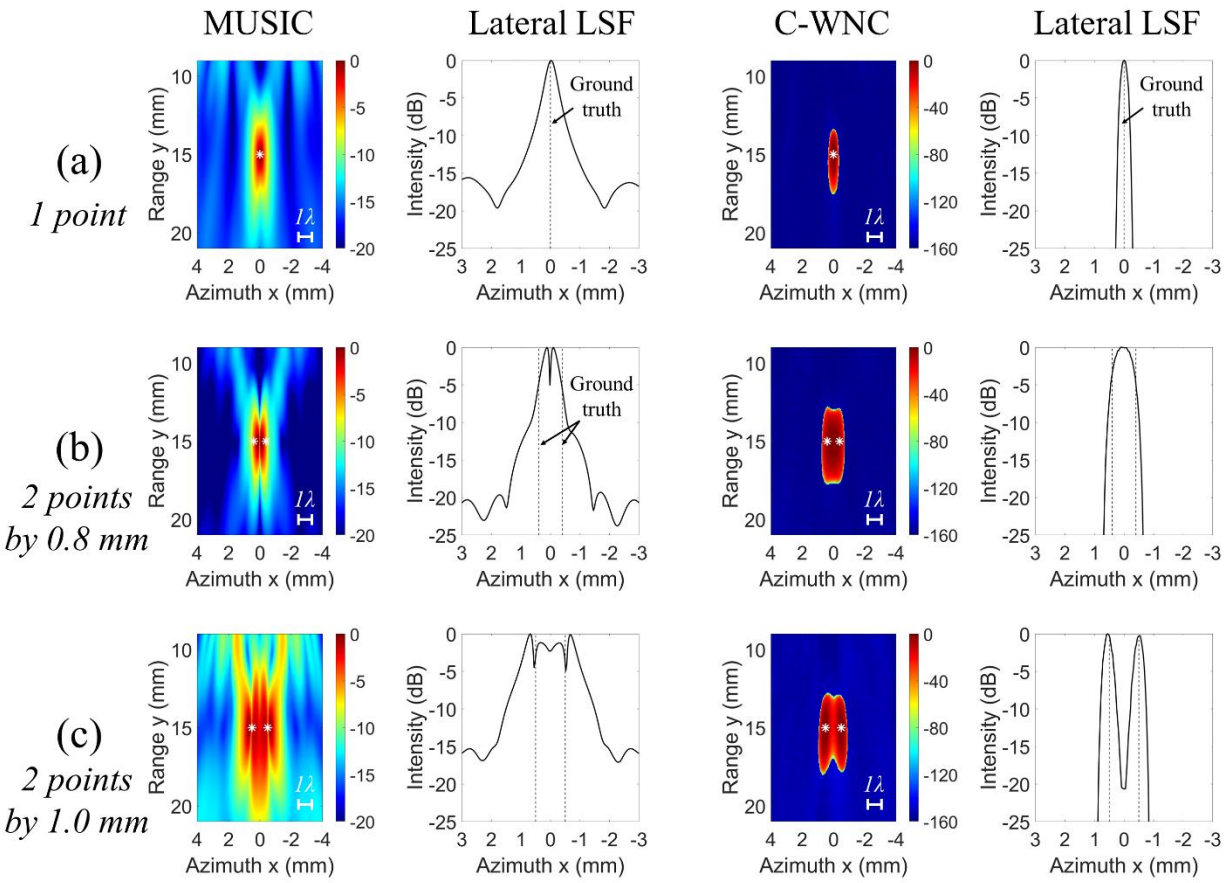

Figure 5.4: Comparison of MUSIC and C-WNC in imaging and differentiating point scatterers. Images and lateral line profiles of (a) a point scatterer, (b) two point scatterers separated by 0.8 mm, and (c) two point scatterers separated by 1.0 mm.

For the case of two point scatterers separated by 0.8 mm, Fig. 5.4(b) shows that neither of the two beamformers can clearly separate the reflectors. MUSIC shows two resolution cells from its high frequency components, but the lateral focus is not accurate as illustrated in the LSF. C-WNC averages the multitone components from previous discussions, and the image shows an overlap of two resolution cells with no separation. A better separation is seen in Fig. 5.4(c) when the points are further separated by a distance of 1.0 mm separating the reflectors. In this case MUSIC has four resolution cells due to high resolution in the 6.5 MHz TRO and possibly from the complexity of multiple scattering. C-WNC is less sensitive to the inter reflector interaction and

only two resolution cells accurately focus on each of the reflectors, with a gap of -20 dB between the cells from the benefit of the dynamic range bias. To summarize, MUSIC has smaller resolution cells by nonlinearly thresholding the singular/eigen subspace, but it does not necessarily guarantee the correct localization of scatterers. Alternatively, C-WNC is an averaged output due to the cross-spectrum coherence of the supervector formulation and thus results in more accurate scatterer locations.

5.4.1.2 Eigen structure of extended targets and mechanism of C-WNC

To have a better understanding of the match field imaging, the resolution cell structures in the TRO of extended targets are illustrated in Fig. 5.5. As shown in Fig. 5.5(a), from one transmit element there are two sources of scattering for longitudinal waves, one being the continuous slit boundary and the other being the slit edge tips. The matched field beamformer tends to look for point sources. Thus, the reflection from the flat surface is taken as a point source in the transfer matrix by mirroring the transmit element to twice axial range. A typical distribution of corresponding resolution cells is shown in Fig. 5.5(b). Besides the resolution cells from the tips, there are also resolution cells from the transmit array superimposed in the signal space. Moreover, there is a passing region where the algorithms find it to be possible locations (azimuth angles) of scattering sources if no optimization/constraint is present. Notice that the strength of each resolution cell (or eigen mode) can change depending on the array aperture and the extended target dimensions.

An example of resolution cell distribution using the proposed adaptive C-WNC algorithm is shown in Fig. 5.5(c)-(e). The extended target is a 12 λ slit located at a 10 λ distance in range. To simplify the eigen structure, the 32 by 32 FMC dataset is reduced to a 4 by 32 sparse matrix capture (SMC) by only using a 4-element transmission array and the full 32-element reception array. The

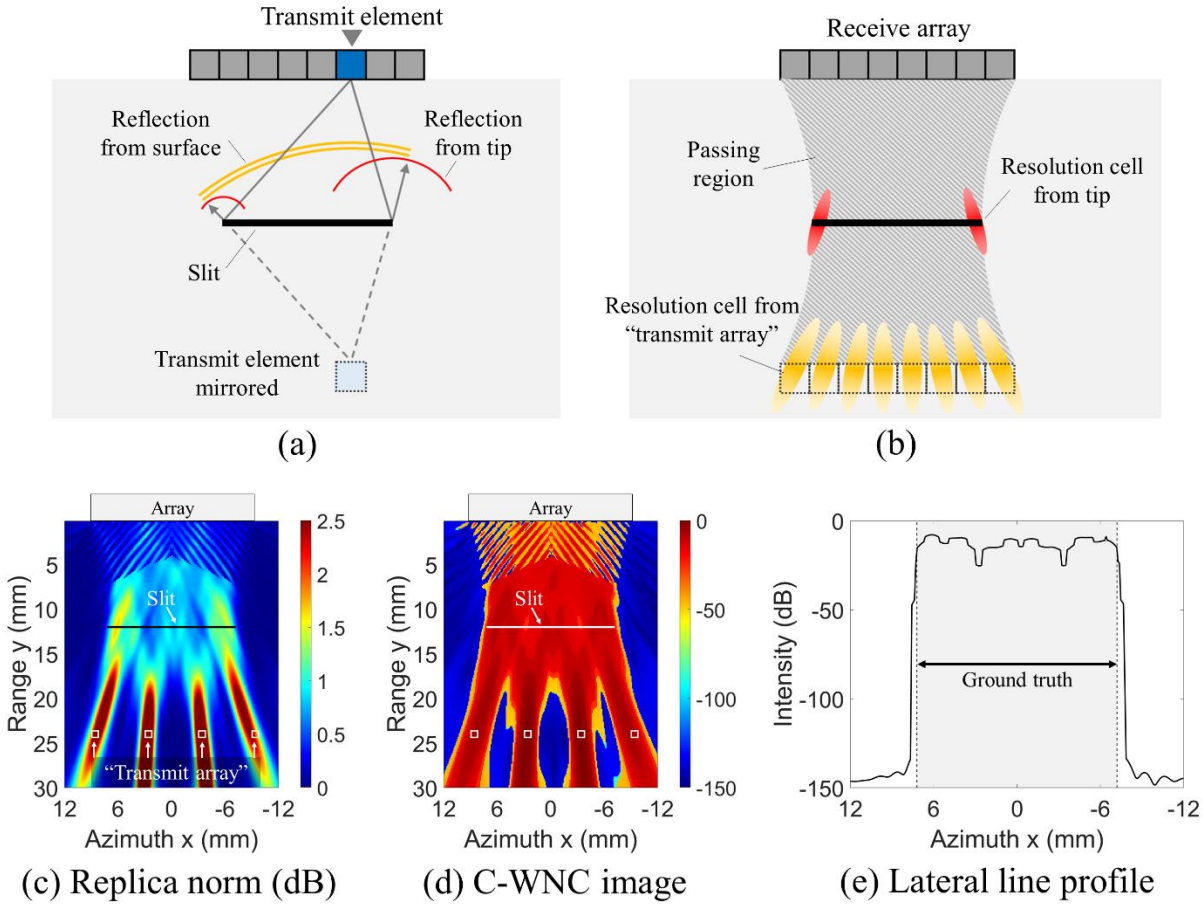

Figure 5.5: Eigen structure of imaging an extended slit target. (a) Reflections from a single transmit element. (b) Distribution of resolution cells. Example of using a sparse 4-element transmit array SMC dataset: (c) the norm of C-WNC replica vectors after optimization using a G_W = -2.5 dB, (d) corresponding C-WNC image, and (e) its lateral line profile.

multitone transfer matrix $\widetilde{K}(\Omega)$ is reduced to (32×3) by (4×3) considering a broadband sampling at 4, 5.25, and 6.5 MHz. The rank of the corresponding covariance matrix $\tilde{C}(\Omega)$ is expected to be M = 4 considering only the transmit array contributions. Using a G_W of -2.5 dB, the norm of the replica vectors in Fig. 5.5(c) shows the result of optimization highlighting the four transmit elements as the "most likelihood" with the largest norm in the C-WNC replicas (that is close to the maximum allowed white noise gain of 2.5 dB). The resolution cells at the two tips of the slit are weaker in this setup (but still 1.6 dB larger than "no likelihood"). The beamformed C-WNC

image shown in Fig. 5.5(d) displays a weak spatial focus including all four resolution cells from the mirrored transmit array, the passing region, and two cells at the tips. This is because the -2.5 dB constraint is so loose that it allows most eigen modes to come through as "signal" after the optimization. Regardless of the loose constraint, the lateral line profile at the ground truth range of the slit in Fig. 5.5(e) shows that the C-WNC image accurately captures the tip of the slit with a significant drop to the biased noise floor.

It is worth stating that there is a blind zone in the near field of C-WNC images, shown in Fig. 5.5(c) and (d) around 0 ~ 7 mm in range in the near field where the results are distorted by a "spatial comb". This is a result of spatial aliasing of the supervector formulation of matched field beamformers, and the pattern is dependent on the choice of sampled frequencies of the augmented broadband array.

The cause of dynamic range bias in the C-WNC beamformer as well as its high-resolution characteristic are illustrated in Fig. 5.6. As revealed by Song et al. [52], the amount of bias to be expected is related to the minimum diagonal loading γ to the CSDM $\tilde{C}(\Omega)$ to make the matrix invertible. Note that the quantity γ is an location independent variable which limits the minimum value allowed in the optimization of $\varepsilon(x, y)$. Fig. 5.6(a) shows the eigenvalues of a typical multitone TRO $\tilde{C}(\Omega)$ of an example slit that is 5 λ wide and 10 λ in range. The dimension of $\tilde{C}(\Omega)$ is 3×32 = 96 due to the formulation of broadband supervector, and the rank of $\tilde{C}(\Omega)$ is M = 32 expected from the orthogonality of single element transmissions. The eigen modes indexed larger than 32 are non-physical modes. Inversion of the multitone TRO is by nature an ill-imposed problem because augmenting the beamformer to supervectors does not add to the rank in the covariance matrix. Song et al. pointed out that when the minimum allowed loading γ is much smaller than the smallest physical eigenvalue λ_n, a power bias $2\times\gamma/\lambda_n$ is present at the source locations in the output of WNC

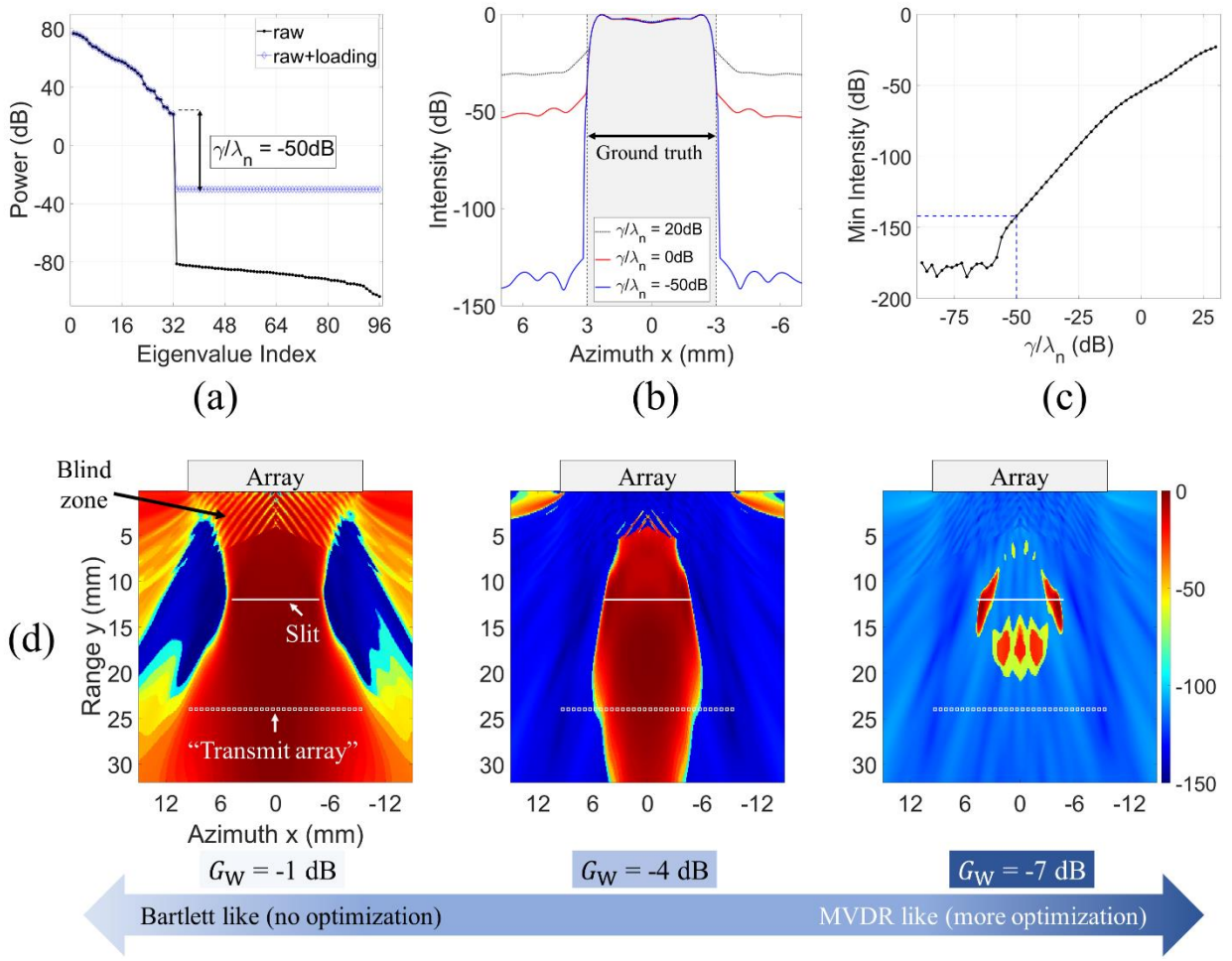

Figure 5.6: Cause of high-contrast and high-resolution features in C-WNC images. (a) Variation of multi-tone TRO eigenvalues with a loading of γ/λ_n = -50 dB. (b) Variation of C-WNC noise floor by setting different γ. (c) Effect of γ on the output bias. (d) The effect of G_W in optimization: C-WNC images with G_W set to -1 dB, -4 dB and -7 dB.

beamforming of a rank deficient covariance matrix. This output bias is not available in traditional MVDR beamformers because the load γ is static that results in the same elevation at all locations. As revealed in [51], the expected peak-to-background ratio of C-WNC is calculated as [–SNR – array gain – white noise constraint + 2 × γ/λ_n]. For example, when γ/λ_n = -50 dB as in Fig. 5.6(a), the SNR (signal amplitude over the waveform's root mean square) is approximately 25 dB in the simulation, the array gain is [10 log(3×32)] = 19.8 dB, and the white noise gain G_W is set as -3.5 dB. The theoretical peak-to-background ratio is -25-19.8-(-3.5)+2×(-50) = -141.3 dB, which is

consistent to the minimum reading of -140 dB in the blue line profile as in Fig. 5.6(b). By repeating the experiment as in Fig. 5.6(b) using different static loading γ in the optimization of $\varepsilon(x, y)$ with increments of 2 dB, Fig. 5.6(c) shows that the noise floor of C-WNC beamformer decreases with the loading γ by a slope of 2 as found in previous literatures. The minimum value of γ that reaches the machine precision for matrix inversion is found to be γ/λ_n = -60 dB where no further bias is observed with a smaller γ.

For the goal of imaging extended targets using a linear array, it is critical to ensure that a moderate control parameter G_W is applied to the optimization to include the eigen modes focusing on the tips of the extended targets. The effect of tightening G_W on C-WNC imaging results is shown in Fig. 5.6(d) using a 32×32 FMC dataset. The example slit is 8 λ wide and 10 λ in range. A loose constraint (G_W = -1 dB) makes the beamformer to be "Bartlett like" which allows all eigen structure components discussed in Fig. 5.5(b) to come in as "target". The good news is that the passing region still indicates the lateral width of the slit with high dynamic range. A medium constraint (G_W = -4 dB) starts to reject the passing region and part of the mirrored transmit array. Finally, a tight constraint (G_W = -7 dB) rejects most of the passing region and only preserves the resolution cells at the tips of the slit. The elevated noise floor in this tight constraint arises from the fact that the added white noise $\varepsilon(x, y)$ is fairly small at the focus (main lobes) which reaches the machine precision limit for matrix inversion of $\tilde{C}(\Omega)$. Since the resolution cells at the tip of the slit is the most significant in the eigen structure of $\tilde{C}(\Omega)$ for this example, the C-WNC images always guarantee a dramatic drop of intensity along the azimuth direction regardless of the constraint used. However, for algorithm robustness, it is always desired to leave enough room to allow more resolution cells to come through in the optimization. For the remaining results in this paper, a constraint of G_W = -3.5 dB seemed reasonable to use as recommended in [51].

5.4.1.3 Imaging results of simulated slits of different sizes and ranges

A comparison between MUSIC and C-WNC on imaging extended targets in the near field (10 λ in range) is made in Fig. 5.7. Again, the noise space threshold of MUSIC is set by Eq. 5.14 with a known lateral size of the target as an input. The constraint G_W is set to -3.5 dB. Fig. 5.7(a) shows the images of a 5 λ wide slit. Both matched field beamformers present good lateral focus on the entire slit since the tip scattering and the passing region is dominant for a small lateral target. The maximum intensity occurs at the resolution cells on the tip of the slit for both algorithms. The advantage of the dynamic range bias is significant for C-WNC to determine the cut-off intensity threshold for lateral size estimation. Fig. 5.7(b) shows the images of a wider 10 λ slit. The eigen structure tends to emphasize part of the mirrored transmit array due to the longer continuous surface reflections. Since the MUSIC image shows the maximum intensity around 20 mm in range, a bias (red line) is added to the lateral line profile at the ground truth axial range to normalize the maximum to 0 dB for comparisons. The C-WNC image still gives a satisfactory result since the moderate G_W allows most eigen modes to come in as "signal". The most difficult task is to image a 15 λ wide slit that is comparable to the 16 λ physical aperture of the array, as shown in Fig. 5.7(c). The MUSIC image shows the maximum at the center of the mirrored transmit array, and even the biased lateral line profile shows low intensity at the tip of the slit. This means that even though the MUSIC beamformer uses an equal weight for all subspace eigenvectors, it cannot erase the unevenness in focusing power between eigen modes. The C-WNC image also suffers from the same issue, but the robust G_W allows the resolution cells at the tips to pass through as "signal" that guarantees a high contrast resolution cell. The peak intensity at the tips is -30 dB (normalized to the maximum at the mirrored transmit array). However, the gap between the resolution cells at the tips and the passing region is still problematic.

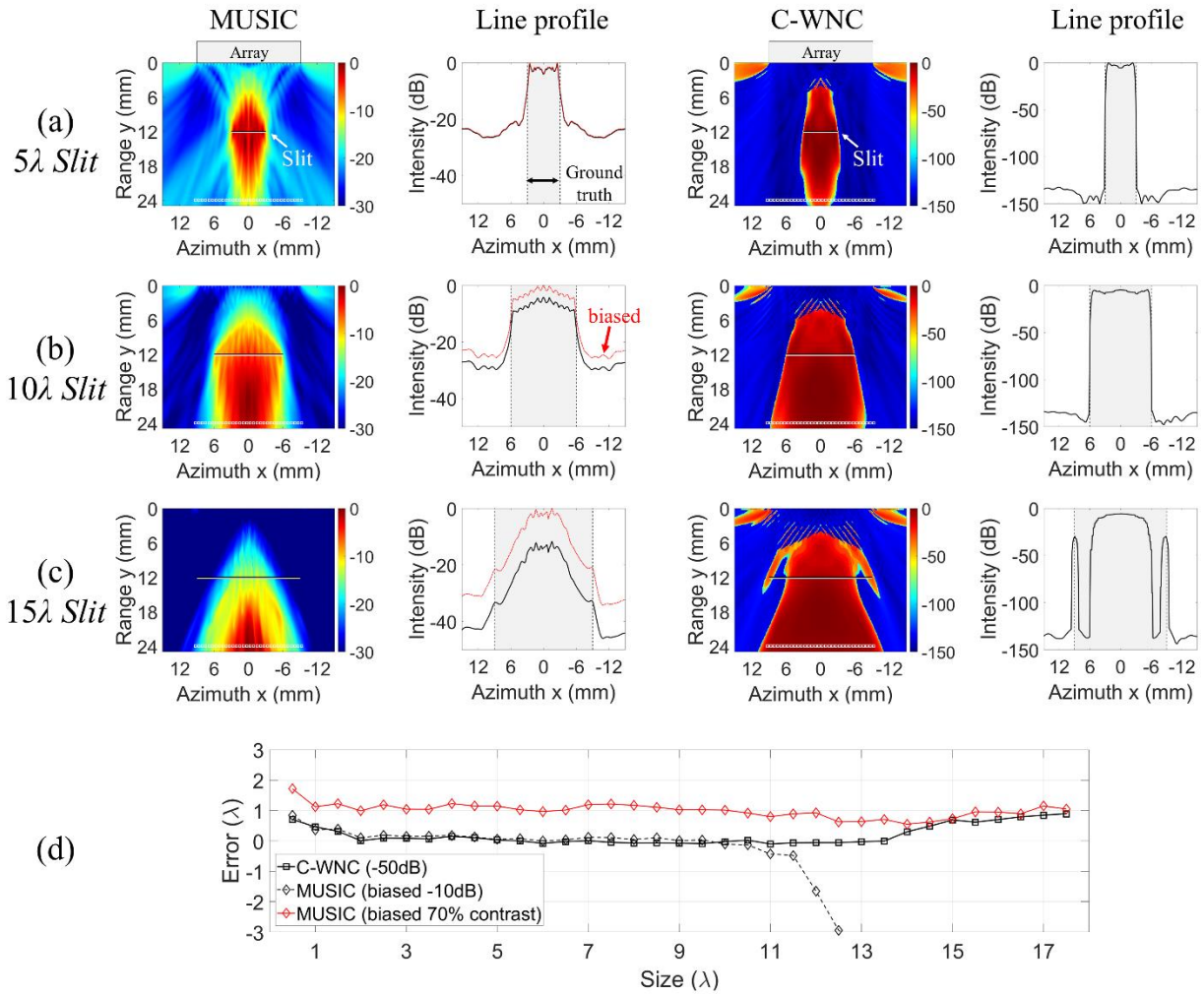

Figure 5.7: Comparison of MUSIC and C-WNC for imaging extended targets in the near field (10 λ in range). Images and lateral line profiles of slits with sizes of (a) 5 λ, (b) 10 λ, and (c) 15 λ. (d) Sizing error of MUSIC and C-WNC images using different thresholding criteria.

Fig. 5.7(d) compares the lateral size estimation of the matched field beamformers using the lateral line profiles at the ground truth axial range. Since the dynamic range is large for C-WNC, the threshold is set to -50 dB. The size is determined by the largest distance between intersections of the line profile and the threshold intensity to avoid underestimation due to the separation of resolution cells as seen in Fig. 5.7(c). For MUSIC two criteria are used. First is to fix the threshold at -10 dB, and second is to set a dynamic threshold equal to 70% of the contrast (maximum over minimum intensity). For either option, the line profile of MUSIC is biased since in most cases the

maximum in the image does not locate the correct axial range. It is shown that for both beamformers the lateral size is overestimated when it is close to the wavelength (0.5 ~ 2 λ). This is because the scattering at the tip of the slit is dominant in the TRO. The center locations of these resolution cells fall exactly on the tips, which leads to an overestimation of one lateral width of the cell. As the size of the slit increases, both C-WNC and MUSIC (-10 dB criteria) shows an accurate lateral sizing, until MUSIC (-10 dB criteria) first fails around 12 λ. The second option of MUSIC (70% contrast criteria) is more stable for all sizes tested with an overestimation of ~1 λ. However, the accurate trace of thresholding in MUSIC is the result of trial and error. In contrast, the C-WNC beamformer is more robust with the variation of the lateral target size. The only limitation in the C-WNC performance is that it tends to overestimate the size by ~1 λ when the slit is comparable to the array physical aperture (>14 λ). The reason is revealed in the example shown in Fig. 5.7(c) where the PSFs at off-axis locations are distorted and tilted due to the azimuth coverage of a physical aperture, resulting in increasing overestimation as the slit grows wider.

Fig. 5.8 shows the comparison of MUSIC and C-WNC when the slit is at 20 λ and 30 λ in range. The 10 λ wide examples in Fig. 5.8(a) and (b) show that the imaging performance is similar for each beamformer regardless of the axial location. For the MUSIC images, the focus is shifted to a deeper range due to the mirroring effect from the surface, while the resolution cells at the tips are ~10 dB weaker than the maximum in the biased line profiles. For the C-WNC images, only the resolution cells at the tips are accepted and other eigen modes are rejected in the optimization. This still guarantees a high contrast focus at the boundary of a slit. Fig. 5.8(c) shows the sizing error of each beamformer at different ranges as a function of lateral size. The MUSIC beamformer shows that the error decreases with increasing slit size. Also, the size estimation of MUSIC at $Y = 30\ \lambda$ is always ~1 λ larger than the one at $Y = 20\ \lambda$. This is because the dynamic range of MUSIC images

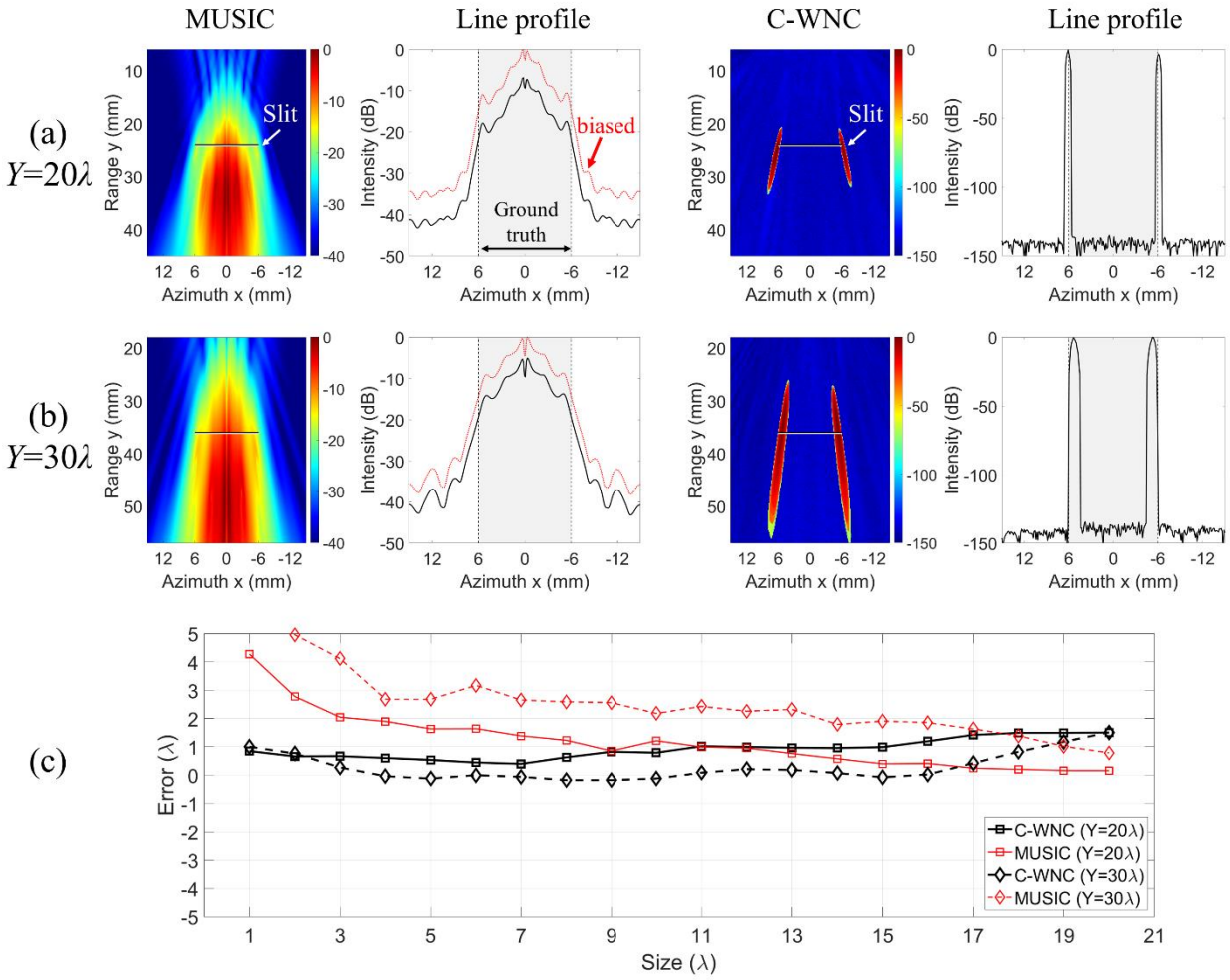

Figure 5.8: Comparison of MUSIC and C-WNC for imaging extended targets at farther ranges. Images and lateral line profiles of slits with sizes of 10 λ at (a) Y = 20 λ and (b) Y = 30 λ. (c) Sizing error of MUSIC and C-WNC images. The threshold for MUSIC is 70% of biased dynamic range, and the threshold for C-WNC is -50 dB.

can vary greatly depending on the lateral size and axial range of an extended target. In contrast, the C-WNC images show a consistent lateral size regardless of the axial range of the slit at 20 λ, with an overestimation of 1 λ due to the finite size of PSFs. For the 30 λ case, there is slight overestimation present when the slit is either too small (e.g. a point scatterer) or too large (e.g. close to the size of the array physical aperture). Regardless, at both tested axial ranges the C-WNC beamformer controls the error within 1 λ when the slit size is smaller than the physical aperture.

5.4.2 Simulation of Time Delay Beamforming

5.4.2.1 Imaging results using Delay-Multiply-and-Sum beamformer

Since the C-WNC beamformer only guarantees the resolution cells at the discontinuous scattering tips of a slit, it is important to look at time-delay type beamformers to highlight the continuous scattering part of an extended target. Fig. 5.9 shows the DMAS imaging results of a 6 mm (5 λ) slit using the k-wave simulation of the same 32-element array as in section 5.4.1. The result in Fig. 5.9(a) uses $r_{nm}(t)$ to approximate the interelement response $k_{nm}(t)$, while in Fig. 5.9(b) a NCPS is performed in the frequency domain using Eq. 5.2 to deconvolve the known transmission signal (5 MHz tone burst with 2 cycles). The comparison of the DMAS images in Fig. 5.9(a) and (b) shows that the NCPS deconvolution scheme corrects the axial range position of the slit at the expense of image contrast. The advantage of the deconvolved transfer function is more eminent in the axial line profile shown in Fig. 5.9(c). Not only does the deconvolved result focus on the ground truth range distance, but the axial main lobe width is also compressed. In the lateral line profile comparison in Fig. 5.9(d), the intensity of DMAS main lobe is more uniform with the deconvolved waveforms with an increase of 4 dB in the main lobe center. Considering that the 5 λ lateral slit is relatively small compared to the 16 λ array, this represents an additional advantage of performing deconvolution for time domain beamformers. An estimation of the slit lateral size can be performed by assigning a threshold between -30 dB to -15 dB, but the result is highly dependent on the SNR. Moreover, the time delay beamformers usually overestimate lateral size due to the finite sized PSF constrained by the Rayleigh diffraction limit. These considerations suggest the combination of matched field beamformers for optimum resolution and contrast of extended target.

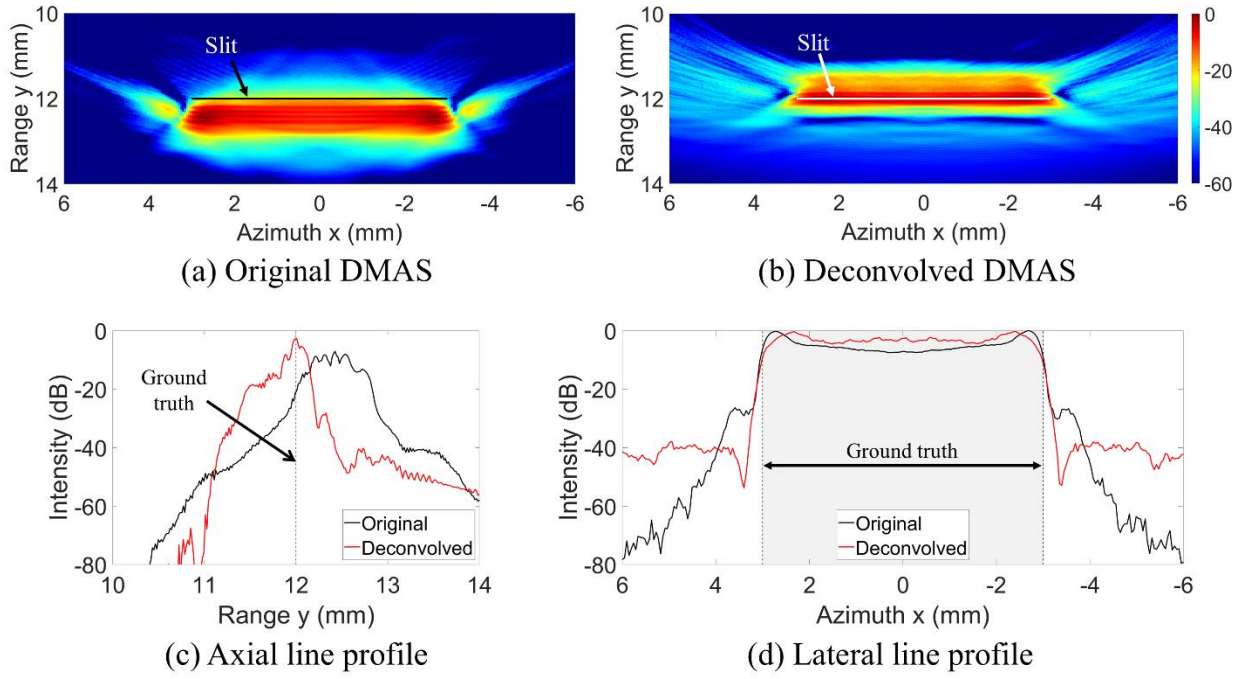

Figure 5.9: Effect of deconvolution in time-delay type beamformers. (a) DMAS image of an extended target with a lateral size of 5λ by beamforming $k_{nm}(t) \approx r_{nm}(t)$ directly. (b) DMAS image by beamforming $k_{nm}(t)$ using cleansed IFFT results after NCPS deconvolution. Line profile comparison in (c) axial direction and (d) lateral direction.

5.4.2.2 Combining time reversal algorithms

Since the matched field beamformers are more sensitive to direction-of-arrival (cross-range), it is valuable to consider the superposition of time-delay beamformers and matched field beamformers to obtain high resolution in both range and azimuth directions as in [53]. A basic combination can be a conditional summation of normalized power outputs from the beamformers in decibels:

$$I^{\text{Combined}}(x,y) = \begin{cases} I^{\text{DMAS}}(x,y), & \text{if } I^{\text{DMAS}}(x,y) \text{ in dB} \geq \kappa \\ I^{\text{DMAS}}(x,y) + I^{\text{C-WNC}}(x,y), & \text{if } I^{\text{DMAS}}(x,y) \text{ in dB} < \kappa \end{cases} \tag{5.27}$$

where the combined image only takes the value of the DMAS beamformer when the value of the decibel scale DMAS image is larger than a threshold κ to preserve the continuous part of the extended target, and the combined image takes advantage of the dynamic range bias and resolution

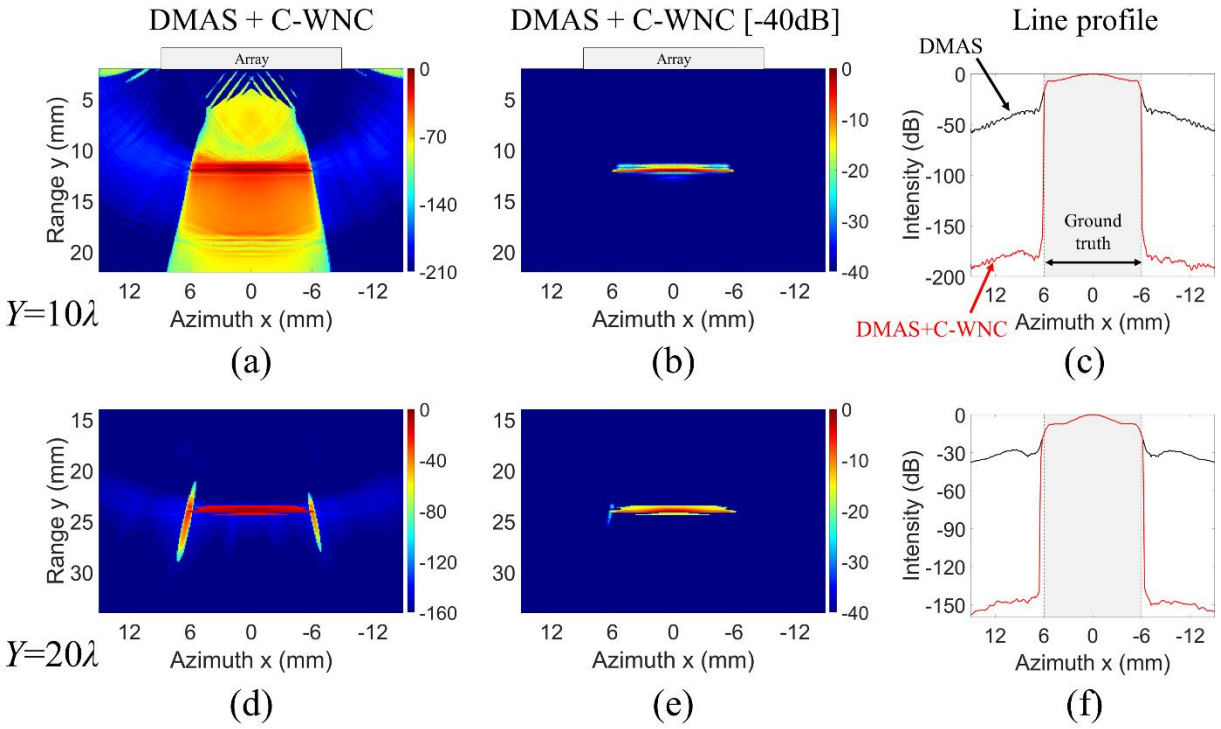

Figure 5.10: Combined DMAS and C-WNC image of a 10 λ lateral slit at 10 λ range, displayed with (a) 200 dB, (b) 20 dB dynamic range, and (c) lateral line profile. Combined DMAS and C-WNC image of a 10 λ lateral slit at 20 λ range, displayed with (d) 200 dB, (e) 20 dB dynamic range, and (f) lateral line profile.

cells from C-WNC image to highlight the discontinuity of the target for regions below the threshold κ. The value of κ should be chosen small enough to include the unevenness in the main lobe of the DMAS beamformer, but large enough to reject the side lobe of the DMAS beamformer to avoid overestimation.

Fig. 5.10 shows the combined images in both near field and far field simulations of a 10 λ slit with κ set to -20 dB. For the near field case, the C-WNC beamformer highlights mostly the passing region with G_W = -3.5 dB, resulting in intensity levels around -70 dB in the passing region of Fig. 5.10(a). A satisfactory image can be displayed by setting the minimum intensity to -40 dB as in Fig. 5.10(b). With the help of the dynamic range bias from C-WNC, the combination of beamformers shows significant contrast improvement in the lateral line profile of Fig. 5.10(c). For

the far field case as in Fig. 5.10(d), the C-WNC beamformer only highlights the resolution cells at the tips. The conditional summation scheme proposed in Eq. 5.27 ensures the main lobe of DMAS is preserved when there is no passing region in C-WNC, so a similar image is obtained by plotting in 40 dB dynamic range as in Fig. 5.10(e). Again, the improvement in contrast is impressive, with an overestimation of lateral size of ~1 λ due to the finite size of C-WNC point spread function at the tip locations, as revealed in the line profile in Fig. 5.10(f). For both examples, the resolution in range is provided by the DMAS beamformer, and the high contrast azimuth focus is provided by the C-WNC beamformer.

5.5 Experimental Results

Experimental tests with the various beamformers were conducted to image drilled holes and slots in an aluminum block. The transducer was a 64-element linear array (Olympus NDT 5L64-A12) with central frequency at 5 MHz, 38.4 mm total active aperture, and 0.6 mm element pitch. The excitation $e_m(t)$ was a 5 MHz square wave with one cycle. As schematized in Fig. 5.11, the imaging targets were: two side drilled holes (SDHs) of 0.5 mm in diameter, and two slits of 6 mm and 30 mm in length (both 1.2mm in height). All targets were drilled to a depth of 5 mm from the surface of the block per safety protocols, so the 2D plane-strain assumption does not perfectly apply to the experimental data. Also, due to the finite size of the drill bits, the two ends of the slots were round, hence different from ideal "sharp" tips of the simulations.

5.5.1 Improved Replica Vectors Using Wave Mode Reception Structure

First, the improvement in replica vectors for better match with experimental data is shown in Fig. 5.12 when imaging the two SDHs. The results using free field Green's function (only the Hankel function in Eq. 5.9) are compared with the results using weighted Green's function with

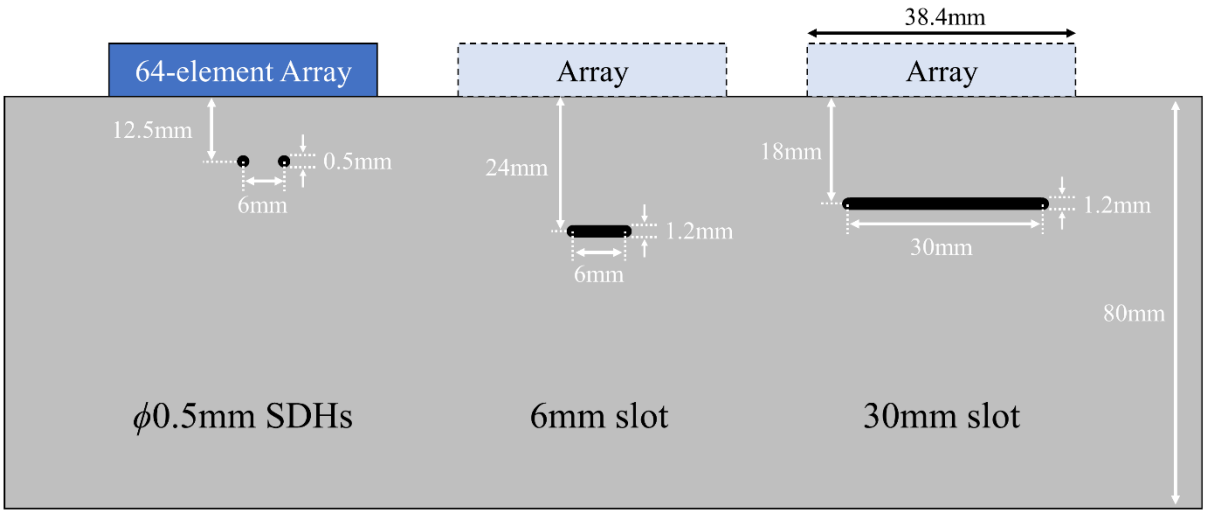

Figure 5.11: Experimental test on reflectors in an aluminum block: two 0.5 mm diameter SDHs at Y = 12.5 mm, a 6 mm wide slot at Y = 24 mm, and a 30 mm wide slot at Y = 18 mm. The slots were drilled by 1.2 mm diameter drill bits.

3D geometrical spreading and wave mode structure weights (full expression in Eq. 5.9). The broadband sampling frequencies are at 4, 5.25, and 6.5 MHz for all experimental results. These SDHs are not point scatterers because their diameter (0.5 mm) is close to half of the wavelength (1.2 mm) at the center band. All five match field beamformers listed in Fig. 5.3 are used for this comparison. Fig. 5.12(a) shows the incoherent MUSIC image using a signal space dimension N_s = 2. Though the two SDHs have sizes comparable to the sampled wavelengths that may result in an N_s larger than 2, the current result shows two distinguishable main lobes with high resolution in both azimuth and axial ranges. Compared to the free field case, the weighted Green's function suppresses the noise floor in the MUSIC image by 5dB except around the off-axis SDH at x = 5 mm. Fig. 5.12(b) shows the incoherent Bartlett image that is an average of the monotone linear beamformer ambiguity surfaces as in Eq. 5.11. Since this is the most standard option (no SVD or adaptive beamforming), the focus is weak at the two SDHs. The improvement in dynamic range using the weighted Green's function is roughly 4 dB seen from the lateral line profile. Fig. 5.12(c)

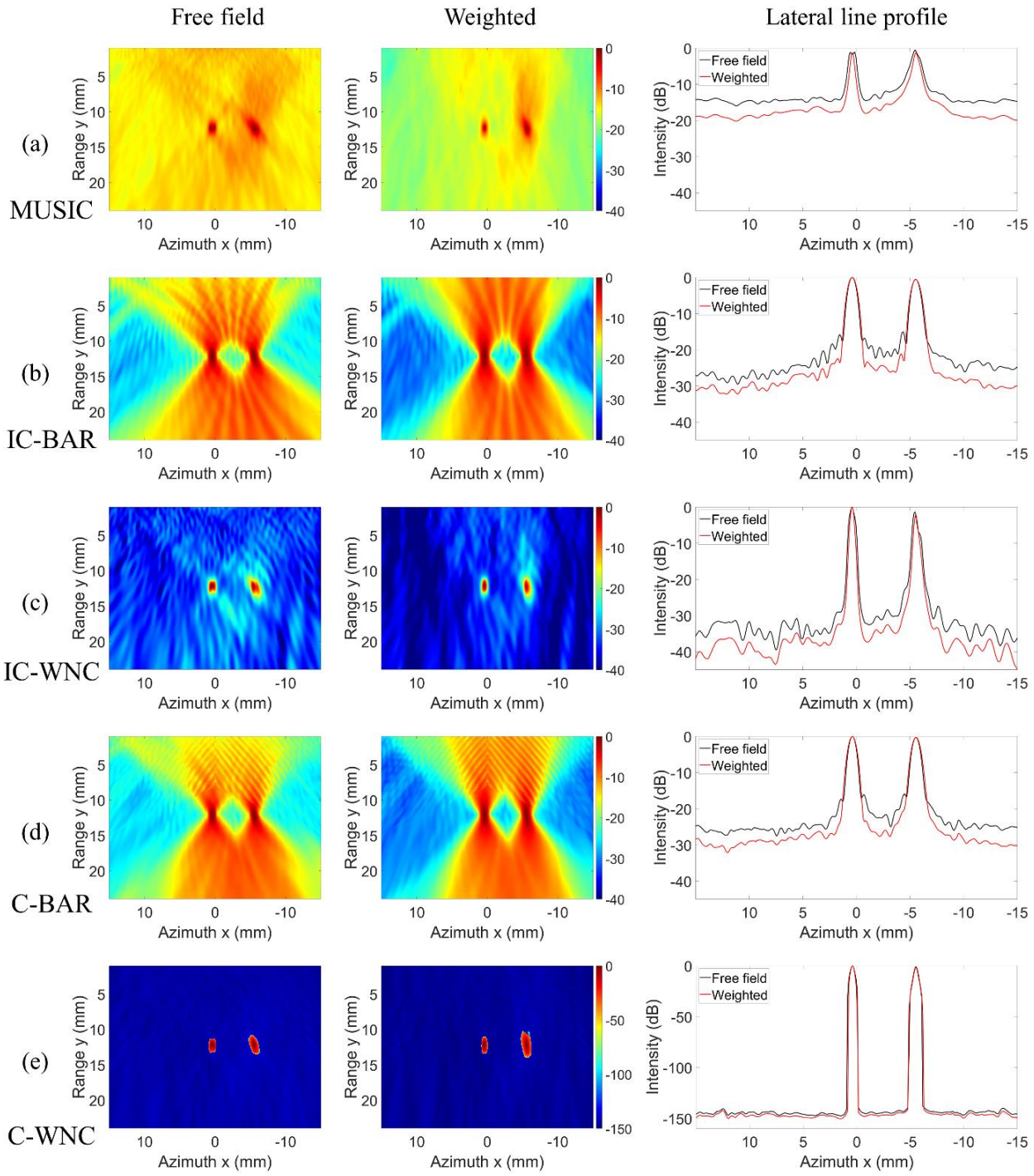

Figure 5.12: Comparison of replica vectors using free field Green's function versus modified Green's function considering geometrical spreading and wave mode reception structure. Imaging results on two SDHs using (a) incoherent MUSIC, (b) incoherent Bartlett, (c) incoherent white noise constraint, (d) coherent Bartlett, and (e) coherent white noise constraint.

shows the incoherent average of the narrowband WNC images by adaptively beamforming the monotone TRO $\hat{C}(\omega)$ at the three sampled frequencies. The optimization of narrowband replica vectors gives high resolution characteristics, but there is no dynamic range bias since $\hat{C}(\omega)$ is full rank as discussed in Eq. 5.7. For the free field case, the image has higher resolution by showing two closely located resolution cells at each SDH. The weighted Green's function image shows a single resolution cell for each SDH, but the noise floor is suppressed by ~6 dB. Fig. 5.12(d) shows the linear beamforming output of coherent supervector formulation of multitone TRO $\tilde{C}(\Omega)$. Though a theoretical [10 log(3)] = 4.7 dB additional array gain is expected with the supervector formulation, modeling mismatch in the broadband frequencies unfavorably makes the linear beamforming of multitone TRO similar to its monotone counterpart as in Fig. 5.12(b). In addition, the near field blind zone is enlarged compared to the 32-element array simulation because the azimuth coverage of spatial aliasing comb is proportional to the physical aperture width. Regardless of these drawbacks, the weighted Green's function in C-BAR still shows suppression of ~4 dB like IC-BAR. The last option is to use the proposed coherent white noise constraint processor (C-WNC) as in Fig. 5.12(e). The dynamic range bias results in high contrast that makes the output binary like. The dynamic range improvement of the weighted case is still around 5 dB, but the change of noise floor is not comparable to the significant power output bias produced by the WNC algorithm. To summarize, all four beamformers confirm that the weighted Green's function improves the azimuth focus at the expense of the axial range focus. The rest of the experimental results use the weighted Green's function to maximize the lateral/azimuth focusing ability of the match field beamformers.

5.5.2 A 6 mm Lateral Slot at 24 mm Range

The first tested slot was drilled 6 mm in length and 24 mm deep from the top surface of the block, and the beamforming results are shown in Fig. 5.13. The extended target is expected to be clearly seen by the array because the lateral size is small compared to the physical aperture, and the location is not too shallow in range. To illustrate, the eigen structure of monotone TRO $\hat{C}(\omega)$ is plotted by sampling at a dense number of frequencies across the transducer bandwidth in Fig. 5.13(a). A clear gap between the signal space and noise space is observed, with more eigen modes joining the signal space as the frequency increases. In addition, the theoretical signal space dimension N_s plotted in bolded black line aligns with the energy gap in eigen structure. The incoherent broadband MUSIC image is shown in Fig. 5.13(b). The collection of resolution cells aligns well with the ground truth in azimuth, but again the exact size indication depends on thresholding the intensity around -25 ~ -15 dB. For the C-WNC image in Fig. 5.13(c), the result shows a passing region as well as two resolution cells on the tips with high contrast. Finally, the DMAS image in Fig. 5.13(d) is combined with the C-WNC image by setting the threshold κ to -25 dB. The combined image is plotted both in full dynamic range (250 dB) in Fig. 5.13(e) and a smaller dynamic range (50 dB) in Fig. 5.13(f). Note that similar results can be obtained using an arbitrary κ within -30 ~ 0 dB that corresponds to the DMAS main lobe fluctuation along the ground truth slot. This shows high robustness to obtain a good quality image with focus in both azimuth and range directions as in Fig. 5.13(f). The accuracy of the combined image is illustrated in the line profiles shown in Fig. 5.13(g) and (h). In the lateral (azimuth) direction, the highest intensity is found at the transition of the slot where the flat surface turns to a round corner due to the finite size of the 1.2 mm drill bit. These two transition points are marked by blue lines in Fig. 5.13(g) and their 6 mm separation exactly correspond to the traveling distance of the center of drill bit.

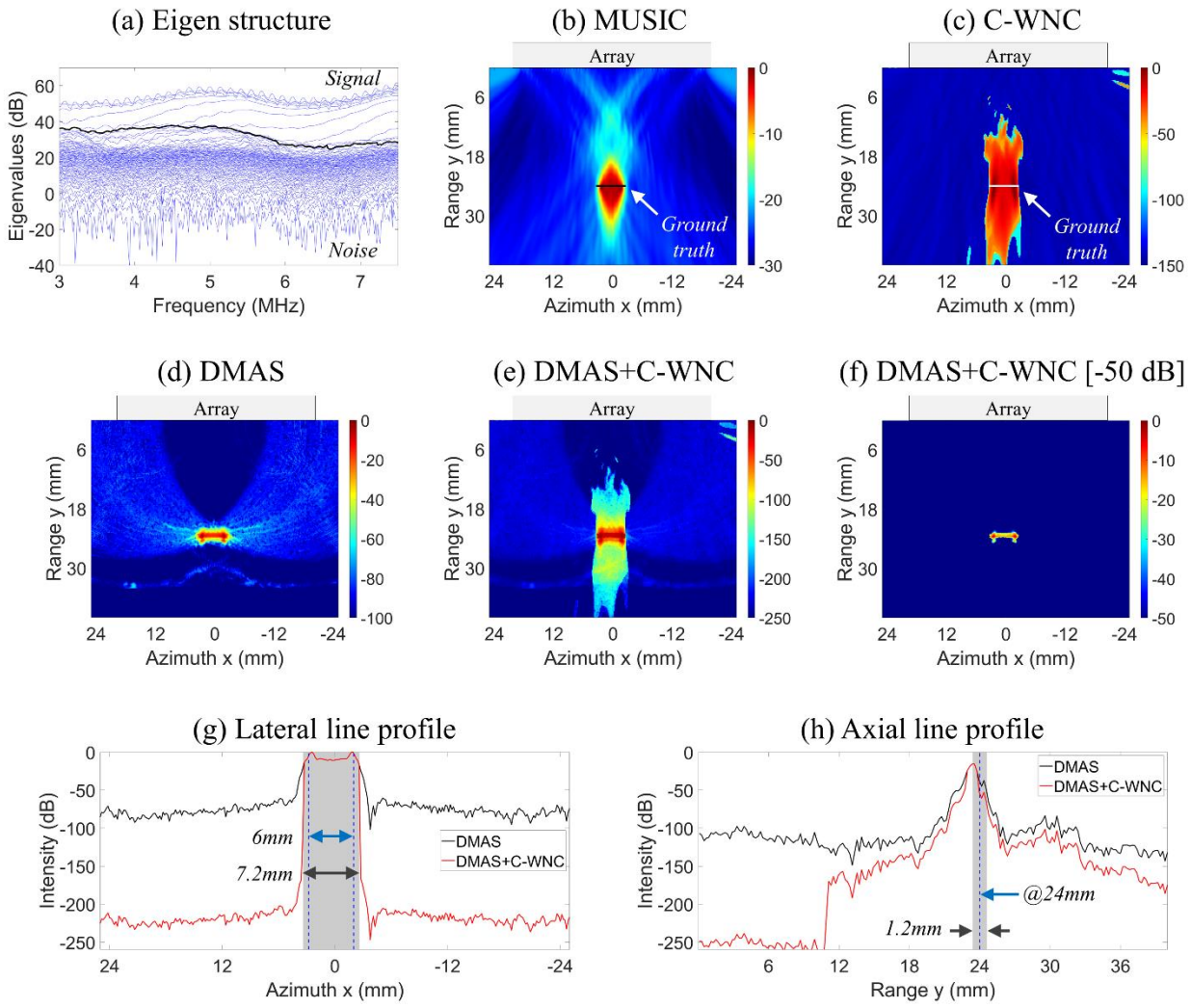

Figure 5.13: Experimental results on a 6 mm lateral slot at 24 mm in range. (a) Variation of eigenvalues. Match field beamforming result using (b) MUSIC and (c) C-WNC. (d) Time-delay beamforming result using DMAS. Combined DMAS and C-WNC image displayed using (e) 250 dB and (f) 50 dB dynamic range. (g) Lateral and (h) axial line profiles.

The boundary of C-WNC resolution cells tend to match the high contrast lateral line profile with the maximum width of the slot (7.2 mm). However, this is a coincidence because the linear array cannot see the side of a curve due to the limited angle of view, and the match is due to the same size of the drill bit as the PSF (1.2 mm resolution) of C-WNC at the 24 mm range. The focus in the axial range direction is provided by the DMAS beamformer, as shown in the axial line profile by cutting along x = 0 in Fig. 5.13(h). The improvement by combining C-WNC is limited because

of the lack of focus in the axial range for match field beamformers. The maximum of the axial line profile is not 0 dB because scattering on the tips is stronger than flat line reflections at the center of the slot. As a benefit from deconvolution, the axial focus matches the front boundary of the slot that is at [24-1.2/2] = 23.4 mm in range considering the finite thickness of the slot.

5.5.3 A 30 mm Lateral Slot at 18 mm Range

The second slot was drilled 30 mm in length at a depth of 18 mm from the top surface of the block. This is a more challenging case because the 25 λ lateral size is comparable to the 32 λ physical aperture of the transducer array. In addition, the 15 λ axial range makes the extended target take up more azimuth coverage in the illuminated region. This complicates the direction-of-arrival beamforming because the discontinuity at the tips can be too weak to be detected. The eigen structure shown in Fig. 5.14(a) contains both signal and noise subspaces with no clear indication of energy gap. The theoretical subspace dimension criteria plotted in bolded black line suggests that the signal space varies dramatically with frequency, and the subspace methods fails over 6.3 MHz since the signal space is saturated. The MUSIC image is shown in Fig. 5.14(b) using the known extended target size and location as inputs to determine N_S as in Eq. 5.14. The MUSIC image seems to capture the lateral width at the ground truth range with low contrast, while the maximum intensity is seen at the "mirrored" transmitter array due to the large flat line reflections. In contrast, the C-WNC image of Fig. 5.14(c) preserves the resolution cells at the tips with high contrast (-20 dB focus compared to the -150 dB noise floor) when normalized to the largest response seen at the mirrored transmit array. The resolution cells at the tips are extended to the blind zone, and their sizes are different due to the tiny asymmetry of the transducer array positioning. The combined image with full dynamic range in Fig. 5.14(e) shows that the proposed conditional acceptance scheme preserves the main lobe response of DMAS beamformer for the

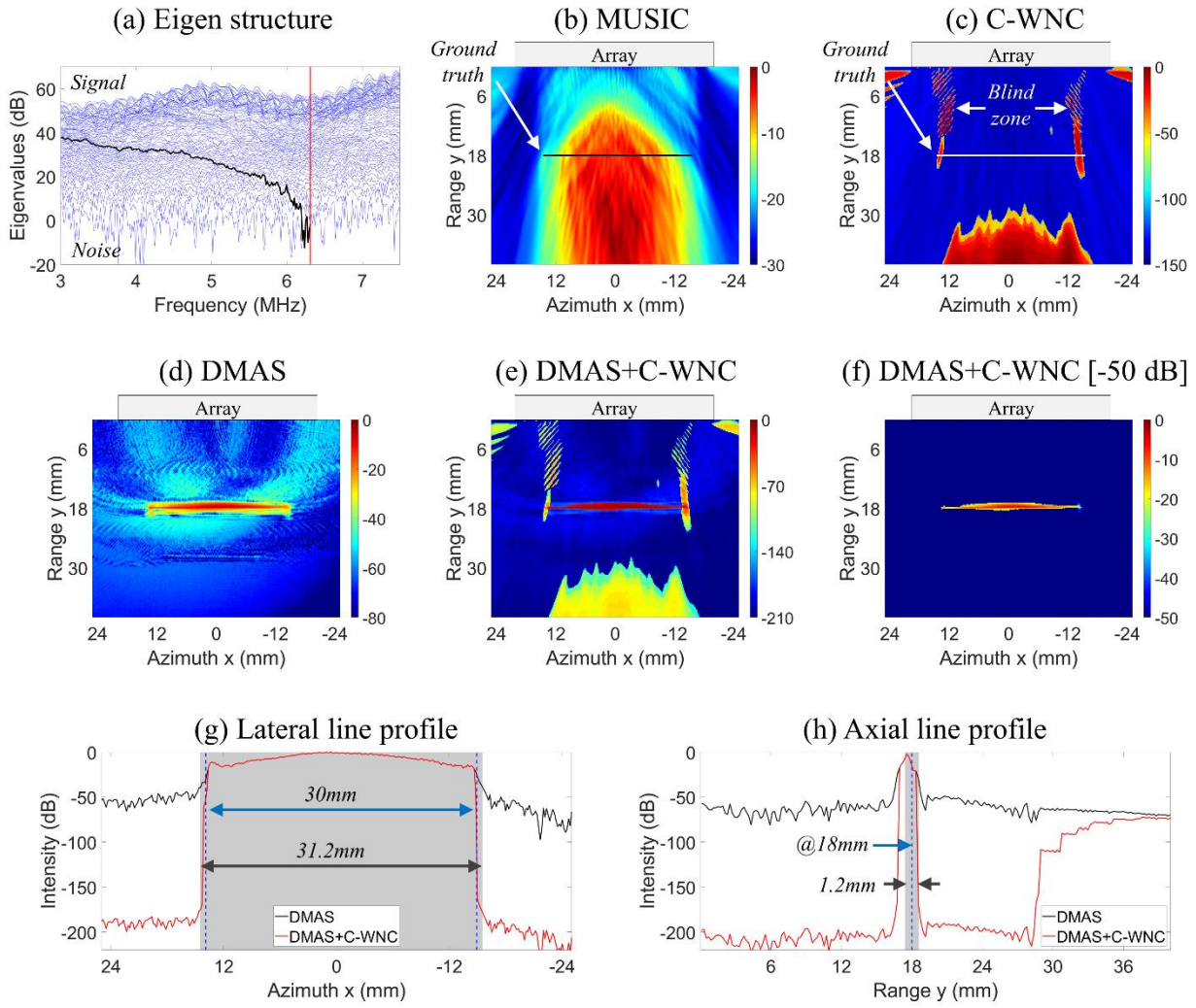

Figure 5.14: Experimental results on a 30 mm lateral slot at 18 mm in range. (a) Variation of eigenvalues. Match field beamforming result using (b) MUSIC and (c) C-WNC. (d) Time-delay beamforming result using DMAS. Combined image displayed using (e) 210 dB and (f) 50 dB dynamic range. (g) Lateral and (h) axial line profiles.

flat surface, and the resolution cells from C-WNC define the end of the lateral width. Although the 50 dB plot in Fig. 5.14(f) still gives a decent high contrast image, the choice of threshold κ is delicate due to the larger variation of the DMAS main lobe for a wide target. Thanks to the noise suppression by exploiting cross term correlations in DMAS, there is still room to determine κ while not dramatically changing the imaging result. The 30 mm slot example uses the same κ = -25 dB as the 6 mm slot. Different from the observations for the 6 mm slot in Fig. 5.13(g), the lateral line

profile of the 30 mm slot in Fig. 5.14(g) coincides with the 30 mm width of the flat surface. However, as seen in Fig. 5.14(c) the C-WNC image underestimates the flat surface with the resolution cells focusing inside the slot. The shift in azimuth is due to the focusing limitations of match field beamformers at off-axis locations. For the axial line profile of Fig. 5.14(h), the maximum is again at the front boundary of the slot (y = [18-1.2/2] = 17.4 mm) and the high contrast focus is the result of preserving the DMAS main lobe using conditional thresholding.

5.6 Discussions and Conclusions

This chapter proposes a method for ultrasonic imaging of extended targets with high resolution and contrast in both azimuth and axial range. The proposed method combines concepts of adaptive match field beamformers and time-delay type beamformers. Specifically, the broadband coherent white noise constraint (C-WNC) beamformer is formulated to obtain high contrast image of scattering coming from the target's sharp tips, whereas the delay-multiply-and-sum (DMAS) beamformer is employed to obtain focused image of scattering coming from the target's extended surface. The C-WNC beamformer provides azimuth resolution and the DMAS beamformer provides axial range resolution. Compared to the SVD based match field beamformers such as MUSIC, the C-WNC requires no knowledge of the signal subspace dimension in the transfer matrix decomposition. By formulating the transfer matrix into cross-band for active sensing, an added improvement in dynamic range is given to the C-WNC image resulting from the rank deficiency of multitone covariance supermatrix.

The transfer function of conventional active FMC scheme is estimated through a deconvolution operation by calculating normalized cross power spectrum with known transmission signals. The deconvolution operation calibrates the arrival time for axial range

estimations in time-delay type beamforming and improves match field beamforming by eliminating the source spectrum.

The popular "super resolution" imaging method aimed at resolving the Rayleigh diffraction limit is to use a SVD analysis of the transfer matrix, as done in MUSIC type algorithms discussed in this paper. However, MUSIC type beamformers face several drawbacks when imaging an extended target in the near field. The theoretical signal space dimension changes dramatically with wavelength, which complicates the task of separating subspaces when sampling at multiple frequencies across the band of interest. It is shown in simulation and experiments that when the size of the extended target is comparable to the physical aperture of the array, the mirroring effect of the continuous surface scattering dominates the signal space, making the subspace decomposition threshold hard to determine. Even though the MUSIC type beamformers discard the relative intensity (i.e. singular values) of the singular modes, the resolution cells at the ends of extended targets are not distinguishable due to the reduced sensitivity at off-axis azimuth locations. Furthermore, the MUSIC beamformer output is highly dependent on the SNR of the eigen structure, which makes it difficult to establish a universal criterion to trace the lateral size.

This chapter approaches high resolution imaging through adaptive beamforming techniques that require no subspace decomposition of the transfer matrix. Since the multitone covariance matrix is found rank deficient and thus needs diagonal loading to allow inversion, the proposed C-WNC algorithm imposes a constraint on the white noise gain to the replica optimization so that the beamformer output at the source locations are controlled by the maximum assigned sensitivity. It is interesting to observe that at these locations of source resolution cells, the C-WNC algorithm puts minimum diagonal loading to inverse the covariance matrix resulting in a significant dynamic range bias over the rejected noise floor. This gives great potential for

correctly identifying the lateral size of an extended target from the pixel intensity map. It is worth stating that the large dynamic range does not guarantee a better detectivity of the C-WNC algorithm under low SNR, as discussed in [51]. Another advantage of C-WNC is that the resolution cells at the ends of extended targets are always available after optimization, whether the target is in the near field or the far field. This is because the adaptive beamformers tend to find point sources such as tip scattering, while rejecting the reflections from a continuous flat surface. If the white noise gain constraint increases, the C-WNC algorithm first rejects the passing region that is extended from the "mirrored" transmit array. Thus, a moderate WNC parameter assures robustness to locate the discontinuous ends of the extended target with extremely high contrast. The C-WNC beamformer was tested on simulated slits with sizes ranging from 1 to 20 λ and axial ranges of 10, 20, and 30 λ from a 5 MHz 32-element array with half λ pitch (a 16 λ aperture width). The proposed C-WNC algorithm was found to outperform MUSIC in all cases, especially when the slit is the near field and is large compared to the array aperture.

The chapter also borrows the concept of wave mode amplitude windowing previously developed for time-delay beamforming to generate improved replica vectors for the match field beamforming. In particular, the amplitude distribution across the reception array is adjusted according to the ray path connecting a candidate focus point and each element. Both the geometric spreading factor and the angle of incidence denoting the sensitivity of transducer elements to the longitudinal wave particle displacements are considered to increase modeling accuracy. Experimental results on drilled holes show that the use of such weighted replica vectors results in a 5 dB gain compared to using free field Green's functions as the model.

Finally, the chapter shows examples in both simulations and experiments where the DMAS and C-WNC intensity maps are combined through a conditional addition scheme. The high

intensity values in robust DMAS images are preserved when C-WNC images fail to highlight the continuous surface reflections from the extended target. For simulation results using a 32-element array, the combined images show superior focus on the extended targets with high resolution and high contrast in both azimuth and axial range, with target sizes ranging from λ to 16 λ (the array physical aperture). For the experimental results using a 64-element array, the combined images still display high focusing ability on the two tested extended targets even though ideal sharp tips could not be created due to the finite size of drill bits.

Although the proposed method has pushed the limit to what a limited view aperture (in our case a linear array) can physically beamform, there are still fundamental limitations to perfect accuracy. These limitations include inaccurate azimuth focus at off-axis locations, and undesired aliasing that blinds the view of an extended target in the near field of a wide aperture array.

The results of this paper solely utilized longitudinal wave modes. Future studies will be performed to add shear wave modes to these algorithms for enhanced match field beamforming, as done in other imaging approaches [4] [11] [54]. Other future applications could include extension to dispersive guided waves in prismatic geometries.

Acknowledgements

The authors thank W. A. Kuperman for helpful discussion on match field beamformers. This research was funded in part by the U.S. Federal Railroad Administration under contract no. 693JJ619C000008 (Dr. Robert Wilson, Program Manager) and in part by MxV Rail through a University Grand Challenge Contract no. 24-0312-008622 (Dr. Anish Poudel, Program Manager). The authors would also like to acknowledge Mr. Gavin Dao of Advanced OEM Solutions (West Chester, OH, USA) for providing technical advice on FMC hardware solutions.

Chapter 5, in full, is a reprint of the material as it appears in C. Huang and F. Lanza di Scalea, "High Resolution Ultrasonic Imaging of Extended Targets via Combined Match Field and Time Delay Beamforming," *Ultrasonics,* vol. 145, p. 107464, 2025. The dissertation author was the primary investigator and author of this paper.

References

[1] M. Fink, "Time reversal of ultrasonic fields. I. Basic principles," *IEEE Trans. Ultrason., Ferroelect., Freq. Contr.*, vol. 39, pp. 555–566, 1992.

[2] C. Holmes, B.W. Drinkwater, and P.D. Wilcox, "Post-processing of the full matrix of ultrasonic transmit–receive array data for non-destructive evaluation," *NDT & E Int.*, vol. 38, pp. 701–711, 2005.

[3] B.W. Drinkwater and P.D. Wilcox, "Ultrasonic arrays for non-destructive evaluation: A review," *NDT & E Int.*, vol. 39, pp. 525–541, 2006.

[4] J. Zhang, B.W. Drinkwater, P.D. Wilcox, and A.J. Hunter, "Defect detection using ultrasonic arrays: The multi-mode total focusing method," *NDT & E Int.*, vol. 43, pp. 123–133, 2010.

[5] J.A. Jensen, S.I. Nikolov, K.L. Gammelmark, and M.H. Pedersen, "Synthetic aperture ultrasound imaging," *Ultrasonics*, vol. 44, pp. e5–e15, 2006.

[6] F. Lanza Di Scalea, S. Sternini, and T.V. Nguyen, "Ultrasonic Imaging in Solids Using Wave Mode Beamforming," *IEEE Trans. Ultrason., Ferroelect., Freq. Contr.*, vol. 64, pp. 602–616, 2017.

[7] G. Montaldo, M. Tanter, J. Bercoff, N. Benech, and M. Fink, "Coherent plane-wave compounding for very high frame rate ultrasonography and transient elastography," *IEEE Trans. Ultrason., Ferroelect., Freq. Contr.*, vol. 56, pp. 489–506, 2009.

[8] M. Tanter and M. Fink, "Ultrafast imaging in biomedical ultrasound," *IEEE Trans. Ultrason., Ferroelect., Freq. Contr.*, vol. 61, pp. 102–119, 2014.

[9] C.H. Frazier and W.D. O'Brien, "Synthetic aperture techniques with a virtual source element," *IEEE Trans. Ultrason., Ferroelect., Freq. Contr.*, vol. 45, pp. 196–207, 1998.

[10] C. Papadacci, M. Pernot, M. Couade, M. Fink, and M. Tanter, "High-contrast ultrafast imaging of the heart," *IEEE Trans. Ultrason., Ferroelect., Freq. Contr.*, vol. 61, pp. 288–301, 2014.

[11] C. Huang and F. Lanza di Scalea, "Application of Sparse Synthetic Aperture Focusing Techniques to Ultrasound Imaging in Solids Using a Transducer Wedge," *IEEE Trans. Ultrason., Ferroelect., Freq. Contr.*, vol. 71, pp. 280–294, 2024.

[12] C. Huang and F. Lanza di Scalea, "Rail Flaw Imaging Prototype Based on Improved Ultrasonic Synthetic Aperture Focus Method," *Mater. Eval.*, vol. 82, pp. 51–59, 2024.

[13] H. Been Lim, N. Thi Tuyet Nhung, E.-P. Li, and N. Duc Thang, "Confocal Microwave Imaging for Breast Cancer Detection: Delay-Multiply-and-Sum Image Reconstruction Algorithm," *IEEE Trans. Biomed. Eng.*, vol. 55, pp. 1697–1704, 2008.

[14] G. Matrone, A.S. Savoia, G. Caliano, and G. Magenes, "The Delay Multiply and Sum Beamforming Algorithm in Ultrasound B-Mode Medical Imaging," *IEEE Trans. Med. Imaging*, vol. 34, pp. 940–949, 2015.

[15] T. Su, D. Li, and S. Zhang, "An efficient subarray average delay multiply and sum beamformer algorithm in ultrasound imaging," *Ultrasonics*, vol. 84, pp. 411–420, 2018.

[16] S. Sternini, A.Y. Liang, and F. Lanza di Scalea, "Ultrasonic synthetic aperture imaging with interposed transducer–medium coupling path," *Struct. Health Monit.*, vol. 18, pp. 1543–1556, 2019.

[17] C. Prada and M. Fink, "Eigenmodes of the time reversal operator: A solution to selective focusing in multiple-target media," *Wave Motion*, vol. 20, pp. 151–163, 1994.

[18] C. Prada, S. Manneville, D. Spoliansky, and M. Fink, "Decomposition of the time reversal operator: Detection and selective focusing on two scatterers," *J. Acoust. Soc. Am.*, vol. 99, pp. 2067–2076, 1996.

[19] C. Prada, J.-L. Thomas, and M. Fink, "The iterative time reversal process: Analysis of the convergence," *J. Acoust. Soc. Am.*, vol. 97, pp. 62–71, 1995.

[20] J.-L. Thomas, and M.A. Fink, "Ultrasonic beam focusing through tissue inhomogeneities with a time reversal mirror: application to transskull therapy," *IEEE Trans. Ultrason., Ferroelect., Freq. Contr.*, vol. 43, pp. 1122–1129, 1996.

[21] M. Fink, D. Cassereau, A. Derode, C. Prada, P. Roux, M. Tanter, J.L. Thomas, and F. Wu, "Time-reversed acoustics," *Rep. Prog. Phys.*, vol. 63, p. 1933, 2000.

[22] S.K. Lehman and A.J. Devaney, "Transmission mode time-reversal super-resolution imaging," *J. Acoust. Soc. Am.*, vol. 113, pp. 2742–2753, 2003.

[23] E. Kerbrat, C. Prada, D. Cassereau, and M. Fink, "Ultrasonic nondestructive testing of scattering media using the decomposition of the time-reversal operator," *IEEE Trans. Ultrason., Ferroelect., Freq. Contr.*, vol. 49, pp. 1103–1113, 2002.

[24] E. Kerbrat, C. Prada, D. Cassereau, and M. Fink, "Imaging in the presence of grain noise using the decomposition of the time reversal operator," *J. Acoust. Soc. Am.* vol. 113, pp. 1230–1240, 2003.

[25] E. Lopez Villaverde, S. Robert, and C. Prada, "Ultrasonic imaging of defects in coarse-grained steels with the decomposition of the time reversal operator," *J. Acoust. Soc. Am.*, vol. 140, pp. 541–550, 2016.

[26] C. Fan, M. Caleap, M. Pan, and B.W. Drinkwater, "A comparison between ultrasonic array beamforming and super resolution imaging algorithms for non-destructive evaluation," *Ultrasonics*, vol. 54, pp. 1842–1850, 2014.

[27] C. Fan, M. Pan, F. Luo, and B. Drinkwater, "Multi-frequency time-reversal-based imaging for ultrasonic nondestructive evaluation using full matrix capture," *IEEE Trans. Ultrason., Ferroelect., Freq. Contr.*, vol. 61, pp. 2067–2074, 2014.

[28] C. Fan, S. Yu, B. Gao, Y. Zhao, and L. Yang, "Ultrasonic time-reversal-based super resolution imaging for defect localization and characterization," *NDT & E Int.*, vol. 131, p. 102698, 2022.

[29] J.B. Elliott, M.J.S. Lowe, P. Huthwaite, R. Phillips, and D.J. Duxbury, "Sizing Subwavelength Defects With Ultrasonic Imagery: An Assessment of Super-Resolution Imaging on Simulated Rough Defects," *IEEE Trans. Ultrason., Ferroelect., Freq. Contr.*, vol. 66, pp. 1634–1648, 2019.

[30] E.A. Marengo, F.K. Gruber, and F. Simonetti, "Time-Reversal MUSIC Imaging of Extended Targets," *IEEE Trans. Image Process.*, vol. 16, pp. 1967–1984, 2007.

[31] W.K. Park and D. Lesselier, "Electromagnetic MUSIC-type imaging of perfectly conducting, arc-like cracks at single frequency," *J. Comput. Phys.*, vol. 228, pp. 8093–8111, 2009.

[32] L. Ambrozinski, T. Stepinski, P. Packo, and T. Uhl, "Self-focusing Lamb waves based on the decomposition of the time-reversal operator using time–frequency representation," *Mech. Syst. Sig. Process.*, vol. 27, pp. 337–349, 2012.

[33] J. He and F.G. Yuan, "Lamb wave-based subwavelength damage imaging using the DORT-MUSIC technique in metallic plates," *Struct. Health Monit.*, vol. 15, pp. 65–80, 2016.

[34] X. Yang, K. Wang, P. Zhou, L. Xu, and Z. Su, "Imaging damage in plate waveguides using frequency-domain multiple signal classification (F-MUSIC)," *Ultrasonics*, vol. 119, p. 106607, 2022.

[35] C. Prada, J. De Rosny, D. Clorennec, J.-G. Minonzio, A. Aubry, M. Fink, L. Berniere, P. Billand, S. Hibral, and T. Folegot, "Experimental detection and focusing in shallow water by decomposition of the time reversal operator," *J. Acoust. Soc. Am.*, vol. 122, pp. 761–768, 2007.

[36] F.D. Philippe, C. Prada, J. De Rosny, D. Clorennec, J.-G. Minonzio, and M. Fink, "Characterization of an elastic target in a shallow water waveguide by decomposition of the time-reversal operator," *J. Acoust. Soc. Am.*, vol. 124, pp. 779–787, 2008.

[37] Y. Labyed and L. Huang, "Ultrasound time-reversal MUSIC imaging with diffraction and attenuation compensation," *IEEE Trans. Ultrason., Ferroelect., Freq. Contr.*, vol. 59, pp. 2186–2200, 2012.

[38] Y. Labyed and L. Huang, "Super-resolution ultrasound imaging using a phase-coherent MUSIC method with compensation for the phase response of transducer elements," *IEEE Trans. Ultrason., Ferroelect., Freq. Contr.*, vol. 60, pp. 1048–1060, 2013.

[39] M.V. Felice and Z. Fan, "Sizing of flaws using ultrasonic bulk wave testing: A review," *Ultrasonics*, vol. 88, pp. 26–42, 2018.

[40] D.H. Chambers and A.K. Gautesen, "Time reversal for a single spherical scatterer," *J. Acoust. Soc. Am.*, vol. 109, pp. 2616–2624, 2001.

[41] F.K. Gruber, E.A. Marengo, and A.J. Devaney, "Time-reversal imaging with multiple signal classification considering multiple scattering between the targets," *J. Acoust. Soc. Am.*, vol. 115, pp. 3042–3047, 2004.

[42] A.J. Devaney, E.A. Marengo, and F.K. Gruber, "Time-reversal-based imaging and inverse scattering of multiply scattering point targets," *J. Acoust. Soc. Am.*, vol. 118, pp. 3129–3138, 2005.

[43] J.-L. Robert and M. Fink, "The prolate spheroidal wave functions as invariants of the time reversal operator for an extended scatterer in the Fraunhofer approximation," *J. Acoust. Soc. Am.*, vol. 125, pp. 218–226, 2009.

[44] S. Hou, K. Huang, K. Solna, and H. Zhao, "A phase and space coherent direct imaging method," *J. Acoust. Soc. Am.*, vol. 125, pp. 227–238, 2009.

[45] E.G. Asgedom, L.-J. Gelius, A. Austeng, S. Holm, and M. Tygel, "Time-reversal multiple signal classification in case of noise: A phase-coherent approach," *J. Acoust. Soc. Am.*, vol. 130, pp. 2024–2034, 2011.

[46] R. Pierri and F. Soldovieri, "On the information content of the radiated fields in the near zone over bounded domains," *Inverse Probl.*, vol. 14, pp. 321–337, 1998.

[47] S. Hou, K. Solna, and H. Zhao, "A direct imaging algorithm for extended targets," *Inverse Probl.*, vol. 22, pp. 1151–1178, 2006.

[48] C. Prada, and J.L. Thomas, "Experimental subwavelength localization of scatterers by decomposition of the time reversal operator interpreted as a covariance matrix," *J. Acoust. Soc. Am.*, vol. 114, pp. 235–243, 2003.

[49] Z.H. Michalopoulou and M.B. Porter, "Matched-field processing for broad-band source localization," *IEEE J. Oceanic Eng.*, vol. 21, pp. 384–392, 1996.

[50] G.J. Orris, M. Nicholas, and J.S. Perkins, "The matched-phase coherent multi-frequency matched-field processor," *J. Acoust. Soc. Am.*, vol. 107, pp. 2563–2575, 2000.

[51] C. Debever and W.A. Kuperman, "Robust matched-field processing using a coherent broadband white noise constraint processor," *J. Acoust. Soc. Am.*, vol. 122, pp. 1979–1986, 2007.

[52] H. Song, W.A. Kuperman, W.S. Hodgkiss, P. Gerstoft, and J.S. Kim, "Null broadening with snapshot-deficient covariance matrices in passive sonar," *IEEE J. Oceanic Eng.*, vol. 28, pp. 250–261, 2003.

[53] J.G. Berryman, L. Borcea, G.C. Papanicolaou, and C. Tsogka, "Statistically stable ultrasonic imaging in random media," *J. Acoust. Soc. Am.*, vol. 112, pp. 1509–1522, 2002.

[54] C. Huang, A.Z. Hosseinzadeh, and F. Lanza di Scalea, "Ultrasparse Ultrasonic Synthetic Aperture Focus Imaging by Passive Sensing," *IEEE Trans. Ultrason., Ferroelect., Freq. Contr.*, vol. 71, pp. 518-535, 2024.

[55] A.B. Baggeroer, W.A. Kuperman, and H. Schmidt, "Matched field processing: Source localization in correlated noise as an optimum parameter estimation problem," *J. Acoust. Soc. Am.*, vol. 83, pp. 571–587, 1988.

[56] A.B. Baggeroer, W.A. Kuperman, and P.N. Mikhalevsky, "An overview of matched field methods in ocean acoustics," *IEEE J. Oceanic Eng.*, vol. 18, pp. 401–424, 1993.

[57] H. Cox, R. Zeskind, and M. Owen, "Robust adaptive beamforming," *IEEE Trans. Acoust., Speech, Signal Process.*, vol. 35, pp. 1365–1376, 1987.

[58] S. Wan, B.I. Raju, and M.A. Srinivasan, "Robust deconvolution of high-frequency ultrasound images using higher-order spectral analysis and wavelets," *IEEE Trans. Ultrason., Ferroelect., Freq. Contr.*, vol. 50, pp. 1286–1295, 2003.

[59] k-Wave: A MATLAB toolbox for the time domain simulation of acoustic wave fields. http://www.k-wave.org/, 2022 (accessed 17 July 2024).

Chapter 6 Application of Coherent White Noise Constraint Beamformer to Imaging in Composite Panels

6.1 Introduction

Plate-like structures are widely used in aviation, maritime, and civil applications. In Structural Health Monitoring (SHM), effective inspection techniques have been developed to identify the occurrence and accumulation of structural damage in these parts. Among various tools available, ultrasonic guided waves are commonly recognized as an efficient and promising tool due to their ability to propagate for long distances and provide sensitivity to various types of damages [1]. In a typical in-situ SHM configuration for imaging waveguide structures, a sparse array of piezoelectric transducers is used for transmission and reception of the ultrasonic signals [2]-[4].

The array processing schemes used for the SHM of the waveguide usually require the isolation of the transfer matrix between the transmitter array and the receiver array [5], or the covariance matrix of the receiver array [6] depending on whether active or passive sensing modes are used. Based on the orthogonality of signal and noise subspaces in the transfer (covariance) matrix, the MUltiple SIgnal Classification (MUSIC) type algorithms have been employed for their high-resolution characteristics in the imaging of the multistatic dataset. Engholm and Stepinski [7] first demonstrated the use of the MUSIC algorithm for passive sensing of an aluminum plate using circular arrays. Yuan et al. presented variations of the MUSIC algorithms for both passive mode impact localization [8] and active mode defect localization [9] [10]. One of the main difficulties in employing MUSIC type algorithms for the imaging of plate-like structures is the dispersion effect of guided waves, especially when a broad frequency band is considered [11]. Zuo et al. [12] presented a model-based MUSIC algorithm by exploiting the cross-correlation between the guided

wave model and the measured signals. Bao et al. [13] proposed an anisotropy compensated MUSIC algorithm to account for the phase errors in modeling waveguide propagations in reinforced composite panels. Another significant challenge is the nature of low Signal-to-Noise Ratio (SNR) due to the relatively small sources inspected over a large structure using a small number of array elements. Efforts have been made to increase the SNR of the multistatic data by beamforming the transmit aperture to synthetically focus the diagnostic signals on aluminum plates [9] [14] and stiffened composite structures [10].

In addition to what summarized above, the most critical deficiency of using MUSIC type beamformers remains the determination of the threshold that separates the signal and noise subspaces [15], which is a critical parameter rarely discussed in the existing literatures of composite SHM. It has been shown that for a simple linear array setup, the one-to-one correspondence in singular mode factorization does not apply when sources are finitely sized or not well resolved in the transfer matrix [16]. For a sparse array setup on complexed waveguide structures, analyzing the singular mode (or eigenmode) composition can be challenging depending on factors such as multiple wave modes, dispersion effects, multiple scattering from boundaries and stiffeners, and specific arrangement of the array [17]. Thus, it is essential to develop an imaging scheme that achieves high resolution for source localization in structural waveguides without requiring singular value decomposition.

Matched Field Processing (MFP) is a family of array processing framework initially developed in underwater acoustics to estimate target locations and medium properties in complex propagation environments such as the ocean waveguide [18]. Similarly to MUSIC type beamformers, MFP algorithms have the potential to exploit the best match between the measured data and the replica of the data (back propagators, or steering vectors) by directly using

experimental measurements as the replica [19]. Such data-driven capability greatly eases the burden of accurately modeling the propagation environments, for example the multimodal and dispersive characteristics in plate-like structures [20]. With the tools developed in the MFP community, it is possible to adaptively beamform waveguide signals sampled across the spectrum of interest coherently. A "supervector" formulation was developed to take advantage of the coherence between each sampled frequency in the magnitude squared inner products by stacking each narrowband data vector [21]. Robust adaptive beamformers such as the White Noise Constraint (WNC) algorithm in the supervector formulation have demonstrated superior image resolution and contrast in low SNR environments, without any knowledge of the singular value structure in the covariance matrix [22]. In structural acoustics, the authors have established the analogy between passive MFP beamformers and active sensing modalities in the nondestructive evaluation of solids using bulk waves [23] [24]. The coherent MFP beamformers are expected to perform even better in imaging plate-like structures considering the opportunity to achieve enhanced signal compression by exploiting the multimode and dispersive wave properties.

This chapter presents a data-driven MFP based framework to image impacts and defects in stiffened composite panels using adaptive coherent beamformers. This framework is decomposed into two steps: recording experimental Green's function and imaging using recorded data. Specifically, the measurements of the structural Green's functions are first performed through a deconvolution operation between recorded signals in a sparse receiver array and a controlled excitations by a hammer impact. These Green's functions directly compose the replica vectors that are therefore established experimentally, given the challenges of accurate numerical modeling of such a complex structure. In the second step, the coherent WNC algorithm is shown to yield high resolution and high contrast when tracking the location of impacts in the panel. To highlight the

weak scattering from the defect that serves as a secondary source in the recorded wavefield, the dominance of the active source is relieved by performing a null operation via eigen structure decomposition of the covariance matrix [25]. Experiments show that the eigen mode associated with the simulated defect as a secondary wave scatterer can be built up in the eigen structure after the null operation with a larger variety of excitations. This eigen mode can finally be focused using adaptive MFP beamformers to generate high quality image of the defect.

6.2 Data-driven Matched Field Processing

6.2.1 Benefits of Using Experimental Data When Imaging Complex Media

Despite the discrepancy of interpreting the transfer matrix between MUSIC type algorithms and conventional matched field processors, these frequency domain beamformers all build their ambiguity surfaces by exploiting the similarity or "match" between a model (known as replica) and experimental measurements (the data). Identified as match-field type beamformers, the best imaging performance are obtained when the replica represents the realistic wave propagation environment [24]. The benefits of using experimental measurements as replica in the imaging of complex waveguide structures are illustrated in Fig. 6.1. Highlighted by the blue box in Fig. 6.1(c), the target experimental signal to match is a typical realistic ultrasonic guided wave time history in a stiffened composite panel. This signal was excited by a hammer impact and recorded by a piezoelectric transducer bonded to the panel (detailed explanation in Fig. 6.3). The dispersive and multi-modal nature of guided wave can be easily observed in the target signal. Three different signals are used as replica for comparison, shown in the first column in Fig. 6.1. Their corresponding cross-correlation outputs with the target signal are shown in the second column in

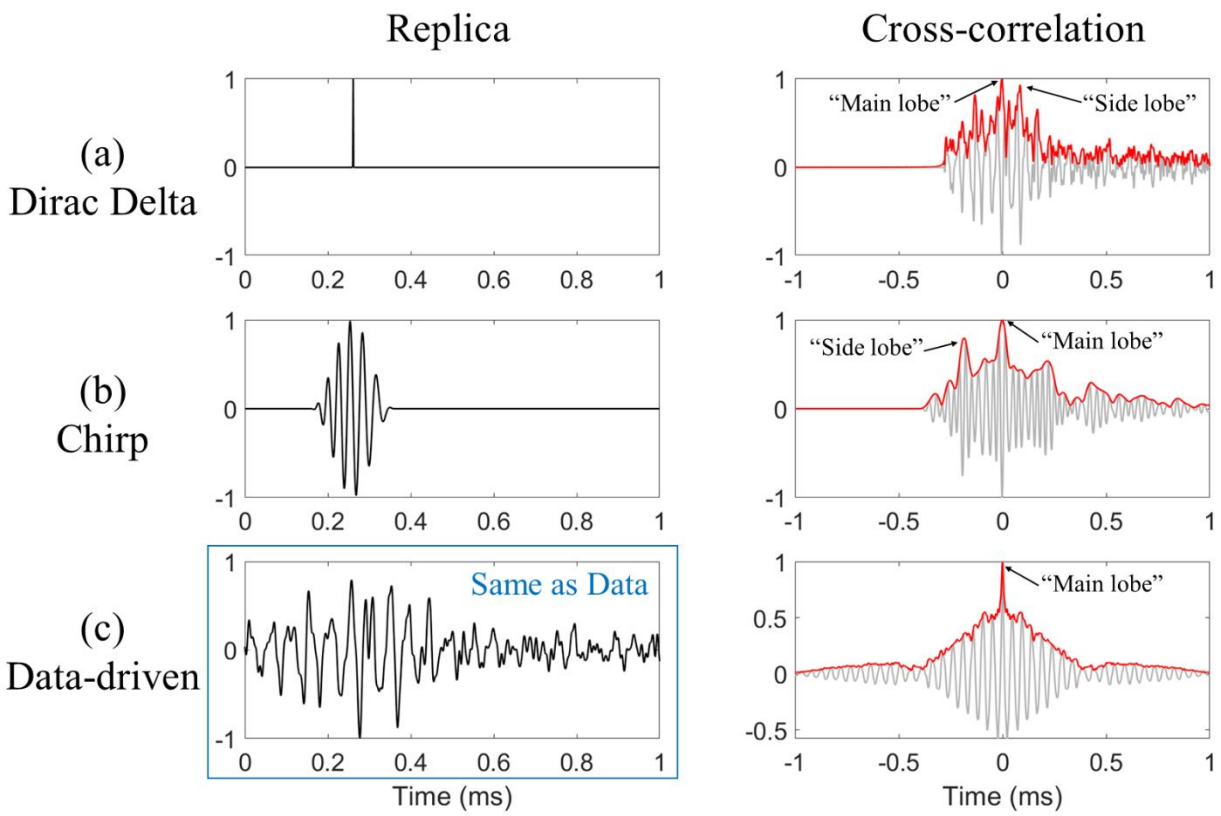

Figure 6.1: Benefits of using an accurate replica in cross-correlation. The target experimental guided wave signal to match is in the blue box of (c). Examples of replica signal using (a) Dirac Delta, (b) chirp, and (c) the same signal as the matched signal.

Fig. 6.1. The envelope of these cross-correlations (shown in red) can be seen as a match-field time-domain beamformer output intensity, without considering coherent array gain.

Fig. 6.1(a) shows the cross-correlation results using a Dirac Delta function shifted by the estimated time of flight of the dominant wave packet. This is similar to using the delay-and-sum type algorithms [24] [31] and considering only the group velocity in guided wave signals as backpropagation time [2]. In this case, the beamforming output is simply a phase shift of the target signal. Since the complex wave propagation information is not included in the replica, high intensity side lobes appear in the cross-correlation, leading to reduced focus and potential false positives in the image.

Fig. 6.1(b) shows the results using a model considering the dispersion in a single wave packet. The replica signal is generated using a chirp signal covering the frequency band of the experimental measurements and Hanning windowed by the same group velocity consideration as in Fig. 6.1(a). This is similar to the results shown in most guided wave imaging literatures by compensating the dispersion effects in plate-like structures [4] [13]. Though an improvement in the cross-correlation beamformer output is seen compared to using a Dirac Delta replica, significant side lobes are still obtained due to various factors missed in the replica model such as reflections from stiffeners and boundaries, multiple wave modes, etc. Besides, the higher frequency components are missing in the simple chirp model, which further degrades the resolution of cross-correlation beamformers.

Finally, Fig. 6.1(c) shows the results using the experimental measurement itself to do the "autocorrelation". When the replica is copied directly from experimental data, all complexities of the propagation environment are encoded in the model (i.e. dispersion, multiple modes, multiple reflections, etc.). As seen in the cross-correlation beamformer output, the side lobes are greatly suppressed and focus in greatly improved with significant signal compression. The side lobe level at locations close to time zero is still approximately half of the intensity normalized to the main lobe since the experimental signal is neither transient nor very wide band. Clearly, adding signal complexities generally increases compression of the autocorrelation.

6.2.2 Extraction of Green's Function

The key to achieve matched field imaging in waveguide structures is to extract the structural Green's function (or equivalently the impulse response function) that encodes the complex wave propagation information. One method to experimentally measure this quantity in using a single-input-single-output scheme with an active excitation and a reception. Consider the

transmitted signal by the active source as $E(\omega)$ and the received signal as $R(\omega)$, the Green's function can be written as the normalized cross power spectrum

$$G(\omega) = \frac{\langle E^*(\omega)R(\omega)\rangle}{\langle E^*(\omega)E(\omega)\rangle} \tag{6.1}$$

where the numerator is the cross correlation of the two signals and the denominator is the autocorrelation of the transmitted signal. The autocorrelation eliminates the power bias in the power spectrum of the cross correlation colored by the spectral density of the active source $E(\omega)$ [26]. Eq. 6.1 is therefore conceptually a form of deconvolution. In practice, the expectations of the power spectra can be estimated using overlapping time segments to calculate ensemble averages [27]. It should be noted that the length of each segment should be 3~4 times larger than the wave arrival of interest since the coherence in these averages is only captured within the supporting time length of each windowed segment [29].

6.2.3 Coherent Adaptive Matched Field Processing

In MFP beamforming both the measured data and the replica are assembled in column vectors with each entry corresponding to an element in the array [19]. The data vector is multiplied by its outer product to form the covariance matrix $C(\omega)$. An example of a linear MFP output is

$$I^{IC-BAR}(x, y, \Omega) = \sum_{\omega} w^{\mathrm{H}}(x, y, \omega) C(\omega) w(x, y, \omega) \tag{6.2}$$

where $w(x, y, \omega)$ is the replica vector denoting the Green's functions between the pixel location (x, y) and the reception array, and $^{\mathrm{H}}$ is the Hermitian operator. Note that although the final "broadband" image averages the ambiguity surfaces of narrowband MFP outputs at each sampled frequency ω, this processor is incoherent across the spectrum of interest Ω.

Due to the dispersive nature of guided wave propagation, it is beneficial to beamform in a coherent manner such that the cross-frequency terms can contribute to the array gain. The authors

have shown that the White Noise Constraint (WNC) beamformer can be used together with the supervector formulated coherent MFP to both achieve high resolution and high contrast in the output image [24]. The coherence between frequencies is exploited by stacking the column vectors from each sampled frequency to a long "supervector" [22]. In this supervector formulation, the WNC replica vector is found adaptively at each pixel (x, y) by first determining the white noise gain G_W that constrains the norm of the optimized WNC replica vector

$$w_{\mathrm{WNC}}{}^{\mathrm{H}}(x,y,\Omega)w_{\mathrm{WNC}}(x,y,\Omega) \leq G_{\mathrm{W}}{}^{-1} \tag{6.3}$$

The solution to the WNC problem can be found by minimizing the magnitude squared output at all candidate pixels except at the true source location [24]. Using the method of Lagrange multiplier, the WNC replica is found as

$$w_{\mathrm{WNC}}(x,y,\Omega,G_{\mathrm{W}}) = \frac{(C(\Omega)+\varepsilon(x,y)I)^{-1}w_{\mathrm{BAR}}(x,y,\Omega)}{w_{\mathrm{BAR}}{}^{\mathrm{H}}(x,y,\Omega)(C(\Omega)+\varepsilon(x,y)I)^{-1}w_{\mathrm{BAR}}(x,y,\Omega)} \tag{6.4}$$

where $\varepsilon(x, y)$ is the diagonal loading applied to the covariance matrix to enable matrix inversion such that the white noise gain constraint in (3) is satisfied. It has been demonstrated previously that in a typical coherent MFP problem, the broadband covariance matrix $C(\Omega)$ is rank deficient and the WNC beamformer outputs the intensity of the source location (focus) with a power bias that leads to a large dynamic range between the main lobe and the noise floor [28]. Such characteristic helps to generate high contrast images in finding sources in composite panels given the poor SNR and the limited dimension of sparse transducer arrays.

One of the most problematic aspects in active sensing is that the presence of the "loud" active source (e.g. hammer impact in the present application) can mask the "weak" secondary source from the damage scatterer. The authors recently worked on a method to eliminate the existence of the active source by considering the passive normalized cross power spectrum of two receivers to reconstruct active impulse response as if one of the receivers was an active source

[29]. Another way to eliminate the active sources that was developed in underwater acoustics and seismology uses an eigenmode decomposition of the covariance matrix [25]. If the active source and the secondary source (defect) are decoupled, the dominant eigenvector should be related to the active source and can be eliminated from the beamforming. The active source can be removed from the covariance matrix by projecting out the dominant eigenvectors $U_m(\Omega)$ as follows

$$C_p(\Omega) = (I - U_m(\Omega){U_m}^{\mathrm{H}}(\Omega))C(\Omega) \tag{6.5}$$

where $U_m(\Omega)$ are the collection of column eigenvectors to be removed from the covariance matrix $C(\Omega)$. Typically, only the first eigenvector associated with the largest eigenvalue is required to be removed in each excitation dataset. Experimentally, the secondary source should be illuminated by excitations from different locations. The final covariance matrix can be the summation of individual projected covariance matrix $C_p(\Omega)$ so that these snapshots build up the eigen mode associated with the defect scatterer after each null operation of the active source.

6.3 Experimental Results

The experimental setup is shown in Fig. 6.2. An array of piezoelectric (PZT) transducers with a diameter of 8 mm was glued to the surface of a skin-stringer stiffened composite panel representative of modern aircraft construction. Eight PZTs were attached to the skin-only part of the panel (outside of the stringer flange) and four PZTs were attached to the stringer heel. Fig. 6.1(a) shows the pristine case with no damage present. The experimental Green's functions were collected by hitting each 1 cm in the ROI grid using an instrumented impulse hammer. Fig. 6.1(b) shows the simulated damage case by sticking an added mass to the surface of the stringer flange using a thin layer of adhesive clay. The effective contact area was a circle with a diameter of 2 cm.

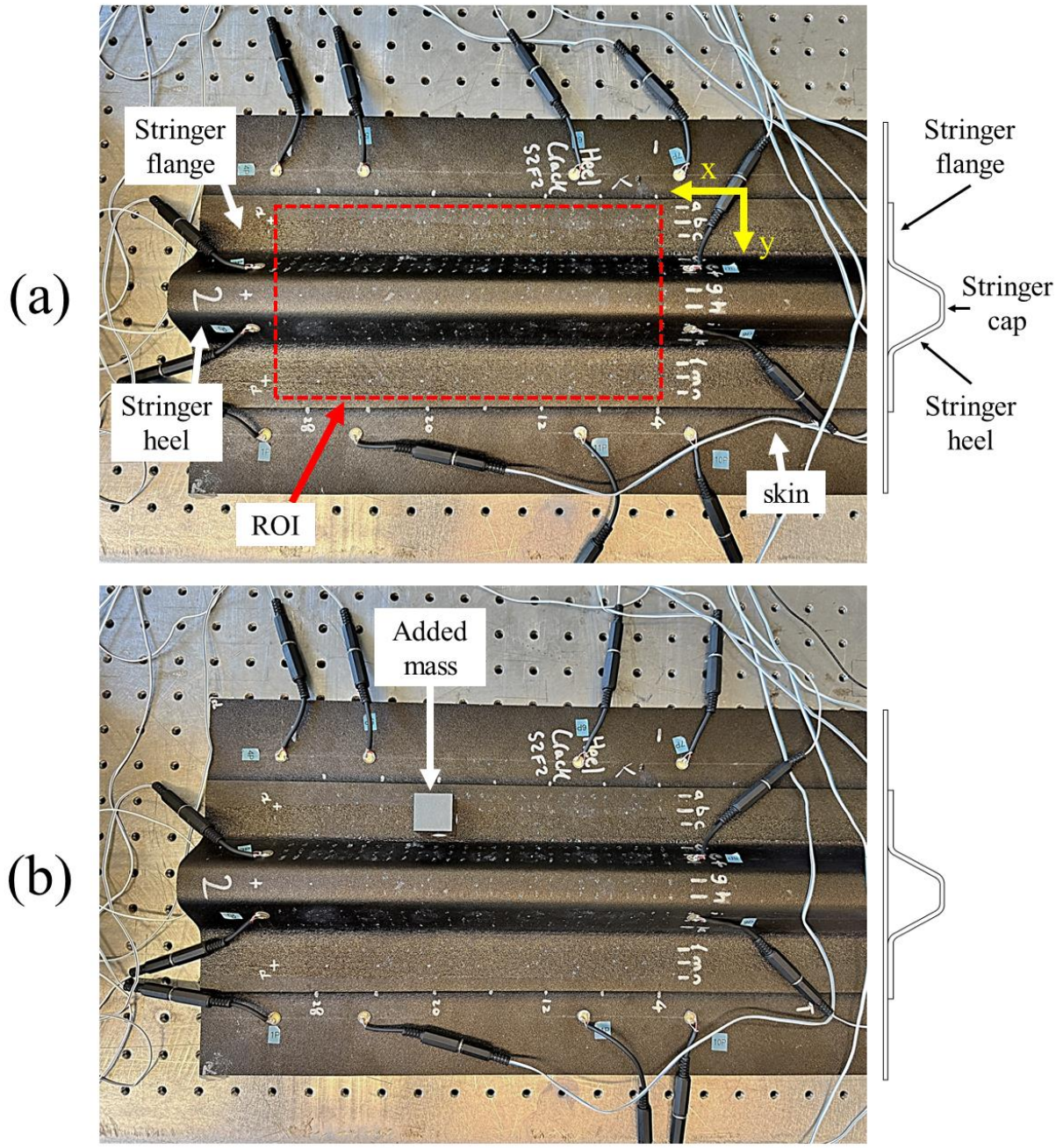

Figure 6.2: Experimental setup of the stiffened composite panel. A 12-element sparse PZT array was attached to the stringer side of the panel. (a) Pristine case for the acquisition of Green's function. The ROI is highlighted in red. (b) An added mass is attached to the stringer flange to simulate a defect.

6.3.1 Experimental Green's Function as Replica Model

Fig. 6.3 shows the results of Green's function extraction. Fig. 6.3(a) shows a typical waveform recorded in the hammer by hitting on one of the pixels in the grid on the stringer flange. Multiple sub-hits were present due to the secondary hits. Fig. 6.3(b) shows two typical waveforms recorded by element #3 and #7. The multimodal and dispersive nature of the excited guided waves is seen in both receptions. Since element #3 was located on the stringer heel, there were multiple wave packet arrivals caused by the complex wave paths in the stiffened panel. For element #7 located close to the excitation on the skin part outside the stiffener, most of the energy is seen in the first arrival packet. Fig. 6.3(c) shows the deconvolution result using the normalized cross power spectrum in (1). The deconvolution operation in the frequency domain takes care of the multiple hits seen in the hammer excitation since only coherent phase lag between the two signals contribute to the cross spectrum. The segmental averaging approach was used to constrain most of the energy within 0~1 ms in causal time. This time length is long enough for any receiver to record the first arrival from the excitation at any location within the ROI shown in Fig. 6.2(a). The effect of signal compression is seen in both signals due to the elimination of excitation spectrum. Comparing the two Green's functions, the response on the stiffener is more complex with multiple arrivals in the wave packet while the response on the skin is more transient with an earlier time of arrival.

6.3.2 Imaging Impacts *In-situ*

This section shows the ability to find impacts passively at various locations of the stiffened composite panel *in-situ* using the proposed MFP imaging algorithms with the sparse PZT array. As shown in Fig. 6.4, the receiver array records the hammer impacts as the data vector and creates the covariance matrix. For now, each entry in the data vector is deconvolved with its excitation signals, similarly to the extraction of Green's function seen in the previous section. Twenty

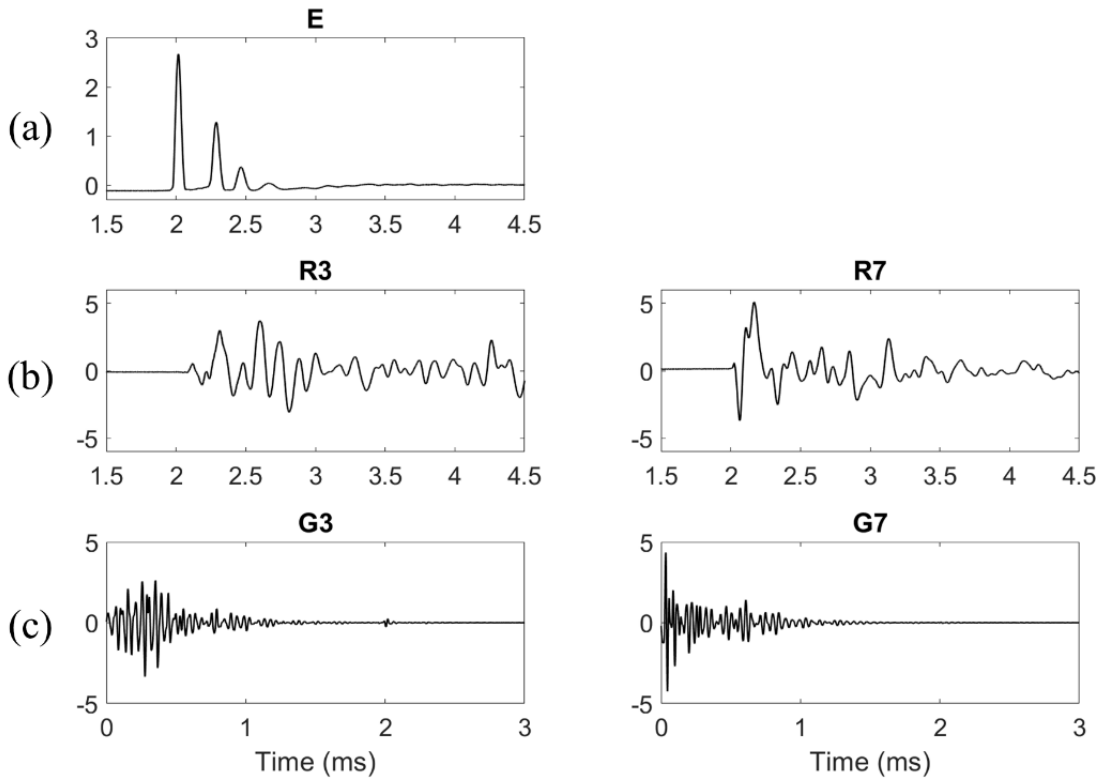

Figure 6.3: Acquisition of the experimental Green's function. (a) Transmitted signal using the instrumented hammer. (b) Raw recorded signals at sensor #3 on the stringer heel and sensor #7 on the skin-only region. (c) Deconvolution results corresponding to the receptions in (b) showing the reconstructed Green's functions in the time domain.

snapshots are used to construct the ensemble averaged covariance matrix. Fig. 6.4(a) shows the incoherent averaging of the narrowband linear (Bartlett) beamformer by sampling every 1 kHz in the 35~60 kHz range (IC-BAR). The maximum intensity denotes the highest likelihood between the replica (candidate source location) and the data in the covariance matrix. In this case, the beamformer focuses on the only active source (the hammer impact) with a contrast of 15 dB. Fig. 6.4(b) shows the image of the broadband "supervector" linear beamformer (C-BAR). By taking advantage of the cross-frequency coherence in the supervector, additional array gain is seen in the larger dynamic range of the linear MFP output. Besides, the high intensity side lobes in the stringer flange region in IC-BAR are suppressed in C-BAR. The most impressive result is obtained using

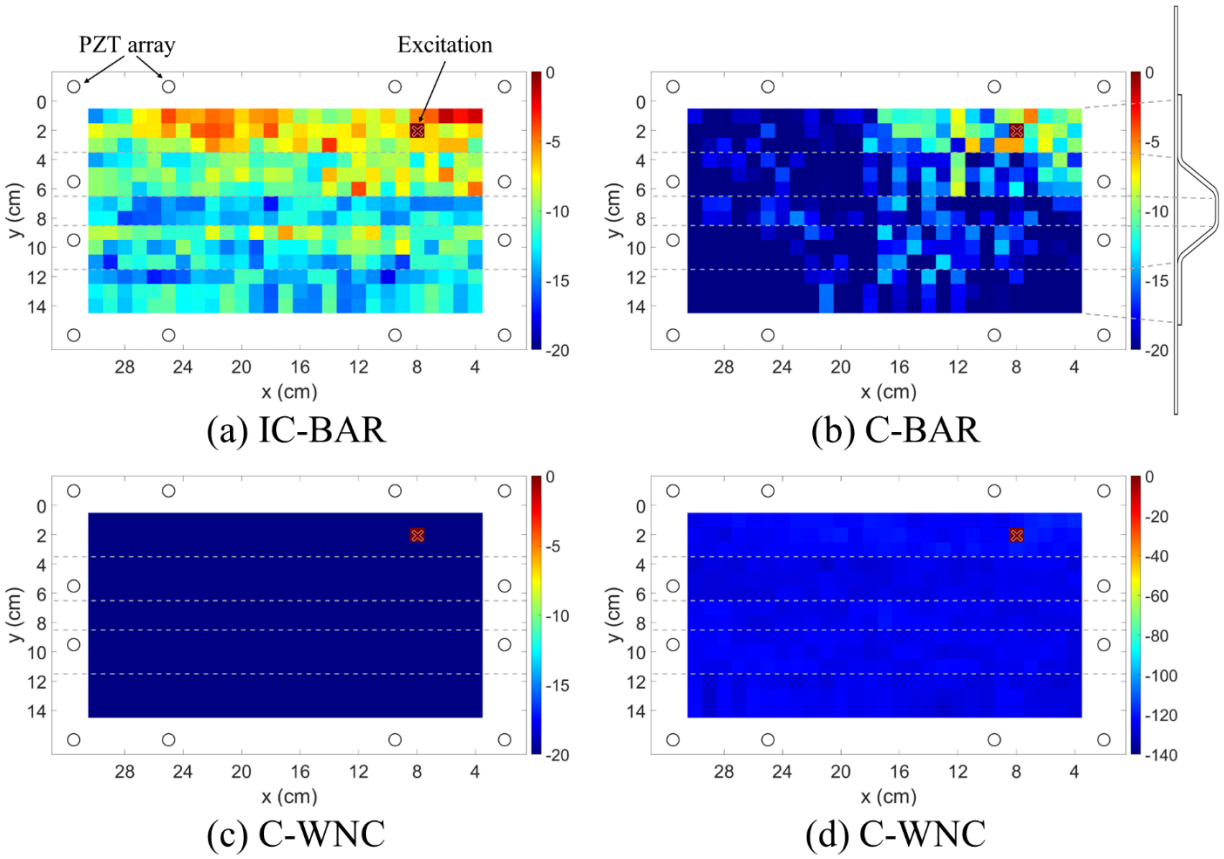

Figure 6.4: Proof-of-principle imaging results by matching the recorded Green's functions with a hammer excitation on the stringer flange. Matched field imaging using (a) incoherent averaging of narrowband Bartlett beamformer, (b) coherent Bartlett beamformer, (c) coherent white noise constraint beamformer, and (d) same as (c) but plotted in a larger dynamic range.

adaptive beamforming, as shown in Fig. 6.4(c). Through the optimization of the replica vector in the WNC algorithm, only the true source location is visible, while the other false positive are suppressed, including the high intensity side lobes in Fig. 6.4(b). The actual contrast of the image is shown in Fig. 6.4(d) by enlarging the displayable dynamic range to 140 dB. As stated in [22], the dynamic range of ~120 dB in C-WNC images seen in this work is due to the power output bias resulting from the diagonal loadings that shift the eigenvalues in the rank deficient covariance matrix. Regardless of the cause of the bias, the C-WNC image provides excellent focus on the primary source of the wave field with both high resolution and high contrast.

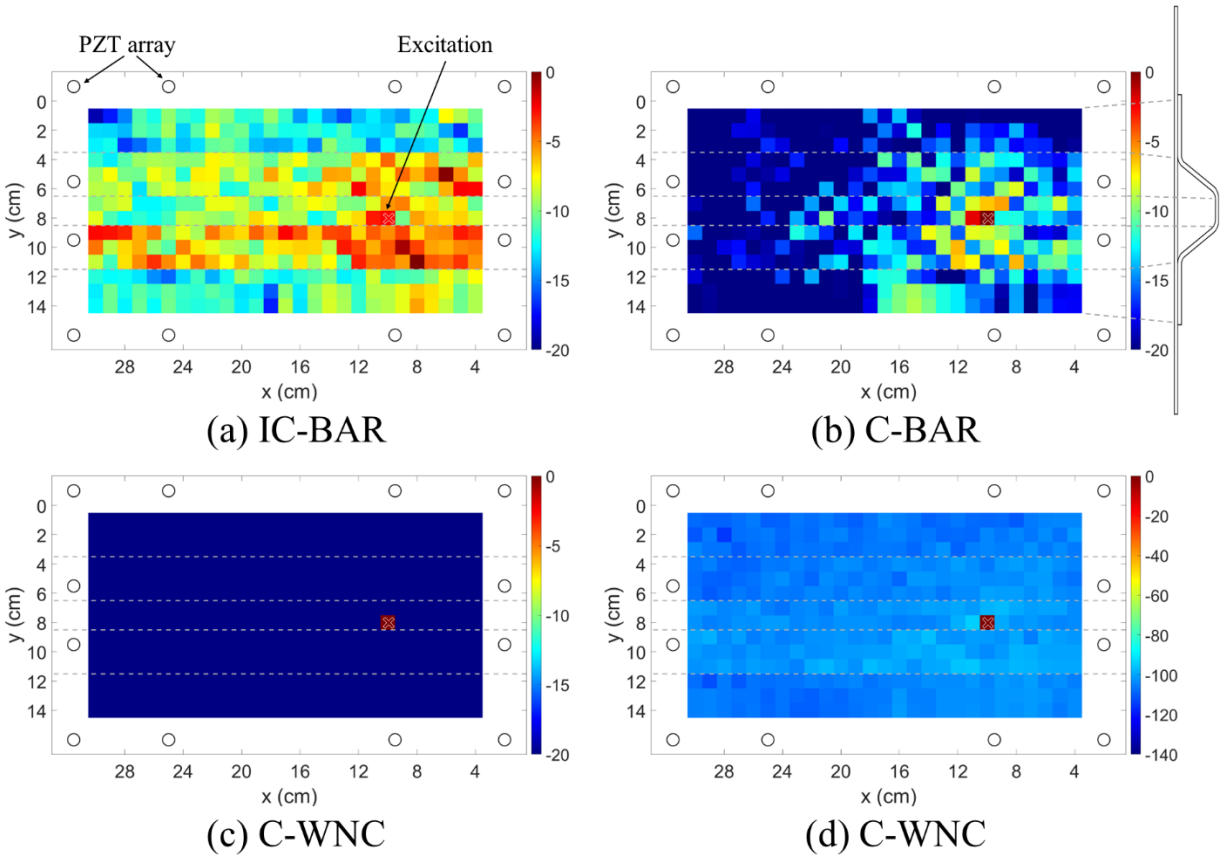

Figure 6.5: Same as Fig. 6.4 except that the hammer excitation is on the stringer cap.

Fig. 6.5 shows another example of imaging the impact by hitting on the stringer cap of the panel and performing deconvolution. This is a more challenging location to detect because the curved surface of the stringer complicates the guided wave propagation. As seen in Fig. 6.5(a), the IC-BAR image fails to focus on the correct impact location. The maximum response is seen at a similar horizontal x location but on the stringer heel. In contrast, the C-BAR image successfully focuses on the correct location with minimum side lobes present. Again, with adaptive beamforming, the C-WNC image in Fig. 6.5(c) further suppresses the side lobes and only maintains the maximum at the correct impact location. A complete study of the achievable spatial resolution should be carried out using interpolation techniques to create a denser mesh of the data-driven Green's function library. It is also interesting to observe in Fig. 6.5(d) that the noise floor

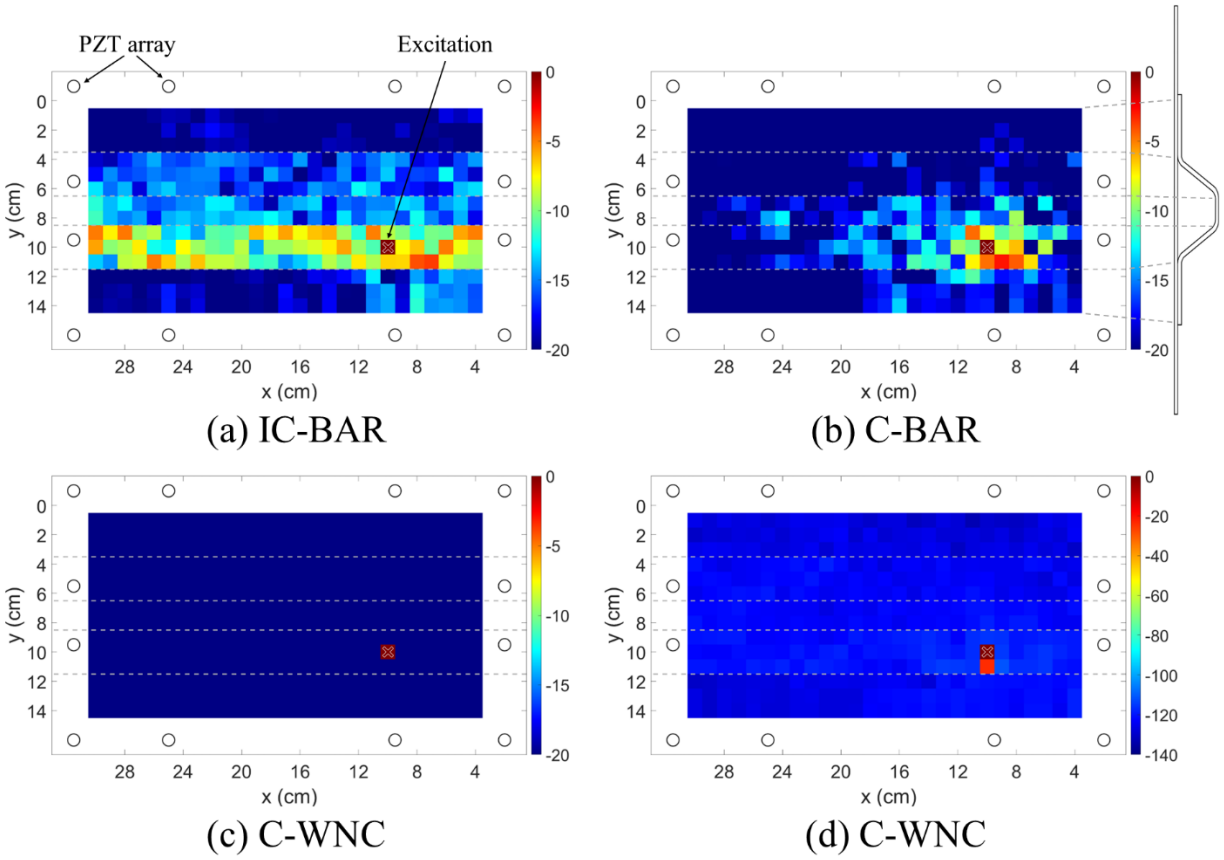

Figure 6.6: Same as Fig. 6.4 except that the hammer excitation is on the stringer heel.

of the biased C-WNC image is elevated compared to the result in Fig. 6.4(d), which confirms the theory of numerical power bias of rank-deficient WNC processors described in [22] [24] [28].

The same experiment was performed by hitting the hammer on the stringer heel. All parameters remain the same to generate Fig. 6.6. The incoherent Bartlett image in Fig. 6.6(a) shows better SNR compared to the impact on the stringer flange in Fig. 6.6(a). For C-BAR in Fig. 6.6(b), the coherent beamformer again results in a better focus in the x-direction as a result of the improved phase match and signal compression. Finally, the C-WNC image in Fig. 6.6(c) and (d) shows a high dynamic range focus, with similar bias as the case in Fig. 6.4 seen at the -120 dB noise floor.

Let us now consider a more general case where the excitation signal from the hammer is not available (no deconvolution possible in the data vector). This means that the covariance matrix

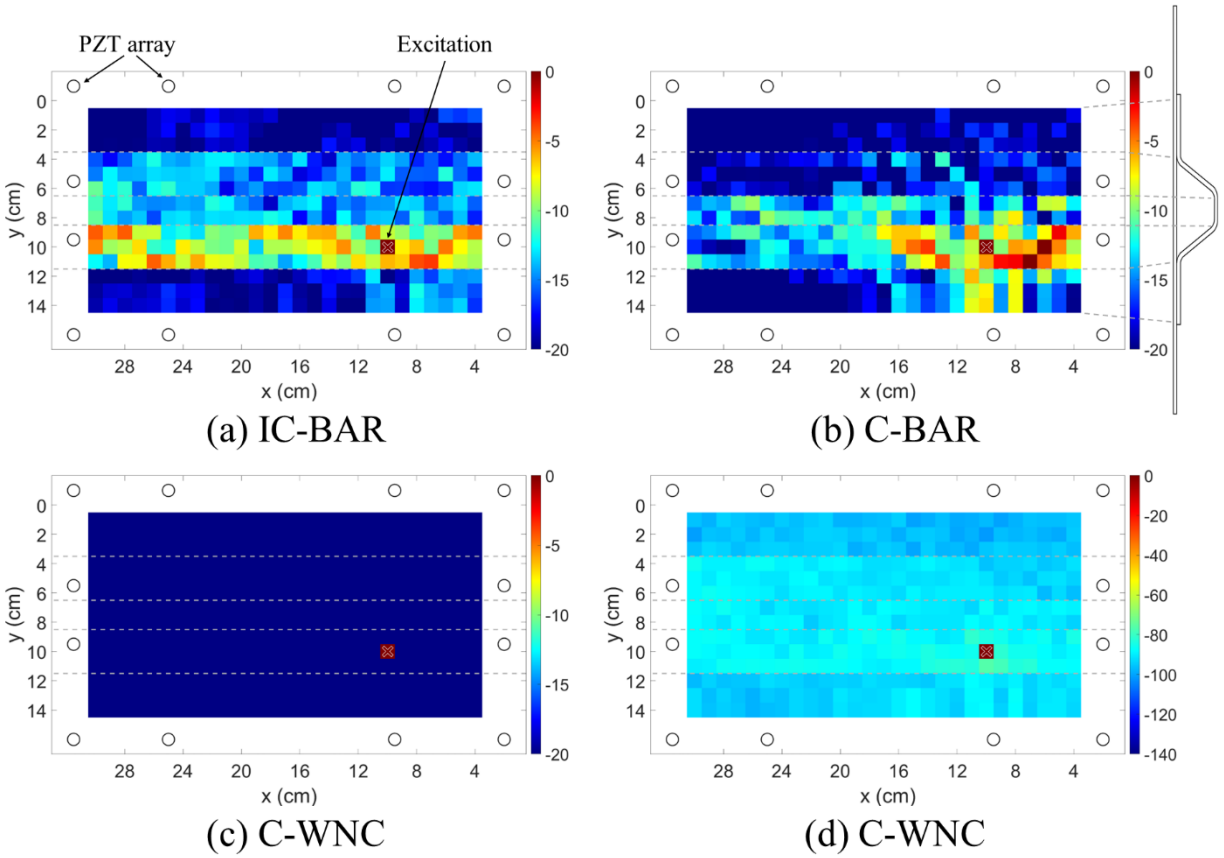

Figure 6.7: Same as Fig. 6.6 except that in this figure the results are generated by the covariance matrix directly composed by the receiver array without deconvolution with the excitation signal.

can be contaminated by the uncontrolled active source in both magnitude and phase. Fig. 6.7 shows the same hammer excitation on the stringer heel but without deconvolving the excitation signal. Surprisingly, the IC-BAR image in Fig. 6.7(a) is still similar to the deconvolved version in Fig. 6.7(a). This is due to the lack of coherence in the narrowband Bartlett (a linear sum of the sampled frequencies) that makes the beamformer insensitive to the excitation spectrum. The C-BAR image in Fig. 6.7(b) shows a significant degradation compared to its deconvolved counterpart in Fig. 6.7(b). Additional side lobes at locations to the right of the correct impact location even have larger intensities. The good news is that when the adaptive beamformer is used as in Fig. 6.7(c), the C-WNC image still outputs the correct impact localization. This result confirms the superior

performance of adaptive matched field beamformers to focus on the correct wavefield source through their optimization scheme. If the C-WNC image is plotted in a 140 dB dynamic range in Fig. 6.7(d), it is obvious that the bias available is less than the examples with deconvolution in Fig. 6.6(d) due to the decreased SNR in the covariance matrix.

6.3.3 Imaging Defects as Secondary Scatterers

Localizing defects is often the primary objective of an SHM system. Fig. 6.8 demonstrates the ability of the primary source null operation to find the secondary source (i.e. a defect scatterer) for the same stiffened composite panel. As mentioned above, the defect is here simulated by an added mass. Since the scattering of from the defect is much weaker than the active impact source, it is impossible to image using incoherent linear processors. Fig. 6.8 shows the results of coherent MFP algorithms by changing the number of excitations (and thus snapshots) in the projected covariance matrix. The sampled frequencies are the same as in the previous section, so the dimension of the super covariance matrix is 26*12 = 312. Fig. 6.8(a) shows the images by only using 20 snapshots (repetitions) of one hammer excitation located on the stringer flange. By removing the first eigenvector associated to the dominant source, the rank of the covariance matrix is 19. Although this is a rank deficient problem in WNC similar to most cases seen in this work, the C-WNC image does not focus on the defect nor give the expected dynamic range bias. This is because there is no “secondary source” after the null operation since the SNR of the added mass is too weak to show in the eigen structure. As seen in the C-BAR image, after removing the first eigenvector, the image still focuses close to the location of the active source. To build up the eigen mode associated with the added mass, four excitations at different locations on the stringer flange were used to construct the ensembled covariance matrix, as shown in Fig. 6.8(b). The null operation was performed for each excitation before the final summation. Considering 20 snapshots

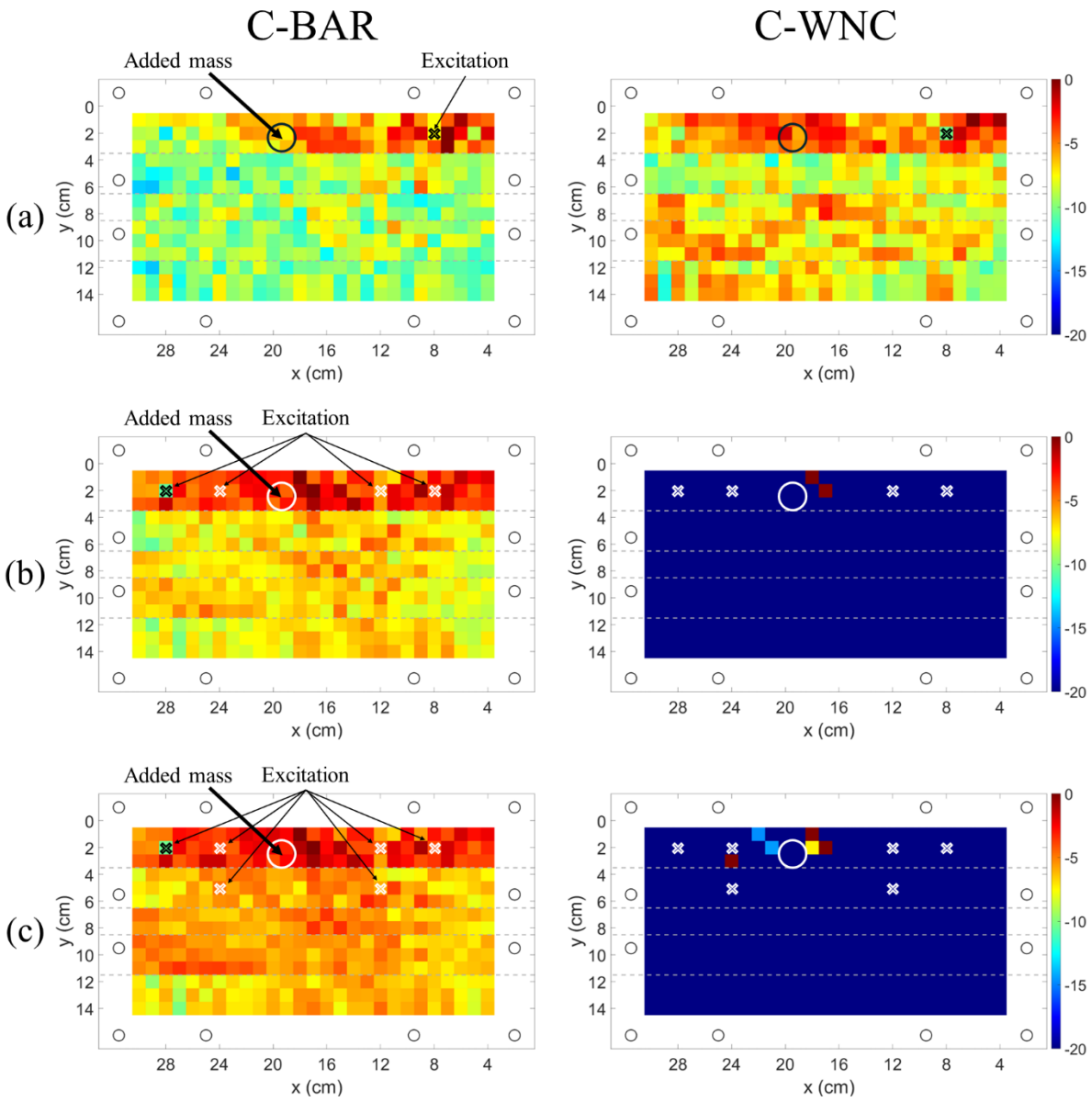

Figure 6.8: Defect imaging using coherent matched field beamformers and dominant source null operation. The defect was simulated by an added mass on the stringer flange. Imaging results using C-BAR and C-WNC beamformers with (a) one excitation on stringer flange, (b) four excitations at different axial locations, and (c) six excitations on stringer flange and heel.

for each excitation, the rank of the covariance matrix is thus 4*(20-1) = 76. It can be seen from the linear C-BAR image that the maximum intensity is focused to the right boundary of the added mass. Besides, large side lobes are observed close to each excitation location. This means that

although the null operation tries to project out the dominant source, the eigen modes associated with the active sources still exist in the remainder of the covariance matrix. Fig. 6.8(c) shows the results by considering six excitations with two additional impacts on the stringer heel. Since the excitations on the stringer heel contribute less to the SNR than those on the stringer flange, the response outside the top stringer flange ($y > 3$ cm) grows even larger in C-BAR due to the introduced sensitivity in the eigen structure compared to Fig. 6.8(b). For the C-WNC image, the adaptive beamformer focuses on both outer boundaries of the added mass. Only one pixel located close to the excitation at $x = 24$ cm remains as the "false positive", due to the incompleteness of null operation as mentioned earlier. The comparison in Fig. 6.8 shows that the more distributed excitations locations, the easier it is to image the secondary wave scatterer. It is worth mentioning that the current case of simulated defect is difficult to be imaged using MFP algorithms because the effective contact area of the added mass is comparable to the smallest wavelength considered. In contrast. the MFP beamformers tend to find point sources instead of extended targets (larger areas). Therefore, it is expected that smaller defects such as cracks or drilled holes should show higher SNR than the added mass considered in the current work.

6.4 Conclusions

This chapter presents an MFP framework to image damage in a stiffened composite panel using experimental data as replica model. A 12-element sparse PZT array was employed as the receiver, and a hammer was used as the active source. First, the Green's function was extracted by performing deconvolution using normalized cross power spectrum between the received signal and the excitation signal. The library of replica vectors was then built by the assembly of the experimentally acquired Green's functions that encoded the complex multimodal and dispersive

wave propagation in the stiffened panel at the various points of an imaging grid. In the imaging stage, the coherent supervector formulation of WNC beamformer generated high resolution and high contrast image of the primary impact source in the wavefield. The dispersive wavefield in the composite waveguide could be beamformed coherently by exploiting cross frequency terms, and the rank deficiency of the super covariance matrix caused the expected dynamic range bias that significantly suppressed the noise floor. The results show that the null operation through eigen space decomposition can effectively remove the dominant active source so that the defect can be imaged as the secondary source. The randomization of the excitation locations was beneficial to image the damage. Future work could involve placing the simulated damage at different locations of the stiffener such as the stringer heel and the stringer cap. Real structural damage such as debonding and cracks should be investigated to further explore the effectiveness of the presented methodology [30]. The authors are also working on employing the passive Green's function extraction framework to reconstruction the active transfer matrix [29] as an alternative approach to ease the complexity of handling the primary source in active sensing modalities.

Acknowledgements

The authors want to thank Prof. Hyonny Kim and his students at UCSD for providing invaluable technical information, designing, and constructing the composite stiffened panels. This research was funded in part by the Federal Aviation Administration Joint Center of Excellence for Advanced Materials (FAA Cooperative Agreement 12-C-AM-UCSD), in part by the U.S. Federal Railroad Administration under contract no. 693JJ619C000008 (Dr. Robert Wilson, Program Manager), and in part by MxV Rail through a University Grand Challenge Contract no. 24-0312-008622 (Dr. Anish Poudel, Program Manager).

Chapter 6, in part, is a reprint of the material as it appears in C. Huang, A.Z. Hosseinzadeh, and F. Lanza di Scalea, "Damage Imaging in Stiffened Composite Panels by Ultrasonic Sparse Array Matched Field Processing," *Proceedings of American Society for Composites 39th Annual Technical Conference*, 2024. The dissertation author was the primary investigator and author of this paper.

References

[1] J.L. Rose, "Ultrasonic guided waves in structural health monitoring," *Key Engr. Mater.*, vol. 270, pp.14-21, 2004.

[2] C.H. Wang, J.T. Rose, and F.K. Chang, "A synthetic time-reversal imaging method for structural health monitoring," *Smart Mater. Struct.,* vol. 13, p.415, 2004.

[3] J.E. Michaels, "Detection, localization and characterization of damage in plates with an in situ array of spatially distributed ultrasonic sensors," *Smart Mater. Struct.,* vol. 17, p. 035035, 2008.

[4] F. Yan, R.L. Royer Jr, and J.L. Rose, "Ultrasonic guided wave imaging techniques in structural health monitoring," *J. Intell. Mater. Syst. Struct*., vol. 21(3), pp.377-384, 2010.

[5] C. Holmes, B.W. Drinkwater, and P.D. Wilcox, "Post-processing of the full matrix of ultrasonic transmit-receive array data for non-destructive evaluation," *NDT&E Int.*, vol. 38, pp. 701–711, 2005.

[6] E. Lubeigt, S. Rakotonarivo, S. Mensah, J.F. Chaix, F. Baqué, and W.A. Kuperman, "Passive structural monitoring based on data-driven matched field processing," *J. Acoust. Soc. Am.*, vol. 145, pp. EL317–EL322, 2019.

[7] M. Engholm and T. Stepinski, "Direction of arrival estimation of Lamb waves using circular arrays," *Struct. Health Monit.*, vol. 10, pp. 467–480, 2011.

[8] S. Yuan, Y. Zhong, L. Qiu and Z. Wang, "Two-dimensional near-field multiple signal classification algorithm–based impact localization," *J. Intell. Mater. Syst. Struct.*, vol. 26, pp. 400–413, 2015.

[9] Q. Bao, S. Yuan, F. Guo and L. Qiu, "Transmitter beamforming and weighted image fusion–based multiple signal classification algorithm for corrosion monitoring," *Struct. Health Monit.*, vol. 18, pp. 621–634, 2019.

[10] Q. Bao, S. Yuan and F. Guo, "A new synthesis aperture-MUSIC algorithm for damage diagnosis on complex aircraft structures," *Mech. Syst. Sig. Process.*, vol. 136, p. 106491, 2020.

[11] P.D. Wilcox, "A rapid signal processing technique to remove the effect of dispersion from guided wave signals," *IEEE Trans. Ultrason., Ferroelect., Freq. Contr.*, vol. 50, pp. 419–427, 2003.

[12] H. Zuo, Z. Yang, C. Xu, S. Tian and X. Chen, "Damage identification for plate-like structures using ultrasonic guided wave based on improved MUSIC method," *Compos. Struct.*, vol. 203, pp. 164–171, 2018.

[13] Q. Bao, S. Yuan, Y. Wang and L. Qiu, "Anisotropy compensated MUSIC algorithm based composite structure damage imaging method," *Compos. Struct.*, vol. 214, pp. 293–303, 2019.

[14] C. Xu, J. Wang, S. Yin and M. Deng, "A focusing MUSIC algorithm for baseline-free Lamb wave damage localization," *Mech. Syst. Sig. Process.*, vol. 164, p. 108242, 2022.

[15] S. Hou, K. Solna and H. Zhao, "A direct imaging algorithm for extended targets," *Inverse Probl.* vol. 22, pp. 1151–1178, 2006.

[16] D.H. Chambers and A.K. Gautesen, "Time reversal for a single spherical scatterer," *J. Acoust. Soc. Am.* vol. 109, pp. 2616–2624, 2001.

[17] R. Pierri and F. Soldovieri, "On the information content of the radiated fields in the near zone over bounded domains," *Inverse Probl.* vol. 14, pp. 321–337, 1998.

[18] A.B. Baggeroer, W.A. Kuperman and P.N. Mikhalevsky, "An overview of matched field methods in ocean acoustics," *IEEE J. Oceanic Eng.* vol. 18, pp. 401–424, 1993.

[19] A.B. Baggeroer, W.A. Kuperman and H. Schmidt, "Matched field processing: Source localization in correlated noise as an optimum parameter estimation problem," *J. Acoust. Soc. Am.* vol. 83, pp. 571–587, 1988.

[20] J.B. Harley and J.M. Moura, "Data-driven matched field processing for Lamb wave structural health monitoring," *J. Acoust. Soc. Am.* vol. 135, pp. 1231–1244, 2014.

[21] Z.H. Michalopoulou and M.B. Porter, "Matched-field processing for broad-band source localization," *IEEE J. Oceanic Eng.* vol. 21, pp. 384–392, 1996.

[22] C. Debever and W.A. Kuperman, "Robust matched-field processing using a coherent broadband white noise constraint processor," *J. Acoust. Soc. Am.* vol. 122, pp. 1979–1986, 2007.

[23] C. Huang and F. Lanza di Scalea, "Ultrasound time reversal imaging of extended targets using a broadband white noise constraint processor," *Proceedings on Medical Imaging 2023: Ultrasonic Imaging and Tomography*, vol. 12470, pp. 15–24. SPIE, San Diego, California, United States, 2023.

[24] C. Huang and F. Lanza di Scalea, "High Resolution Ultrasonic Imaging of Extended Targets via Combined Match Field and Time Delay Beamforming," *Ultrasonics*, vol. 145, p. 107464, 2024.

[25] J. D. Tippmann and F. Lanza di Scalea, "Passive-only defect detection and imaging in composites using diffuse fields," in *Mechanics of Composite and Multi-functional Materials*, Conference Proceedings of the Society for Experimental Mechanics Series, vol. 7, pp. 67–72, 2016.

[26] F. Lanza di Scalea, S. Sternini and A.Y. Liang, "Robust passive reconstruction of dynamic transfer function in dual-output systems," *J. Acoust. Soc. Am.* vol. 143, pp. 1019–1028, 2018.

[27] G.C. Carter, C.H. Knapp and A.H. Nuttall, "Estimation of the magnitude-squared coherence function via overlapped Fast Fourier Transform processing," *IEEE Trans. Audio Electroacoust.*, vol. AU-21, pp. 337–344, 1973.

[28] H. Song, W.A. Kuperman, W.S. Hodgkiss, P. Gerstoft and J.S. Kim, "Null broadening with snapshot-deficient covariance matrices in passive sonar," *IEEE J. Oceanic Eng.* vol. 28, pp. 250–261, 2003.

[29] C. Huang, A.Z. Hosseinzadeh and F. Lanza di Scalea, "Ultrasparse Ultrasonic Synthetic Aperture Focus Imaging by Passive Sensing," *IEEE Trans. Ultrason., Ferroelect., Freq. Contr.* vol. 71, pp. 518-535, 2024.

[30] C. Huang and F. Lanza di Scalea, "An ultrasonic scanning system for the inspection of composite stiffened panels from elastic constant identification via inversion of guided waves," *Compos. Struct.*, vol. 322, p. 117373, Oct. 2023.

[31] C. Huang and F. Lanza di Scalea, "Application of Sparse Synthetic Aperture Focusing Techniques to Ultrasound Imaging in Solids Using a Transducer Wedge," *IEEE Trans. Ultrason., Ferroelect., Freq. Contr.* vol. 71, pp. 280–294, 2024.

Chapter 7 Elastic Constant Identification via Inversion of Guided Wave Dispersion Curves for the in-situ Inspection of Composite Stiffened Panels

7.1 Introduction

The non-destructive inspection of aerospace composite structures is of paramount important to ensure safety and proper operation. The most common objective of such inspections is to detect structural damage or structural degradation. Identifying the elastic constants of a composite part can be an invaluable tool for not only detecting damage but also estimating residual strength. It is also desirable that such capability be available without the necessity to disassemble the part, i.e. available for an *in-situ* test on a given structure in service.

A common testing technique utilized to identify the elastic constants of composite panels is vibrational modal analysis, as recently reviewed by Tam et al. [1]. The majority of these efforts have focused on finding the four in-plane elastic properties (longitudinal and transverse in-plane Young's moduli, in-plane shear modulus and in-plane Poisson's ratio) [2-4], with additional investigations expanding to the out-of-plane moduli (out-of-plane shear modulus, out-of-plane Poisson's ratio, engineering bending stiffness, etc.) [5-7]. Most of these studies were based on minimizing the discrepancy between the experimental modal behavior and the predicted behavior obtained from a given set of trial elastic constants [7, 8]. The largest drawback in the application of vibrational techniques is the requirement of free boundary conditions of the test part, which makes it quite challenging to apply as an *in-situ* test on a structure in-service.

The use of ultrasonic guided waves is an alternative approach for the non-destructive identification of composite constants. The advantage of this method is the insensitivity to the part's boundary conditions that enables an implementation *in-situ* [9-11]. Ultrasonic guided waves

propagating in the 100's kHz frequency range have been commonly used for defect detection in composite parts [12-14]. However, predicting guided wave propagation can be challenging in laminated composites owing to the wave multimode and dispersive characteristics. Due to these complexities, the majority of guided wave testing has aimed at defect detection, with much fewer studies on elastic property identification. Similarly to the modal vibrational techniques, property identification using guided waves involves modeling the multimode and dispersive wave propagation behavior in the composite waveguide, and then utilizing an optimization scheme to match the model to experimental responses. Balasubramaniam [15] first accomplished this task using the dispersion relations of the fundamental axial and flexural mode phase velocity using Genetic Algorithm as the optimization and the transfer matrix method as the forward model. Vishnuvardhan et al. [16] used a single transmitter and multiple receivers to sample the spatial guided wave field in orthotropic plates. Nine elastic constants were inverted using the narrowband Christoffel equation as the forward model. Glushkov et al. [17] explored the group velocity dispersion curve optimization for the elastic identification of unidirectional and cross-ply laminates. The forward model was the general elasto-dynamic theory involving Green's function integral for layered media. Another study [18] implemented elastic property inversion using guided waves in non-contact transduction modes. More recent works on ultrasonic guided waves for property identification in composites have used either genetic algorithms [19, 20] or convolutional neural networks [21] for the dispersion inversion routine. The pulsed ultrasonic polar scan (P-UPS) method is another successful ultrasonic-based technique able to invert the viscoelastic properties of composites without prior knowledge of the material symmetry orientation [22]. The property inversion is based on a forward model followed by an optimization routine. The P-UPS method is a local technique that identifies properties at a specific point of the test piece.

The typical guided wave propagation models in previous studies involve close-form solutions that can be computationally intensive in the case of multilayered waveguide. As an alternative to the theoretical forward methods, the Semi-Analytical Finite Element (SAFE) technique has gained favor in modeling the complex multimode and dispersive guided wave solutions with limited computational efforts [23-26]. The SAFE technique only requires the finite element discretization of the cross-section of the waveguide and assumes harmonic solutions in the wave propagation direction. The SAFE technique was utilized by Marzani et al. [9] to identify lamina constants in unidirectional and cross-ply laminates by inverting group velocity curves. Specifically, this study estimated constants along with two directions for the unidirectional laminate and four directions for the cross-ply laminate utilizing pseudo-experimental data.

In practice, inverting phase velocity dispersion curves requires the experimental measurement of these curves on the test part. This is typically accomplished utilizing a 2D Fast Fourier Transform (2D-FFT) method [27] that requires a series of wave measurement points sampled over several spatial locations along the wave propagation direction. For an application requiring scanning the part to map several zones, the requirement for multiple sensing points at each scanning position would be both cumbersome and slow. In this case, a better approach would involve measuring the wave at only one detection point and extracting the experimental dispersion curves from the one measurement. This can be accomplished by analyzing the phase spectrum of the measured signals as originally discussed by Sachse and Pao [28]. That paper also discusses the importance of unwrapping the phase data to resolve the +/- π uncertainties arising from the arctan function. However, the extraction of dispersion curves using a single transmitter and a single receiver ("single-input single-output"-SISO- scheme) requires knowledge of the excitation signal to appropriately deconvolve that from the output [29]. The excitation signal is difficult to

determine given the unknown effects of the transmitter frequency response and the transmitter-to-structure coupling. Consequently, a more robust way to extract wave information from the test piece is to utilize two receivers ("single-input dual-output" -SIDO- scheme) [30]. The "dual-output" modality enables the isolation of the true structural transfer function (or Green's function) by eliminating the effect of the excitation and of the receiver-to-structure coupling. This approach was utilized by Allen et al. [31] to measure phase velocity dispersion curves in metals for the purpose of determining residual stresses. More recently, Capriotti and Lanza di Scalea [32] utilized the SIDO approach in an ultrasonic scanning prototype system that employed an impact as the wave generation and two non-contact air-coupled transducers for the wave detection. In that paper, the scanning system was applied to the detection of impact damage in a built-up composite aerospace panel by tracking changes in the panel's wave transfer function.

The present paper combines elements of the SIDO scanning approach for damage detection by Capriotti and Lanza di Scalea [32], the elastic constant estimation by inversion of phase velocity curves by Cui and Lanza di Scalea [10, 11] and the phase-spectrum method to measure dispersion curves from a single excitation by Sachse and Pao [28] to present a new technique demonstrating the estimation of elastic constants in aerospace stiffened composite panels by inversion of phase velocity curves extracted in a SIDO approach from an ultrasonic scanning prototype. As discussed above, the typical use of ultrasonic scanning systems is to track changes in the wave scattering behavior (i.e. tracking wave amplitude or arrival times) to detect structural damage. An ability to also relate wave information to the elastic constants of the composite along the wave propagation path adds to the performance of the scanning process because of the direct link between damage and elastic constants. This link, which is well established for some structural materials such as concrete [33, 34] and is also expected for composites [35], although dependent on the specific

material and manufacturing process, can be further exploited to not only detect and quantify structural damage (resulting in a degradation of the elastic constants), but also to potentially estimate the remaining strength of the part. Proof-of-principle experiments were first conducted on skin-only isotropic and anisotropic plates to show the accuracy of the elastic constant inversion using the proposed method. Validation experiments were then performed on stiffened skin-to-stringer Carbon-Fiber-Reinforced Polymer (CFRP) panels with impact-type damage. The estimation of the elastic constants by the inversion of the flexural guided wave mode shows an excellent correlation with the severity of the damage.

7.2 Elastic Constant Identification Algorithm

7.2.1 Semi-analytical Finite Element (SAFE) as the forward model

The inversion of the composite elastic constants using optimization requires a forward model with low computational effort. The SAFE method of the type presented in [23, 24] is a good candidate for this purpose. As schematized in Fig. 7.1, SAFE only requires the finite element discretization of the laminate in the cross-sectional plane (y, z) and assumes harmonic motion along the wave propagation direction, x. The displacement field for each mono-directional element is expressed as

$$\boldsymbol{u}^{(e)}(x,y,z,t) = \begin{bmatrix} \sum_{j=1}^{n} N_j(y,z)U_{xj} \\ \sum_{j=1}^{n} N_j(y,z)U_{yj} \\ \sum_{j=1}^{n} N_j(y,z)U_{zj} \end{bmatrix}^{(e)} e^{i(\xi x-\omega t)} = \boldsymbol{N}(y,z)\boldsymbol{q}^{(e)}e^{i(\xi x-\omega t)} \qquad (7.1)$$

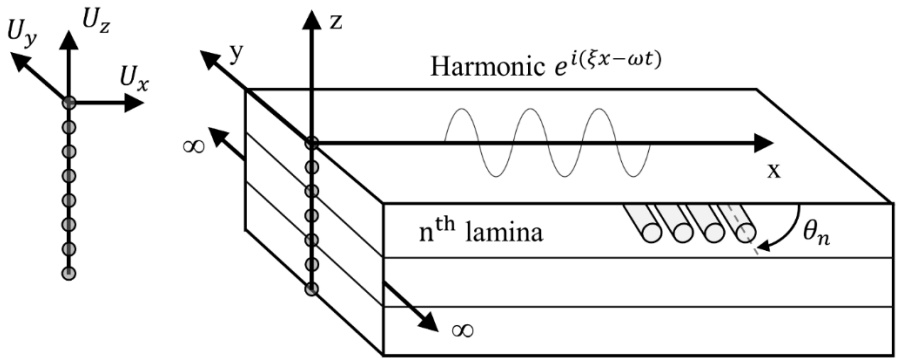

Figure 7.1: SAFE model of wave propagation in laminated composites.

where n is the number of nodes per element, $N_j(y,z)$ are the shape functions, U is the nodal displacement, ξ is the wavenumber, ω is the frequency.

In the case of a multilayered laminate, the lamina stiffness matrix $\boldsymbol{C}$ can be rotated from the local (1,2,3) onto the global (x,y,z) coordinate system using the following transformation

$$\boldsymbol{C}_\theta = \boldsymbol{R}_{rot1}\boldsymbol{C}\boldsymbol{R}_{rot2}^{-1} \tag{7.2}$$

and the global stiffness matrix $\boldsymbol{C}_\theta$ is then assembled in the mono-directional FE discretization to characterize the entire laminate. Following standard FE assembling procedures, an *M*-degree of freedom system that can be formulated as [23]

$$[\boldsymbol{H} - \xi\boldsymbol{L}]_{2M}\boldsymbol{Q} = 0 \tag{7.3}$$

where $\boldsymbol{H}$ and $\boldsymbol{L}$ are real symmetric matrices containing stiffness terms, mass terms, and $\boldsymbol{Q} = [\boldsymbol{U} \quad \xi\boldsymbol{U}]^T$ is the displacement vector. The eigensystem is solved by finding the 2*M* wavenumbers ξ for each frequency ω, and the corresponding eigenvectors representing the cross-sectional displacement mode shapes. The phase velocity can be then calculated by

$$c_p = \omega/\xi_{Re} \tag{7.4}$$

For a given composite layup, SAFE can directly calculate the phase velocity dispersion curves from a set of trial lamina constants $(E_{11}, E_{22}, \upsilon_{12}, G_{12}, \upsilon_{23})$. For the evaluation of overall

strength reduction of a panel, it is of more interest to obtain the "effective" or engineering laminate moduli ($E_x, E_y, \upsilon_{xy}, G_{xy}, \mathrm{K}_x, \mathrm{K}_y, \mathrm{K}_{xy}$) that characterize the average elastic behavior. Classical Lamination Theory (CLT) can be used to estimate the seven laminate's engineering elastic properties from the inversion output of the five lamina constants [10, 11]:

$$\begin{bmatrix} \boldsymbol{\varepsilon}^0 \\ \boldsymbol{\kappa} \end{bmatrix} = \begin{bmatrix} \boldsymbol{A}^{-1} & 0 \\ 0 & \boldsymbol{D}^{-1} \end{bmatrix} \begin{bmatrix} \boldsymbol{N} \\ \boldsymbol{M} \end{bmatrix} \tag{7.5}$$

where $\boldsymbol{\varepsilon}^0$ is the mid-plate in-plane strain, $\boldsymbol{\kappa}$ is the out-of-plane curvature, $\boldsymbol{A}$ and $\boldsymbol{D}$ are the laminate stiffness matrices calculated from lamina stiffness matrices in the global reference system, and $\boldsymbol{N}$ and $\boldsymbol{M}$ are the external force and moment loadings. The seven effective moduli of the laminate can be calculated by properly setting the boundary conditions in Eq. 7.5, including four in-plane properties (axial stiffness E_x, axial stiffness E_y, in-plane Poisson's ratio υ_{xy}, and in-plane shear stiffness G_{xy}) and three out-of-plane properties (flexural rigidity K_x, flexural rigidity K_y, and torsional rigidity K_{xy}).

7.2.2 Simulated Annealing Algorithm as the optimization scheme

The goal of the inversion procedure is to find a set of lamina constants ($E_{11}, E_{22}, \upsilon_{12}, G_{12}, \upsilon_{23}$) whose corresponding phase velocity spectrum best matches the measured spectrum. With the primary application being the inspection of stiffened composite panels, the focus of the inversion algorithm is not necessarily on estimating the "true" elastic moduli, but rather on tracking any reduction in constants in a damaged zone relative to a pristine zone of the panel. The optimization process requires to minimize the objective function defined as the following:

$$d = \frac{1}{N} \sqrt{\sum_{i=1}^{N} \left(\frac{c_{p,pred}(\omega_i) - c_{p,exp}(\omega_i)}{c_{p,exp}(\omega_i)} \right)^2} \tag{7.6}$$

where d is the discrepancy metric, $c_{p,pred}(\omega_i)$ is the phase velocity spectrum from SAFE analysis, $c_{p,exp}(\omega_i)$ is the phase velocity spectrum from experimental measurements, and N is the number of samples in the spectrum. Simulated annealing (SA), as schematized in Fig. 7.2, is a global Monte Carlo method developed to find the global minimum of multi-variable functions with many local minima [36]. Each iteration j involves a random perturbation of each parameter in Z_j followed by a forward model (SAFE in this case) and mismatch calculation. If the calculated mismatch is smaller than the previously accepted model stored in Z_i, the new model may be accepted if

$$r < P = e^{-\Delta d/T} \tag{7.7}$$

where r is a random number from 0 to 1, Δd is the mismatch difference between the current trial model $d(Z_j)$ and the previously accepted model $d(Z_i)$, and T is the current temperature that is decreased with the number of accepted model updates i according to the cooling schedule

$$T = T_0 \alpha^i \tag{7.8}$$

where T_0 is the initial temperature, and α is the cooling parameter.

After each model updating, each parameter in accepted model Z_i is perturbed to obtain a new test value $Z_j = Z_i + \Delta Z_i$ according to

$$\Delta Z_i = \Delta Z_0 \left(\frac{T}{T_0}\right)\left(\eta_1 \tan\left(\frac{\eta_2 \pi}{2}\right)\right) \tag{7.9}$$

where ΔZ_0 is the predefined initial perturbation, and η_1 and η_2 are two uniformly random numbers from -1 to 1. All parameters in Z_j are perturbed at once after each trial j, which speeds up the convergence for correlated parameters in composite elasticity. In this paper, the SA algorithm is run 1000 iterations to ensure full coverage of the search domain based on the Cauchy distribution and the specific choices of T_0 and α.

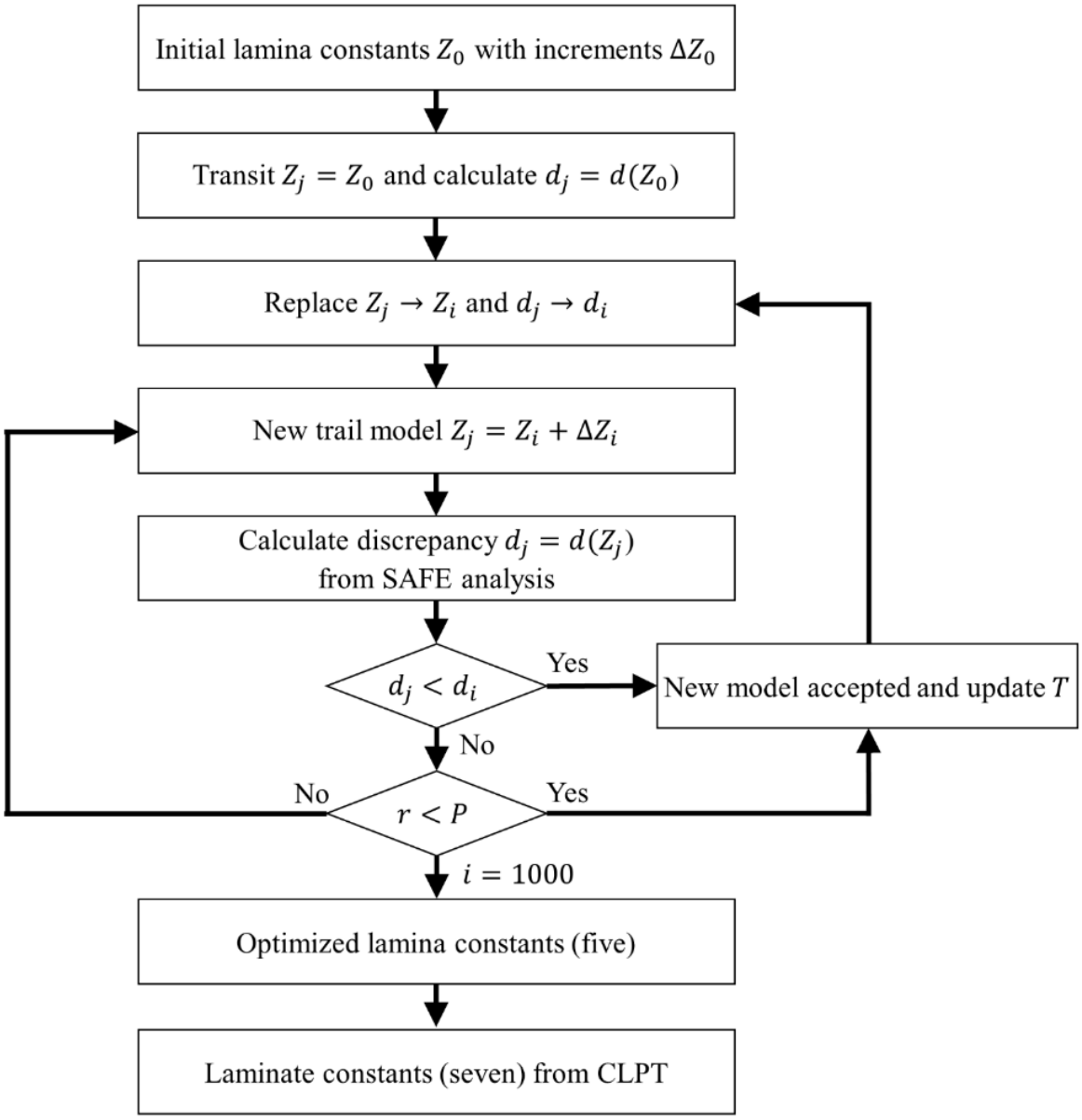

Figure 7.2: Flowchart of the simulated annealing algorithm to optimize lamina constants using SAFE as a forward model.

The seven engineering constants ($E_x, E_y, \upsilon_{xy}, G_{xy}, K_x, K_y, K_{xy}$) can be finally calculated from the five lamina constants using CLT. The resulting effective elastic constants include four in-plane (compressional and shear) and three out-of-plane (flexural and torsional) properties.

7.3 Experimental Extraction of Phase Velocity Dispersion Curves from Dual-Output Systems

According to the SIDO scheme, in the scanning system presented in this work the phase velocity curve is extracted at each scan line using a single (impact) excitation and tracking the difference in phase spectra measured by two receiver points (air-coupled transducers) (Fig. 7.3). At each scanning position, the two receivers R_1 and R_2 are positioned across the interest zone, i.e. the structurally critical zone where integrity needs to be assessed (the stringer-stiffened area of the test panel in our case).

The deconvolution between the two received signals, $R_1(\omega)$ and $R_2(\omega)$, leads to [30]

$$\frac{R_2(\omega)}{R_1(\omega)} = G(\omega) \cdot \frac{S_2(\omega)}{S_1(\omega)} \cong G(\omega) \tag{7.10}$$

where $G(\omega)$ is the structure Green's function between point 1 and point 2 and assuming the transfer functions of the two sensors, $S_1(\omega)$ and $S_2(\omega)$, are equal. Hence the deconvolution operation between the two receivers successfully isolates the Green's function $G(\omega)$ without the influence of the excitation $E(\omega)$, which can be highly variable in the subject case of an impactor. Even if the response of the two receivers is different, the deconvolution in Eq. 7.10 is still effective for the structural inspection objective since any discrepancy in $S_1(\omega)$ and $S_2(\omega)$ only leads to a phase factor that is consistent throughout the scan, i.e. still able to discriminate structure-related changes such as damage.

The final phase spectrum of the wave propagating in the structure is simply the phase of $G(\omega)$ in Eq. 7.10

$$\phi_G(\omega) = \phi_{R_2}(\omega) - \phi_{R_1}(\omega) \tag{7.11}$$

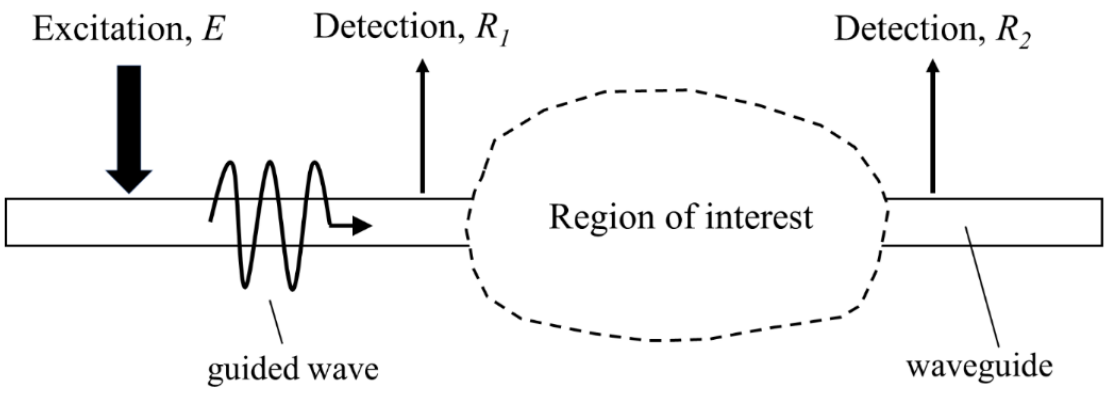

Figure 7.3: The basic idea of the Single-Input-Dual-Output (SIDO) scheme for structural inspection.

where $\phi_{R_1}(\omega)$ and $\phi_{R_2}(\omega)$ are the unwrapped phases from the Fast Fourier Transforms (FFTs) of the measurements from $R_1(\omega)$ and $R_2(\omega)$, respectively.

Traditional time-of-flight measurements cannot evaluate the phase velocities for a dispersive, broadband transient wave. Therefore, the phase spectrum method by Sachse and Pao [28] is here adapted to the dual-output system. The phase spectrum of the Green's function in Eq. 7.11 is linearly related to the propagation path by:

$$\phi_G(\omega) = \xi_{Re} L \tag{7.12}$$

where ξ_{Re} is the real part of the wavenumber and L is the wave travel distance. Accordingly, the dispersion relation of the test part can be extracted by the phase spectrum difference of a propagating wave at the two receiving points

$$c_p = \frac{\omega}{\xi_{Re}} = \frac{-\omega L}{\phi_{R_2}(\omega) - \phi_{R_1}(\omega) \pm 2m\pi} \tag{7.13}$$

Phase unwrapping is needed to resolve the $\pm\pi$ phase ambiguity resulting from the arctan function. The unwrapping step is particularly critical for ultrasonic signals which lack DC component and hence have low signal-to-noise ratio at low frequencies. The problem of tracking the accurate phase spectrum of these signals can be best addressed by using an additional time

marker T_i for each received signal that is placed just before the arrival of the wave packet of interest, as originally discussed in Ref. [31]. In this case, the phase spectrum in each signal R_i can be defined as

$$\phi_{R_i}(\omega) = \phi_{R_i win}(\omega) + \phi_{d_i} = \phi_{R_i win}(\omega) - \omega T_i \tag{7.14}$$

where $\phi_{R_i win}(\omega)$ is the "fine" phase component unwrapped from the windowed signal spectrum after the time marker, and ϕ_{d_i} is the "coarse" delay that absorbs most of the large phase angle before the arrival of the wave packet. If placed correctly, the "fine" phase is constrained in the range of $\pm\pi$ at low frequencies where phase unwrapping is the most problematic. Using this approach, the phase velocity of the test part can be finally expressed as

$$c_p = \frac{-\omega L}{\phi_{R_2 win}(\omega) - \phi_{R_1 win}(\omega) - \omega(T_2 - T_1)} \tag{7.15}$$

where the phase ambiguity $2m\pi$ from Eq (13) is now resolved.

7.4 Proof-of-Principle Experiments: Elastic Constant Identification in Composite Laminate

7.4.1 Experimental methodology

Proof-of-principle experiments for elastic constant identification were conducted on an isotropic (Aluminum) plate and on a CFRP composite laminate representative of the skin of the aerospace panel. The SIDO configuration is shown in Fig. 7.4(a) and the scanning prototype is shown in Fig. 7.4(b). The excitation (*E*) was provided by an impactor that was custom-built by using a CFRP laminated strip with an aluminum tip to provide wave energy at frequencies up to ~ 250 kHz. The two receivers R_1 and R_2 were broadband, micro-machined capacitive air-coupled transducers (BAT-1, Microacoustics Corporation) with a frequency response of 20 kHz to 2MHz.

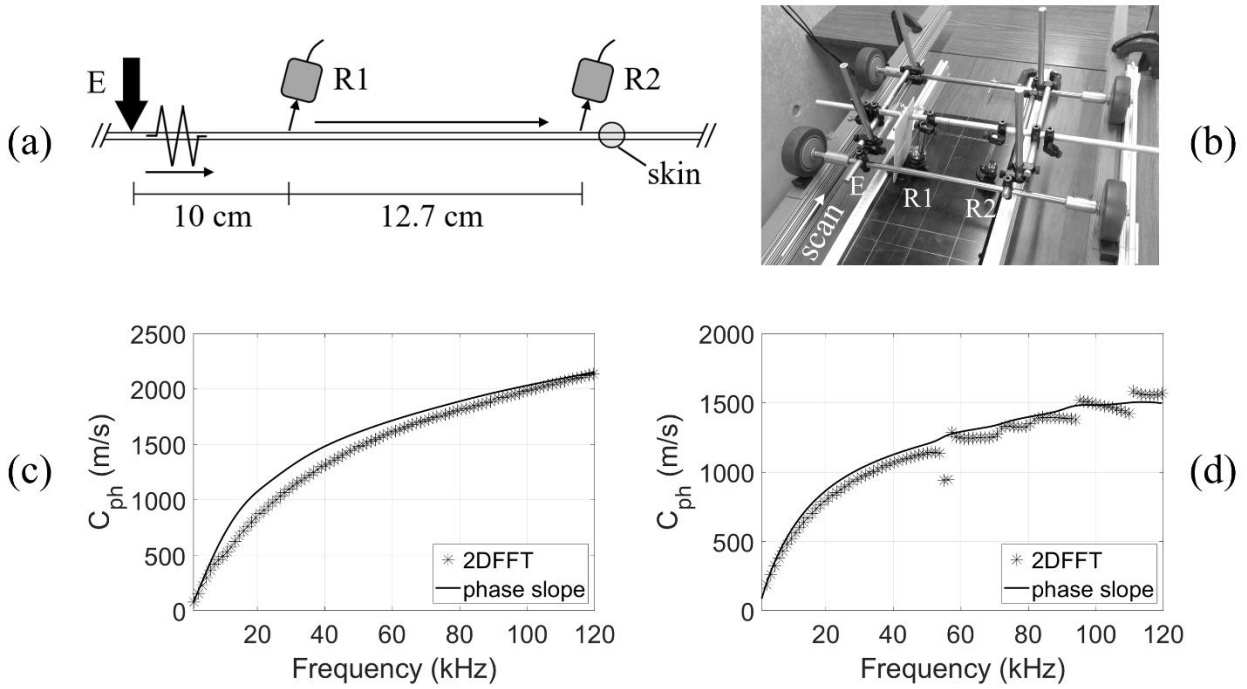

Figure 7.4: (a) Phase spectrum extraction from skin-only panels. (b) The SIDO scanning vehicle on the skin side of a stiffened composite panel. Comparison of experimental dispersion curves of (c) aluminum and (d) CFRP using 2D FFT and phase spectrum technique.

Following Snell's law of refraction, the transducers were oriented at an angle that maximized the detection of the fundamental flexural mode of the plate in a significant frequency range.

At each scanning position, the excitation was performed manually by bending the CFRP impactor and letting the aluminum tip hit the plate's surface. The responses at each position were averaged for ten impacts before converting to the frequency domain. Since the phase spectrum difference technique is independent of the excitation signal, there was no need to instrument the impactor with a piezoelectric sensor. All components were mounted on a wheeled cart with an encoder to track the scanning position along the "scan" direction shown in Fig. 7.4(b). For the proof-of-principle experiments, the cart was fixed and only one line scan data was used. First, the phase spectrum method of extracting phase velocity dispersion curves was compared to the traditional 2D-FFT method. Since the latter method requires acqusitions at several points along

the wave propagation direction, several impacts were performed while receiver R2 was moved by 1 mm each time for a total of 130 detection positions. The comparison is shown in Figs. 4(c) and 4(d) for the aliminum plate and the CFRP laminate, respectively. The reasonable match is expected since both approaches are viable techniques for phase velocity extraction as discussed above.

7.4.2 Isotropic plate

The first test specimen was an isotropic (Aluminum) plate with a thickness of 3.175 mm, Young's modulus $E = 73.1\,\text{GPa}$, Poisson's ratio $\upsilon = 0.33$ and density $\rho = 2700\,\text{kg/m}^3$. The objective was to evaluate the two independent elastic constants E and υ using the proposed inversion strategy. The waveforms received by the two receivers in the SIDO system are shown in Fig. 7.5(a) and (b). The impactor excited the structure with high SNR to generate clear arrival wave packets. A Hanning window was applied to each received signal to regularize the waveforms. The waveforms in Fig. 7.5(a) and (b) clearly show the typical shape of the flexural dispersive Lamb mode (A_0).

The experimental A_0 phase velocity dispersion curve was extracted using the proposed phase spectrum difference discussed in section 3. Accurate phase spectrum unwrapping was accomplished by tracing the arrival of each wave packet using the time marker, as shown in Fig. 7.5(a) and (b) using a cross marking the start of the "fine" phase time window. Fig. 7.5(d) compares the experimentally extracted curve to the curve predicted by the SAFE forward model at the end of the SA optimization routine (minimum of the objective function in Eq. 7.6). The good match between measurements and predictions suggests an expected accurate estimation of the plate's elastic constants.

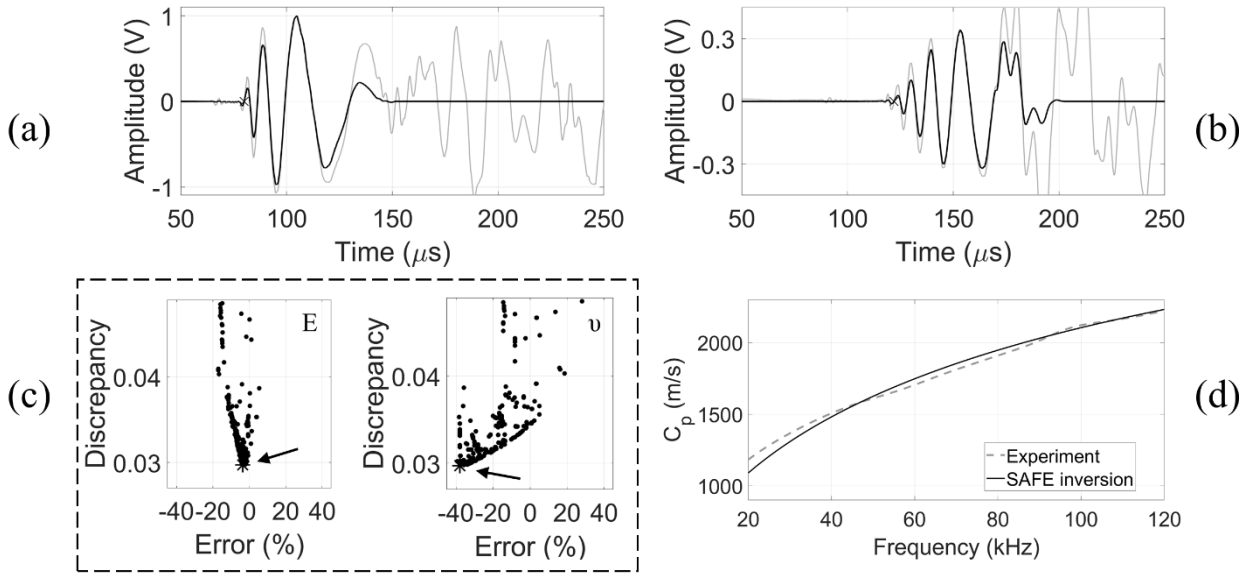

Figure 7.5: Proof-of-principle experimental results on the aluminum plate. Raw and windowed waveforms recorded by the air-coupled ultrasonic sensors R1 (a) and R2 (b). (c) Inversion of Young's modulus and Poisson's ratio. (d) Experimental phase velocity dispersion curve versus SAFE prediction at the end of the optimization routine.

The elastic moduli inversion analysis was conducted using the FSA optimization algorithm with the SAFE model as a forward solver as discussed in section 2. The trial dispersion curves were calculated by SAFE using the tentative model Z_j containing the two independent variables E and υ for the isotropic case. The 2D property inversion convergence results are shown in Fig. 7.5(c), with the horizontal axis representing the error between the identified constants and the ground truth values, and the vertical axis representing the discrepancy metric d as calculated in Eq. 7.6. The final identification results at the end of the FSA optimization procedure (minima points) are marked by a star with a pointing arrow in each plot. The closer the star is to the middle of the plot, the more accurate the particular elastic constant inversion outcome. The plots in Fig. 7.5(c) only show the ranges for d that correspond to a zoom-in view around the minimum of the objective function to better evaluate the convergence performance of different elastic constants. The convergence plot of Young's modulus E in Fig. 7.5(c) shows high sensitivity of the flexural

mode to the elastic stiffness. The final estimation for E is within a 5% error of the ground truth. However, the identification of the Poisson's ratio υ in Fig. 7.5(c) is more challenging since this property refers to the transverse behavior relative to the longitudinal motion of the wave propagation. The general difficulty in identifying Poisson's ratio from a single wave propagation direction was also previously identified by Cui and Lanza di Scalea [10, 11].

7.4.3 Composite laminate

The second specimen for the proof-of-principle tests was a 10-layer, Hexcel 282PW CFRP laminate with a layup of $[0/45/0/-45/0]_s$, plate thickness of 2.175 mm, and density of 1380 $\mathrm{kg/m^3}$. The ground truth constants for each woven ply (plain weave balanced) were given as $\mathrm{E_{11}} = 58\ \mathrm{GPa}, \mathrm{E_{22}} = 58\ \mathrm{GPa}, \upsilon_{12} = 0.3, \mathrm{G_{12}} = 5\ \mathrm{GPa}, \upsilon_{23} = 0.35$. The typical waveforms recorded by the two receivers in this case are shown in Fig. 7.6(a) and (b). Compared to the measurements on the isotropic plate in Fig. 7.5, the wave packets contain lower frequency components due to the increased material attenuation. The convergence plots are visualized in Fig. 7.6(c) in terms of the laminate engineering properties calculated using CLT following each accepted model Z_j. Again, the plots are zoomed-in to the final convergence regions with the smallest discrepancy values. The comparison between the experimental phase velocity dispersion curve and the SAFE predicted curve at the end of the optimization routine, Fig. 7.6(d), shows again a good match suggesting an accurate identification of the relevant constants. This is also confirmed in the final value of the discrepancy metric d that is much closer to 0 than the isotropic plate for all constants in Fig. 7.6(c). The fact that the property identification by inversion of dispersion data from a single wave propagation direction can actually more accurate in an anisotropic laminate compared to isotropic plates was already noticed by Cui and Lanza di Scalea [10, 11]. As amply discussed in those previous works, the reason for this is the normal-shear coupling and the in-

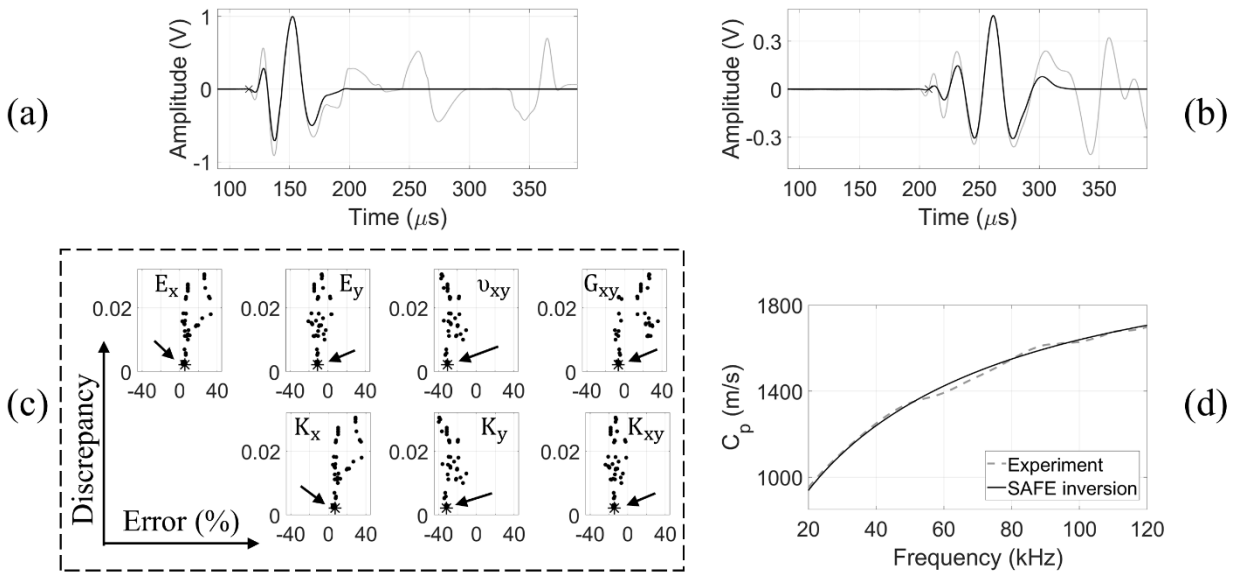

Figure 7.6: Proof-of-principle experimental results on the CFRP laminate. Raw and windowed waveforms recorded by the air-coupled ultrasonic sensors R1 (a) and R2 (b). (c) Inversion of four in-plane and three out-of-plane elastic constants. (d) Experimental phase velocity dispersion curve versus SAFE prediction at the end of the optimization routine.

plane/out-of-plane coupling that affects the wave mechanics in the anisotropic laminate and enhances the sensitivity of the wave propagating in one direction to elastic constants in transverse directions. The final property identification results of Fig. 7.6(c) indicate, as expected, best results for constants affecting the wave propagation direction, i.e. E_x and K_x that are estimated within a 5% error from the ground truth values. The in-plane stiffness in the transverse direction, E_y is estimated within an error as small as ~ 15% error which is still a remarkable result considering that the property is in a direction orthogonal to the wave propagation. The identification of the shear stiffness G_{xy} is also surprisingly accurate with only ~ 10% error, owing again to the stress-strain couplings previously discussed in Refs. [10, 11]. The tortional rigidity K_{xy} also benefits from the normal-shear couplings with a final estimation within a ~ 20% error. As expected, the identification of the Poisson's ratio remains the most challenging with an error of ~ 30%. Overall, the results in Fig. 7.6(c) indicate the possibility to estimate, with a good level of accuracy, several

key elastic constants of the laminate using a single wave propagation direction and a single excitation.

7.5 Scanning System Applied to Damage Quantification in Stringer Stiffened Composite Panels via Elastic Constants Identification

Two stringer-stiffened composite panels (herein referred to as panel A and panel B) were used for the validation of the damage detection and quantification capabilities of the proposed scanning prototype based on the elastic constant identification. These skin-to-stringer assemblies are typically found in modern commercial composite aircraft construction (e.g. B787) [37]. These panels were previously scanned by a SIDO scanning system tracking changes in the part's transfer function to detect damage [32]. The schematic drawings of the two test panels are shown in Fig. 7.7(a) and (b), respectively. Both panels consisted of a CFRP skin with a length of 1.10 m along the "location" axis, and co-cured hat-shape CFRP stringers. Both the skin material and the stringers were 16-ply CFRP laminates with a thickness of 2.62 mm, density of 1550 $\mathrm{kg/m^3}$, and a quasi-isotropic layup $[45/-45/0/45/90/-45/0/90]_s$. The lamina constants from the manufacturer were given as $\mathrm{E_{11}} = 160.08\ \mathrm{GPa}, \mathrm{E_{22}} = 8.97\ \mathrm{GPa}, \upsilon_{12} = 0.28, \mathrm{G_{12}} = 6.21\ \mathrm{GPa}, \upsilon_{23} = 0.36$. The stringers were co-cured on the skin along the skin surface ply's fiber direction, with an additional 90º ply at the bonding interface.

The goal of the experiments was to validate the ability of identifying the reduction in elastic constants of the panels using the SIDO scanning prototype with access only to the skin side (Fig. 7.7(c)). The setup was to mimic a practical inspection at an airport depot where access to the interior aircraft structure is generally not allowed. The objective was to detect structural damage present not only in the skin but, more importantly, in the underlying stringer. Accordingly, the

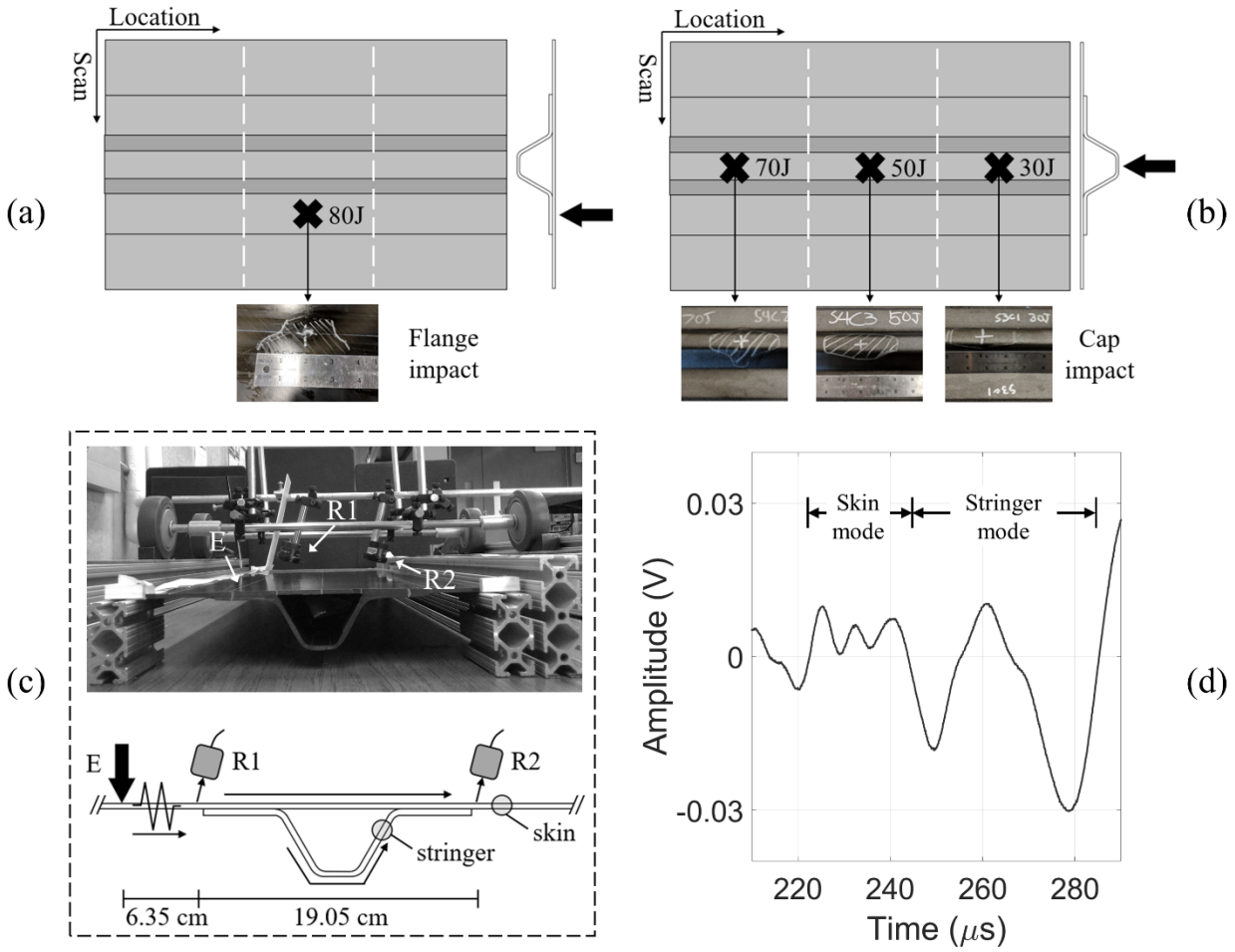

Figure 7.7: (a) The CFRP stiffened panel A with a flange impact damage. (b) The CFRP stiffened panel B with three cap impact damages. (c) The SIDO scanning cart on the test panel (d) The wave skin mode and stringer mode from different wave paths separated in R2 recording.

receivers R_1 and R_2 were positioned across the stringer (Fig. 7.7 (c)). It was also important that the wave energy generated by the impact excitation *E* in the skin be able to "penetrate" into the stringer. Referring to the schematic in Fig. 7.7(c), in addition to the direct flexural guided-wave mode propagating within the skin (the "skin wave mode"), it therefore existed a second wave path through the stringer (the "stringer wave mode"). The analysis of the "stringer mode" is the key to detect damage in the stringer. As shown by a typical waveform recorded by receiver R_2 in Fig. 7.7(d), the arrivals of both the "skin mode" and the "stringer mode" can be identified. Similarly to

the previous findings on the same test specimens [32], only lower frequency components were able to penetrate through the stringer, making the shape of the "stringer mode" wave packet easily distinguishable from the earlier "skin mode" arrival.

The two panels contained two kinds of defects that were of interest to this study. Shown in Fig. 7.7(a), panel A contained an 80 J impact damage located on the top surface of the skin side on the stringer flange ("flange impact"). Shown in Fig. 7.7(b), panel B contained three impact damage sites on the center of the stringer cap ("cap impacts"), with energies of 30 J, 50 J, and 70 J, respectively. Extensive inspections of the damage on the two panels were conducted by Ellison [38] using ultrasonic C-scan and Computed Tomography (CT) techniques. These scans revealed extensive damage that was expected to significantly degrade the elastic stiffness constants.

7.5.1 Panel with stringer flange impact damage

Typical waveforms recorded by the SIDO cart on panel A are shown in Fig. 7.8(a) and (b) for each of the two receivers, R_1 and R_2 respectively. These waveforms are normalized to the maximum amplitude of R1 for easy comparison with the case of the skin-only laminate in Fig. 7.6. Comparing the R2 waveforms in the stiffened panel of Fig. 7.8(b) to that of the skin-only laminate in Fig. 7.6(b), the flexural skin mode wave packet is attenuated nearly 10 times due to wave leakage and scattering added by the co-cured stringer. The time marker for fine phase tracing is carefully placed at the start of the skin mode wave packet, as shown by the cross mark in Fig. 7.8(b). The choice of the arrival time of the wave packet is dictated by the phase velocity estimation from SAFE using the manufacturer's constants and the observation of wave shapes. The center of the Hanning window is placed at the point of maximum amplitude for a certain arrival time region. The length of the window is 80 microsec for the skin mode and 100 microsec for the stringer mode. A comparison of the windowed flexural skin modes between a pristine region and the flange

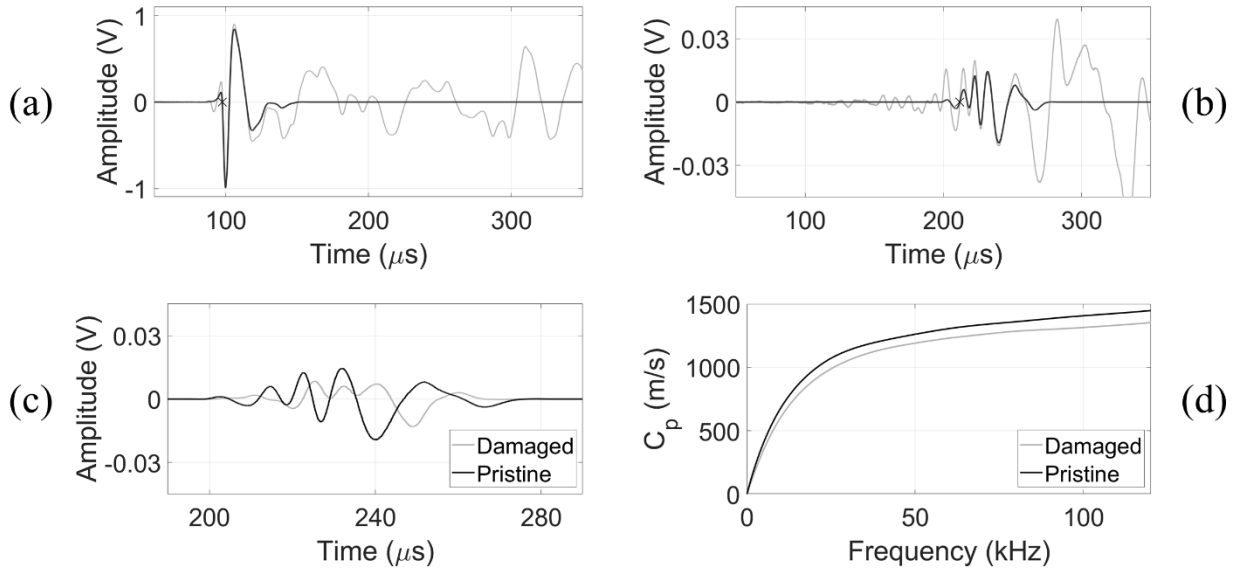

Figure 7.8: Effect of the stringer flange impact damage on wave dispersion in the test stiffened panel A. Typical raw waveform and windowed wave packet from R1 and (b) R2. (c) Phase delay of the skin mode from a line scan of the flange impact damage. (d) Drop of phase velocity dispersion curve of the impact flange damage relative to a pristine region.

impact region is shown in Fig. 7.8(c). The phase of the waveform recorded at the damaged location is significantly delayed (nearly half a period) compared to the pristine phase. The phase velocity dispersion curves in Fig. 7.8(d) further confirm this observation, showing a drop of phase velocity across the entire frequency spectrum of interest.

The inversion of seven effective elastic constants from one scan on panel A is shown in Fig. 7.9. The SIDO cart was scanned along the horizontal direction in the schematic, and the wave propagation direction was along the vertical direction (across the stringer). Each data point denotes the location of a line scan. The ground truth region of the flange impact damage from the ultrasonic and CT scans is shown and marked as shaded area in all plots. All engineering constants, with the exception of the Poisson's ratio, show a marked reduction corresponding to the damaged region. The constants E_x and E_y are numerically equal due to the quasi-isotropic layup. The drop of elastic constants as a parabola shape at the damage region is due to the extended area of matrix cracking

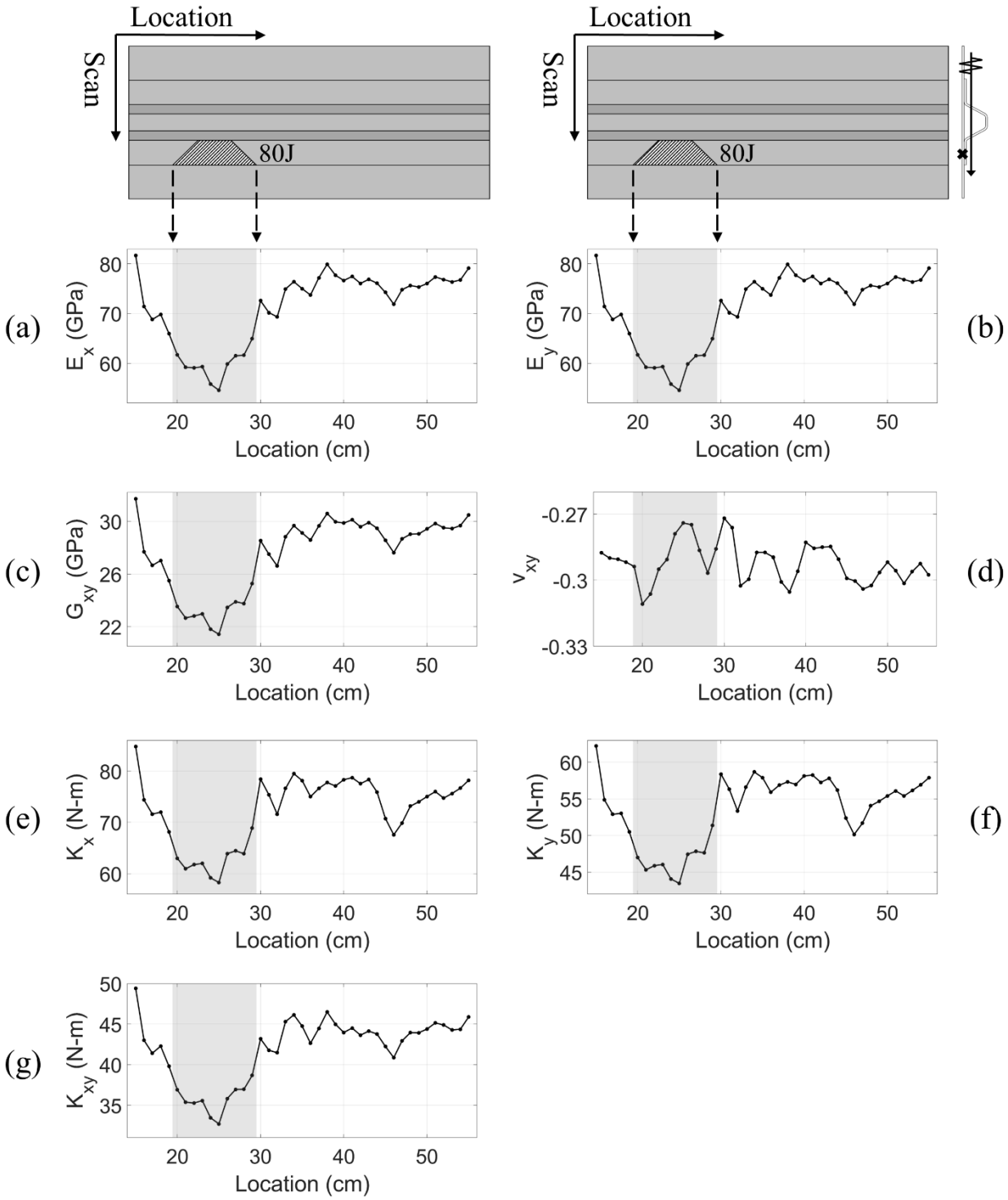

Figure 7.9: Effective elastic constants identified at several locations of the scan through the stringer flange impact in panel A. Inversion results of (a) axial stiffness $\boldsymbol{E_x}$, (b) transverse stiffness $\boldsymbol{E_y}$, (c) shear stiffness $\boldsymbol{G_{xy}}$, (d) Poisson's ratio $\boldsymbol{\upsilon_{xy}}$, (e) flexural rigidity $\boldsymbol{K_x}$, (f) flexural rigidity $\boldsymbol{K_y}$, and (g) torsional rigidity $\boldsymbol{K_{xy}}$.

and delamination produced by the impact, that was also shown in the independent ultrasonic C-scans of Ref. [38]. It is also interesting to observe the additional reduction in constants at the center of the damaged region (location 24 cm and 25 cm). The range of this further reduction coincides with the diameter of the impact hammer that created the damage (2 cm). Overall, the elastic constants inversion from the phase velocity dispersion curves shows a reasonable match with the known damage location. Interestingly, a smaller drop in most of the constants is also seen at a location of 46 cm. This could be an unknown damage or a manufacturing inhomogeneity.

7.5.2 Panel with stringer cap impact damage

Typical waveforms recorded by the system on panel B are shown in Fig. 7.10(a) and (b). The positioning of the "stringer mode" Hanning window at receiver R_2 overlaps one cycle with the earlier "skin mode" arrival, as confirmed by the time marker in Fig. 7.10(b). A flexural mode reception recorded by R_2 at a pristine location is compared to that recorded at a damaged location in Fig. 7.10(c). Contrarily to what was observed for stringer flange damage of panel A in Fig. 7.8(c), the guided wave packet at the stringer cap damage location has smaller phase lag compared to the pristine locations. The phase velocity dispersion curves in Fig. 7.10(d), measured at a pristine location and at a damaged location, also confirm this observation since the drop of velocity is only seen in a limited bandwidth.

For this case, the objective function of the optimization scheme was weighted/biased to put more emphasis on the lower frequency spectrum by using a logarithmically spaced sampling in the dispersion plot. The inversion of seven effective elastic constants, identified using the stringer wave mode from one scan on panel B, is shown in Fig. 7.11. As for panel A, the SIDO cart was scanned along the horizontal direction in the schematic, and the wave propagation was in the vertical direction (across the stringer). Unfortunately, additional measurement points between the

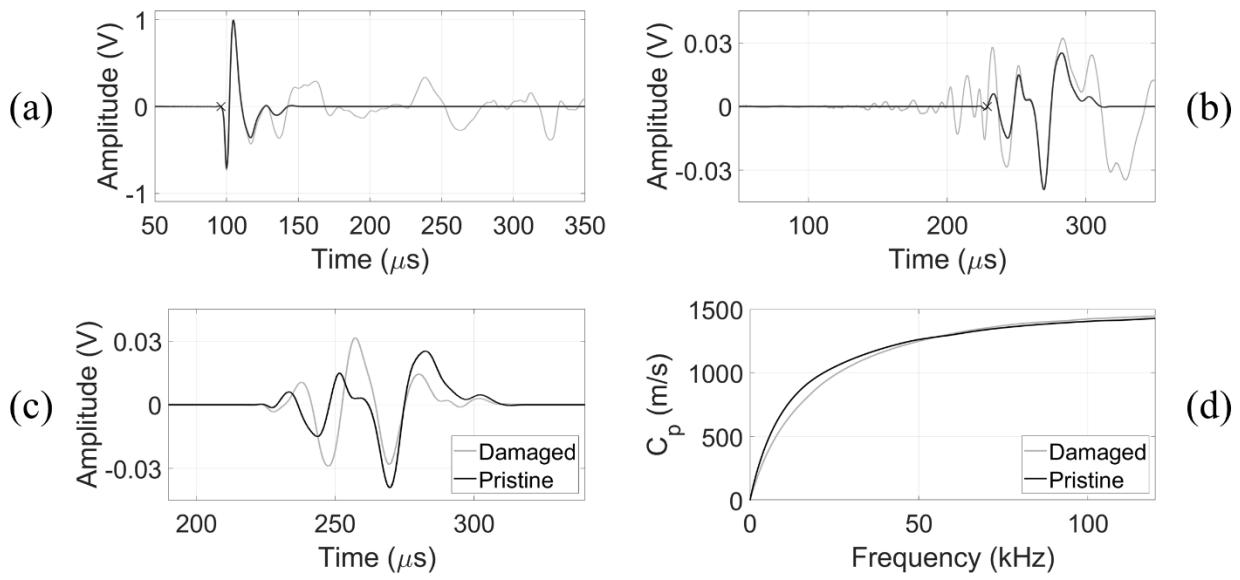

Figure 7.10: Effect of the stringer cap impact damage on the wave dispersion in the test stiffened panel B. Typical raw waveform and windowed wave packet from (a) R1 and (b) R2. (c) Phase delay of the stringer mode from a line scan of the cap impact damage. (d) Drop of phase velocity dispersion curve of the impact cap damage relative to a pristine region.

damaged locations, beyond the ones already shown, were not available. Shear ties installed transversely to the stringer between the damage sites, whose positions are marked by the white dashed lines in the top row of Fig. 7.11, prevented the cart from scanning these regions. Despite the limited drop in phase velocity dispersion curves discussed in the previous Fig. 7.10(d), all engineering constants in Fig. 7.11, with the usual exception of the Poisson's ratio, show a remarkable sensitivity to all damage sites, with the expected drop in values as a result of the structural degradation. The profile of the scan confirms the parabolic shape noted in panel A. The additional reduction in constants at the center of the impact is also observed for the 50 J impact at 50-51 cm and the 30 J impact at 81-82 cm. For the 70 J impact, the highest reduction is seen slightly off the center of the impact. Another notable observation is that the reduction of the constants increases with the level of impact energy, with the smallest reduction seen for the 30 J impact and the largest reduction seen for the 70 J impact. This correlation shows the potential to

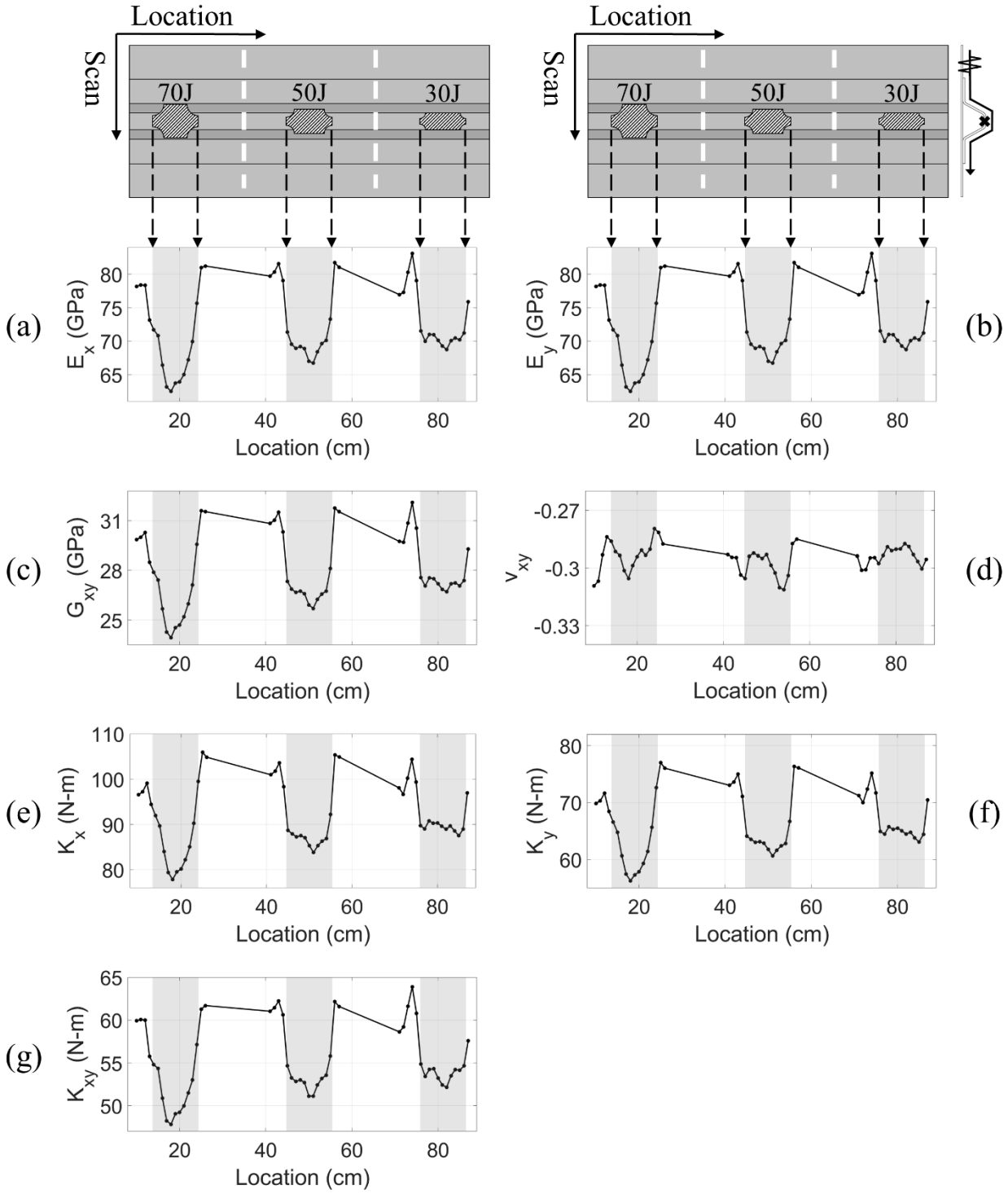

Figure 7.11: Effective elastic constants identified at several locations of the scan through the three stringer cap impacts in panel B using the stringer wave mode. Inversion results of (a) axial stiffness $\boldsymbol{E_x}$, (b) transverse stiffness $\boldsymbol{E_y}$, (c) shear stiffness $\boldsymbol{G_{xy}}$, and (d) Poisson's ratio $\boldsymbol{\upsilon_{xy}}$, (e) flexural rigidity $\boldsymbol{K_x}$, (f) flexural rigidity $\boldsymbol{K_y}$, and (g) torsional rigidity $\boldsymbol{K_{xy}}$.

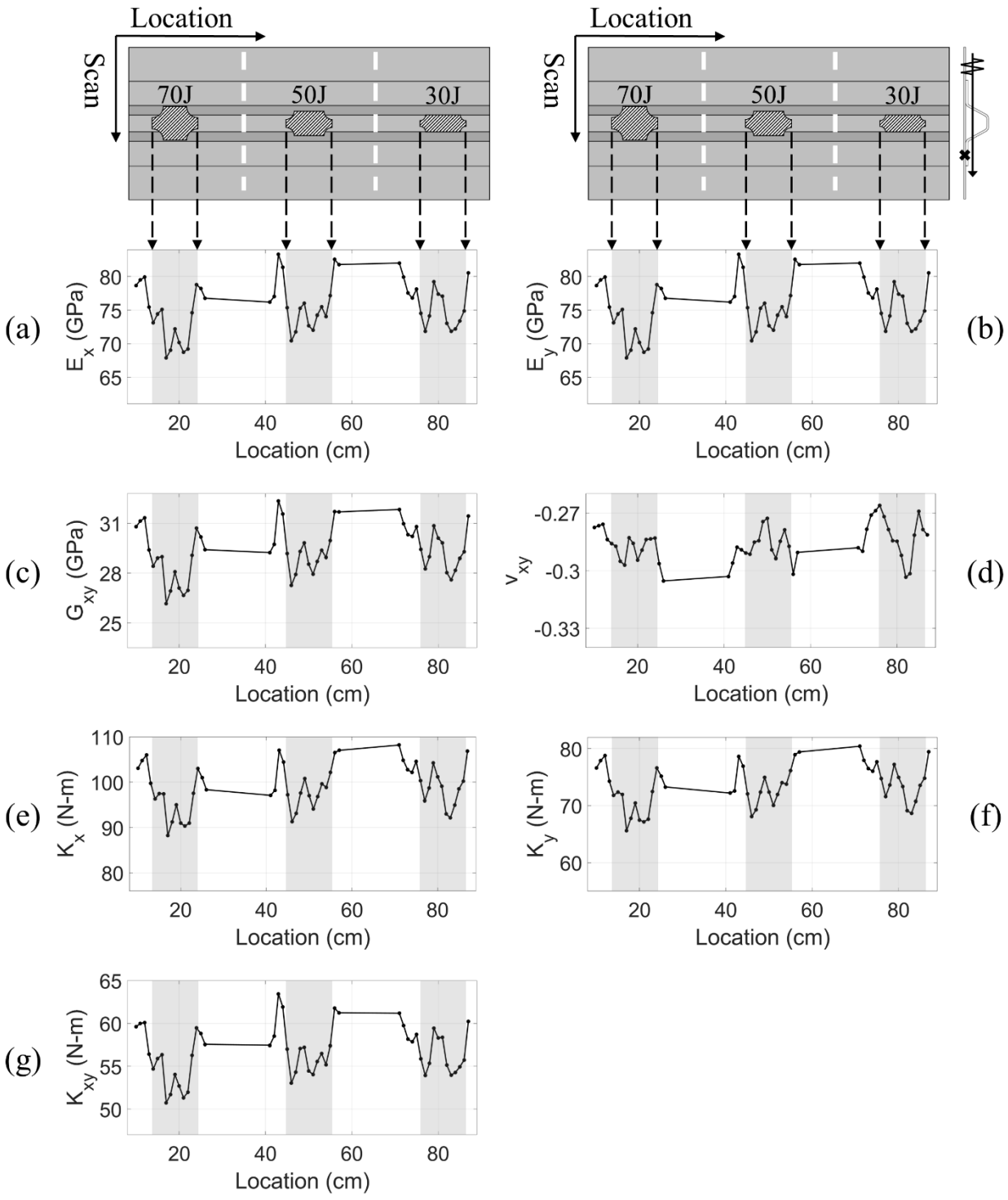

Figure 7.12: Effective elastic constants identified at several locations of the scan through the three stringer cap impacts in panel B using the skin wave mode. Inversion results of (a) axial stiffness $\boldsymbol{E_x}$, (b) transverse stiffness $\boldsymbol{E_y}$, (c) shear stiffness $\boldsymbol{G_{xy}}$, and (d) Poisson's ratio $\boldsymbol{\upsilon_{xy}}$, (e) flexural rigidity $\boldsymbol{K_x}$, (f) flexural rigidity $\boldsymbol{K_y}$, and (g) torsional rigidity $\boldsymbol{K_{xy}}$.

not only *detect* internal damage in the stringer from a skin-only access, but also to *quantify* the level of this damage and hence also to potentially determine residual strength.

A final analysis was carried out by utilizing the "skin wave mode" to identify the elastic constants in panel B. In this case the recorded waveforms were windowed to isolate the earlier arrival of the skin mode at receiver R_2. This was possible by visual inspection of the recorded waveforms that showed clear time separation between the two arrivals. The property identification results along a scan are shown in Fig. 7.12. Remarkably, a significant reduction in constants is again seen for all of the impact damage regions. As expected, this reduction is generally smaller than that seen in the previous Fig. 7.11 by tracking the "stringer wave mode" that propagates directly through the cap impact damage. The reason for the sensitivity of the skin mode to damage deep into the stringer cap is the changing boundary conditions at the stringer-to-skin connection. As also expected, the largest reduction in properties is seen for the strongest 70 J impact where damage directly extends to the stringer flange. In addition, the effect of increasing the window to extract wave modes may result in leakage into other modes.

7.6 Discussions and Conclusions

This chapter has presented a "single-input dual-output" (SIDO) ultrasonic scanning system for damage detection of stiffened composite panels based on the estimation of the elastic constants obtained by inverting phase velocity dispersion curves. The scanning system utilizes a light impactor as the wave generator and two air-coupled transducers as the non-contact wave detectors. The setup was designed to generate ultrasonic guided wave in a broad frequency range (DC-120 kHz) to increase the accuracy of the elastic constant identification and also to probe internal components of the panels. In order to enable constant identification in a scanning mode, the system

utilizes a phase-spectrum technique with a “coarse phase” vs. “fine phase” windowing that allows to experimentally measure the phase velocity dispersion curve of the dominant flexural mode from a single impact. The property identification algorithm utilizes a SAFE analysis as the forward model and Simulated Annealing as the optimization algorithm.

The technique was first tested on an aluminum plate and on a composite laminate. It was then applied to the inspection of stiffened skin-to-stringer composite panels with impact damage in the stringer flange and in the stringer cap. The results show a significant reduction in stiffness elastic constants in the damaged regions compared to the pristine regions of the test panel. More importantly, the drop in stiffness constants was monotonically correlated with the severity of damage, indicating the potential for damage quantification beyond damage detection. Beyond the identified trend, attempting to define a quantitative correlation between constants and damage severity would require additional work that would likely have to include the establishment of a ground truth for the impact damage such as from an ultrasonic C-scan analysis.

The results show the possibility to inspect built-up panels by only accessing the skin side. With proper time gating, the ultrasonic guided waves are not sensitive to the global boundary conditions of the part, and hence can be used for an *in-situ* inspection on a part in service. The technique is even more effective for anisotropic composite parts, where the propagating guided waves create normal/shear and in-plane/out-of-plane coupling phenomena. Clearly, the dispersion behavior of the wave in the anisotropic parts depends on the wave propagation direction. This coupling allows a reasonable identification of multiple elastic constants in various directions using a single wave propagation direction as restricted by the line scan configuration. The ability to identify elastic constants during an ultrasonic scan shown in this chapter brings additional information that opens the possibility to estimate residual strength.

The technique averages the wave propagation behavior between the two receivers. The elastic constant inversions are line average values for this distance. Consequently, it is not possible to resolve the precise position of damage along the ray path between the two receivers.

The SAFE forward model used in these results assumes the same properties for each lamina comprising the laminates (homogeneous laminate). Hence the optimization problem only involved five independent lamina constants (transversely isotropic). This model makes it impossible to discriminate damage within the cross-section of the waveguide. Discriminating damage in individual laminae would be possible by iterating the properties of each lamina in SAFE, which would increase the dimension of the optimization problem with additional computational burden.

In addition, the SAFE model assumes uniform cross-section along the wave propagation direction. The predicted dispersion curves for the stiffened composite panel presented in section 5 were modeled considering a flat laminate equal to the skin panel. Therefore there is an approximation in this case for the determination of the predicted dispersion curves. A more precise analysis would have to account for the stiffener discontinuity via, for example, a sophisticated Global-Local model [39]. While the absolute values of the phase velocities may be affected by this approximation, the reduction in velocities corresponding to the damaged sites (and therefore the corresponding reduction in elastic constants) was still clearly measurable. At the same time, since the detected modes in the stiffened panel were clearly separated as a "skin" mode and a "stinger" mode, the SAFE prediction considering an unstiffened panel should lead to a reasonable phase velocity curve for each of these modes tracked separately. Another generalization could be made to extend the inverse problem to visco-elastic property identification using complex stiffness coefficients in the SAFE formulation [24]. Such generalization could yield information on wave attenuation behavior that could provide an additional metric for damage quantification.

The flexural modes of guided waves were selected in this work due to their easy identification in the time domain. Other suitable wave receivers could be used to detect additional wave modes with higher SNR. For example, it was shown in [11] that combining the dispersion curves of the axial and flexural mode in a "joint" optimization scheme can sometime better identify the elastic properties in transverse directions.

The results presented here were limited to damage in the stringer component of the stiffened panel. Detecting damage in deeper components (e.g. the shear ties) would likely require a lower frequency transduction setup for deeper wave penetration from the skin side. Future work should be dedicated to establishing the sensitivity limit of the technique (using lower impact levels) and the overall statistical confidence of the property identification and damage detection. Additional studies should be also performed to directly relate the estimated engineering constants to the residual strength of the test panels. This step will likely require a series of load tests to failure for various degrees of damage.

Acknowledgements

This work was funded in part by the Federal Aviation Administration Joint Center of Excellence for Advanced Materials (FAA Cooperative Agreement 12-C-AM-UCSD) and by the Federal Railroad Administration (contract # 693JJ619C000008). The authors want to thank Prof. Hyonny Kim and his students at UCSD for providing invaluable technical information, designing, and constructing the composite stiffened panels and creating the impact damage in these panels. Thanks are also extended to Dr. Benjamin Katko for designing and constructing the high frequency CFRP impactor and collecting the 2D-FFT data in section 4, and to Dr. Margherita Capriotti for designing and constructing the frame of the scanning cart.

Chapter 7, in full, is a reprint of the material as it appears in C. Huang and F. Lanza di Scalea, "An Ultrasonic Scanning System for the Inspection of Composite Stiffened Panels from Elastic Constant Identification via Inversion of Guided Waves," *Composite Structures,* vol. 322, p. 117373, 2023. The dissertation author was the primary investigator and author of this paper.

References

[1] J. H. Tam, Z. C. Ong, Z. Ismail, B. C. Ang, and S. Y. Khoo, "Identification of material properties of composite materials using nondestructive vibrational evaluation approaches: A review," *Mech. Adv. Mater. Struct.*, vol. 24, no. 12, pp. 971–986, Sep. 2017.

[2] E. O. Ayorinde and R. F. Gibson, "Elastic constants of orthotropic composite materials using plate resonance frequencies, classical lamination theory and an optimized three-mode rayleigh formulation," *Compos. Eng.*, vol. 3, no. 5, pp. 395–407, Jan. 1993.

[3] J. De Visscher, H. Sol, W. P. De Wilde, and J. Vantomme, "Identification of the Damping Properties of Orthotropic Composite Materials Using a Mixed Numerical Experimental Method," *Appl. Compos. Mater.*, vol. 4, no. 1, pp. 13–33, Jan. 1997.

[4] R. F. Gibson, "Modal vibration response measurements for characterization of composite materials and structures," *Compos. Sci. Tech.*, vol. 60, no. 15, pp. 2769–2780, Nov. 2000.

[5] F. Daghia, S. de Miranda, F. Ubertini, and E. Viola, "Estimation of elastic constants of thick laminated plates within a Bayesian framework," *Compos. Struct.*, vol. 80, no. 3, pp. 461–473, Oct. 2007.

[6] J. Cugnoni, T. Gmür, and A. Schorderet, "Inverse method based on modal analysis for characterizing the constitutive properties of thick composite plates," *Comput. Struct.*, vol. 85, no. 17, pp. 1310–1320, Sep. 2007.

[7] S.-F. Hwang, J.-C. Wu, and R.-S. He, "Identification of effective elastic constants of composite plates based on a hybrid genetic algorithm," *Compos. Struct.*, vol. 90, no. 2, pp. 217–224, Sep. 2009.

[8] J. Cunha, S. Cogan, and C. Berthod, "Application of genetic algorithms for the identification of elastic constants of composite materials from dynamic tests," *Int. J. Numer. Meth. Eng.*, vol. 45, no. 7, pp. 891–900, 1999.

[9] A. Marzani and L. De Marchi, "Characterization of the elastic moduli in composite plates via dispersive guided waves data and genetic algorithms," *J. Intell. Mater. Syst. Struct.*, vol. 24, no. 17, pp. 2135–2147, Nov. 2013, doi: 10.1177/1045389X12462645.

[10] R. Cui and F. Lanza di Scalea, "On the identification of the elastic properties of composites by ultrasonic guided waves and optimization algorithm," *Compos. Struct.*, vol. 223, p. 110969, Sep. 2019.

[11] R. Cui and F. Lanza di Scalea, "Identification of Elastic Properties of Composites by Inversion of Ultrasonic Guided Wave Data," *Exp. Mech.*, vol. 61, no. 5, pp. 803–816, Jun. 2021.

[12] W. Staszewski, C. Boller, and G. R. Tomlinson, Health Monitoring of Aerospace Structures: Smart Sensor Technologies and Signal Processing. John Wiley & Sons, 2004.

[13] J. L. Rose, Ultrasonic Guided Waves in Solid Media. Cambridge University Press, 2014.

[14] V. Giurgiutiu, "17 - Structural health monitoring (SHM) of aerospace composites," in *Polymer Composites in the Aerospace Industry* (Second Edition), P. Irving and C. Soutis, Eds., in Woodhead Publishing Series in Composites Science and Engineering., Woodhead Publishing, 2020, pp. 491–558.

[15] K. Balasubramaniam, "Inversion of the Ply Lay-up Sequence for Multi-Layered Fiber Reinforced Composite Plates Using Genetic Algorithm," *Nondestruct. Test. Eval.*, vol. 15, no. 5, pp. 311–331, Nov. 1998.

[16] J. Vishnuvardhan, C. V. Krishnamurthy, and K. Balasubramaniam, "Genetic algorithm based reconstruction of the elastic moduli of orthotropic plates using an ultrasonic guided wave single-transmitter-multiple-receiver SHM array," *Smart Mater. Struct.*, vol. 16, no. 5, p. 1639, Aug. 2007, doi: 10.1088/0964-1726/16/5/017.

[17] E. V. Glushkov, N. V. Glushkova, and A. A. Eremin, "Guided wave based nondestructive testing and evaluation of effective elastic moduli of layered composite materials," *Mater. Phys. Mech.*, vol. 40, no. 1, pp. 56–60, 2015.

[18] B. Hosten, M. Castaings, H. Tretout, and H. Voillaume, "Identification of composite materials elastic moduli from Lamb wave velocities measured with single sided, contactless ultrasonic method," AIP Conference Proceedings, vol. 557, no. 1, pp. 1023–1030, Apr. 2001.

[19] P. Kudela, M. Radzienski, P. Fiborek, and T. Wandowski, "Elastic constants identification of woven fabric reinforced composites by using guided wave dispersion curves and genetic algorithm," *Compos. Struct.*, vol. 249, p. 112569, Oct. 2020.

[20] P. Kudela, M. Radzienski, P. Fiborek, and T. Wandowski, "Elastic constants identification of fibre-reinforced composites by using guided wave dispersion curves and genetic algorithm for improved simulations," *Compos. Struct.*, vol. 272, p. 114178, Sep. 2021.

[21] M. Rautela, A. Huber, J. Senthilnath, and S. Gopalakrishnan, "Inverse characterization of composites using guided waves and convolutional neural networks with dual-branch feature fusion," *Mech. Adv. Mater. Struct.*, vol. 29, no. 27, pp. 6595–6611, Dec. 2022.

[22] A. Martens, M. Kersemans, J. Daemen, E. Verboven, W. Van Paepegem, S. Delrue, and K. Van Den Abeele, "Characterization of the orthotropic viscoelastic tensor of composites using the Ultrasonic Polar Scan," *Compos. Struct.*, vol. 230, p. 111499, Dec. 2019.

[23] T. Hayashi, W.-J. Song, and J. L. Rose, "Guided wave dispersion curves for a bar with an arbitrary cross-section, a rod and rail example," *Ultrasonics*, vol. 41, no. 3, pp. 175–183, May 2003.

[24] I. Bartoli, A. Marzani, F. Lanza di Scalea, and E. Viola, "Modeling wave propagation in damped waveguides of arbitrary cross-section," *J. Sound Vib.*, vol. 295, no. 3, pp. 685–707, Aug. 2006.

[25] A. Marzani, "Time–transient response for ultrasonic guided waves propagating in damped cylinders," *Int. J. Solids Struct.*, vol. 45, no. 25, pp. 6347–6368, Dec. 2008.

[26] P. W. Loveday, "Simulation of piezoelectric excitation of guided waves using waveguide finite elements," *IEEE Trans. Ultrason., Ferroelect., Freq. Contr.*, vol. 55, no. 9, pp. 2038–2045, Sep. 2008.

[27] D. Alleyne and P. Cawley, "A two-dimensional Fourier transform method for the measurement of propagating multimode signals," *J. Acoust. Soc. Am.*, vol. 89, no. 3, pp. 1159–1168, Mar. 1991.

[28] W. Sachse and Y. Pao, "On the determination of phase and group velocities of dispersive waves in solids," *J. Appl. Phys.*, vol. 49, no. 8, pp. 4320–4327, Aug. 1978.

[29] P. R. Roth, "Effective measurements using digital signal analysis," *IEEE Spectr.*, vol. 8, no. 4, pp. 62–70, Apr. 1971.

[30] F. Lanza di Scalea, S. Sternini, and A. Y. Liang, "Robust passive reconstruction of dynamic transfer function in dual-output systems," *J. Acoust. Soc. Am.*, vol. 143, no. 2, pp. 1019–1028, Feb. 2018.

[31] D. R. Allen and W. H. B. Cooper, "A Fourier transform technique that measures phase delays between ultrasonic impulses with sufficient accuracy to determine residual stresses in metals," *NDT Int.*, vol. 16, no. 4, pp. 205–217, Aug. 1983.

[32] M. Capriotti and F. Lanza di Scalea, "Robust non-destructive inspection of composite aerospace structures by extraction of ultrasonic guided-wave transfer function in single-input dual-output scanning systems," *J. Intell. Mater. Syst. Struct.*, vol. 31, no. 5, pp. 651–664, Mar. 2020.

[33] P. Code, Eurocode 2: Design of concrete structures - Part 1-1: General rules and rules for buildings, British Standard Institution, London; 2005.

[34] ACI Committee. Building Code Requirements for Structural Concrete and Commentary (ACI 318-05). America Concrete Institute, 2005.

[35] C. E. Okafor, C. C. Ihueze, C. E. Okafor, and C. C. Ihueze, "Strength Analysis and Variation of Elastic Properties in Plantain Fiber/Polyester Composites for Structural Applications," in

Composite and Nanocomposite Materials - From Knowledge to Industrial Applications, IntechOpen, 2020.

[36] N. Ryden and C. B. Park, "Fast simulated annealing inversion of surface waves on pavement using phase-velocity spectra," *Geophysics*, vol. 71, no. 4, pp. R49–R58, Jul. 2006.

[37] M. Capriotti, H. E. Kim, F. L. di Scalea, and H. Kim, "Non-Destructive Inspection of Impact Damage in Composite Aircraft Panels by Ultrasonic Guided Waves and Statistical Processing," *Materials*, vol. 10, no. 6, Art. no. 6, Jun. 2017.

[38] A. C. Ellison, "Segmentation of X-Ray CT and Ultrasonic Scans of Impacted Composite Structures for Damage State Interpretation and Model Generation," Ph.D., University of California, San Diego, United States -- California, 2020. Accessed: Sep. 12, 2024.

[39] A. Spada, M. Capriotti, and F. Lanza di Scalea, "Global-Local model for guided wave scattering problems with application to defect characterization in built-up composite structures," *Int. J. Solids Struct.*, vol. 182–183, pp. 267–280, Jan. 2020.

Chapter 8 Conclusions and Opportunities for Future Research

This dissertation explores recent advancements in ultrasonic testing for nondestructive evaluation (NDE) and structural health monitoring (SHM) applications. The primary focus is on ultrasonic imaging techniques in bulk solids and waveguide structures, as well as the inversion of elastic constants in composite panels. Active SAFT modalities are investigated for defect imaging in bulk solids using a transducer wedge setup, and their implementation for quasi real-time rail flaw imaging is demonstrated through the development of two prototype systems. A passive SAFT modality is introduced, utilizing a deconvolution scheme in a dual-output system with normalized cross-power spectrum (NCPS) analysis. The results indicate robust and efficient passive reconstruction of transfer functions between receivers, applicable to active beamforming with a linear array. Additionally, a coherent and robust broadband adaptive matched field beamformer is proposed for achieving super-resolution imaging with a linear array. Unlike traditional MUSIC-type beamformers, the proposed coherent white noise constraint (C-WNC) algorithm does not require transfer matrix factorization. The results demonstrate high-quality focusing on the tips of horizontally extended targets, with a large dynamic range achieved through the adaptive beamformer's power output bias. The C-WNC image is further combined with delay-multiply-and-sum (DMAS) imaging to enhance resolution in both azimuth and range directions. The C-WNC algorithm is also applied to the imaging of impacts and defects in stiffened composite structures. A data-driven matched field beamforming approach is implemented to exploit the coherence of multimodal and dispersive ultrasonic guided waves. Imaging results demonstrate excellent target tracking using a sparse array, even under low signal-to-noise ratio (SNR) conditions. Finally, the dissertation introduces a scanning system for elastic constant inversion using non-contact

ultrasonic inspection of stiffened composite panels. The Semi-Analytical Finite Element (SAFE) model is employed as the forward model, and the inverse process is performed by minimizing the discrepancy between experimental dispersion curves and SAFE predictions using the simulated annealing optimization algorithm. An efficient method for measuring ultrasonic guided wave dispersion curves is demonstrated through phase difference spectrum analysis in a single-input dual-output system with uncontrolled sources.

Among the signal processing strategies explored in this dissertation, the search for coherent signals is critical to the success of ultrasonic testing in NDE and SHM applications. In basic SAFT imaging within an FMC framework, spatial coherence between inter-element response functions (transfer functions) allows for the generation of high-resolution, high-contrast images through a direct summation of all transmitter-receiver pairs in a standard DAS algorithm. The DMAS algorithm discussed in Chapter 5 further exploits this coherence while introducing increased algorithmic complexity. Besides spatial coherence, Chapter 2 demonstrates that temporal coherence in subaperture transmissions, such as virtual element or plane wave methods, enhances the physical signal-to-noise ratio (SNR) in each transmission event. These subaperture transmissions can be modeled similarly to standard synthetic aperture imaging techniques while maintaining algorithmic simplicity. Additionally, Chapter 2 highlights the benefits of accounting for multiple arrivals of ultrasonic wave modes. Even when the SAFT images from individual wave modes are incoherently summed, the spatial coherence of the scatterer ensures that the main lobe contributions are reinforced. In essence, the synthetic aperture in Chapter 2 comprises three elements: (1) physical synthesis of the wavefront through subaperture transmission, (2) synthetic summation of subapertures swept across the physical aperture, and (3) synthetic summation of wave modes as individual apertures, effectively augmenting the angular coverage of a limited-

view linear aperture without changing its physical size. The author is currently working on utilizing these coherence factors to improve 3D ultrasonic imaging using RSUs for rail flaw inspection.

The reconstruction of the pure structural transfer functions (or IRFs) in Chapter 4 also relies on the coherence of scattered signals received by passive listeners. It is widely accepted that the SNR of the reconstructed IRF is improved through extended passive recordings of these coherent arrivals over time, i.e. coda waves. Chapter 4 demonstrates that such coherence can be further enhanced by employing segmental averaging of the passive recordings in the estimation of the cross-power spectrum. Considering the potential application of passive SAFT for ultrafast imaging, the requirement for high framerate limits the duration of passive recordings available for IRF reconstruction. To address this, the coherence of identical ray paths in both causal and acausal times is leveraged to mitigate the challenges posed by limited recording times. The passive SAFT introduced in Chapter 4 can also be beneficial to the extraction of IRFs in waveguide structures, where the signal recordings are interfered with the transfer function of piezoelectric transducers. The signal deconvolution scheme using NCPS has high potential to overcome the frequency tuning effects commonly seen in these applications.

Chapter 5 introduces an adaptive matched field beamformer that exploits frequency coherence. The coherent white noise constraint (C-WNC) algorithm, originally designed for passive beamforming in underwater acoustics, is adapted for active imaging using the FMC dataset for defect detection in solids. By utilizing cross-frequency coherence in the supervector formulation, C-WNC overcomes several limitations of traditional MUSIC-type algorithms, such as difficulties in separating signal and noise subspaces, poor performance in low SNR conditions, and challenges in tracking off-axis targets with limited-view linear apertures. The advantages of C-WNC are further highlighted in Chapter 6, where it is applied to waveguide environment

exhibiting multimodal and dispersive characteristics. In data-driven matched field beamforming where experimental measurements encode complex wave propagation information into the replica vectors, the coherent summation of phase across frequency bands results in enhanced imaging when there is a precise match between the replica and the data. By fully exploiting these coherent factors, C-WNC demonstrates superior ability in tracking point-like scatterers within stiffened composite panels, even under conditions of low SNR and array gain.

Chapter 7 introduces an efficient method for extracting experimental phase velocity dispersion curves by utilizing phase coherence in a single-input dual-output system, as opposed to traditional 2D-FFT methods that require heavy spatial sampling. In the inspection of composite parts, active modalities with controlled acoustic sources are often unavailable. Similar to the passive IRF reconstruction in Chapter 4, this chapter employs a dual-output non-contact ultrasonic receiver system to extract the phase of the structural IRF. The phase velocity is estimated by calculating the phase spectrum difference between the two receivers, which can be transformed into phase velocity as a function of frequency, assuming both receivers embody the same IRFs and no 2π error present in phase unwrapping process. While this chapter primarily examines the reduction in average stiffness due to impact damage, the same methodology can be extended to various aspects of composite panel monitoring *in-situ*. These include estimating elastic properties in specific plies (e.g., surface ply in additive manufacturing), tracking stiffness changes during curing processes, and detecting common defects of automated fiber placement (AFP) processes such as poor consolidation, inter-laminar porosity, fiber angle deviations, gaps, overlaps, and wrinkles. The author is actively pursuing these extensions in ongoing work.